



DISSERTATION

Search for supersymmetric partners and anomalous couplings of the top quark with the CMS experiment

Ausgeführt zum Zwecke der Erlangung des Akademischen Grades eines Doktors der
Technischen Wissenschaften unter der Leitung von

Univ.Prof. Dipl.-Phys. Dr.rer.nat. Jochen Schieck

und

Dipl.-Ing. Dr.tech. Robert Schöffbeck

als verantwortlich mitwirkender Assistent

am Institut für Hochenergiephysik der Österreichischen Akademie der Wissenschaften
und am Atominstitut der TU Wien (E141)

EINGEREICHT AN DER TECHNISCHEN UNIVERSITÄT WIEN
FAKULTÄT FÜR PHYSIK

VON

Dipl.-Ing. Daniel Spitzbart, BSc.

Matrikelnummer 1027561

Deinhardsteingasse 29/34, 1160 Wien

daniel.spitzbart@gmail.com

Wien, am 12. Juli 2019



Die approbierte gedruckte Originalversion dieser Dissertation ist an der TU Wien Bibliothek verfügbar.
The approved original version of this doctoral thesis is available in print at TU Wien Bibliothek.

Abstract

The standard model of particle physics (SM) comprises our current understanding of elementary particles and their interactions, describing results of experiments at vastly different energy scales at the highest precision. However, several shortcomings of the SM, such as the naturalness problem of the Higgs boson, a missing dark matter candidate, and the lack of gauge coupling unification motivate searches for physics beyond the SM (BSM).

Supersymmetry (SUSY) is among the most promising theories to extend the SM and predicts the existence of several new elementary particles. In many SUSY scenarios, the mass of the top squark, the SUSY partner of the SM top quark, is expected to be not much larger than the top quark mass, enabling its pair production in the high energetic proton-proton collisions at the LHC. Events with two oppositely charged leptons, jets identified as originating from b quarks, and large missing transverse momentum are selected from collision data collected by the CMS experiment in 2016 at a center-of-mass energy of 13 TeV in order to search for hints of top squark pair production. Transverse mass variables are used to separate the potential signal from the dominant top quark pair production background. Under certain model assumptions, the search is sensitive to the production of top squarks with masses up to 1.3 TeV.

The production of a Z boson in association with a top quark pair ($t\bar{t}Z$) is a large irreducible background for this search. A precise measurement of its cross section is therefore of great importance to reduce systematic uncertainties. Additionally, the coupling of the top quark to the Z boson is sensitive to corrections from physics beyond the standard model and is therefore a promising probe of new physics. A sample with high purity of $t\bar{t}Z$ events is selected by requiring at least three charged leptons, out of which two leptons with same flavor form a Z boson candidate, and at least one jet is required to be b-tagged. The combined 2016 and 2017 collision data recorded by the CMS experiment is used for this measurement, allowing for the first differential cross section measurement of the process. The large data set, together with precise evaluation of signal and background acceptance and efficiency, results in the most precise determination of the $t\bar{t}Z$ cross section to date. Measurements of the momentum of the Z boson candidate and the angular distribution its decay products are used to set tight direct constraints on the top quark dipole moments and dimension six operators in the context of the SM effective field theory (SMEFT).



Die approbierte gedruckte Originalversion dieser Dissertation ist an der TU Wien Bibliothek verfügbar.
The approved original version of this doctoral thesis is available in print at TU Wien Bibliothek.

Kurzfassung

Die bekannten Elementarteilchen und deren Wechselwirkungen werden vom Standardmodell der Teilchenphysik (SM) beschrieben. Experimentelle Ergebnisse auf unterschiedlichsten Energieskalen können mithilfe des SM verstanden werden. Trotz dieser Erfolge ist das SM unvollständig, etwa weil die unnatürlich kleine Masse des Higgs-Bosons nicht zufriedenstellend erklärt werden kann. Das SM beinhaltet außerdem kein Teilchen, das die dunkle Materie ausmachen könnte. Auch die Vereinheitlichung der Grundkräfte kann nicht erreicht werden. Diese Unzulänglichkeiten haben zur Entwicklung von Theorien jenseits des SM (BSM) geführt. Die Supersymmetrie (SUSY) ist eine Theorie zur Erweiterung des SM, die die Existenz von neuen Elementarteilchen vorhersagt. In vielen SUSY Szenarien ist die Masse des Top-Squarks nicht viel höher als jene seines SM Partners, dem Top-Quark. Daher könnte es in den hochenergetischen Proton-Proton-Kollisionen am LHC paarweise erzeugt werden. Um nach Hinweisen auf die Produktion der Top-Squarks zu suchen, werden Ereignisse mit zwei gegengleich geladenen Leptonen, Jets von Bottom-Quarks, und einem hohen transversalen Impulsungleichgewicht, selektiert. Die Kollisionsdaten, die für diese Suche verwendet werden, wurden mit dem CMS Experiment im Jahr 2016 bei einer Schwerpunktsenergie von 13 TeV aufgezeichnet. Um SM und SUSY Ereignisse zu unterscheiden werden Variablen verwendet, die die transversale Masse der Leptonen und anderer Objekte beschreiben. Top-Squarks mit Massen bis zu 1.3 TeV können für bestimmte SUSY Modelle ausgeschlossen werden.

Die gemeinsame Produktion eines Top-Quark-Paars mit einem Z-Boson ($t\bar{t}Z$) ist der größte irreduzible SM Hintergrund für diese Suche. Eine genaue Messung des Produktionswirkungsquerschnitts dieses Prozesses ist daher eine Möglichkeit, die Sensitivität von SUSY Suchen zu erhöhen. Außerdem sagen viele BSM Theorien eine modifizierte Kopplung des Top-Quarks an das Z-Boson vorher. Um diese Kopplung zu messen werden Ereignisse mit drei Leptonen und zumindest einem Jet von einem Bottom-Quark aus den 2016 und 2017 aufgezeichneten Kollisionsdaten des CMS Experiments selektiert. Die große Anzahl an aufgezeichneten Kollisionen ermöglicht die differenzielle Messung des $t\bar{t}Z$ Wirkungsquerschnitts und erlaubt daher erstmals eine Einschränkung der elektro-schwachen Dipolmomente des Top-Quarks durch eine direkte Messung. Weiters werden enge Grenzen für eine modifizierte Top-Z Wechselwirkung im Kontext einer Effektiven Feldtheorie (SMEFT) gesetzt.

Contents

1	Introduction	1
2	The Standard Model and Beyond	3
2.1	The Standard Model of Particle Physics	3
2.2	Supersymmetry	11
2.3	Effective Field Theories	17
2.4	Simplified Models	21
3	The CMS experiment at the CERN LHC	23
3.1	The Large Hadron Collider	23
3.2	The CMS detector	25
3.3	Reconstruction of particles	30
3.4	Simulation of events	35
4	Search for top squarks and dark matter particles in dilepton final states	37
4.1	Data sets and simulation	41
4.2	Event triggers	42
4.3	Object and event selection	43
4.4	Background estimation	49
4.5	Systematic uncertainties	65
4.6	Results	67
4.7	Interpretation	67
4.8	Improvements towards an analysis of the full Run 2 data set	78
4.9	Summary	82
5	Search for anomalous top-Z couplings	85
5.1	Data sets and simulation	87
5.2	Event triggers	87
5.3	Object and event selection	89
5.4	Backgrounds	91

5.5	Observables and signal regions	97
5.6	Signal scans	102
5.7	Systematic uncertainties	102
5.8	Results	108
5.9	Summary	116
6	Conclusions	117
A	Appendix	119
A.1	Trigger efficiencies	119
A.2	Control region plots	123
A.3	Correlation studies	125
A.4	Curriculum vitae	127
	Bibliography	133
	Acknowledgements	153

Introduction

THE FIELD OF HIGH ENERGY PHYSICS is currently observing a triumph of the standard model of particle physics. The SM describes interactions between elementary particles from sub-electronvolts (eV) up to the TeV range. The SM has been completed by the discovery of a Higgs boson in 2012, jointly observed by the ATLAS and CMS collaborations [1, 2]. Predicted already in the 1960's [3, 4] in order to solve the puzzle of the mass of the mediators of the weak force (W and Z bosons), it took about half a century and enormous technical efforts for experimental confirmation. Before that, the discovery of heavy particles like the τ lepton [5] or the top quark [6, 7] had paved the way for establishing the SM. Precision measurements of the properties of the W and Z bosons allowed the prediction of the top quark mass with good accuracy [8]. Now, only two decades after its discovery, top quarks are abundantly produced at the Large Hadron Collider (LHC) at CERN. From 2015 to 2018, more than 100 million top quark pairs have been produced and can now be studied to further test the validity of the SM. Despite its success and predictive power, the SM is an incomplete theory. Most prominently, it lacks a conclusive explanation for Dark Matter, it does not describe gravity, and it leaves the question about the smallness of the Higgs boson mass unanswered.

At particle colliders, there are two general strategies to search for effects beyond the SM: If new particles are light enough, they can be directly produced in the proton-proton collisions at the LHC. A theory that predicts an abundance of new particles is supersymmetry (SUSY), described in Chapter 2. Each known SM particle is predicted to have a SUSY partner. One of these new particles therefore is the top squark, the scalar partner of the top quark. With an expected mass of about 1 TeV, it could be produced in pairs and then decay to its SUSY partner, the top quark, and a stable SUSY particle. After a short introduction to the CMS experiment at the CERN LHC in Chapter 3, the following Chapter 4 describes the search for the production of top squarks in final states with two charged leptons with the CMS experiment. By analyzing the data set recorded in 2016, stringent limits on the allowed masses of the top squark can be obtained. At the same time, the results are also used to test models of Dark Matter production via heavy mediators, and to constrain the decay of the Higgs boson

into invisible particles.

The second approach to searches for BSM physics is to look out for subtle deviations in the data resulting from coupling modifications between SM particles. For example, new particles that are too heavy to be resonantly produced, can modify the couplings of the top quark to the weak gauge bosons. Chapter 5 describes the measurement and interpretation of the coupling of the Z boson to the top quark in events where a top quark pair is produced in association with a Z boson ($t\bar{t}Z$). For the first time, the differential distributions of the Z boson momentum and its polarization are used to improve sensitivity to deviations from the SM predictions.

The $t\bar{t}Z$ process with $Z \rightarrow \nu\nu$ is moreover the largest expected irreducible SM background in the most sensitive SUSY signal regions. Therefore, the precise knowledge of the cross section of the $t\bar{t}Z$ process directly improves sensitivity to top squark pair production.

During the work on this thesis contributions to several publications were provided:

Peer-reviewed

[9] CMS Collaboration, “Measurement of top quark pair production in association with a Z boson in proton-proton collisions at $\sqrt{s} = 13$ TeV”, CMS-PAS-TOP-18-009, CERN, 2019, *Submitted to JHEP*

[10] CMS Collaboration, “Performance of missing transverse momentum reconstruction in proton-proton collisions at $\sqrt{s} = 13$ TeV using the CMS detector”, *JINST* **14** (2019), P07004

[11] CMS Collaboration, “Search for top squarks and dark matter particles in opposite-charge dilepton final at CMS”, *PoS ALPS2018* (2018) 055

[12] CMS Collaboration, “Search for top squarks and dark matter particles in opposite-charge dilepton final states at $\sqrt{s} = 13$ TeV”, *Phys. Rev.* **D97** (2018) 3, 032009

[13] CMS Collaboration, “Search for supersymmetry in events with one lepton and multiple jets exploiting the angular correlation between the lepton and the missing transverse momentum in proton-proton collisions at $\sqrt{s} = 13$ TeV”, *Phys. Lett.* **B780** (2018) 384-409

Non-peer-reviewed

[14] CMS Collaboration, “First constraints on invisible Higgs boson decays using $t\bar{t}H$ production at $\sqrt{s} = 13$ TeV”, CMS-PAS-HIG-18-008, CERN, 2019

[15] HL-LHC and HE-LHC Working Group, “Standard Model Physics at the HL-LHC and HE-LHC”, CERN-LPCC-2018-03, CERN, 2019

The Standard Model and Beyond

2.1 The Standard Model of Particle Physics

Elementary matter particles and their interactions are described by the SM with impressive precision up to the highest energies that are achievable in earth-bound particle collisions. Because of its high predictive power and, despite enormous efforts, the absence of experimental evidence contradicting the SM, it is referred to as “the unsung triumph of modern physics”. The SM incorporates the strong, the weak, as well as the electromagnetic interaction. A description of gravity is not part of the SM, however, it can be neglected due to its weakness on the microscopic scale. Table 2.1 gives an overview of the four fundamental forces and their respective strength.

Elementary particles are classified into two groups: matter particles with half integer spin, called fermions, which obey the Pauli exclusion principle, and mediator particles with integer spin, called bosons. Fermions are grouped in three generations with the same gauge quantum numbers, each containing two quarks and leptons. Anti-particles of fermions carry the negative electric charge of the respective particle.

Table 2.1: The fundamental interactions. The graviton is a hypothetical particle and mentioned for completeness only.

Interaction	Gauge Boson	Mass (GeV)	Associated Charge	Range	Relative Strength
strong	gluon g	0	color	short	1
electromagnetic	photon γ	0	electric	infinite	10^{-2}
weak	W^\pm	80.38	isospin	short	10^{-7}
	Z	91.18			
gravity	graviton	0		infinite	10^{-39}

Table 2.2: Fermion generations, electric charges and masses.

	Charge	1 st generation		2 nd generation		3 rd generation	
		Name	Mass (MeV)	Name	Mass (GeV)	Name	Mass (GeV)
up-type quark	+2/3	up	2.2	charm	1.275	top	173
down-type quark	-1/3	down	4.7	strange	0.095	bottom	4.18
charged lepton	-1	electron	0.511	muon	0.106	tauon	1.77
neutrino	0	ν_e	< 2 eV	ν_μ	< 2 eV	ν_τ	< 2 eV

Quarks

Quarks participate in all SM interactions and carry fractional electric charge. Protons and neutrons, the constituents of atomic nuclei, are bound states of the quarks of the first generation, the up (electric charge +2/3) and the down quark (electric charge -1/3). Second and third generation quarks can be viewed as heavier replicas of the up and down quark, and can form bound states with short lifetimes. An overview of the quarks and their quantum numbers is given in Tab. 2.2.

Leptons

The quantum numbers of leptons follow the same pattern. Charged leptons, like the first generation electron, participate in electromagnetic and weak interactions. Neutral leptons, also called neutrinos (*light neutron*), only interact via the weak force and are therefore hard to detect in particle collider experiments. All three lepton generations are shown in Tab. 2.2.

Vector Bosons

Vector bosons carry a spin of 1 and are the mediators of the SM interactions. Gluons are the massless carriers of the strong force and couple to the so-called color charge. Since gluons themselves are color charged, they can also self-interact. The force carrier of the electromagnetic interaction is the massless photon. The weak force is mediated by the massive W and Z bosons. Due to the large mass of these bosons, the weak interaction is short ranged.

Scalar Bosons

The existence of a Higgs Boson, the only fundamental scalar (spin 0) particle, was experimentally confirmed in 2012. Quarks and charged leptons acquire their masses by couplings to the Higgs boson, as will be described in Sec. 2.1.1.

2.1.1 Symmetries of the Standard Model

Symmetries play a fundamental role in the construction of the SM: the Poincare symmetry is the symmetry group of space-time (Lorentz transformations and space-time translations). According to the Coleman-Mandula theorem, it can be extended by a gauge group as a direct product with the Poincare group. These symmetries are used to classify particles by the conserved quantum numbers associated with the symmetries. The gauge symmetry specifies the interaction of the force carrier with the matter particle. The gauge group that defines the interactions of the SM matter particles is

$$G_{SM} = SU(3)_C \times SU(2)_L \times U(1)_Y \quad . \quad (2.1)$$

According to the principle of local gauge symmetry, each generator of the symmetry group introduces a gauge field, which can be associated with a vector boson field. In order to define a gauge invariant action $\mathcal{S} = \int \mathcal{L} d^4x$ the Lagrangian \mathcal{L} itself is required to be invariant. As an example, one can start with the Lagrangian of a complex scalar field ϕ

$$\mathcal{L} = \partial_\mu \phi \partial^\mu \phi^* - V(\phi, \phi^*) \quad , \quad (2.2)$$

which is invariant under a global transformation $\phi \rightarrow e^{i\alpha} \phi$ with α constant (independent of x). However, for a local variation $\alpha = \alpha(x)$, the kinetic term of the Lagrangian is not invariant:

$$\partial_\mu \phi \rightarrow e^{i\alpha} (\partial_\mu \phi + i(\partial_\mu \alpha) \phi) \quad . \quad (2.3)$$

Symmetry can be restored by defining the covariant derivative

$$D_\mu \phi = \partial_\mu \phi + iA_\mu \phi \quad (2.4)$$

with a gauge potential A_μ that transforms as $A_\mu \rightarrow A'_\mu = A_\mu - \partial_\mu \alpha$. One can then show that by using the covariant derivative, the kinetic term is again invariant

$$D_\mu \phi \rightarrow e^{i\alpha} (\partial_\mu \phi + i(\partial_\mu \alpha) \phi + i(A_\mu - \partial_\mu \alpha) \phi) = e^{i\alpha} D_\mu \phi \quad . \quad (2.5)$$

The Lagrangian becomes

$$\mathcal{L} = D_\mu \phi D^\mu \phi^* - V(\phi, \phi^*) \quad (2.6)$$

which contains interaction terms between ϕ and A_μ of the form of $A_\mu \phi A^\mu \phi$. Similarly, a Lagrangian for a spin- $\frac{1}{2}$ fermion ψ of the form

$$\mathcal{L} = \bar{\psi} \gamma^\mu D_\mu \psi \quad (2.7)$$

includes an interaction term of the fermion fields and the gauge field, $\bar{\psi}A_\mu\psi$. The previously free Lagrangian is thus extended by interaction terms with the gauge fields by requiring local gauge invariance.

Strong interaction: the $SU(3)_C$ group

The $SU(3)_C$ group is the symmetry group of the strong interaction which is described by quantum chromodynamics (QCD). The strong force is associated with a charge that can take three different states and is therefore commonly called *color* charge. In this case, the covariant derivative takes the form

$$D_\mu = \partial_\mu + ig\mathbf{G}_\mu \quad , \quad (2.8)$$

with the strong coupling constant g and the gauge fields \mathbf{G}_μ , given by

$$\mathbf{G}_\mu = \sum_{a=1}^8 G_\mu^a T_a \quad . \quad (2.9)$$

T_a are the Gell-Mann matrices, which are one potential representation of the 8 generators of the $SU(3)$ group that are associated with the 8 gluons. The generators satisfy the commutator relations

$$[T_a, T_b] = if_{abc}T_c \quad . \quad (2.10)$$

The non-abelian gauge structure of the strong interaction has two fundamental consequences: confinement and asymptotic freedom [16,17]. Color confinement predicts that only color neutral states can be observed in nature, which can be formed by different combinations of quarks. Mesons consist of a quark-antiquark pair ($q\bar{q}$), where color and anti-color form a neutral state, while baryons (qqq) are colorless due to the combination of three different colors. Tetraquarks ($q\bar{q}q\bar{q}$) and pentaquarks ($qqq\bar{q}q$) have been observed only recently [18,19]. When a single quark is emitted from e.g. a high energetic pp collision, a color neutral state is reestablished by the production of a $q\bar{q}$ pair from the vacuum, a process that is called hadronization. As a consequence, the strong interaction has only short range since no long range color-charged currents can be established. On the contrary, at short distances corresponding to high energies, quarks behave like free particles because the strong coupling constant decreases as a function of the momentum transfer. This asymptotic freedom allows for perturbative calculations at high collision energies.

Electroweak interaction: the $SU(2)_L \times U(1)_Y$ group

The electromagnetic and weak interactions can be formulated as a unified theory with the $SU(2)_L \times U(1)_Y$ gauge group [20,21]. The covariant derivative is defined as

$$D_\mu = \partial_\mu + i\frac{g'}{2}B_\mu + i\frac{g}{2}\mathbf{W}_\mu \quad , \quad (2.11)$$

where B_μ corresponds to the $U(1)$ gauge field, and \mathbf{W}_μ to the $SU(2)$ gauge fields. The corresponding couplings of the $SU(2)_L$ and $U(1)_Y$ group are the weak isospin g and the weak hypercharge g' , respectively. The three generators of the non-abelian weak isospin group $SU(2)_L$, W_1 , W_2 and W_3 , form a so-called isospin triplet, while the generator of the $U(1)_Y$ group, B , forms a hypercharge singlet. Due to symmetry breaking, discussed in the following section, the W_3 and B fields mix and form the massive Z boson and the massless photon according to

$$\begin{pmatrix} \gamma \\ Z \end{pmatrix} = \begin{pmatrix} \cos \theta_W & \sin \theta_W \\ -\sin \theta_W & \cos \theta_W \end{pmatrix} \begin{pmatrix} B \\ W_3 \end{pmatrix}, \quad (2.12)$$

where θ_W is the weak mixing angle, also called Weinberg angle. The $SU(2)_L$ and $U(1)_Y$ couplings relate to the Weinberg angle according to

$$\cos \theta_W = \frac{g}{\sqrt{g^2 + g'^2}}. \quad (2.13)$$

The electrically charged W^\pm bosons are linear combinations of the W_1 and W_2 , given by

$$W^\pm = \frac{1}{\sqrt{2}} (W_1 \mp iW_2). \quad (2.14)$$

Spontaneous symmetry predicts a tree-level relation between the couplings and gauge boson masses of the form

$$\cos \theta_W = \frac{M_W}{M_Z}. \quad (2.15)$$

Spontaneous Symmetry Breaking

In the unbroken electroweak theory, fermions of different chirality are treated as different fields. Dirac mass terms are bilinear in the chiral components, and therefore, a gauge invariant coupling would predict that the chiral components have the same gauge quantum numbers, in contrast to experiments. Similarly, masses for gauge bosons break gauge invariance. However, experimental observations clearly show that fermions and weak gauge bosons are massive. Therefore, a different mechanism is needed to generate masses for elementary particles. This mechanism is known as Brout-Englert-Higgs (BEH) mechanism and was first discussed in 1964 [3, 4]. One starts with introducing a complex scalar doublet

$$\phi = \begin{pmatrix} \phi^+ \\ \phi^0 \end{pmatrix}. \quad (2.16)$$

The Lagrangian density of scalar fields has the form of

$$\mathcal{L} = (D_\mu \phi)^\dagger (D^\mu \phi) - V(\phi^\dagger \phi) \quad (2.17)$$

with a covariant derivative D_μ , similarly to Eq. 2.11. The potential V has the form of

$$V(\phi^\dagger\phi) = -\mu^2\phi^\dagger\phi + \lambda(\phi^\dagger\phi)^2 \quad (2.18)$$

which, by implying the condition $\mu^2, \lambda > 0$, is the infamous *mexican hat* potential with a minimum at

$$|\phi|^2 = \frac{\mu^2}{2\lambda} \equiv \frac{v^2}{2} \quad . \quad (2.19)$$

Here, v is the vacuum expectation value (VEV) of the neutral component of the Higgs doublet. One can expand ϕ around the minimum and apply a $SU(2)_L$ transformation to obtain the vacuum state

$$\phi(x) = \frac{1}{\sqrt{2}} \begin{pmatrix} 0 \\ v + H(x) \end{pmatrix} \quad . \quad (2.20)$$

Physically, the rotation is equivalent to the W and Z bosons absorbing three Goldstone bosons and, as a consequence, acquire their mass. By inserting Eq. 2.20 into Eq. 2.18 one obtains

$$V = \frac{1}{2}(2\lambda v^2)H^2 + \lambda v H^3 + \frac{\lambda}{4}H^4 + \text{const.} \quad . \quad (2.21)$$

From this formulation of the scalar potential, one can read off the mass of the Higgs boson as $m_H^2 = 2\lambda v^2$. The second and third term of Eq. 2.21 are cubic and quartic self couplings of the Higgs boson. The dynamical part of Eq. 2.17 becomes

$$\begin{aligned} (D^\mu\phi)^\dagger(D_\mu\phi) &= \frac{1}{2}\partial^\mu H\partial_\mu H + \left[\frac{1}{2}\left(\frac{gv}{2}\right)^2 W^{\mu+}W_\mu^- + \right. \\ &\quad \left. + \frac{1}{2}(g^2 + g'^2)\left(\frac{v}{2}\right)^2 Z^\mu Z_\mu\right] \left(1 + \frac{H}{v}\right)^2 \quad . \end{aligned} \quad (2.22)$$

The W and Z gauge bosons have thus acquired masses of $m_W^2 = \left(\frac{gv}{2}\right)^2$ and $m_Z^2 = (g^2 + g'^2)\left(\frac{v}{2}\right)^2$, while the photon stays massless. One consequence irrespective of the knowledge of the Higgs boson mass is that the Z boson is heavier than the W bosons. This has been confirmed experimentally [22, 23]. The mass relation of Eq. 2.15 is approximately respected by the W and Z bosons.

Fermion masses are generated via a Yukawa couplings to the Higgs field, hence the coupling of the Higgs boson to fermions is proportional to their mass. The mass term for quarks has the form of

$$\mathcal{L}_{\text{mass}} = -Y_{ij}^d \bar{Q}^i \phi d_R^j - Y_{ij}^u \bar{Q}^i \tilde{\phi} u_R^j + h.c. \quad , \quad (2.23)$$

where Y_{ij}^u and Y_{ij}^d are complex 3×3 matrices for up- and down-type quarks. After symmetry breaking the mass term can be written as

$$\mathcal{L}_{\text{mass}} = -\frac{v}{\sqrt{2}} Y_{ij}^d \bar{d}_L^i d_R^j - \frac{v}{\sqrt{2}} Y_{ij}^u \bar{u}_L^i u_R^j + h.c. \quad . \quad (2.24)$$

By changing from the flavor to the mass basis the mass terms become

$$\mathcal{L}_{\text{mass}} = -m_j^d \bar{d}_L^j d_R^j - m_j^u \bar{u}_L^j u_R^j + h.c. \quad . \quad (2.25)$$

This basis change also modifies the kinetic terms of the Lagrangian. In the flavor basis, gauge boson interactions do not mix flavor families. B_μ and W_μ^3 couplings are not affected by performing the flavor rotation, however, W_μ^\pm terms are modified to $W_\mu^+ \bar{u}_L^i \gamma^\mu V^{ij} d_L^j$ and $W_\mu^- \bar{d}_L^i \gamma^\mu V^{\dagger ij} u_L^j$, respectively. Interactions of fermions with the W bosons therefore change the flavor, while interactions with the Z boson or photon preserve flavor. All effects from flavor mixing by the charged gauge bosons are given by one matrix V , the Cabibbo-Kobayashi-Maskawa (CKM) matrix [24]. The CKM matrix is a complex unitary matrix. Removing unobservable phases, the degrees of freedom are reduced to four, three angles and one phase. The angles are small, making the CKM matrix nearly diagonal.

Neutrino masses, although experimentally verified by the observation of neutrino flavor oscillations [25, 26], are not considered to be part of the SM. The mass generation mechanism is unknown and may be different from a Yukawa-type coupling. Potential mixing of neutrino flavors was proposed in the 1960's [27, 28] and later confirmed experimentally [25, 26], showing that neutrinos have non-zero mass. The neutrino propagators are only diagonal in the mass basis, hence, the neutrino flavors oscillate. If the sub-eV neutrino masses are generated after electroweak symmetry breaking, the Yukawa-like couplings have to be very small. Therefore, other mass generation mechanisms like the see-saw mechanism [29] are often considered as more natural. The see-saw mechanism involves heavy right-handed neutrinos which are not part of the SM. The mismatch of the flavor and mass eigenstates is parametrized in the Pontecorvo–Maki–Nakagawa–Sakata (PMNS) matrix, regardless of the mass generation mechanism. This PMNS matrix is the lepton equivalent to the CKM matrix of the quark sector. Similarly, three mixing angles and one complex phase define this matrix. If the neutrino masses have a Majorana component, two additional phases occur.

2.1.2 Free parameters in the Standard Model

Several parameters cannot be predicted within the SM itself but need to be measured experimentally. If the neutrino masses and the cosmological constant are included, the SM has 27 parameters: 10 parameters each in the lepton and quark sector (six masses, three angles and one complex phase) as well as three gauge couplings, the QCD vacuum angle, the Higgs VEV and mass, and the cosmological constant. The angles and phases of the quark sector enter in the CKM matrix.

Electroweak hierarchy problem

The SM has to be considered as an effective low-energy theory. Close to the Planck scale, SM predictions do not hold as gravitational effects become important which are not described by the SM. The large hierarchy between the weak scale of 10^2 GeV to the Planck scale of 10^{19} GeV is not understood.

Naturalness problem

The observed Higgs boson mass of $m_H = 125$ GeV is of the order of the weak scale. However, the mass is not naturally small since there is no approximate symmetry protecting it from large radiative corrections. Therefore, the Higgs mass would receive corrections from particles with masses close to the planck scale, promoting the Higgs mass itself to Planck scale values.

Gauge coupling unification

A unification of the gauge couplings is expected to happen at the grand unification scale at 10^{16} GeV. Within the SM, this is not achieved.

More motivations

Even more difficulties arise in the context of the SM, e.g. related to the observed size of the CP violation which is not enough to account for the observed matter/antimatter asymmetry, the smallness of the CP violation in the strong sector or the significant difference between the predicted and observed muon anomalous magnetic moment [35]. Other questions concern the form of the Higgs potential that may seem to be ad-hoc and missing an explanation for the negative sign of the quadratic term causing electroweak symmetry breaking. Effects related to cosmology, like the origin of Dark Energy, the driving force behind the expansion of the universe, the fast expanding phase of the universe (“inflation”), and the incorporation of quantum gravitational effects are also eagerly awaiting an answer that the SM cannot provide.

2.2 Supersymmetry

Our current understanding of elementary particle physics is based on two types of symmetries: Symmetries of space-time in the form of the Poincare group, and internal symmetries, the gauge groups of the SM. First ideas on expanding the Poincare group in the early 1970’s [36–42] met the no-go theorem by Coleman and Mandula [43]. This theorem states that there exists no non-trivial combination of Poincare and internal gauge symmetries. The most general symmetry (Lie) group is the direct product of the Lorentz group and an inner group. There is a way out, however, by using a graded (or super) Lie algebra, the generators of which must be spinors under the Lorentz algebra [44]. This supersymmetry (SUSY) unifies bosonic and fermionic particles in supermultiplets. Supercharge operators Q that transform the fermionic

and bosonic states are anti-commuting spinors:

$$\begin{aligned} Q |\text{fermion}\rangle &\propto |\text{boson}\rangle \quad , \\ Q |\text{boson}\rangle &\propto |\text{fermion}\rangle \quad , \end{aligned} \tag{2.26}$$

that satisfy an algebra of commutators and anti-commutators of the form

$$\begin{aligned} \{Q_\alpha, Q_\alpha^\dagger\} &= -2\sigma_{\alpha,\dot{\alpha}}^\mu P_\mu \quad , \\ \{Q_\alpha, Q_\beta\} &= 0, \quad \{Q_\alpha^\dagger, Q_\beta^\dagger\} = 0 \quad , \\ [Q_\alpha, P^\mu] &= 0, \quad [Q_\alpha^\dagger, P^\mu] = 0 \quad . \end{aligned} \tag{2.27}$$

Here, α and β are spinor indices, and P^μ is the generator of spacetime translations [45]. Depending on the number \mathcal{N} of supercharge generators the respective theory is called \mathcal{N} supersymmetry. Theories with *extended* SUSY ($\mathcal{N} > 1$) are mainly of theoretical interest because they cannot resemble well-known features of the SM like parity violation or chiral fermions. Therefore, $\mathcal{N} = 1$ SUSY will be considered in what follows.

Irreducible representations of the SUSY algebra, the supermultiplets, contain the same number of boson and fermion states. The newly introduced supersymmetric partners of the SM particles are called superpartners, and differ only by their spin. For scalar partners, the names of their corresponding SM fermions are prepended with “s-” in order to indicate their scalar nature, e.g. the selectron is the scalar partner of the electron. In contrast, for fermionic partners of gauge bosons, “-ino” is appended to the name of the SM bosons, e.g. the photino is the SUSY partner of the photon. Electric charge, color charge and weak isospin as well as the masses of SUSY particles are identical with their SM counterparts as long as SUSY is an exact symmetry, i.e. is unbroken. Experimental results show that such new particles do not exist. Therefore, if SUSY is a symmetry of nature, it has to be broken in order to generate a mass difference between the SM and SUSY particles.

It turns out that SUSY, originally developed with purely aesthetic motivation, is able to answer some of the most striking open questions of the SM, making it one of the most prominent theories beyond the SM. A variety of models based on the basic principle of SUSY can be constructed. In order to keep the numbers of new parameters small, the minimal supersymmetric extension of the SM (MSSM) is defined as the model which contains the minimum number of supermultiplets that are phenomenologically viable, i.e. contain the SM.

2.2.1 The Minimal Supersymmetric Model

The MSSM is built on four assumptions [46]: The minimal gauge group, based on the SM $SU(3) \times SU(2) \times U(1)$ symmetry group, a minimal particle content, conservation of R-parity [47, 48], and soft breaking of SUSY [49–51].

R-parity is a discrete symmetry with the conserved quantity $R = (-1)^{3B+L+2s}$ where B and L are the baryon and lepton numbers, respectively, and s the spin of the particle. SM fields have R-parity of $+1$, while the SUSY partners have -1 . Its conservation is motivated by the non-observation of rapid proton decay that is introduced by R-parity violating interactions. It predicts that SUSY particles are produced in pairs. In collider experiments, SM particles form the initial state which therefore carries R-parity $+1$. Hence, a SUSY particle pair, e.g. squark-antisquark or a gluino pair, is needed for an R-parity of $(-1)^2 = +1$. R-parity conservation predicts stable lightest supersymmetric particles (LSPs) in collider final states. The reason is that the LSP has R-parity of -1 and therefore cannot decay into SM particles. It is clear from experimental results, that SUSY is a broken symmetry, at least at the electroweak scale. Additional interactions can be introduced that spontaneously break SUSY at low scales. Two frequently used candidates are gravity mediated and gauge mediated SUSY breaking. Since the breaking mechanism at high mass scales is unknown, it is parametrized by *soft* SUSY breaking terms in the MSSM, which explicitly break the symmetry. Soft breaking terms contain only operators with dimensionful coupling constants in order to avoid generation of quadratic divergences. The high scale SUSY breaking then constrains the large number of soft terms.

The particle content of the MSSM in the form of the chiral and gauge supermultiplets is given in Tab. 2.3. Two Higgs supermultiplets have to be introduced in order to keep the theory anomaly free, as well as to provide Yukawa couplings to both up- and down-type quarks. In contrast to the SM, the complex conjugate of the Higgs doublet can not be used to provide down-type fermions with masses. The higgsinos, winos and binos mix and form mass eigenstates called charginos χ^\pm and neutralinos χ^0 according to their electric charge. Mixing of squarks and sleptons is small for first and second generation sfermions for sufficiently small $\tan\beta$, where $\tan\beta$ is the ratio of the vacuum expectation values of the two Higgs doublets. However, the right- and left-handed top squarks are usually assumed to significantly mix, which lowers the lighter top squark mass and, in many models, makes \tilde{t}_1 the lightest squark. An overview of the mass eigenstates is given in Tab. 2.4.

Without applying any further constraints, the MSSM has 105 new free parameters, making experimental searches as well as theoretical predictions challenging. In the phenomenological MSSM (pMSSM) the number of parameters is largely reduced by excluding new CP violating sources and flavor changing neutral currents as well as imposing universality of the first two generations.

2.2.2 Solving the naturalness problem of the Higgs mass

As mentioned earlier, SUSY is not only a very compelling theory in the sense that it extends the Poincare algebra in a nontrivial way, but it also provides answers to some of the hardest

Table 2.3: The chiral and gauge supermultiplets of the MSSM.

Name	spin 0	spin 1/2	spin 1	$(SU(3)_C, SU(2)_L, U(1)_Y)$
squarks, quarks	$(\tilde{u}_L \tilde{d}_L)$	$(u_L d_L)$		$(\mathbf{3}, \mathbf{2}, \frac{1}{6})$
(3 generations)	\tilde{u}_R^* \tilde{d}_R^*	u_R^\dagger d_R^\dagger		$(\mathbf{3}, \mathbf{1}, -\frac{2}{3})$ $(\mathbf{3}, \mathbf{1}, \frac{1}{3})$
sleptons, leptons	$(\tilde{\nu} \tilde{\ell}_L)$	$(\nu \ell_L)$		$(\mathbf{1}, \mathbf{2}, -\frac{1}{2})$
(3 generations)	$\tilde{\ell}_R^*$	ℓ_R^\dagger		$(\mathbf{1}, \mathbf{1}, 1)$
Higgs, higgsinos	$(H_u^+ H_u^0)$ $(H_d^0 H_d^-)$	$(\tilde{H}_u^+ \tilde{H}_u^0)$ $(\tilde{H}_d^0 \tilde{H}_d^-)$		$(\mathbf{1}, \mathbf{2}, \frac{1}{2})$ $(\mathbf{1}, \mathbf{2}, -\frac{1}{2})$
gluino, gluon		\tilde{g}	g	$(\mathbf{8}, \mathbf{1}, 0)$
winos, W boson		$\tilde{W}^\pm, \tilde{W}^0$	W^\pm, W^0	$(\mathbf{1}, \mathbf{3}, 0)$
zinos, B boson		\tilde{B}^0	B^0	$(\mathbf{1}, \mathbf{1}, 0)$

puzzles in current day particle physics. In the SM, the Higgs boson, as the only fundamental scalar of the theory, is not protected against large higher-order corrections by any symmetry. This opens the question why the Higgs boson in fact is so light ($m_H \approx 125$ GeV) compared to the Planck scale, since every particle that couples to the Higgs field provides corrections to m_H^2 . Fermions lead to corrections to the Higgs mass of

$$\Delta m_H^2 = \frac{|\lambda_f|^2}{8\pi^2} [-\Lambda_{UV}^2 + 3m_f^2 \ln(\Lambda_{UV}/m_f) + \dots] \quad , \quad (2.28)$$

with an ultraviolet momentum cutoff Λ_{UV} to regulate the loop integral. A Higgs boson with the observed physical mass requires a significant, and often considered unnatural, fine-tuning of

$$m_H^2|_{\text{physical}} = m_H^2|_{\text{bare}} - \Delta m_H^2 \quad . \quad (2.29)$$

For a scalar particle, the sign of the correction is reversed, giving terms of the form

$$\Delta m_H^2 = \frac{\lambda_S}{16\pi^2} [\Lambda_{UV}^2 - 2m_S^2 \ln(\Lambda_{UV}/m_S) + \dots] \quad , \quad (2.30)$$

leading to systematic cancellations of the quadratic correction terms in the case of an unbroken SUSY, corresponding to diagrams in Fig. 2.2. To avoid reintroducing quadratic divergences by SUSY breaking, one excludes all breaking terms that contribute corrections quadratic in the mass terms. The remainder are the soft SUSY breaking terms [52]. The structure of the

Table 2.4: The gauge and mass eigenstates of the MSSM. Mixing of the first two sfermion generations is assumed to be negligible.

Name	Spin	P_R	Gauge Eigenstate	Mass Eigenstate
Higgs bosons	0	+1	$H_u^0 \ H_d^0 \ H_u^+ \ H_d^-$	$h^0 \ H^0 \ A^0 \ H^\pm$
squarks	0	-1	$\tilde{u}_L \ \tilde{u}_R \ \tilde{d}_L \ \tilde{d}_R$ $\tilde{s}_L \ \tilde{s}_R \ \tilde{c}_L \ \tilde{c}_R$ $\tilde{t}_L \ \tilde{t}_R \ \tilde{b}_L \ \tilde{b}_R$	(same) (same) $\tilde{t}_1 \ \tilde{t}_2 \ \tilde{b}_1 \ \tilde{b}_2$
sleptons	0	-1	$\tilde{e}_L \ \tilde{e}_R \ \tilde{\nu}_e$ $\tilde{\mu}_L \ \tilde{\mu}_R \ \tilde{\nu}_\mu$ $\tilde{\tau}_L \ \tilde{\tau}_R \ \tilde{\nu}_\tau$	(same) (same) $\tilde{\tau}_1 \ \tilde{\tau}_2 \ \tilde{\nu}_\tau$
neutralinos	1/2	-1	$\tilde{B}^0 \ \tilde{W}^0 \ \tilde{H}_u^0 \ \tilde{H}_d^0$	$\tilde{\chi}_1^0 \ \tilde{\chi}_2^0 \ \tilde{\chi}_3^0 \ \tilde{\chi}_4^0$
charginos	1/2	-1	$\tilde{W}^\pm \ \tilde{H}_u^\pm \ \tilde{H}_d^\pm$	$\tilde{\chi}_1^\pm \ \tilde{\chi}_2^\pm$
gluino	1/2	-1	\tilde{g}	(same)
goldstino	1/2	-1	\tilde{G}	(same)
gravitino	3/2			

divergences is reduced to a logarithmic behaviour

$$\Delta m_H^2 = -m_{\text{soft}}^2 \left[\frac{\lambda}{16\pi^2} \ln(\Lambda_{\text{UV}}/m_{\text{soft}}) + \dots \right] , \quad (2.31)$$

where m_{soft} is the largest mass scale of the soft terms. Implying naturalness by restricting the correction terms to be of the order of the physical mass $|\Delta m_H^2| < m_H^2|_{\text{physical}}$ leads to a prediction of SUSY particle masses in the TeV range, potentially accessible at the LHC.

2.2.3 Gauge coupling unification

Unification of the gauge couplings of the strong, weak and electromagnetic interactions into a single gauge interaction is expected to happen at an energy scale below the Planck scale of 10^{19} GeV. The energy scale of unified couplings is generally referred to as grand unification energy, or grand unified theory (GUT) scale. Using renormalization group evolution one indeed finds that the SM couplings are approaching each other at higher scales, however, within the SM they fail to unify at a single point. With the particle content of the MSSM, gauge coupling

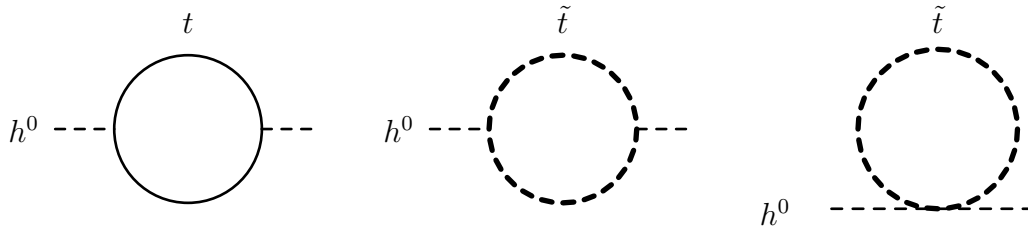


Figure 2.2: Diagrams of corrections to the Higgs mass from a Dirac fermion, e.g. the top quark t (left), and a scalar, e.g. the top squark \tilde{t} (center and right).

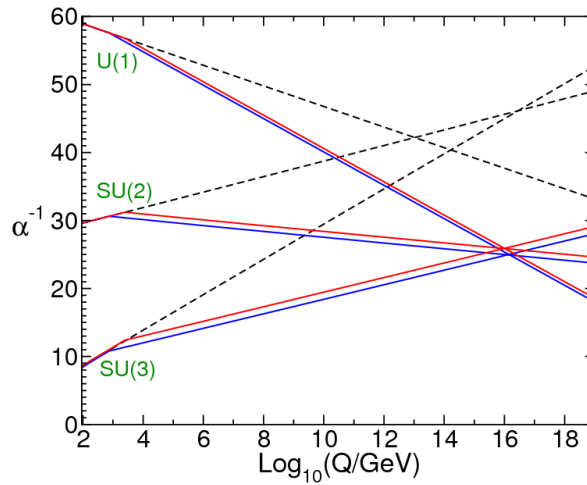


Figure 2.3: Renormalization group evolution for the fundamental couplings, for the SM (dotted lines) and the MSSM (solid lines), with different values for sparticle masses [45].

unification is indeed achievable around 10^{16} GeV, the SUSY GUT scale, shown in Fig. 2.3.

2.2.4 Dark Matter candidate

From astrophysical observations, it is known that the matter-energy content of the universe includes about 27% Dark Matter (DM), compared to only about 5% ordinary matter, while the rest is attributed to Dark Energy [33]. Among the viable options, experimental data is consistent with cold dark matter (CDM), with a weakly interacting massive particle (WIMP) in the range of GeV to TeV. As was discussed above, R-parity conserving SUSY is well motivated by the stability of the proton. As a consequence, the LSP, in many models the lightest neutralino $\tilde{\chi}_1^0$, is stable and therefore a WIMP, making it a viable candidate for CDM. In contrast, sneutrino DM has been ruled out for masses up to several TeV [53]. SUSY models with gauge mediated symmetry breaking predict the gravitino to be the LSP, which is interacting too weakly to be detected with direct detection experiments.

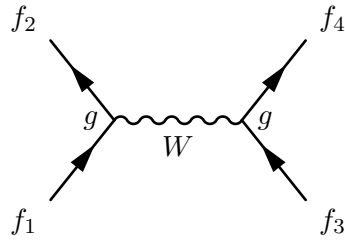


Figure 2.4: Fermion scattering via a W boson as described in the SM.

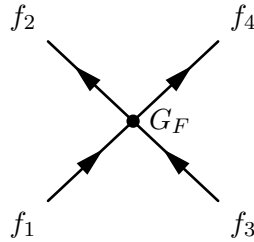


Figure 2.5: Effective fermion scattering as described by the Fermi theory of weak interactions.

2.3 Effective Field Theories

If the masses of BSM particles are at a scale $M \simeq \Lambda$ that is too high to allow for on-shell production at the LHC, effects from new physics can still emerge as subtle modifications of total cross sections or kinematic distributions of the SM particles. As long as the energy scale of the scattering process is small, $E \ll \Lambda$, an effective field theory (EFT) approach can be used to parametrize the effects of the underlying theory [54–58].

A well known example of an effective theory is Fermi’s four-fermion theory [59]. Here, the SM is the underlying theory, and the four-fermion theory its low energy effective theory. In the SM, scattering of fermions is mediated via the weak bosons, e.g. a W boson in Fig. 2.4. The matrix element of the interaction can be written down as

$$\mathcal{M}_{\text{full}} \sim \frac{g^2}{q^2 - m_W^2} \quad , \quad (2.32)$$

with the momentum transfer q , the coupling constant g and the W boson mass m_W . For $q^2 \ll m_W^2$, the W propagator can be collapsed to a four-fermion contact interaction, shown in Fig. 2.5. Then, the matrix element is proportional to the Fermi constant G_F and given by

$$\mathcal{M}_{\text{EFT}} \propto G_F \sim \frac{g^2}{m_W^2} \quad . \quad (2.33)$$

The two approaches increasingly differ for $E \geq m_W$ when the W boson is produced on-shell. Therefore, the Fermi theory is only valid below the mass scale of the W boson.

The Standard Model Effective Field Theory (SMEFT) is used to identify and parametrize potential deviations of measured inclusive and differential cross section from SM predictions [60].

The BSM effects originating from new physics at high scales $E \simeq \Lambda$ are parametrized as higher-dimensional operators in a model-independent way. These operators are constructed from the SM fields, and respect gauge and Lorentz symmetries. Similarly to the Fermi theory, the SMEFT is valid as long as $E \ll \Lambda$, however, the fundamental theory is unknown. The SM Lagrangian is extended by terms containing higher-dimensional operators

$$\mathcal{L}_{\text{SMEFT}} = \mathcal{L}_{\text{SM}} + \sum_i \frac{c_i}{\Lambda^{D_i-4}} \mathcal{O}_i \quad , \quad (2.34)$$

with the dimensionless Wilson coefficients c_i and the dimensionality D_i of the operator \mathcal{O}_i . Operators with dimensionality of $D = 5$ and $D = 7$ violate lepton and baryon number conservation [61, 62] and are not considered in the following, as well as operators with $D \geq 8$. The Warsaw basis is used for the remaining $D = 6$ operators, and the relations to different base choices are given in [63]. Inclusive or differential cross sections are modified by the dimension-6 SMEFT operators as

$$\sigma = \sigma_{\text{SM}} + \sum_i \sigma_i \frac{c_i}{\Lambda^2} + \sum_{i,j} \sigma_{ij} \frac{c_i c_j}{\Lambda^4} \quad , \quad (2.35)$$

where σ_{SM} reflects the SM prediction. The interference of dimension-6 operators with the SM is given by the second term, and the squared amplitudes of the operators that are independent of interference with the SM in the third term. Despite a suppression of $1/\Lambda^4$ the latter term can provide the dominant correction in cases where the interference with the SM is suppressed. In total, 59 dimension-6 operators for just one generation of fermions [60] are found, increasing to 2499 independent degrees in the most general flavor structure [64]. Following the recommendations of the LHC Top Working Group [65], minimal flavor violation (MFV), a diagonal CKM matrix and finite Yukawa couplings only for third-generation quarks are imposed. The operators relevant for top quark interactions are given in Eq. 2.36, 2.37, 2.39 and 2.38, following [65]. They are categorized into four-quark, two-quark, two-quark and two-lepton, as well as baryon- and lepton-number violating operators. In the following, flavor indices are labelled by $ijkl$; left-handed fermion doublets by q, l ; right-handed fermion singlets by u, d, e ; the Higgs doublet by φ ; the antisymmetric $SU(2)$ tensor by $\varepsilon \equiv i\tau^2$; $\tilde{\varphi} = \varepsilon\varphi^*$; τ^I the Pauli matrices; $T^A \equiv \lambda^A/2$ where λ^A are the Gell-Mann matrices; and $(\varphi^\dagger \overleftrightarrow{iD}_\mu \varphi) \equiv \varphi^\dagger (iD_\mu \varphi) - (iD_\mu \varphi^\dagger) \varphi$; as well as $(\varphi^\dagger \overleftrightarrow{iD}_\mu^I \varphi) \equiv \varphi^\dagger \tau^I (iD_\mu \varphi) - (iD_\mu \varphi^\dagger) \tau^I \varphi$. A double dagger indicates non-hermitian operators.

Four-quark operators

$$\begin{aligned}
\mathcal{O}_{qq}^{1(ijkl)} &= (\bar{q}_i \gamma^\mu q_j) (\bar{q}_k \gamma_\mu q_l) \\
\mathcal{O}_{qq}^{3(ijkl)} &= (\bar{q}_i \gamma^\mu \tau^I q_j) (\bar{q}_k \gamma_\mu \tau^I q_l) \\
\mathcal{O}_{qu}^{1(ijkl)} &= (\bar{q}_i \gamma^\mu q_j) (\bar{u}_k \gamma_\mu u_l) \\
\mathcal{O}_{qu}^{8(ijkl)} &= (\bar{q}_i \gamma^\mu T^A q_j) (\bar{u}_k \gamma_\mu T^A u_l) \\
\mathcal{O}_{qd}^{1(ijkl)} &= (\bar{q}_i \gamma^\mu q_j) (\bar{d}_k \gamma_\mu d_l) \\
\mathcal{O}_{qd}^{8(ijkl)} &= (\bar{q}_i \gamma^\mu T^A q_j) (\bar{d}_k \gamma_\mu T^A d_l) \\
\mathcal{O}_{uu}^{(ijkl)} &= (\bar{u}_i \gamma^\mu u_j) (\bar{u}_k \gamma_\mu u_l) \\
\mathcal{O}_{ud}^{1(ijkl)} &= (\bar{u}_i \gamma^\mu u_j) (\bar{d}_k \gamma_\mu d_l) \\
\mathcal{O}_{ud}^{8(ijkl)} &= (\bar{u}_i \gamma^\mu T^A u_j) (\bar{d}_k \gamma_\mu T^A d_l) \\
\ddagger \mathcal{O}_{quqd}^{1(ijkl)} &= (\bar{q}_i u_j) \varepsilon (\bar{q}_k d_l) \\
\ddagger \mathcal{O}_{quqd}^{8(ijkl)} &= (\bar{q}_i T^A u_j) \varepsilon (\bar{q}_k T^A d_l)
\end{aligned} \tag{2.36}$$

Two-quark operators

$$\begin{aligned}
\ddagger \mathcal{O}_{u\varphi}^{(ij)} &= \bar{q}_i u_j \tilde{\varphi} (\varphi^\dagger \varphi) \\
\mathcal{O}_{\varphi q}^{1(ij)} &= (\varphi^\dagger \overleftrightarrow{iD}_\mu \varphi) (\bar{q}_i \gamma^\mu q_j) \\
\mathcal{O}_{\varphi q}^{3(ij)} &= (\varphi^\dagger \overleftrightarrow{iD}_\mu \tau^I \varphi) (\bar{q}_i \gamma^\mu \tau^I q_j) \\
\mathcal{O}_{\varphi u}^{(ij)} &= (\varphi^\dagger \overleftrightarrow{iD}_\mu \varphi) (\bar{u}_i \gamma^\mu u_j) \\
\ddagger \mathcal{O}_{\varphi ud}^{(ij)} &= (\tilde{\varphi}^\dagger iD_\mu \varphi) (\bar{u}_i \gamma^\mu d_j) \\
\ddagger \mathcal{O}_{uW}^{(ij)} &= (\bar{q}_i \sigma^{\mu\nu} \tau^I u_j) \tilde{\varphi} W_{\mu\nu}^I \\
\ddagger \mathcal{O}_{dW}^{(ij)} &= (\bar{q}_i \sigma^{\mu\nu} \tau^I d_j) \varphi W_{\mu\nu}^I \\
\ddagger \mathcal{O}_{uB}^{(ij)} &= (\bar{q}_i \sigma^{\mu\nu} u_j) \tilde{\varphi} B_{\mu\nu} \\
\ddagger \mathcal{O}_{uG}^{(ij)} &= (\bar{q}_i \sigma^{\mu\nu} T^A u_j) \tilde{\varphi} G_{\mu\nu}^A
\end{aligned} \tag{2.37}$$

Baryon- and lepton-number violating operators

$$\begin{aligned}
\ddagger \mathcal{O}_{duq}^{(ijkl)} &= (\bar{d}^c_{i\alpha} u_{j\beta}) (\bar{q}^c_{k\gamma} \varepsilon_l) \epsilon^{\alpha\beta\gamma} \\
\ddagger \mathcal{O}_{quq}^{(ijkl)} &= (\bar{q}^c_{i\alpha} \varepsilon q_{j\beta}) (\bar{u}^c_{k\gamma} e_l) \epsilon^{\alpha\beta\gamma} \\
\ddagger \mathcal{O}_{qqq}^{1(ijkl)} &= (\bar{q}^c_{i\alpha} \varepsilon q_{j\beta}) (\bar{q}^c_{k\gamma} \varepsilon_l) \epsilon^{\alpha\beta\gamma} \\
\ddagger \mathcal{O}_{qqq}^{3(ijkl)} &= (\bar{q}^c_{i\alpha} \tau^I \varepsilon q_{j\beta}) (\bar{q}^c_{k\gamma} \tau^I \varepsilon_l) \epsilon^{\alpha\beta\gamma} \\
\ddagger \mathcal{O}_{duu}^{(ijkl)} &= (\bar{d}^c_{i\alpha} u_{j\beta}) (\bar{u}^c_{k\gamma} e_l) \epsilon^{\alpha\beta\gamma}
\end{aligned} \tag{2.38}$$

Two-quark, two-lepton operators

$$\begin{aligned}
 \mathcal{O}_{lq}^{1(ijkl)} &= (\bar{l}_i \gamma^\mu l_j) (\bar{q}_k \gamma^\mu q_l) \\
 \mathcal{O}_{lq}^{3(ijkl)} &= (\bar{l}_i \gamma^\mu \tau^I l_j) (\bar{q}_k \gamma^\mu \tau^I q_l) \\
 \mathcal{O}_{lu}^{(ijkl)} &= (\bar{l}_i \gamma^\mu l_j) (\bar{u}_k \gamma^\mu u_l) \\
 \mathcal{O}_{eq}^{(ijkl)} &= (\bar{e}_i \gamma^\mu e_j) (\bar{q}_k \gamma^\mu q_l) \\
 \mathcal{O}_{eu}^{(ijkl)} &= (\bar{e}_i \gamma^\mu e_j) (\bar{u}_k \gamma^\mu u_l) \\
 \dagger \mathcal{O}_{lequ}^{1(ijkl)} &= (\bar{l}_i e_j) \varepsilon (\bar{q}_k u_l) \\
 \dagger \mathcal{O}_{lequ}^{3(ijkl)} &= (\bar{l}_i \sigma^{\mu\nu} e_j) \varepsilon (\bar{q}_k \sigma_{\mu\nu} u_l) \\
 \dagger \mathcal{O}_{ledq}^{(ijkl)} &= (\bar{l}_i e_j) (\bar{d}_k q_l)
 \end{aligned} \tag{2.39}$$

The EFT degrees of freedom, imposing lepton and baryon number conservation and MFV, are defined in terms of the Warsaw basis. As an example, choices for the definitions of $\mathcal{O}_{\varphi q}$ are made in terms of the $SU(2)$ broken phase decomposition:

$$\begin{pmatrix} \mathcal{O}_{\varphi q}^{1(33)} \\ \mathcal{O}_{\varphi q}^{3(33)} \end{pmatrix} = \begin{pmatrix} -1 & 1 \\ 1 & 1 \\ 0 & 1 \\ 0 & 1 \end{pmatrix}^T \begin{pmatrix} \frac{e}{2s_W c_W} (\bar{t} \gamma^\mu P_L t) Z_\mu (v+h)^2 \\ \frac{-e}{2s_W c_W} (\bar{b} \gamma^\mu P_L b) Z_\mu (v+h)^2 \\ \frac{e}{s_W \sqrt{2}} (\bar{t} \gamma^\mu P_L b) W_\mu^+ (v+h)^2 \\ \frac{e}{s_W \sqrt{2}} (\bar{b} \gamma^\mu P_L t) W_\mu^- (v+h)^2 \end{pmatrix}, \tag{2.40}$$

and similarly, for the electroweak dipole operators

$$\begin{pmatrix} \mathcal{O}_{uB}^{(33)} \\ \mathcal{O}_{uW}^{(33)} \end{pmatrix} = \begin{pmatrix} c_W & s_W \\ -s_W & c_W \\ 0 & 2 \end{pmatrix}^T \begin{pmatrix} (\bar{t} \sigma^{\mu\nu} P_R t) A_{\mu\nu} (v+h) \\ (\bar{t} \sigma^{\mu\nu} P_R t) Z_{\mu\nu} (v+h) \\ (\bar{b} \sigma^{\mu\nu} P_R t) W_{\mu\nu}^- (v+h) \end{pmatrix}, \tag{2.41}$$

where s_W and c_W are the sine and cosine of the Weinberg angle. Again following [65], degrees of freedom are chosen as combinations of the operators such that W and Z bosons in the broken phase as well as top quarks are involved, e.g.

$$\begin{aligned}
 c_{\varphi Q}^- &\equiv C_{\varphi q}^{1(33)} - C_{\varphi q}^{3(33)} \\
 c_{\varphi Q}^3 &\equiv C_{\varphi q}^{3(33)} \\
 c_{\varphi t} &\equiv C_{\varphi u}^{(33)} \\
 c_{tW}^{[I]} &\equiv \frac{[\text{Im}]}{\text{Re}} \{C_{uW}^{(33)}\} \\
 c_{tZ}^{[I]} &\equiv \frac{[\text{Im}]}{\text{Re}} \{-s_W C_{uB}^{(33)} + c_W C_{uW}^{(33)}\}
 \end{aligned} \tag{2.42}$$

where C_i are the Wilson coefficients corresponding to the operators \mathcal{O}_i in Eq. 2.40 and 2.41, and c_j and $c_j^{[I]}$ the CP-conserving and CP-violating degrees of freedom used to interpret

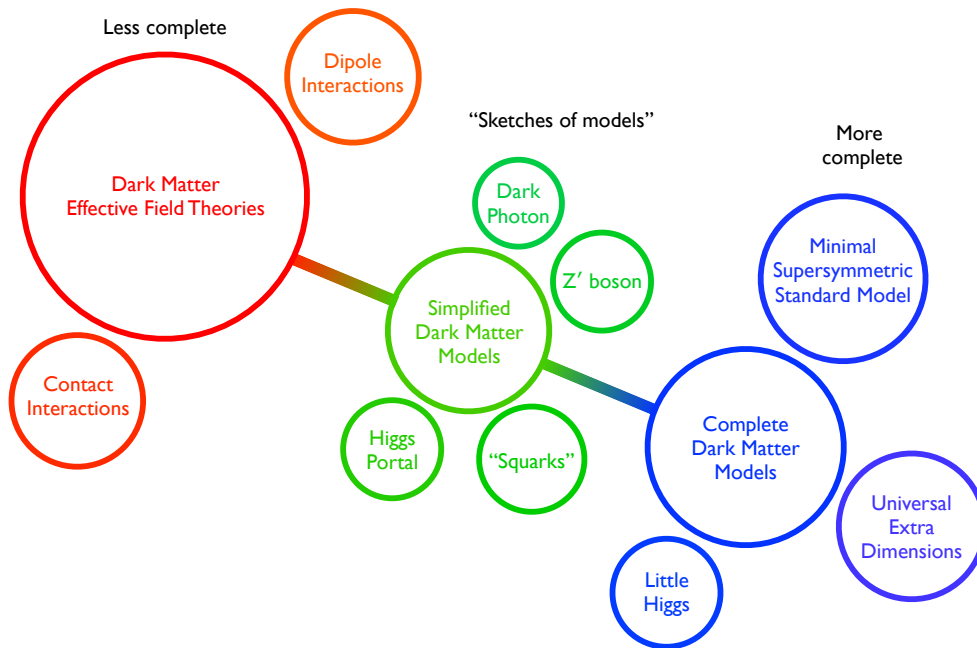


Figure 2.6: Artistic view of the DM theory space [72]. Simplified models can be seen as compromise between complete models with large numbers of parameters, and EFTs that assume heavy mediator masses.

experimental results. The Wilson coefficients shown in Eq. 2.42 will be further discussed in Chapter 5. A full review of operators and degrees of freedom of the top quark sector of the SMEFT can be found in [65].

2.4 Simplified Models

Simplified models are another bottom-up approach to interpret LHC results. The main challenge in top-down interpretations starting from full models are the large number of free parameters, 124 in the case of the MSSM. Additionally, comparisons of interpretations in different full models are hard to perform, and the evolving indirect constraints on individual parameters pose additional challenges. In contrast, simplified models introduce a minimal set of new particles and therefore free parameters in the form of masses, cross sections and couplings, e.g. for SUSY [66, 67] and DM [68–71]. Other particles of the full model are assumed to be heavy and therefore out of reach of the LHC, i.e. the particles are decoupled. An illustration of the theory space in terms of DM models is given in Fig. 2.6, with a hierarchy of completeness of the models from left to right. EFTs usually depend on the least number of parameters, but also rely on the assumption that the scale of new physics is high. Simplified models are located in between EFTs and full models in terms of completeness and complexity. Simplified SUSY models are described by the masses and the production cross section of the

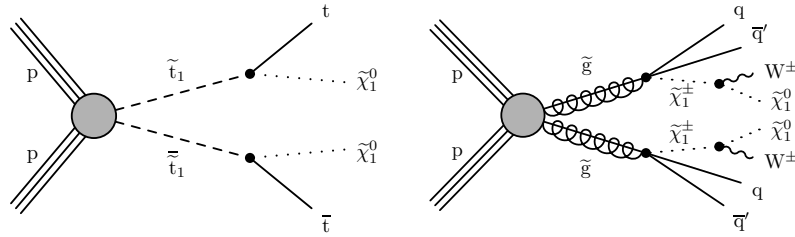


Figure 2.7: Diagrams of simplified SUSY models, for top squark pair production with direct decay to the lightest neutralino $\tilde{t} \rightarrow t\tilde{\chi}_1^0$ (left), and for gluino pair production with cascade decays to a chargino and subsequently the lightest neutralino $\tilde{g} \rightarrow q\bar{q}'\tilde{\chi}_1^\pm \rightarrow W\tilde{\chi}_1^0$ (right).

SUSY particles. For a model of top squark pair production with direct decay to the LSP $\tilde{t} \rightarrow t\tilde{\chi}_1^0$ this results in two mass parameters and the corresponding cross section for top squark pairs. If the model describes a cascade decay, e.g. the pair production of gluinos that decay to the LSP via an intermediate chargino $\tilde{g} \rightarrow q\bar{q}'\tilde{\chi}_1^\pm \rightarrow W\tilde{\chi}_1^0$, the branching fraction of this decay chain is set to 100%. The corresponding diagrams to the mentioned simplified models are shown in Fig. 2.7.

DM particles could be produced at the LHC via massive mediator particles. Amongst others, DM models where the DM particle, a Dirac fermion χ , is pair produced via scalar or pseudoscalar mediators, have been studied [68–71]. In a simplified DM model, only the real scalar or pseudoscalar mediators are considered, while the associated scalar is decoupled [72, 73]. $SU(2)_L$ invariance of the singlet can be restored by including mixing of the mediator with the SM Higgs sector. For simplicity, this mixing is neglected in the simplified model shown in Fig. 2.8. One universal coupling of the mediator to all SM fermions is assumed which is chosen to be of SM Higgs Yukawa type. In this model, the only remaining free parameters are the masses of the mediator and the DM particle, as well as the coupling strengths of the mediator to SM fermions and the DM particle.

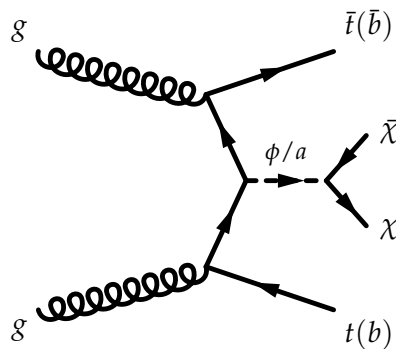


Figure 2.8: Diagram of a simplified DM model with production of a scalar (ϕ) or pseudoscalar (a) mediator in the $t\bar{t}$ or $b\bar{b}$ t -channel. The mediator decays to a pair of Dirac fermions, the DM particles χ .

The CMS experiment at the CERN LHC

THE CMS EXPERIMENT, short for “Compact Muon Solenoid” [74], is one of four experiments at the CERN Large Hadron Collider (LHC) [75]. It is accompanied by the ALICE (A Large Ion Collider Experiment) [76], ATLAS (A Torroidal LHC ApparatuS) [77] and LHCb (LHC beauty) [78] experiments.

3.1 The Large Hadron Collider

The LHC is a particle accelerator and storage ring for protons and heavy ions with a total circumference of 27 km. Two counter-rotating beams with similar energy are collided in the four interaction regions. During the Run 2 data taking period from 2015 to 2018, the center-of-mass energy for proton-proton collisions was 13 TeV, almost reaching the nominal value of 14 TeV. In order to achieve this high energy several steps of pre-acceleration are necessary. In the first step, hydrogen is positively ionized and accelerated to 50 MeV in the Linac2 linear accelerator. After long shutdown 2 (LS2) from 2018 to 2020 Linac2 will be replaced by a newer accelerator, Linac4, that will accelerate negative hydrogen ions to an output energy of 160 MeV. The electrons of the hydrogen ions are then stripped during the injection into the proton synchrotron booster (PSB) using a graphite foil [79]. The PSB consists of four superimposed synchrotron rings, and accelerates protons to energies of 1.4 GeV, which are then subsequently brought to energies of 25 GeV in the proton synchrotron (PS). The final step of pre-acceleration takes place in the super proton synchrotron (SPS), where the protons reach an energy of 450 GeV. Protons are then filled into the LHC in 2808 bunches of about 10^{11} protons each, resulting in a total of 3×10^{14} protons per beam. The bunches are separated by 25 ns, resulting in a collision rate of 40 MHz. Superconducting dipole magnets producing a magnetic field corresponding to 8.3 T are used to keep the protons on a circular track. The LHC uses twin bore magnets consisting of two sets of coils and vacuum pipes within the same mechanical structure and cryostat system due to the tight spacial constraints of the underground tunnel. Quadrupole and sextupole magnets are used for orbital and momentum

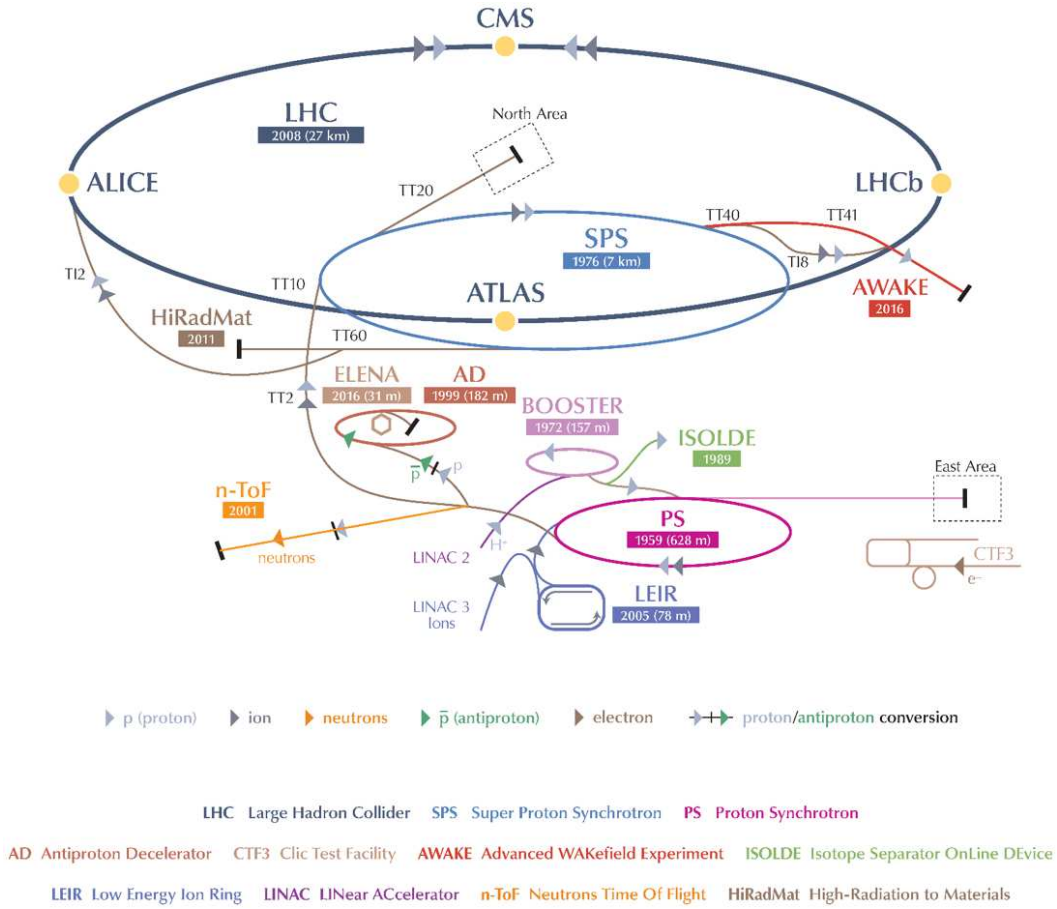


Figure 3.1: Sketch of the accelerator complex at CERN. The path of the protons that are eventually collided in the LHC starts at Linac2, and then follows through the PSB, PS and SPS to the LHC.

focussing, respectively. A sketch of the accelerator complex at CERN, including the PSB, PS, SPS and LHC among other accelerators and decelerators and experimental sites, is shown in Fig. 3.1.

The instantaneous luminosity \mathcal{L} is one of the defining parameters of a particle collider. The expected rate of a given process with production cross section σ is given by

$$\frac{dN}{dt} = \mathcal{L} \cdot \sigma \quad . \quad (3.1)$$

The instantaneous luminosity evaluates to

$$\mathcal{L} = \frac{N_b^2 n_b \nu \gamma}{4\pi \epsilon_n \beta^*} F \quad , \quad (3.2)$$

where N_b are the number protons per bunch, n_b the total number of bunches, ν the revolution frequency, γ the Lorentz factor, ϵ_n the normalized transverse beam emittance, β^* the beta

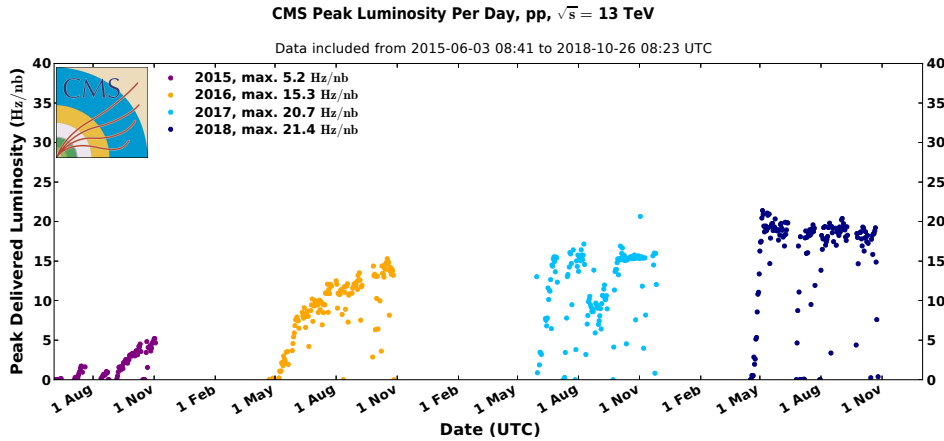


Figure 3.2: Peak luminosity versus day delivered to CMS during stable beams and for pp collisions between 2015 and 2018.

function at the collision point, and F the geometric luminosity reduction factor due to the crossing angle at the interaction point (IP). This factor is defined by

$$F = \frac{1}{\sqrt{1 + \left(\frac{\theta_c \sigma_z}{2\sigma^*}\right)^2}}, \quad (3.3)$$

with θ_c the crossing angle at the IP, σ_z the RMS of the bunch length, and σ^* the RMS of the transverse beam size. To achieve a high rate of events with small cross section, high intensity beams with small emittance and β^* are necessary. The design luminosity of the LHC machine is $10^{34} \text{ cm}^{-2} \text{ s}^{-1} = 10 \text{ nb}^{-1} \text{ s}^{-1}$, which was surpassed during the 2017 run by a factor of two, shown in Fig. 3.2. The high luminosity comes at the price of several simultaneous collisions at the same or neighboring bunch crossings, called pileup. In the 2018 data taking period this lead to an average of 37 interactions, posing a challenge for identifying, reconstructing and measuring the products of the hard scattering event. The measured pileup distribution is shown in Fig. 3.3. During the Run 2 period from 2015 to 2018, the integrated luminosity $L = \int \mathcal{L} dt$ delivered to the CMS experiment amounted to 163 fb^{-1} . Fig. 3.4 shows the evolution of the integrated luminosity for this time period.

3.2 The CMS detector

The CMS detector is located at interaction point 5 (P5) of the LHC and is designed to study proton-proton collisions at centre-of-mass energies up to 14 TeV, as well as lead-lead collisions at up to 5.5 TeV per nucleon. Its core element is a superconducting solenoid magnet with a inner diameter of 6.3 m, producing a magnetic field of 3.8 T. The silicon tracker, electromagnetic calorimeter (ECAL) and hadronic calorimeter (HCAL) are accommodated

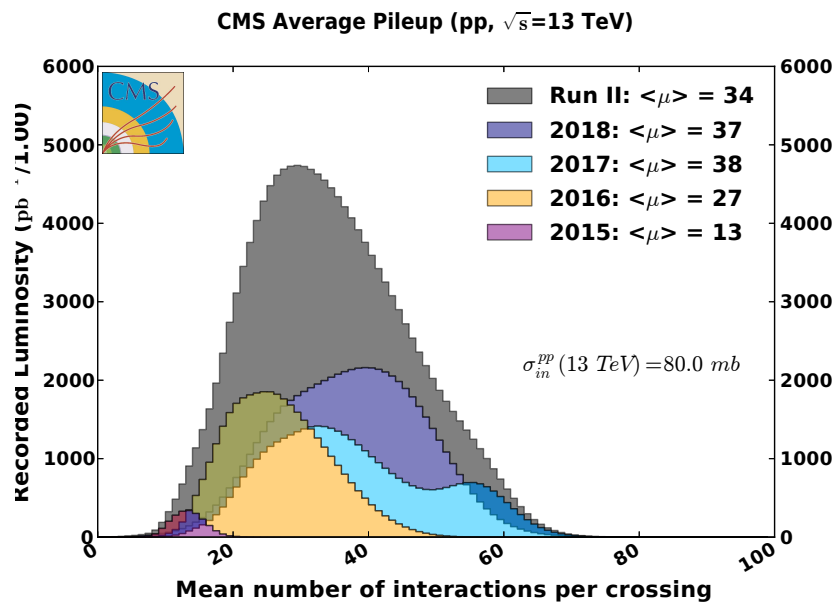


Figure 3.3: The pileup profile of proton-proton collisions in the CMS experiment. On average, 27 simultaneous collisions took place in the 2016 data taking period, and 38 and 37 in 2017 and 2018, respectively.

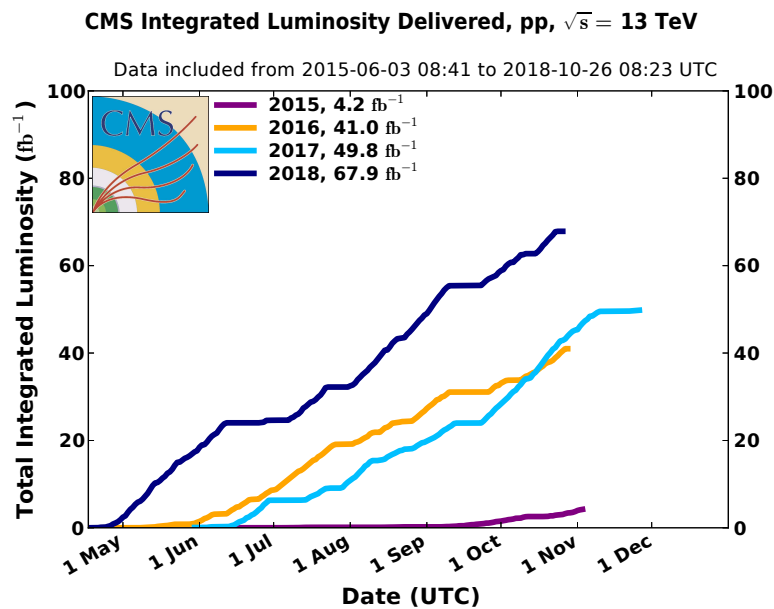


Figure 3.4: The delivered luminosity to the CMS experiment during the Run 2 of the LHC from 2015 to 2018.

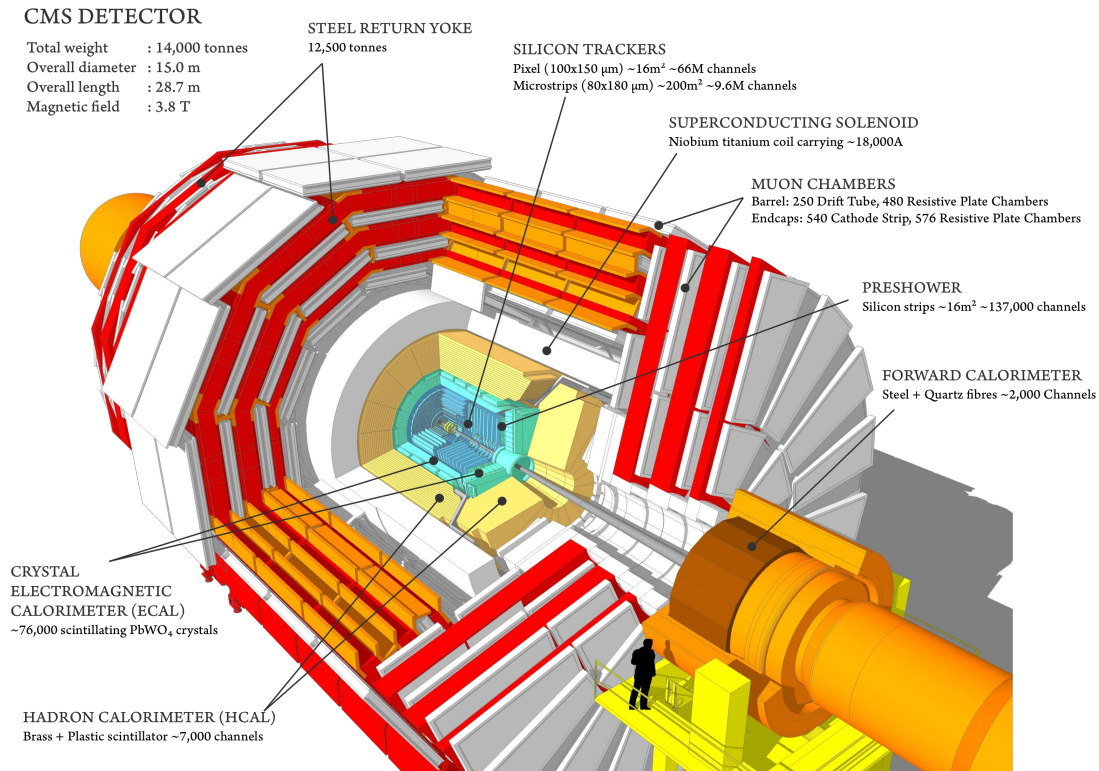


Figure 3.5: Overview of the CMS detector with all its subdetectors, arranged in an onion-like structure. The layer closest to the interaction point is the silicon tracker, followed by the electromagnetic and hadron calorimeters, the superconducting magnet, and the muon system [80].

within the magnet. The muon system surrounds the magnet, giving the detector its final dimensions with a length of 21.6 m and a diameter of 14.6 m, and a mass of about 12500 t. An overview of the CMS detector is given in Fig. 3.5. A detailed description of the CMS detector can be found in Ref. [74].

3.2.1 Coordinate system

The origin of the coordinate system is located at the nominal interaction point. The x axis points radially inwards to the center of the LHC, the y axis vertically upwards and the z axis in beam direction towards the Jura mountains as seen from the experimental hall at P5. The azimuthal angle ϕ is measured from the x axis in the transverse plane spanned by the x and y axis. The transverse momentum p_T is defined as the projection of the momentum on the x - y plane. The polar angle θ is measured from the z axis, and the pseudorapidity is defined as $\eta = -\ln \tan(\theta/2)$. The CMS detector is divided into the barrel ($|\eta| < 1.3$), endcap ($1.3 < |\eta| < 3.0$) and forward region ($3.0 < |\eta| < 5.0$).

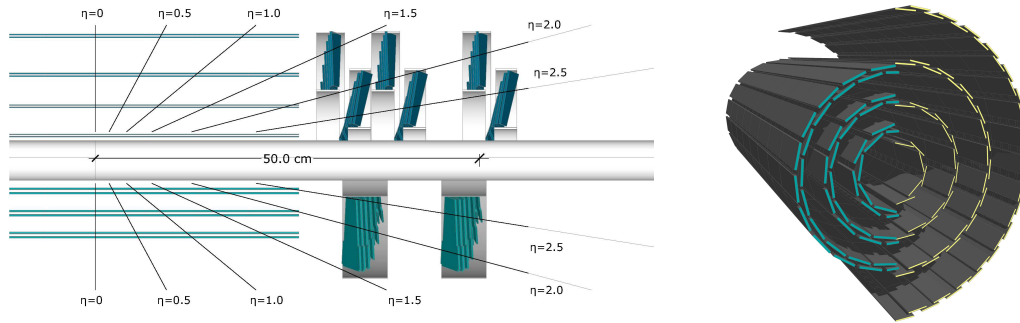


Figure 3.6: Sketch of the initial layout of the CMS pixel detector (lower half) and the updated layout (upper half), installed early 2017 [80]. The first pixel layer is located closer to the beam pipe, improving the vertex reconstruction in high pileup conditions.

3.2.2 Magnet

The core element of the CMS detector is its superconducting solenoid magnet which is operated at a temperature of 4.5 K. The inner bore has a cold diameter of 6.3 m with a 12.5 m length. At full current the stored energy is 2.6 GJ, resulting in a large ratio between stored energy and cold mass of the magnet which causes a large mechanical deformation of 0.15% during energizing. The magnetic flux is returned through a 10000 t steel yoke comprised of 6 endcap disks and 5 barrel wheels, housing the muon chambers.

3.2.3 Inner tracker

The CMS tracking system consists of silicon pixel and strip sensors, making a silicon sensor with a total area of about 200 m² that measures the trajectories of charged particles. The tracker is 5.8 m long, with a diameter of 2.5 m. In the barrel region, particles first pass through four layers of pixel sensors, before traversing 10 layers of strip sensors. The initial pixel detector comprised of three pixel layers in the barrel region and was designed to cope with an instantaneous luminosity of up to $1 \times 10^{34} \text{ cm}^{-2}$. An upgraded system with an additional layer closer to the interaction region was developed and installed early 2017 that is better equipped for an instantaneous luminosity of $2 \times 10^{34} \text{ cm}^{-2}$ [81]. The upgraded version features an additional layer in both the barrel and endcap regions, adding redundancy and allowing for better vertex reconstruction and tracking. Additionally, new read-out chips were designed with larger buffer size and higher bandwidth in order to avoid dynamic inefficiencies caused by buffer overflows in the original pixel detector. A comparison of the structures of the pixel detectors is shown in Fig. 3.6.

3.2.4 Electromagnetic calorimeter

The energy of photons and electrons is measured in the hermetic homogeneous calorimeter using lead tungstate (PbWO_4) crystals, which are read out by avalanche photodiodes and vacuum phototriodes. The barrel part of the ECAL (EB) covers a pseudorapidity range up to $|\eta| < 1.479$ and consists of 61200 crystals. The ECAL endcap part (EE) consists of 7324 crystals each and covers a region of $1.479 < |\eta| < 3.0$. The length of the crystals corresponds to a radiation length of 25.8 in the barrel region, and 24.7 in the endcap region. Neutral pions can be misidentified as photons, therefore, a preshower is placed in front of the EE crystals. The crystals suffer from a wavelength dependent loss of light transmission due to the high radiation levels and particle fluxes, without changes to the scintillation mechanism. This damage can be tracked and corrected for by measuring the optical transparency with injected laser light. In beam tests, the energy resolution of the ECAL was measured to be

$$\left(\frac{\sigma}{E}\right)^2 = \left(\frac{2.8\%}{\sqrt{E}}\right)^2 + \left(\frac{0.12}{E}\right)^2 + (0.30\%)^2, \quad (3.4)$$

where the first term parametrizes stochastic effects, the second term is the noise term, and the constant term is mainly due to non-uniformities, intercalibration errors and energy leakage from the back of the crystal. The above parametrization is valid for energies below about 500 GeV, above that threshold shower leakage from the rear of the crystals becomes significant. Therefore, a resolution of 0.5% for a 120 GeV electron is found.

3.2.5 Hadronic calorimeter

The HCAL is particularly important for the measurement of hadronic jets, but also missing transverse momentum that arises from undetectable particles like neutrinos or exotic, new elementary particles. It is subdivided into the barrel (HB), endcap (HE) and forward (HF) parts, and an additional outer (HO) calorimeter in the barrel region to catch late showering hadrons. The HB covers a pseudorapidity region of $|\eta| < 1.3$ and is a sampling calorimeter using brass absorbers and plastic scintillators. The scintillation light is extracted and shifted to the visible region using wavelength shifting cables, and detected by hybrid photodiodes. The scintillators of the HO are installed in the iron return yoke of the magnet, and it utilizes the magnet as absorber material. The HE covers a range of $1.3 < |\eta| < 3.0$ and is attached to the muon endcap yoke. The HF, extending the calorimeter coverage to up to $|\eta| < 5.0$, experiences highest particle fluxes. In order to achieve the necessary radiation hardness, quartz fibres are chosen as active material, with steel plates being used as absorber material.

3.2.6 Muon system

The muon system is used to identify, measure and trigger on muons. Three different detector types are used to achieve these goals. In the barrel region, covering a range of $|\eta| < 1.2$, drift tube (DT) chambers are mounted between the layers of the flux return yoke. In the endcap region of $0.9 < |\eta| < 2.4$ the magnetic field is larger and less uniform, therefore, cathode strip chambers (CSC) are employed which feature a fast response time and fine segmentation. Additionally, they are more radiation resistant, which is important due to the higher neutron flux in the more forward directions. A complementary system of resistive plate chambers (RPC) was added in the barrel and endcap region which provide an independent, fast and highly segmented trigger. Although the position resolution is coarser compared to the remaining muon system, the RPCs provide a fast response and a good timing resolution.

3.2.7 Trigger system

A two stage trigger system is used to preselect physics events of interest out of the 40 billion events taking place in the CMS detector every second. The first stage, or level 1 trigger (L1T), comprises of programmable custom hardware and reduces the event rate to below 100 kHz. The decision to keep or discard an event is based on coarse grained detector information from the calorimeters and muon system, without input from the tracking system. Trigger objects, called trigger primitives (TP), are built from these inputs which are combined and ranked by the regional triggers. The global trigger (GT) decision is based on the trigger objects delivered by the global muon and calorimeter triggers. The high level trigger (HLT) is based on specialized reconstruction software close to the offline software and runs on a farm of processors. The event rate after the HLT is below 1 kHz, keeping the data rate that has to be distributed to storage at around 1 GB/s.

3.3 Reconstruction of particles

Particles and physics objects are reconstructed and identified using the Particle Flow (PF) reconstruction algorithm [82]. By correlating information from all detector subsystems in a holistic manner, a significantly improved event description is achieved. The PF algorithm was first adopted in the ALEPH experiment at LEP, but has not been used in a hadron collider experiment before CMS. Fine granularity of the subdetectors is an essential requirement, and the CMS detector was designed in order to meet these needs.

As a first step the basic PF elements, namely tracks in the tracking and muon system, and energy clusters in the preshower, ECAL and HCAL, are reconstructed. Traditional track finding is based on Kalman Filtering (KF) [83]: Initial seeds are generated with few hits that

are compatible with charged particle trajectories, and pattern recognition is used to collect hits compatible with the trajectory. The origin, momentum, and direction of the charged particle are then determined by a final fit. An iterative tracking approach is employed to increase the efficiency of reconstructing low momentum, low quality tracks. Tracks with a large number of hits using pixel triplets as seeds are reconstructed first, and with a low misreconstruction rate. Associated tracks are then masked for the next iteration, reducing the probability for tracks made of randomly associated hits. Ten iterations with different track seeds, targeting tracks from prompt and high momentum particles to displaced tracks and muons, are performed. Detection inefficiencies at high momentum are mitigated by the calorimeters and the muon system.

Electron reconstruction is seeded by an ECAL-based and a tracker-based approach. Seeding from ECAL superclusters, clusters with a small window in η and extended window in ϕ to collect the energy emitted by bremsstrahlung photons, is the traditional approach which becomes inefficient at low momentum or electrons in jets. Tracker-based seeding recovers efficiency by using all tracks from the iterative tracking including low momentum tracks. Electrons are disentangled from charged hadrons by exploiting the probability of electrons to radiate. A Gaussian-sum filter (GSF) [84] is used to fit selected tracks which is better suited for finding tracks with changing momentum than the KF that is used in iterative tracking.

With electrons, photons and hadrons absorbed in the calorimeters located inside the solenoid magnet, muons are identified with high efficiency by the muon system over the full detector acceptance. Muons are reconstructed in three different ways: The track of a standalone-muon is fitted from hits in the DT, CSC and RPC systems, with the trajectory reconstructed from seeds using the DT and CSC detector. For a global muon, the standalone-muon track is matched to a track of the inner tracker, forming a global-muon track. This improves the momentum resolution for muons with transverse momenta above 200 GeV with respect to the tracker-only fit. Tracks found in the inner tracking system are extrapolated to the muon system if their p_T is larger than 0.5 GeV and the total momentum above 2.5 GeV. At least one muon segment has to be compatible with the extrapolated track in order for the inner track to qualify as a tracker muon track. Global and tracker muons that share the same inner track are merged into a single candidate.

The clustering algorithm in the calorimeters is essential for the energy and direction measurement of photons and neutral hadrons, to separate energy deposits of charged hadrons from these neutral particles and for reconstructing and identifying electrons and its bremsstrahlung photons. Additionally, in cases of inaccurate track measurements of charged hadrons it assists their energy measurement, especially for tracks with high p_T or low quality.

PF elements from the different subdetectors are linked to form PF blocks of associated elements. Within each block, particles are reconstructed in a hierarchical order. Muons are first reconstructed, and the corresponding tracks and clusters are then removed from the block.

Electrons and their radiated photons as well as isolated photons are reconstructed in the next step, again removing corresponding PF elements from the block. Charged and neutral hadrons are identified afterwards. Tracks with p_T uncertainties larger than the expected calorimetric energy resolution are masked, which rejects a large number of misreconstructed jets. In cases where the rejected track comes from a genuine high momentum hadron its energy is measured more accurately in the calorimeter. Charged and neutral hadrons are then cross-identified from the remaining elements in the block.

The reconstructed vertex with the largest value of summed physics-object p_T^2 is taken to be the primary pp interaction vertex (PV). The physics objects are the jets, clustered using the jet finding algorithm [85, 86] with the tracks assigned to the vertex as inputs, and the associated missing transverse momentum, taken as the negative vector sum of the p_T of those jets.

3.3.1 Muons

Isolation of muons is measured using additional inner tracks and calorimeter deposits within a distance of $\Delta R = \sqrt{\Delta\phi^2 + \Delta\eta^2} < 0.3$. For an isolated muon the sum of p_T of the tracks and E_T of the deposits has to be below 10% of the muon p_T . The muon momentum measurement is solely based on the inner track for $p_T < 200$ GeV. Above that threshold the momentum is extracted from the track fit with the smallest χ^2 probability, out of the tracker only, tracker and first muon detector plane, global and global without the muon detector planes featuring high occupancy. Loose and medium working points for muon identification are defined based on quality requirements [87]. Loose muons are defined as muons that are selected by the PF algorithm that are also either a tracker or global muon. Prompt muons from the primary vertex or muons from light and heavy flavor decays are targeted with the loose identification (ID). The medium muon ID is tuned towards an overall efficiency of 99.5% for muons from simulated W or Z boson decays. Several additional requirements on top of the loose muon ID, mainly on the muon segment compatibility and the track quality, are applied to target prompt muons and those from heavy flavor decays.

3.3.2 Electrons and Photons

Electrons and photons are reconstructed in the same step due to the interplay caused by bremsstrahlung photons emitted by electrons, and photons converting into electron-positron pairs. Electron candidates are seeded from GSF tracks with a corresponding ECAL cluster, while photon candidates are seeded from ECAL superclusters with minimum E_T of 10 GeV, given that no link to a GSF track exists. For ECAL based electron and photon candidates the energy deposit in closeby HCAL cells is restricted to be less than 10% of the supercluster energy. Corrections to the measured energy are applied as function of the energy and η ,

accounting for missed energy in the process, e.g. in the tracker material.

Electrons are further identified using multivariate analysis (MVA) techniques [88]. Boosted decision trees (BDT) are used which are based on input variables that compare measurements from the ECAL and the tracker, purely calorimetric observables that are used to separate genuine electrons from misidentified ones, and tracking observables that improve the discrimination of electrons and charged hadrons.

Photons are identified using sequential requirements or MVA based tools [89]. For the former, selections are made in terms of isolation sums, the hadronic fraction and the lateral extension of the shower, after applying an electron veto. The MVA based ID employs BDTs which uses several input variables describing shower shapes, isolation, the median energy per unit area ρ which is a measure for pileup, and the η and uncorrected energy of the supercluster of the photon candidate.

3.3.3 Jets

Jets are the collimated showers of charged and neutral hadrons, mostly charged and neutral pions (π^\pm , π^0), kaons (K^\pm , K^0), protons and neutrons, and photons, originating from single quarks or gluons as a consequence of parton showers and hadronization. Leptons can also be part of jets, especially when light or heavy meson decays are involved. The hadrons are reconstructed from tracks and calorimeter deposits with the PF algorithm, and finally clustered into jets with the anti- k_t algorithm [85,86] using a distance parameter of $R=0.4$. The jet energy scale is corrected in three steps [90]. First, energy from pileup interactions is removed using simulated samples of dijet events with and without simulated pileup. Additional corrections extracted from data samples are applied to jets in data samples. Next, the jet response, defined as the ratio of the reconstructed to the reference jet energy, is measured in simulated samples. Corrections to the jet response are applied as a function of jet p_T and η , making the response uniform over these two variables. Remaining differences of the response between data and simulated samples are corrected by residual corrections extracted from samples enriched in Z+jets, γ +jets and multijet events.

3.3.4 Missing transverse momentum

Particles that are invisible to the detector can be measured indirectly using the momentum imbalance in the transverse plane which is calculated as the negative vector sum of particle transverse momenta

$$\vec{p}_T^{\text{miss}} = - \sum_{\text{particles}} \vec{p}_T \quad , \quad (3.5)$$

where the particles are given by the collection of PF candidates. The magnitude of \vec{p}_T^{miss} is referred to as missing transverse momentum p_T^{miss} . Corrections to the jet energy scale are propagated to p_T^{miss} by subtracting the applied correction from the \vec{p}_T^{miss} , referred to as type-1 (T1) correction

$$\vec{p}_T^{\text{miss}}(\text{T1}) = \vec{p}_T^{\text{miss}} - \sum_{\text{jets}} (\vec{p}_{T\text{jet}}^{\text{corr}} - \vec{p}_{T\text{jet}}) \quad . \quad (3.6)$$

The resolution and scale of p_T^{miss} is measured in samples enriched $Z+\text{jets}(Z \rightarrow \ell\ell)$ or $\gamma+\text{jets}$ which involve no neutrinos, and are therefore without genuine p_T^{miss} .

3.3.5 Lepton isolation

Prompt leptons from decays of W and Z bosons can be distinguished from those produced in jets using isolation. Different measures for lepton isolation are defined. The absolute isolation of a lepton using PF objects is measured as the sum of the p_T of charged (h^\pm) and neutral hadrons (h^0) and photons

$$I_{\text{PF}} = \sum_{h^\pm} p_T^{h^\pm} + \sum_{\gamma} p_T^\gamma + \sum_{h^0} p_T^{h^0} \quad , \quad (3.7)$$

where particles within a certain distance ΔR (usually 0.3 or 0.4) of the lepton are considered. The contributions from neutral hadrons and photons are corrected for pileup effects. The relative isolation is calculated with respect to the lepton p_T

$$I_{\text{rel}} = \frac{I_{\text{PF}}}{p_T} \quad . \quad (3.8)$$

One can also use a p_T dependent distance parameter ΔR where the cone around softer leptons is larger, first introduced in [91], and commonly called mini-isolation I_{mini} . A smaller cone for leptons with high p_T enhances the efficiency of the isolation requirement in events with boosted top quarks of W bosons, while the small cone at low p_T ensures good rejection of nonprompt leptons. The distance parameter ΔR is chosen as

$$\Delta R = \begin{cases} 0.2 & p_T \leq 50 \text{ GeV} \\ \frac{10 \text{ GeV}}{p_T} & p_T \in (50, 200) \text{ GeV} \\ 0.05 & p_T \geq 200 \text{ GeV} \end{cases} \quad . \quad (3.9)$$

3.4 Simulation of events

Simulated events are used for studies of physics objects, background predictions or signal efficiency and acceptance determinations. A crucial ingredient to be able to simulate the complicated events at hadron colliders is factorization, which allows to separate the treatment of processes happening at different momentum transfer scales. The hard scatter of the incoming partons happens at the highest involved scale, and can be treated perturbatively. Soft processes that finally lead to the formation of the observed final state hadrons cannot yet be calculated from first principles and therefore need to be modeled. Secondary interactions of other constituent partons of the colliding hadrons are called underlying event. Although the hard and soft process are distinct, they are connected by an evolutionary Markov process that leads to parton showering. The partons produced in this process eventually participate in the hadron formation (hadronization) where color singlet states are formed. Monte Carlo techniques can be used for simulating the Markov process, efficient integration of the high dimensional hard scatter problem, and the hadronization models.

The cross section of the hard subprocess at a hadron collider can be computed using a factorization approach [92, 93]

$$\sigma = \sum_{a,b} \int_0^1 dx_a dx_b \int f_a^{h_1}(x_a, \mu_F) f_b^{h_2}(x_b, \mu_F) d\hat{\sigma}_{ab \rightarrow n}(\mu_F, \mu_R) \quad , \quad (3.10)$$

where $f_a^h(x, \mu_F)$ are the parton distribution functions (PDFs) depending on the momentum fraction x of parton a with respect to the parent hadron h and the factorization scale μ_F . The parton-level cross section of the $ab \rightarrow n$ process, $\hat{\sigma}_{ab \rightarrow n}(\mu_F, \mu_R)$, depends on the momenta given by the final-state phase space as well as the factorization and renormalization scale, μ_R and μ_F . The parton-level cross section is given by the product of the matrix element (ME) squared, which in turn is generated at leading order (LO) or next-to-leading order (NLO) of perturbation theory using matrix element generators. In CMS, the majority of processes is generated using the MADGRAPH5_aMC@NLO [94] or POWHEG v2.0 [95] generators. No first principle exists for the choice of the unphysical renormalization and factorization scales. A reasonable choice is to set $\mu_R = \mu_F = Q^2$, and choose Q^2 according to the mass scale of the process. As an example, for a massive particle of mass M produced in the s-channel the scale can be chosen as $Q^2 = M^2$.

PDFs are determined from fit of theoretical predictions based on QCD theory at different orders of perturbation theory to data from various experiments. At leading order, the PDF has a probabilistic interpretation that is lost when correction terms from higher perturbative order are added. In CMS, PDFs from the NNPDF collaboration [96–98] are widely used.

The PYTHIA 8.2 code [99] is used for simulating the parton shower (PS) and hadronization. Different tunes defining the underlying-event parameters are obtained by fitting proton-proton

collision data at various center-of-mass energies [100, 101].

The nominal vertex of an event is exactly at the origin of the CMS coordinate system in simulation. A vertex smearing software is used in order to model the natural spread of the interaction region.

The interaction of the particles with the detector is simulated using the GEANT4 program [102]. This part of the event generation is the most time consuming, therefore, large scale signal sample production is often done using a faster simulation tool [103], referred to as FASTSIM, where the detector response is parametrized. As a next step, the output of the detector readout electronics is modelled, called digitization. The effect of pileup is taken care of by adding simulated hits of pileup in the digitization step of the event simulation. The pileup events, also called minimum bias events, are generated using the PYTHIA 8.2 event generator. The reconstruction of the digitized event is then done with the same software that is used for experimental data.

Search for top squarks and dark matter particles in dilepton final states

TOP SQUARKS, the scalar partners of the top quark in SUSY, are the lightest strongly coupled superpartner in many theories. The focus in this analysis lies on R-parity conserving models, therefore, the top squarks, denoted as \tilde{t} , are always produced in pairs $\tilde{t}\tilde{t}^*$. These top squarks can have a variety of decay modes depending on the mass hierarchy of the SUSY particles. The simplest top squark decay mode is $\tilde{t} \rightarrow t\tilde{\chi}_1^0$, where t and $\tilde{\chi}_1^0$ are the top quark and the lightest neutralino, respectively. This mode is represented by the Simplified Model Spectra (SMS) [66, 104, 105] labeled “T2tt” following the conventions introduced in [67], and is shown on the top left of Fig. 4.1. Two variations of this decay mode are shown in Fig. 4.1 top right and bottom left. The former shows the “T2bW” model in which each top squark decays into a bottom quark and a chargino with a mass given by the arithmetic mean of the top squark and the neutralino. The chargino subsequently decays into a W boson and the lightest neutralino. The latter shows a model with a mixed decay of top squarks into bottom and top quarks, which is called “T2bt”. Here, the mass of the chargino is 5 GeV higher than the mass of the neutralino. The relative branching ratio in each of the modes is 50% and hence it contains 25% of T2tt at each mass point. The sensitivity to this model is studied, and indeed it is found that the acceptance for the soft lepton from the chargino decay is very small and hence the 25% contribution from T2tt drive the sensitivity. Therefore, no dedicated interpretation of the observed results will be provided for this model.

Another interesting decay mode is $\tilde{t} \rightarrow b\tilde{\chi}_1^\pm \rightarrow \nu\tilde{\ell} \rightarrow \ell\tilde{\chi}_1^0$, where the additional SUSY particles $\tilde{\chi}_1^\pm$, the lightest chargino, and $\tilde{\ell}$, one of the sleptons, are included in a cascade decay of the top squark. In this interpretation of the results a chargino mass of $m_{\tilde{\chi}_1^\pm} = (m_{\tilde{t}} + m_{\tilde{\chi}_1^0})/2$ is assumed. Three different slepton masses $m_{\tilde{\ell}} = x \times (m_{\tilde{\chi}_1^\pm} - m_{\tilde{\chi}_1^0}) + m_{\tilde{\chi}_1^0}$ are chosen where the slepton mass is either close to the chargino ($x = 0.95$), half way between chargino and neutralino ($x = 0.5$) or close to the neutralino ($x = 0.05$). A visualization of the mass spectrum of this simplified model is given in Fig. 4.2. This mode has a 100% branching ratio into the

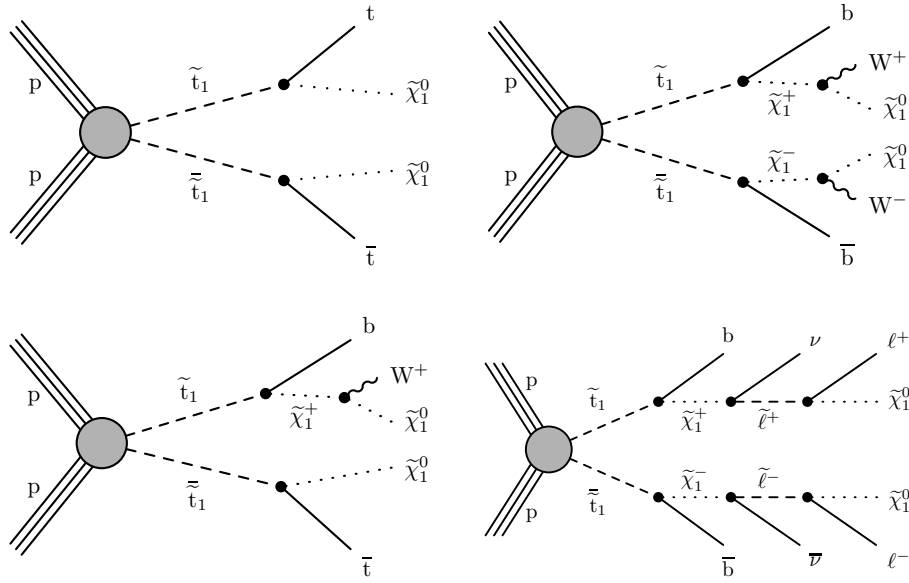


Figure 4.1: Diagrams representing the simplified model T2tt of direct top squark production with decay via an on-shell top quark (top left), top squark decay into a bottom quark and chargino (T2bW, top right), mixed decay into top and bottom quarks (T2bt, bottom left), and the simplified model T8bb $\ell\ell\nu\nu$ where the pair produced top squarks undergo a cascade decay to the lightest chargino, a slepton and the lightest neutralino (bottom right).

two opposite-sign lepton final state and therefore exhibits the sensitivity of the analysis nicely. Following SMS conventions, this decay mode is called “T8bb $\ell\ell\nu\nu$ ” and is shown to the bottom right of Figure 4.1. Previous searches for direct top squark pair production that have been carried out by the ATLAS and CMS collaborations [106–113] have not found a significant excess of data over the SM prediction.

The search presented in this note is model independent, therefore the results are also interpreted in terms of simplified DM models. The simplest and most relevant model for DM production with $t\bar{t}$ proposes a spin-0 interaction between DM and SM particles [68–71]. If the new physics associated with DM satisfies minimal flavour violation, where the couplings between the mediator and the SM particles are Yukawa-type, then heavy flavour (top quark) production is favoured. At leading order, the process is gluon-induced and a $t\bar{t}$ pair is produced with a pair of DM fermions, shown in Fig. 4.3. Searches for production of DM particles in association with heavy flavor quarks, either in interpreted in terms of EFTs or simplified models including scalar or pseudoscalar mediators, have been carried out at the LHC by the ATLAS and CMS collaborations [114–118], observing no significant deviation from the SM predictions.

Events with two opposite charge isolated leptons, and two jets with at least one b-tagged jet are selected to perform the search. The transverse mass variable $M_{T2}(\ell\ell)$ [119, 120] is used to separate the top squark signal from the SM background, which consists primarily of

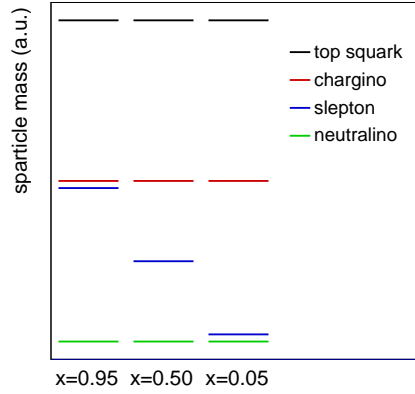


Figure 4.2: Illustration of the mass spectrum of the T8bb $\ell\ell\nu\nu$ model. The chargino mass is always half way between the top squark and neutralino mass. The parameter x defines whether the slepton mass is close to the chargino mass ($x = 0.95$), the neutralino mass ($x = 0.05$), or half way between both masses ($x = 0.5$).

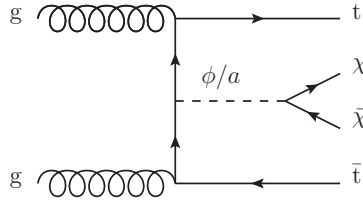


Figure 4.3: Leading order diagram for a simplified model of $t\bar{t}$ +DM production.

$t\bar{t}$ decaying into dileptons. The transverse mass is a generalization of the transverse mass M_T to a system of pair produced particles that decay semi-invisibly. In the case of W boson production, M_T is formed from the transverse momentum of a high p_T lepton (from the W decay) and the missing transverse momentum (p_T^{miss}) in the event, which is assumed to come from the corresponding neutrino. The definition of M_T in the limit where the masses of the daughter particles can be neglected is given by

$$M_T = \sqrt{2p_T(\ell)p_T^{\text{miss}} [1 - \cos(\Delta\phi)]} \quad . \quad (4.1)$$

By construction, the transverse mass of the lepton and the p_T^{miss} is below the mass of the mother particle, in the case of a leptonic W decay $M_T \leq m_W$. In order to generalize to a system with two particles of the same mass, each decaying semi-invisibly, the measured p_T^{miss} has to be decomposed into a sum of two missing transverse momentum vectors according to

$$\vec{p}_T^{\text{miss}} = \vec{p}_{T,1}^{\text{miss}} + \vec{p}_{T,2}^{\text{miss}} \quad . \quad (4.2)$$

Each missing transverse momentum vector can then be paired with the visible products of the decay in order to form M_T for each leg of the pair production. However, since the correct division of the \vec{p}_T^{miss} into two components is not known, a useful method is to minimize the maximum of the two transverse masses formed under all possible combinations satisfying Eq. 4.2. This effectively means scanning the entire parameter space of hypothetical neutrino momenta which satisfy Eq. 4.2. For each point, M_T is calculated for each leg of the event, and the maximum of the two values is determined. $M_{T2}(\ell\ell)$ is then the minimum value of the larger M_T calculated of all possible pairings. This is equivalent to

$$M_{T2}(\ell\ell) = \min_{\vec{p}_{T,1}^{\text{miss}} + \vec{p}_{T,2}^{\text{miss}} = \vec{p}_T^{\text{miss}}} \left(\max \left[M_T^2(\vec{p}_T^{\ell 1}, \vec{p}_{T,1}^{\text{miss}}), M_T^2(\vec{p}_T^{\ell 2}, \vec{p}_{T,2}^{\text{miss}}) \right] \right) . \quad (4.3)$$

It can be shown [120] that $M_{T2}(\ell\ell)$ has the same convenient property as the transverse mass M_T : it has an upper bound at the mass of the pair-produced semi-invisibly decaying particle. In the case of top squark ($\tilde{t} \rightarrow t\tilde{\chi}_1^0$) searches in the dilepton channel, the primary challenge comes from separating SM $t\bar{t}$ production from the signal, since the composition of the final states is identical except for the additional invisible particles. In dileptonic $t\bar{t}$ events the final state is

$$pp \rightarrow t + \bar{t} + X \rightarrow bW^+ + \bar{b}W^- + X \rightarrow b\bar{\nu}_\ell + \bar{b}\bar{\nu}_\ell + X .$$

Assuming that the contribution of the other products X to the p_T^{miss} is not large, the assumptions made in the definition of $M_{T2}(\ell\ell)$ hold for the lepton- p_T^{miss} system and its value has an upper bound at the W mass. On the other hand, top squark pair production events with a dileptonic final state will have at least four invisible particles so long as lepton number and R-parity are both conserved. The top squark decays can proceed differently depending on the model considered but a typical example for the models used here is

$$pp \rightarrow \tilde{t} + \bar{\tilde{t}} + X \rightarrow \tilde{\chi}_1^0 t + \tilde{\chi}_1^0 \bar{t} + X \rightarrow \tilde{\chi}_1^0 bW^+ + \tilde{\chi}_1^0 \bar{b}W^- + X \rightarrow \tilde{\chi}_1^0 b\bar{\nu}_\ell + \tilde{\chi}_1^0 \bar{b}\bar{\nu}_\ell + X.$$

Now there are two invisible particles on each side of the decay, and so the partition of the p_T^{miss} into two components no longer has an upper bound at the W mass. Similarly, one is also able to construct other variants on the $M_{T2}(\ell\ell)$ variable, which e.g. take into account the b-tagged jets and are expected to have an upper bound at the top mass:

$$M_{T2}(\ell b \ell b) = \min_{\vec{p}_{T,1}^{\text{miss}} + \vec{p}_{T,2}^{\text{miss}} = \vec{p}_T^{\text{miss}}} \left(\max_{b \in b_1, b_2; \ell \in \ell_1, \ell_2; i \in 1, 2} \left[M_T^2(\vec{p}_T^b + \vec{p}_T^\ell, \vec{p}_{T,i}^{\text{miss}}) \right] \right) \quad (4.4)$$

If there is only one b-tagged jet in the event, the jet with the highest p_T failing the b-tagging requirement is used. There are two choices how to pair the two leptons and the two b-tagged jets in the case of $M_{T2}(\ell b \ell b)$. This ambiguity is resolved by minimizing the maximum invariant mass of the two lepton-jet pairs.

The properties of $M_{T2}(\ell\ell)$ and $M_{T2}(\ell b\ell b)$ as well as p_T^{miss} are used in order to construct signal regions, all with $M_{T2}(\ell\ell)$ above the W mass, that only have a small contamination from dileptonic top decays stemming from the SM. The simulated distributions of the observables using a minimum requirement of $M_{T2}(\ell\ell) > 100$ GeV are shown in Fig. 4.4. The main SM backgrounds in the high $M_{T2}(\ell\ell)$ signal regions are residual $t\bar{t}$ events that enter the tail of the distribution, Drell-Yan (DY) processes and production of two or more W or Z bosons (multiboson), and production of $t\bar{t}$ in association with a Z, W or Higgs boson.

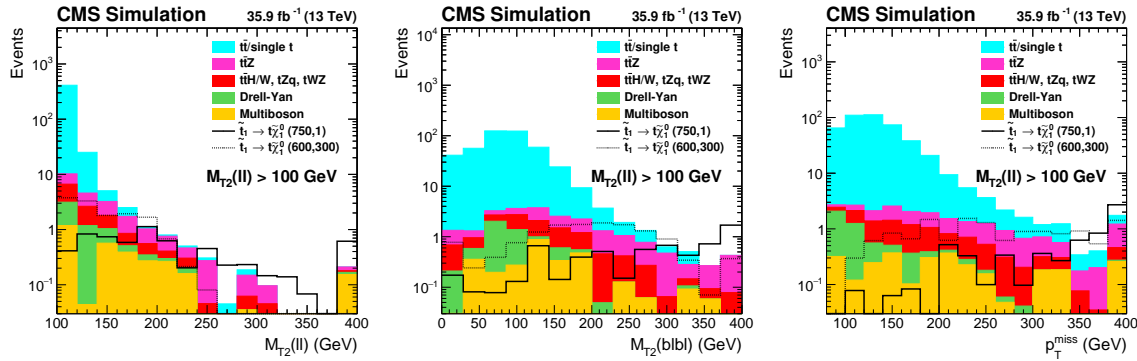


Figure 4.4: Simulated distributions of the observables that define the signal regions after the pre-selection defined in Tab. 4.2 including $M_{T2}(\ell\ell) > 100$ GeV, $M_{T2}(\ell\ell)$ (left), $M_{T2}(\ell b\ell b)$ (center) and p_T^{miss} (right). Two mass points of the potential SUSY signal are shown as solid and dashed lines, respectively. The SM backgrounds are shown as colored stacked histograms [12].

4.1 Data sets and simulation

The analysis uses 2016 pp collision data at $\sqrt{s} = 13$ TeV, corresponding to an integrated luminosity of $L = 35.9 \text{ fb}^{-1}$. The average number of interactions per bunch crossing in this data set is 27, shown in Fig. 3.3. The data set is split into primary data sets (PDs) based on the L1 trigger that selected the events. The single electron and muon, double electron and muon and muon/electron PDs are used for the analysis, while PDs selected by p_T^{miss} and jet or hadronic activity triggers are used to measure the efficiencies of the lepton triggers.

Samples for SM backgrounds are generated with MC event generators, using an assumed average pileup of $\langle \mu \rangle = 20$ and a bunch crossing spacing of 25 ns. Simulated events are then reweighted to match the true pileup profile in data. The target pileup distribution in data is generated using the instantaneous luminosity per bunch crossing for each luminosity section, and assuming a total pp inelastic cross section of 69.2 mb. A variation of $\pm 5\%$ on this cross section is used to estimate the uncertainties due to the pileup modeling.

Simulated samples of $t\bar{t}$ production as well as $t\bar{t}$ production in association with a Higgs boson are generated at NLO using the POWHEG v2 generator [95, 121–124], and PYTHIA 8.2 [99] with

the CUETP8M2T4 tune [100, 125] is used for parton showering and hadronization. The $t\bar{t}$ process is normalized to the NNLO cross sections [126]. Single top quark production in the s-, t- and tW-channel is simulated with the POWHEG v1 generator [127, 128].

Drell-Yan events are generated at LO with up to four extra jets in the ME calculation using the MADGRAPH5_aMC@NLO v2.3.3 generator [94], with the cross section being normalized to the NNLO calculation [129]. Double counting of jets from the generator and the PS is taken into account using the MLM jet matching scheme [130].

Single top quark or $t\bar{t}$ production in association with a Z boson, e.g. $t\bar{t}Z$, tZW and tZq , and production of three W or Z bosons is simulated using the MADGRAPH5_aMC@NLO generator at NLO precision. Events for diboson production as well as the $t\bar{t}W$ process are generated at NLO with up to one extra jet in the ME calculation, using the MADGRAPH5_aMC@NLO generator and the FxFX scheme [131] to match jets between the generator and the PS code. DM and SUSY signal samples are generated at LO with one or two extra jets, respectively, using the MADGRAPH5_aMC@NLO generator. The top squark production cross section is calculated at NLO and next-to-leading logarithmic (NLL) precision [132]. A fast detector simulation is used for SUSY signal samples in order to enable the production of scans over a large variety of mass combinations [103].

For all the above samples using the MADGRAPH5_aMC@NLO code the generator is interfaced with PYTHIA 8.2 using the CUETP8M1 tune [100]. NNPDF3.0 [97] PDF sets at LO or NLO using $\alpha_S = 0.130$ or $\alpha_S = 0.118$, respectively, are consistently used for the SM samples generated at LO or NLO accuracy.

4.2 Event triggers

Various sets of triggers are used in order to achieve an optimal selection efficiency. For each dilepton channel (ee , $\mu\mu$ and $e\mu$) the logical OR of dilepton triggers is taken, therefore combining triggers selecting isolated and non-isolated leptons. Moreover, the partially inefficient dilepton triggers are complemented by single lepton triggers. The overlap between the PDs is removed by vetoing events in the single lepton primary data sets that also fired a dilepton trigger. Because the $e\mu$ channel is complemented by two single lepton primary data sets, the procedure has two steps: First, events are added from the *SingleElectron* PD that fired single electron triggers but failed the double lepton triggers that are used to select events in the *MuonEG* primary data set. Furthermore, events are added from the *SingleMuon* PD that fired single muon triggers but fired none of the triggers used to select events in either the *MuonEG* or the *SingleElectron* primary data set. The selection threshold for single muons and electrons is 24 and 27 GeV, respectively. For dilepton triggers, the threshold for the leading leptons is lowered to 17 and 23 GeV for muons and electrons, while the threshold for the trailing lepton

is 8 to 12 GeV.

The trigger efficiencies are measured in the *MET* and *JetHT* data sets, where events are selected with orthogonal triggers, and consistent results are obtained with the two measurements. The measurement obtained in the *MET* data set is used because of the smaller statistical uncertainties. There is a significant inefficiency for muons with high transverse momentum in the muon endcaps, therefore the trigger inefficiency is parametrized as a function of the two lepton momenta. Two bins of the η of the leading lepton separated at $|\eta| = 1.5$ are defined. In the $e\mu$ channel, the measurement is binned in the same way but the η of the muon is taken, whether it is leading or not. The measured trigger efficiencies are applied as scale factors to the simulation.

Figure 4.5 shows the gain in trigger efficiency by including the non-isolated double-lepton and, additionally, the single-lepton triggers for the $\mu\mu$ channel and $|\eta| > 1.5$ of the leading muon. Significant improvement at high transverse momentum of the muon is observed. All other trigger efficiency maps show less prominent effects and are collected in Appendix A.1.

4.3 Object and event selection

Leptons, jets and $p_{\text{T}}^{\text{miss}}$ are reconstructed using the PF algorithm as described in Sec. 3.3. First, the selection criteria for leptons and jets are defined, before discussing baseline requirements for events in order to be selected for the analysis. Based on this event selection, signal and background enriched regions are constructed, which are called signal and control region in the following.

4.3.1 Object selection

Leptons

Leptons are selected according to a set of identification and isolation criteria which are summarized in Table 4.1 and discussed in the following. Selected leptons must have a minimum transverse momentum of 20 GeV and be within the region bounded by $|\eta| < 2.4$. In order to reject leptons that are not originating from prompt W or Z boson decays a relative isolation of the leptons of $I_{\text{rel}} < 0.12$ has to be passed. Additional requirements on the distance from the PV (d_{xy} and d_z) and the significance of the 3D impact parameter to the event vertex ($\text{SIP}_{3\text{D}}$) are placed. Standard identification methods are used for electrons and muons [87, 88], using the tight and medium working points for electrons and muons, respectively.

The lepton identification and isolation efficiencies are measured per lepton leg in $Z/\gamma^* \rightarrow \ell\ell$ events using the tag-and-probe technique [88, 133]. The resulting factors to scale simulation to data are derived in bins of lepton p_{T} and $|\eta|$. They are close to unity and shown for electrons

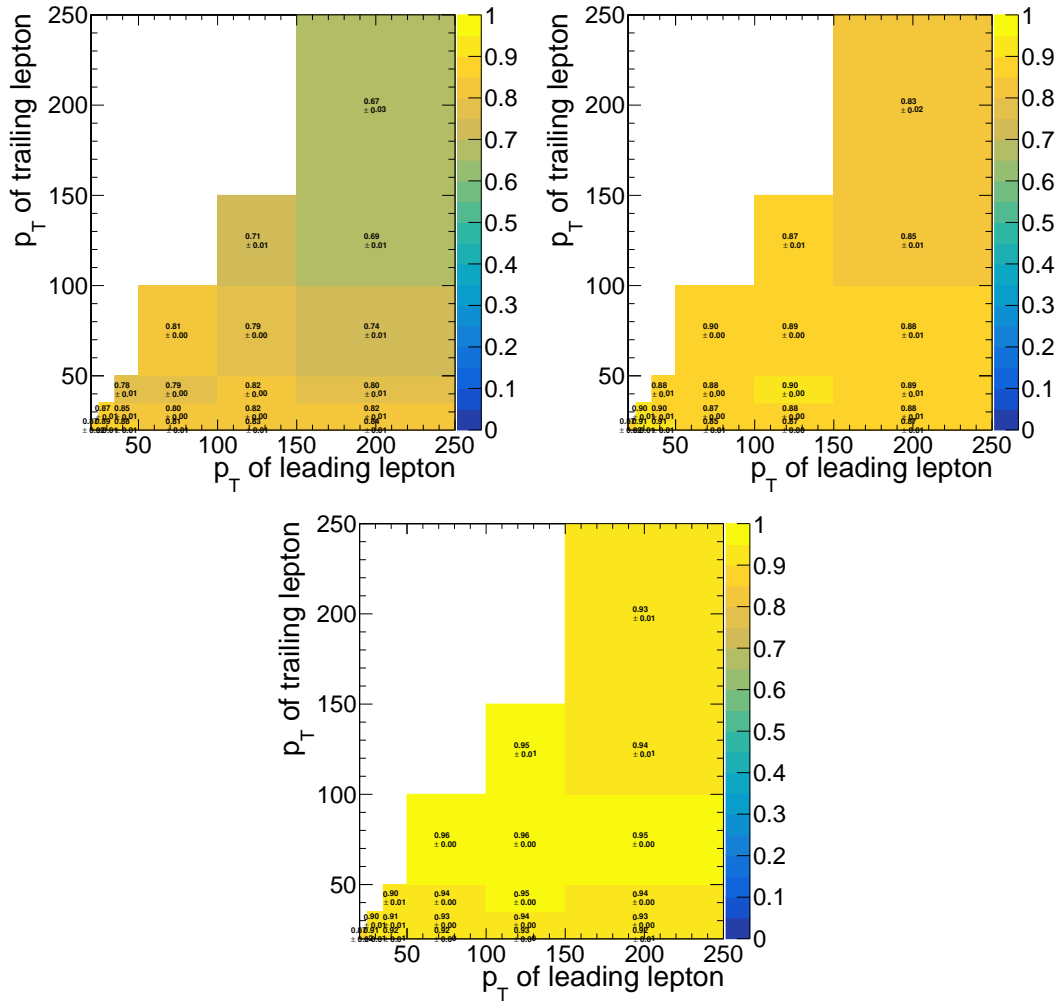


Figure 4.5: The trigger efficiency for the $\mu\mu$ channel for different combinations of triggers: only isolated dimuon triggers (top left), using the logical OR of isolated and non-isolated dimuon triggers (top right), and additionally also using the single muon triggers (bottom).

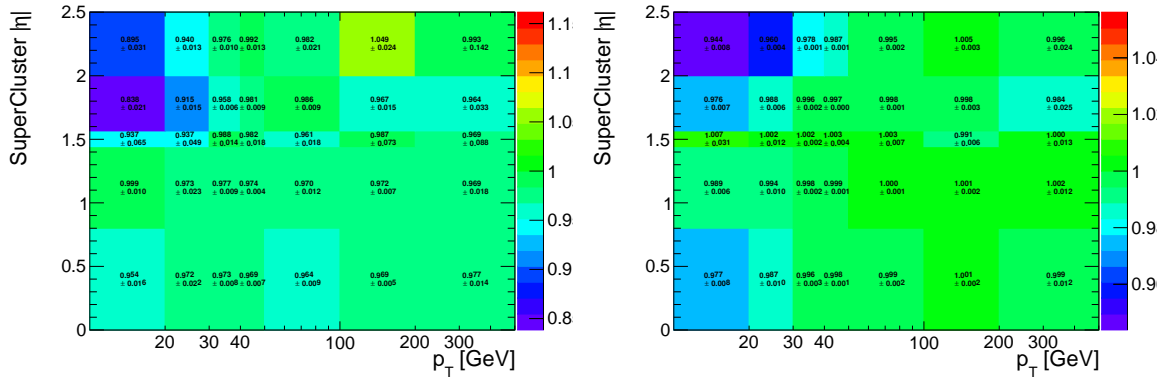
and muons in Fig. 4.6 and Fig. 4.7, respectively. Efficiencies in simulated samples using the fast detector simulation are considerably different from those measured in samples using the full detector simulation due to the different modeling of showers and pileup. Therefore, additional scale factors are applied to the SUSY signal samples. Finally, the loss of lepton reconstruction efficiency due to tracking inefficiencies is taken into account by applying additional scale factors to each of the lepton legs.

Jets

Particle candidates found by the PF algorithm are clustered into jets using the anti- k_t algorithm with a distance parameter $R=0.4$. As described previously, the jet energy scale is corrected to account for pileup and the detector response. Corrected jets with $p_T > 30$ GeV and $|\eta| < 2.4$ are selected if they pass the loose jet identification criteria, i.e. the neutral electromagnetic and

Table 4.1: Lepton selection criteria for the two selected leptons and the veto of additional leptons.

	dilepton selection		3 rd lepton veto	
	electrons	muons	electrons	muons
p_T	> 20 GeV	> 20 GeV	> 15 GeV	> 15 GeV
$ \eta $	< 2.4	< 2.4	< 2.4	< 2.4
I_{rel}	< 0.12	< 0.12	< 0.4	< 0.4
$ d_{xy} $	< 0.05	< 0.05	< 0.05	< 0.05
$ d_z $	< 0.1	< 0.1	< 0.1	< 0.1
SIP _{3D}	< 4	< 4	< 4	< 4
identification	cut based tight ID	medium muon ID	cut based veto ID	veto muon ID
missing hits	0	-	-	-

**Figure 4.6:** Scale factors for electrons for the identification and impact parameter requirements (left), and the isolation working point (right).

hadron fractions are $< 99\%$ and the jet consists of at least two PF candidates. Furthermore, both the charged hadron fraction and multiplicity are required to be > 0 and the charged electromagnetic fraction has to be $< 99\%$. Leptons can be clustered into jets, resulting in a potential overlap of jets with one of the selected leptons. To prevent this overlap jets are removed from the set of selected jets if they are found within a cone of $R = 0.4$ around any of the selected signal leptons.

4.3.2 Event selection

Events with spurious p_T^{miss} due to excessive detector noise, beam halo or low quality muon reconstruction are removed using dedicated filters [10]. Two leptons (ee , $\mu\mu$ or $e\mu$) with opposite charge with a minimum dilepton invariant mass of $m_{\ell\ell}$ of 20 GeV are required, and the leading lepton is required to exceed $p_T > 25$ GeV. Events containing additional leptons passing looser selection requirements shown in Tab. 4.1 are rejected. The invariant mass requirement successfully rejects events from QCD multijet processes. For same-flavor dilepton events (ee or $\mu\mu$), events with a $m_{\ell\ell}$ falling within a 15 GeV range from the Z boson mass

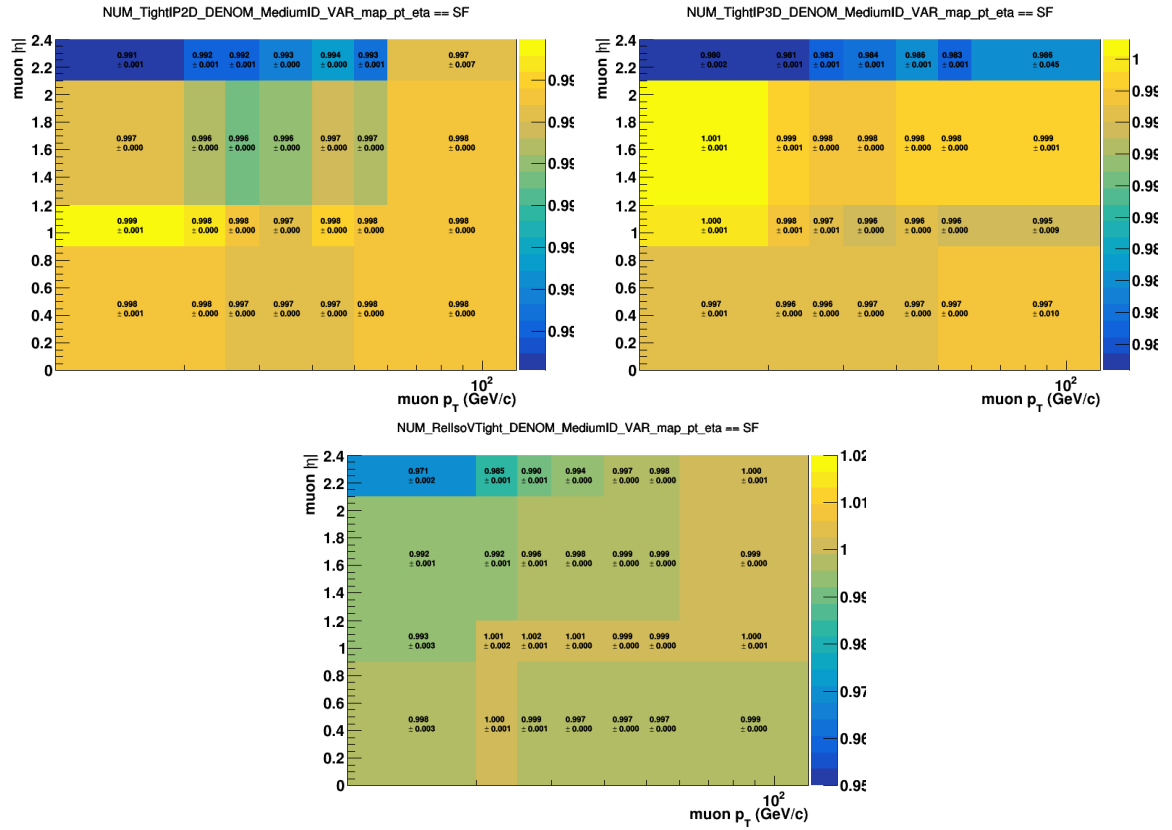


Figure 4.7: Scale factors for the muon identification (top left), SIP_{3D} (top right), and the isolation working point requirements (bottom).

are rejected (off-Z) in order to minimize DY background contamination. At least two jets are required, out of which at least one has to be tagged as originating from b quarks, using the CSVv2 algorithm [134] at the medium working point which has an average tagging efficiency of 65%. A minimum requirement of $p_T^{\text{miss}} > 80$ GeV is applied in order to reduce DY and multiboson events. Additionally, a cut on a proxy of the p_T^{miss} significance defined as $p_T^{\text{miss}}/\sqrt{H_T}$ is applied to further reduce the DY background. It takes the hadronic activity of the event H_T into account, which is defined as the scalar sum of the p_T of the selected jets. The distributions of p_T^{miss} and $p_T^{\text{miss}}/\sqrt{H_T}$ are shown in Fig. 4.8.

Furthermore, the two jets are required to be separated from the p_T^{miss} in the azimuthal plane by requiring $\cos \Delta\phi(p_T^{\text{miss}}, j_1) < 0.8$ for the leading jet and $\cos(\Delta\phi(p_T^{\text{miss}}, j_2)) < \cos(0.25)$ for the sub-leading jet. Vetoing events with small angular separation of p_T^{miss} and the subleading jet ($\cos(0.25) \approx 0.96$) protects from drastic jet mismeasurements in cases when the detector response for the leading generated jet is low enough that it is erroneously reconstructed as the subleading jet. In such cases, p_T^{miss} is typically aligned with the subleading jet to within half the jet clustering distance. The distributions of these angular distances are shown in Fig. 4.9. The event selection is summarized in Tab. 4.2. An overview of the background, signal and

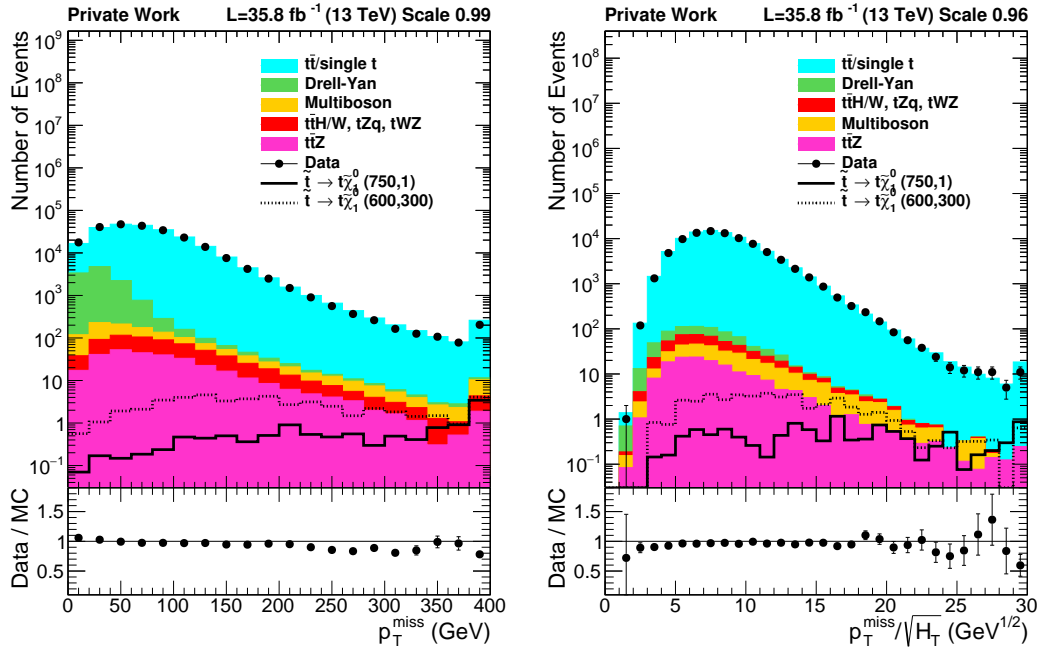


Figure 4.8: Distributions of p_T^{miss} after the $m_{\ell\ell}$ selections (left) and $p_T^{\text{miss}}/\sqrt{H_T}$ after the $p_T^{\text{miss}} > 80$ GeV selection (right).

data yields at different stages of the selection is given in Table 4.3.

4.3.3 Signal and control regions

In addition to the preselection discussed in the previous section a minimum requirement of $M_{T2}(\ell\ell)$ of 100 GeV is applied in order to suppress the majority of the $t\bar{t}$ background. The region of $M_{T2}(\ell\ell) < 100$ GeV is very pure in $t\bar{t}$ events and can therefore serve as control region for the process, and the measurement of its normalization.

While the $Z \rightarrow \ell\ell$ process is a considerably large contribution to backgrounds in same-flavor (SF) events, it is negligible in opposite-flavor (OF) events. Therefore, the background composition differs in these two channels and motivates separate signal and control regions. Signal regions are defined in terms of $M_{T2}(\ell\ell)$, $M_{T2}(\ell b\ell b)$ and p_T^{miss} in order to maximize sensitivity to different mass points of the top squark pair production models. At the same time, reasonable statistical uncertainties in simulated samples are required, hence extreme combinations of selection requirements are avoided. This way, the $M_{T2}(\ell\ell) > 100$ GeV region is sliced into bins of the other two variables starting with a relatively fine binning of 50 GeV and a large number of signal regions. Signal and background yields are estimated from simulation, and expected exclusion limits are calculated including all systematic uncertainties applicable to the fully simulation based estimation. Signal regions with a vanishing background estimation are excluded in this procedure as those would otherwise bias the result towards finer binning.

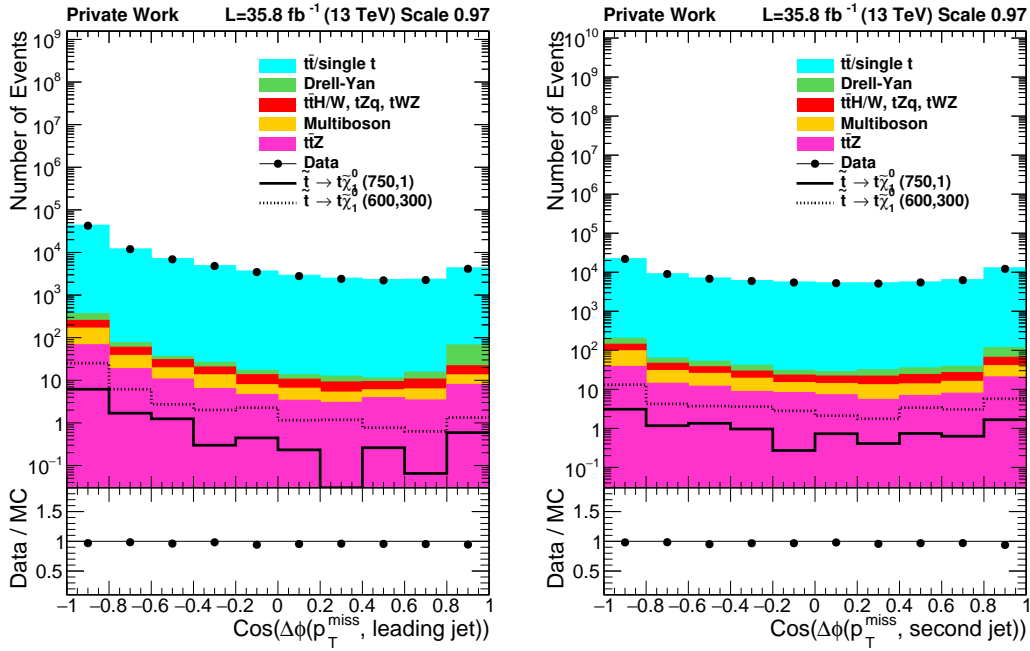


Figure 4.9: Distributions of $\cos \Delta\phi(p_T^{\text{miss}}, j)$ for the leading and second leading jet, after the p_T^{miss} and $p_T^{\text{miss}}/\sqrt{H_T}$ selections.

As a next step, signal regions are collapsed starting at the highest bins in each of the variables until no more empty regions are observed. The expected limit is calculated at each step, and the small loss in sensitivity is weighed up against the smaller number of signal regions. As a result, three bins of $M_{T2}(\ell b \ell b)$ separated at 100 and 200 GeV are found to be sufficient. Two bins of p_T^{miss} , divided at 200 GeV are introduced, while two $M_{T2}(\ell \ell)$ thresholds at 140 and 240 GeV are defined. Same-flavor events are not further split into e and μ categories as no additional gain in sensitivity was found. The regions above $M_{T2}(\ell \ell) > 240$ GeV are merged in order to still allow for a reliable background prediction. The resulting set of signal regions is shown in Table 4.4.

Two series of control regions are defined to constrain the normalizations of the DY and multiboson as well as the $t\bar{t}Z$ backgrounds. The DY and multiboson contributions are measured in 13 regions orthogonal to the signal regions by inverting the b-tagged jet and off-Z requirement in each region, using only events with a same-flavor lepton pair. Five control regions are used for constraining the $t\bar{t}Z$ background, requiring three leptons out of which one same flavor pair has to be reconstructed as Z boson candidate, requiring $|m_{\ell\ell} - m_Z| < 15$ GeV. The events are further categorized in terms of jet and b-tagged jet multiplicity. The control regions are further discussed in Subsections 4.4.2 and 4.4.3.

Table 4.2: Summary of the applied event selection.

Event selection
spurious p_T^{miss} filters
$N_\ell = 2$, opposite charge, 3 rd lepton veto
$p_T(\text{lead. } \ell) > 25 \text{ GeV}$
$N_j \geq 2$
$N_b \geq 1$
$m_{\ell\ell} > 20 \text{ GeV}$
$ m_{\ell\ell} - m_Z > 15 \text{ GeV}$
$p_T^{\text{miss}} > 80 \text{ GeV}$
$p_T^{\text{miss}}/\sqrt{H_T} > 5 \text{ GeV}^{1/2}$
$\cos \Delta\phi(p_T^{\text{miss}}, \text{leading jet}) < 0.8$
$\cos \Delta\phi(p_T^{\text{miss}}, \text{2nd leading jet}) < \cos(0.25)$

Table 4.3: Cutflow table showing the background and signal yields at the different stages of the selection.

	t \bar{t} Z	t \bar{t} H/W, tZq, tWZ	Multiboson	Drell-Yan	t \bar{t} /t	750/1	600/300
$N_\ell = 2$	1178.9	1849.4	99419.2	31424321.1	502437.8	36.3	140.6
opposite charge	1063.3	1419.5	96035.9	31350089.6	500203.8	36.2	140.1
loose lepton veto	934.8	1280.9	93499.9	31321503.1	492117.4	35.4	138.4
$m(\ell\ell) > 20 \text{ GeV}$	917.9	1262.9	91728.6	31252804.6	480995.8	34.9	136.4
$ m(\ell\ell) - m_Z > 15 \text{ GeV}$ (SF)	450.1	717.5	43973.0	2296561.4	426762.4	33.1	121.0
$N_j \geq 2$	420.4	654.6	6740.4	115131.3	296727.2	29.0	103.3
$N_b \geq 1$	319.2	477.4	565.1	10838.5	231978.0	21.4	85.3
$p_T^{\text{miss}} > 80 \text{ GeV}$	161.0	239.4	175.6	279.9	93229.9	20.2	75.6
$p_T^{\text{miss}}/\sqrt{H_T} > 5$	132.4	196.6	156.4	207.8	86516.9	19.8	72.9
$\phi(p_T^{\text{miss}}, \text{jets}) \text{ veto}$	116.5	174.2	143.6	144.3	77367.1	17.7	67.4
$M_{T2}(\ell\ell) > 140 \text{ GeV}$	3.8	1.7	1.7	0.8	3.6	8.8	11.5

4.4 Background estimation

In this section the estimation procedures for the different background components are summarized. The t \bar{t} , Drell-Yan, di- and multiboson, and t \bar{t} Z backgrounds are separately estimated for each signal region.

4.4.1 Top quark pair production

The estimation of the t \bar{t} background estimation is based on normalizing simulated templates in a $M_{T2}(\ell\ell) < 100 \text{ GeV}$ control region, similar to the previous analysis [110] using data at a center-of-mass energy of 8 TeV. Several checks are performed in order to verify the predictability of the simulation in the shoulder and tail region of the $M_{T2}(\ell\ell)$ distribution. Figure 4.4 exhibits the importance of a reliable background estimation in the tails where

Table 4.4: Definition of the signal regions.

$M_{T_2}(\ell b \ell b)$ (GeV)	p_T^{miss} (GeV)	$100 \leq M_{T_2}(\ell \ell) < 140$ GeV	$140 \leq M_{T_2}(\ell \ell) < 240$ GeV	$M_{T_2}(\ell \ell) \geq 240$ GeV
0–100	80–200	SR0	SR6	SR12
	≥ 200	SR1	SR7	
100–200	80–200	SR2	SR8	
	≥ 200	SR3	SR9	
≥ 200	80–200	SR4	SR10	
	≥ 200	SR5	SR11	

the potential signal becomes visible. Therefore, the origin of simulated $t\bar{t}$ events entering the $M_{T_2}(\ell \ell) > 140$ GeV region is checked one by one, using a large sample corresponding to an integrated luminosity of 1.2 ab^{-1} , resulting in a weight of 0.03 for each simulated event. Perfectly measured events from single top quark or $t\bar{t}$ production populate the low $M_{T_2}(\ell \ell)$ and $M_{T_2}(\ell b \ell b)$ regions. Moreover, $t\bar{t}$ events where only one of the W bosons from the top quark decays into a lepton neutrino pair, but with an additional lepton that is either a misidentified jet or originating from a heavy flavor decay, cannot enter the $M_{T_2}(\ell \ell)$ tail. In this case the p_T^{miss} originates from the neutrino of the W boson decay, therefore, the transverse mass of the prompt lepton and the p_T^{miss} is still bound by the W boson mass. The hypothesis $p_T(\nu_2) = 0$ is one of the possible solutions in the minimization, hence $M_{T_2}(\ell \ell)$ is subject to the same upper bound. In short, the kinematical endpoint of $M_{T_2}(\ell \ell)$ is also respected by semileptonic $t\bar{t}$ with fake or non-prompt leptons. Consequently, not a single simulated event of the semi-leptonic $t\bar{t}$ process is found above $M_{T_2}(\ell \ell) > 140$ GeV.

Events in the $M_{T_2}(\ell \ell)$ tail fall into three broad categories. First, drastic mismeasurements of p_T^{miss} can be enough to promote events with two prompt leptons to the tail. This can happen either by neutral particles like photons showering in a dead crystal of the ECAL, or by a high energetic neutrino in a jet. Roughly 60% of $t\bar{t}$ events in the tail come from this category. Second, one of the leptons of a dileptonic $t\bar{t}$ event can be outside the experimental acceptance, either because it doesn't pass reconstruction thresholds, ID requirements, or because it is outside the geometrical acceptance of the detector. If a fake or nonprompt lepton is picked up in the event the $M_{T_2}(\ell \ell)$ endpoint is not respected anymore. Finally, there are events with hadronically decaying tau leptons which have extra genuine p_T^{miss} .

In total, 87 simulated events exceed $M_{T_2}(\ell \ell) > 140$ GeV, out of which 32 events were found in the $\mu\mu$ channel, 17 in the ee channel and 38 in the $e\mu$ channel. The majority of the events contains mismeasured jets, 65 events in total. These events are distributed approximately independently of lepton flavor and 53 have highly energetic photons or pions showering in dead ECAL crystals. The generated particles were traced individually and their disappearance was correlated with known cracks in the detector. All dead ECAL cells were correctly implemented in the simulation. The remaining 12 events each had a neutrino produced inside a jet in excess of 40 GeV which is enough to promote the event to the tail. When trating the the

neutrino momentum as visible energy the value for $M_{T2}(\ell\ell)$ is again in the bulk of the $M_{T2}(\ell\ell)$ distribution, confirming that the neutrino is the origin of the promotion of the event to the $M_{T2}(\ell\ell)$ tail. In one extreme case, a 1.6 TeV b jet produced a 200 GeV neutrino. The other source events with high $M_{T2}(\ell\ell)$ are, as discussed, lost electrons or muons, or a hadronically decaying tau lepton from one of the W bosons combined with a nonprompt or fake lepton passing the lepton selections. In such events a lepton from a W and a fake lepton are used to compute the $M_{T2}(\ell\ell)$ and the resulting value does not respect to the W transverse mass endpoint anymore. There were 14 events involving a τ lepton of which 6 decayed leptonically. Control regions are used to constrain the different sources for tail events.

Check of p_T^{miss} tails in Drell-Yan events

The rate of events with significantly mismeasured jets is checked in data events without b-tagged jets and a same flavor lepton pair with an invariant mass close to the Z boson mass. This selection gives a very pure sample of Drell-Yan events which have no genuine p_T^{miss} . The distribution of the reconstructed p_T^{miss} is shown in Fig. 4.10 (right). The region with high $M_{T2}(\ell\ell)$ is dominated by the remaining $t\bar{t}$ events in this selection, which do have genuine p_T^{miss} . To overcome this issue one can again exploit the $M_{T2}(\ell\ell)$ observable. First, the simulated Drell-Yan sample is split into three subsamples with increasing fake p_T^{miss} which is defined as the magnitude of the vectorial difference of reconstructed and generated p_T^{miss} . Figure 4.10 (left) shows that for $M_{T2}(\ell\ell) > 100$ GeV the distribution is dominated by DY events with large fake p_T^{miss} , corresponding to large jet mismeasurements, while the $t\bar{t}$ events with genuine p_T^{miss} are contained in the low $M_{T2}(\ell\ell)$ region. No significant excess of data over the prediction from simulation is observed in the high $M_{T2}(\ell\ell)$ region dominated by events with mismeasurements.

Shape analysis of fake lepton backgrounds

In order to check whether the $M_{T2}(\ell\ell)$ shape is correctly simulated the lepton misidentification is mimicked by selecting events with three leptons where the third lepton is non-isolated and fulfills $p_T > 7$ GeV or $p_T > 5$ GeV for electrons or muons, respectively. The loss of one lepton is emulated by recomputing $M_{T2}(\ell\ell)$ using either the combination of the leading or sub-leading lepton with the non-isolated lepton. The change of flavor composition of the recomputed event has to be carefully taken into account. In contrast to the lepton momenta the p_T^{miss} remains unchanged because of the high detection efficiency and the hermetic nature of the CMS detector. The described procedure is applied to data and simulation, and the resulting $M_{T2}(\ell\ell)$ distributions are shown in Fig. 4.11. Excellent agreement between data and simulation is observed.

It remains to be shown that the swapping procedure correctly mimics the lost lepton contribution. This is done in Fig. 4.12 where the two-lepton simulation with an inverted isolation requirement $I_{\text{rel}} > 0.12$ on the trailing lepton (red line) is overlaid with the three-lepton prediction from the swapping procedure (blue area). The distributions are normalized for

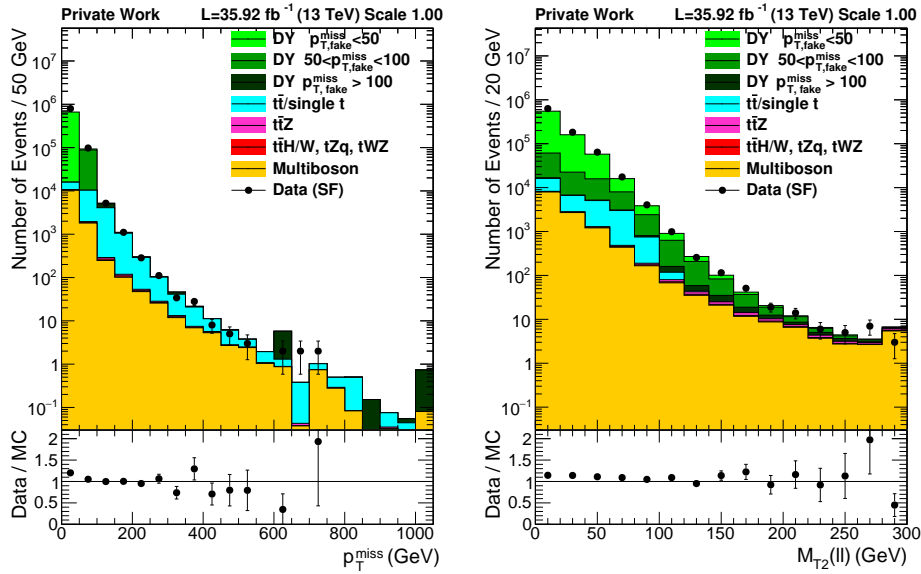


Figure 4.10: p_T^{miss} and $M_{T2}(\ell\ell)$ distribution of the same flavour channel in the on-Z selection and $N_b = 0$.

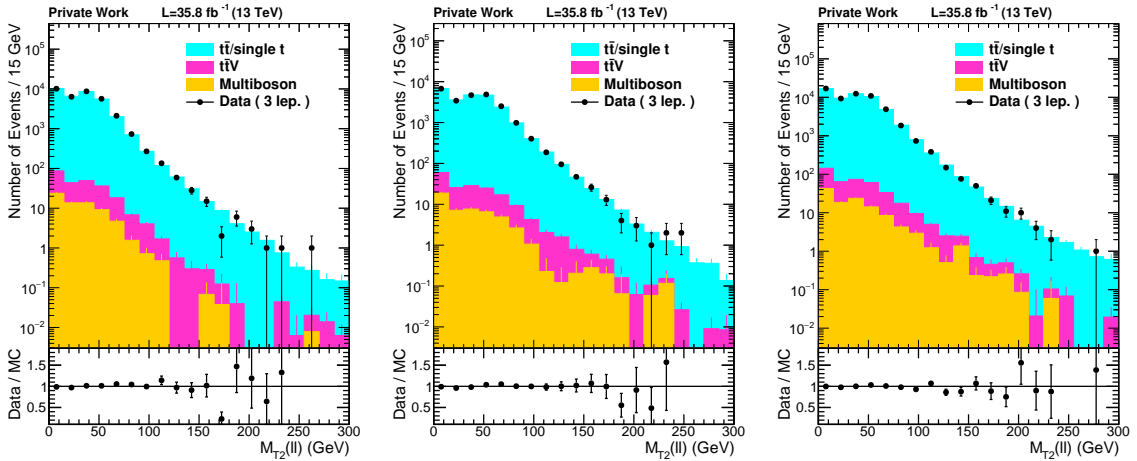


Figure 4.11: $M_{T2}(\ell\ell)$ distributions a three lepton control region for events where the final lepton pair is composed of two muons (left) or two electrons (center) and for the $e\mu$ channel (right). Changes of flavour and p_T due to the lepton swapping are taken into account. MC yields are normalized to data using the yields at $M_{T2}(\ell\ell) < 100$ GeV.

$M_{T2}(\ell\ell) > 100$ GeV and the almost perfect agreement confirms that the swapping procedure indeed mimics the loss of a lepton very well for $M_{T2}(\ell\ell) > 80$ GeV. It should be noted that the swapping procedure is not strongly dependent on the details of the selection of the extra leptons. As long as the loose selection guarantees that extra leptons are dominated by nonprompt decays in b jets, the reconstructed value of $M_{T2}(\ell\ell)$ is governed by the relative angular position of the extra lepton and less by its transverse momentum which is typically too small to have a very large effect. No signs of a discrepancy in the $M_{T2}(\ell\ell)$ shape for events with a lost lepton are observed.

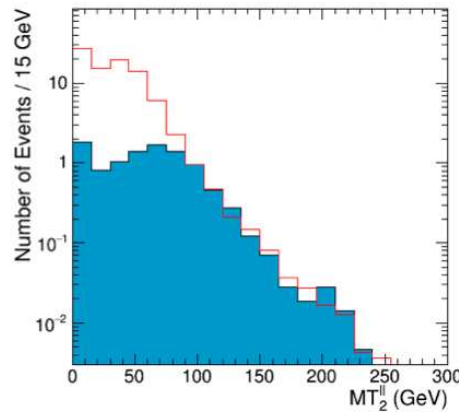


Figure 4.12: Comparison of the three lepton simulation (blue area) and the two lepton simulation with inverted isolation requirements on one lepton (red line), normalized at $M_{T2}(\ell\ell) > 100$ GeV.

Check of the lepton fake rate

The description of the fake rate in simulation is checked in a similar selection. Again, one additional lepton with relaxed isolation requirements is required in order to select an event. In addition, $N_j \geq 2$, $N_b \geq 1$ and $m_{\ell\ell} > 30$ GeV are required to select a similar phase space. The distribution of I_{rel} is shown in Fig. 4.13, and the fake rate can be derived from the ratio of the first bin, which contains the events with $I_{\text{rel}} < 0.12$, to the rest of the distribution. From the reasonably good agreement between data and simulation for the shape of the distributions it is concluded that the fake rate in data is well described by simulation.

Validating the $t\bar{t}$ shape in control regions at high and low p_T^{miss}

Finally, the simulated shape of the $M_{T2}(\ell\ell)$ distribution in $t\bar{t}$ is checked in several control regions. In order to remove contamination from DY events lepton pairs with different flavor are required. Figure 4.14 shows the $M_{T2}(\ell\ell)$ distribution compared to simulation for one of the various control regions, selecting events with $N_j \geq 2$, $N_b \geq 1$ and $p_T^{\text{miss}} < 80$ GeV. Other control regions with inverted N_j or N_b requirement, but $p_T^{\text{miss}} > 80$ GeV, are used as well. The resulting plots are shown in Appendix A.2. The signal region is omitted by skipping the case

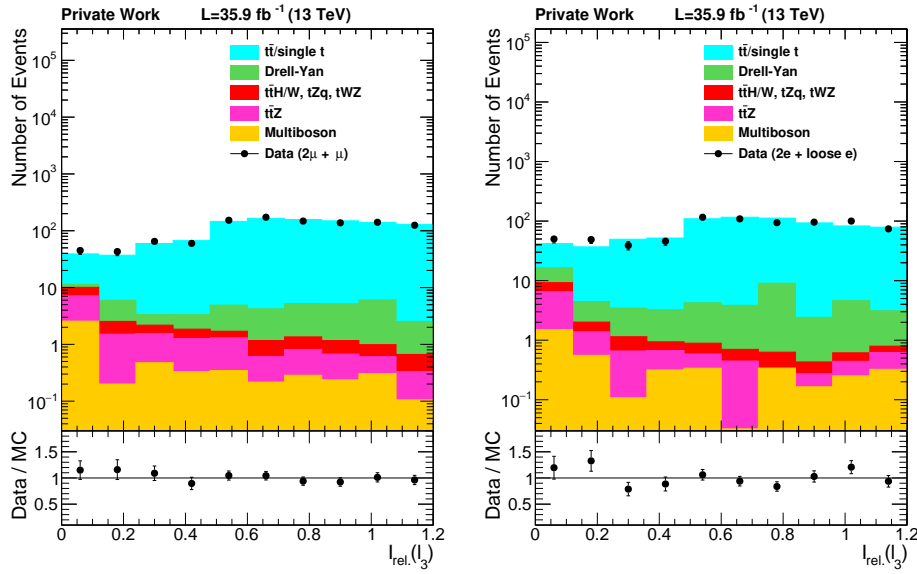


Figure 4.13: I_{rel} distributions of the third non-isolated lepton in the $\mu\mu\mu$ (left) and eee (right) channels. The first bin corresponds to events passing the $I_{\text{rel}} < 0.12$ requirement. In order to obtain a reasonable amount of statistics of events with three electrons, the identification requirement on the electron is loosened to the loose electron identification working point.

$$N_j \geq 2 \text{ and } N_b \geq 1.$$

Good agreement between $M_{T2}(\ell\ell)$ shape from data and simulation is observed over a change of yields per bin of several orders of magnitude. The uncertainty due to experimental effects is shown with a hatched band.

Summary of $t\bar{t}$ background estimation and correlation pattern

Based on these checks in the control regions the $t\bar{t}$ background contribution is predicted using simulated samples. Data events in $M_{T2}(\ell\ell) < 100$ GeV are used to constrain the absolute normalization of the $t\bar{t}$ events. The normalization measurement is done in each of the channels and yields the following scale factors: 1.003 ± 0.006 in the $\mu\mu$ channel, 0.939 ± 0.009 in the ee channel and 0.956 ± 0.004 for $e\mu$ events. In this way, the experimental uncertainties affecting the overall normalization are largely reduced.

If the uncertainty in the $t\bar{t}$ process is treated as fully correlated between all signal regions, the corresponding nuisance parameter can get constrained in the signal extraction fit by the high statistics regions with $100 \leq M_{T2}(\ell\ell) < 140$ GeV. As a test, uncertainties of 50% for $M_{T2}(\ell\ell) < 140$ and 100% for $M_{T2}(\ell\ell) > 140$ that are fully correlated are injected. The resulting constraint is visible in Fig. 4.15(top). Several drastically different correlation scenarios were tested, e.g. decorrelating SR0–5 and SR6–12, individually decorrelating SR0,1,2,3,4,5 and SR6–12, and entirely removing SR0 and SR2 from the fit. No significant impact on the final result in terms of the expected T2tt and DM exclusion limit was found. In each case,

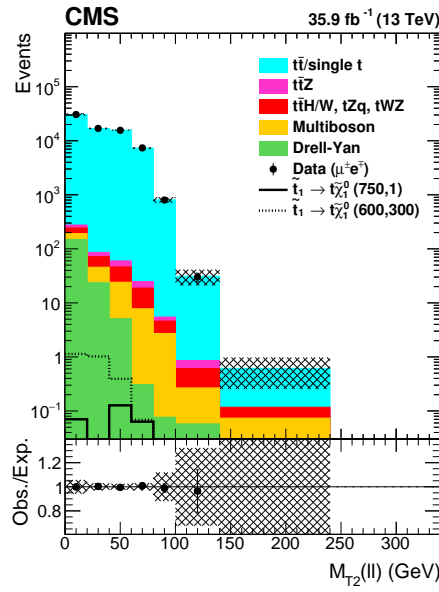


Figure 4.14: $M_{T2}(\ell\ell)$ distribution in the opposite flavor control region enriched in $t\bar{t}$ events, defined by $N_j \geq 2$, $N_b \geq 1$ and $p_T^{\text{miss}} < 80$ GeV. The background estimations are obtained from simulation and are normalized to data in the $M_{T2}(\ell\ell) < 100$ GeV region. The hatched band shows the uncertainties from experimental effects [12].

the constraint was largely removed while the expected limit stayed unchanged; a consequence of the fact that $t\bar{t}$ is a comparably small contribution in the most sensitive regions, and that the sensitivity is driven by acceptance, not precision control of the backgrounds. More details on these tests are in Appendix A.3.

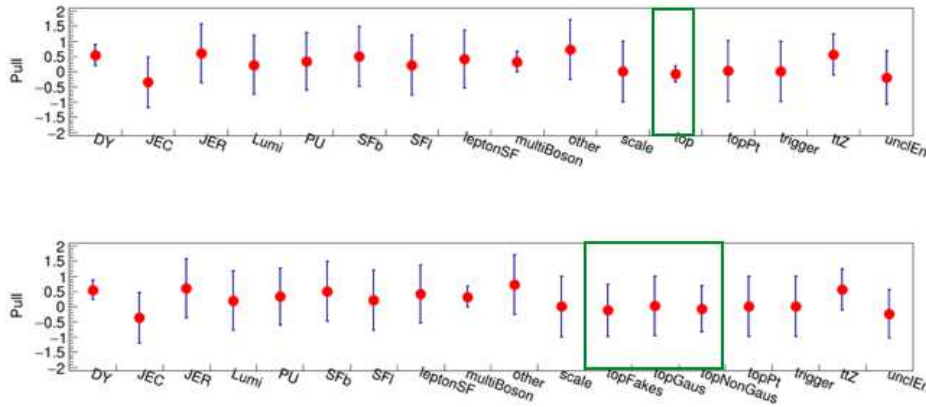


Figure 4.15: Pull distribution of the systematic uncertainties. A fully correlated uncertainty described in the text on the top background is constrained by the fit (top), which is not used in the final result. Disentangling the three components and assigning a realistic correlation pattern does no longer constrain the nuisances (bottom).

Despite the insensitivity to the correlation pattern, a well motivated correlation pattern was

constructed. The $t\bar{t}$ background is split into three categories and each is assigned a systematic uncertainty.

- Gaussian 15%: Events that are promoted to the $M_{T2}(\ell\ell)$ tail due to Gaussian jet mismeasurements. The category is defined by fake $p_T^{\text{miss}} < 50 \text{ GeV}$, corresponding to approximately $2\sigma(p_T^{\text{miss}})$.
- Non-Gaussian 30%: Events containing severely mismeasured jets, defined by fake- $p_T^{\text{miss}} > 50 \text{ GeV}$. The uncertainty of 30% is assigned based on the agreement in the tail of Fig. 4.10.
- Fake 50%: Events with misidentified leptons. The uncertainty is based on the agreement in the first bins in Fig. 4.13.

The fractions of events in these categories are measured in simulation and shown in Tab. 4.5 and Tab. 4.6. Despite the very high effective luminosity of 1.2 ab^{-1} , some of the effects are predicted to be extremely rare and hence the numbers in bins of $100 \leq M_{T2}(\ell\ell) < 140 \text{ GeV}$ and $M_{T2}(\ell\ell) \geq 140 \text{ GeV}$ are averaged. The result of the procedure is shown in Tab. 4.7. No correlations are assumed between the three components. Injecting the uncertainties with this correlation pattern into the fit (described in Sec. 4.7) it is found that it does not constrain the respective nuisances. The result is shown in Fig. 4.15 (bottom). The expected limits for the T2tt and DM models are unchanged with this more elaborate model of correlations.

Table 4.5: Total counts and fractions of $e\mu$ events of top background components in simulation.

signal region	gaussian	%	non-gaussian	%	fakes	%
0	83.66 ± 1.94	58	60.08 ± 1.62	42	0.34 ± 0.11	0
1	1.78 ± 0.25	47	2.01 ± 0.26	53	0.03 ± 0.03	1
2	37.64 ± 1.24	53	32.12 ± 1.14	46	0.62 ± 0.15	1
3	1.56 ± 0.24	48	1.71 ± 0.24	52	0.00 ± 0.00	0
4	0.11 ± 0.07	17	0.54 ± 0.14	83	0.00 ± 0.00	0
5	0.86 ± 0.24	66	0.40 ± 0.12	31	0.04 ± 0.04	3
6	0.15 ± 0.07	48	0.13 ± 0.07	41	0.03 ± 0.03	11
7	0.04 ± 0.04	58	0.03 ± 0.03	42	0.00 ± 0.00	0
8	0.15 ± 0.07	33	0.22 ± 0.09	50	0.07 ± 0.05	17
9	0.00 ± 0.00	0	0.08 ± 0.06	26	0.24 ± 0.21	74
10	0.00 ± 0.00	0	0.08 ± 0.06	68	0.04 ± 0.04	32
11	0.00 ± 0.00	0	0.15 ± 0.08	100	0.00 ± 0.00	0
12	0.04 ± 0.04	18	0.16 ± 0.16	68	0.03 ± 0.03	14

Table 4.6: Total counts and fractions of same flavor events of top background components in simulation.

signal region	gaussian	%	non-gaussian	%	fakes	%
0	75.42 ± 1.85	59	52.93 ± 1.56	41	0.39 ± 0.12	0
1	2.15 ± 0.34	56	1.70 ± 0.24	44	0.00 ± 0.00	0
2	32.51 ± 1.26	56	24.88 ± 1.02	43	0.41 ± 0.12	1
3	2.05 ± 0.32	52	1.87 ± 0.26	47	0.03 ± 0.03	1
4	0.16 ± 0.07	37	0.28 ± 0.11	63	0.00 ± 0.00	0
5	0.98 ± 0.26	73	0.37 ± 0.12	27	0.00 ± 0.00	0
6	0.24 ± 0.20	59	0.09 ± 0.06	23	0.07 ± 0.05	18
7	0.00 ± 0.00	0	0.07 ± 0.05	100	0.00 ± 0.00	0
8	0.21 ± 0.19	69	0.05 ± 0.04	18	0.04 ± 0.04	13
9	0.20 ± 0.20	37	0.31 ± 0.11	58	0.02 ± 0.02	5
10	0.00 ± 0.00	0	0.11 ± 0.07	100	0.00 ± 0.00	0
11	0.00 ± 0.00	0	0.10 ± 0.06	72	0.04 ± 0.04	28
12	0.00 ± 0.00	0	0.00 ± 0.00	0	0.04 ± 0.04	100

Table 4.7: Systematic uncertainties on the top-background components.

signal regions	$M_{T2}(\ell\ell)$ (GeV)	Gaussian (%)	non-Gaussian (%)	fake lepton (%)
0 – 5	100 – 140	55	44	1
6 – 12	≥ 140	25	50	25

4.4.2 Z boson production in association with top quark pairs

One of the main backgrounds in the $M_{T2}(\ell\ell)$ tail is $t\bar{t}Z$ with a decay of the Z boson $Z \rightarrow \nu\nu$. The neutrinos provide additional missing transverse momentum to the event which promotes $t\bar{t}Z$ events from to bulk into the tail of the $M_{T2}(\ell\ell)$ distribution. Two complementary methods are used to verify the cross section normalization and $M_{T2}(\ell\ell)$ shape description, respectively.

Normalization in the $t\bar{t}Z \rightarrow 3\ell$ region

The normalization of the $t\bar{t}Z$ background can be estimated using data control samples by selecting events with three leptons, in which the Z boson decays into two leptons, one top decays leptonically and the other hadronically

$$t\bar{t}Z \rightarrow (b\ell\nu)(bjj)(\ell\ell) \quad .$$

Leptons are required to exceed p_T thresholds of 40, 20 and 10 GeV. Jets and b-tagged jets are required to have a p_T of at least 30 GeV, similar to jets used in the main part of the analysis. Two leptons with same flavour are required to have opposite charge and fall within a Z boson

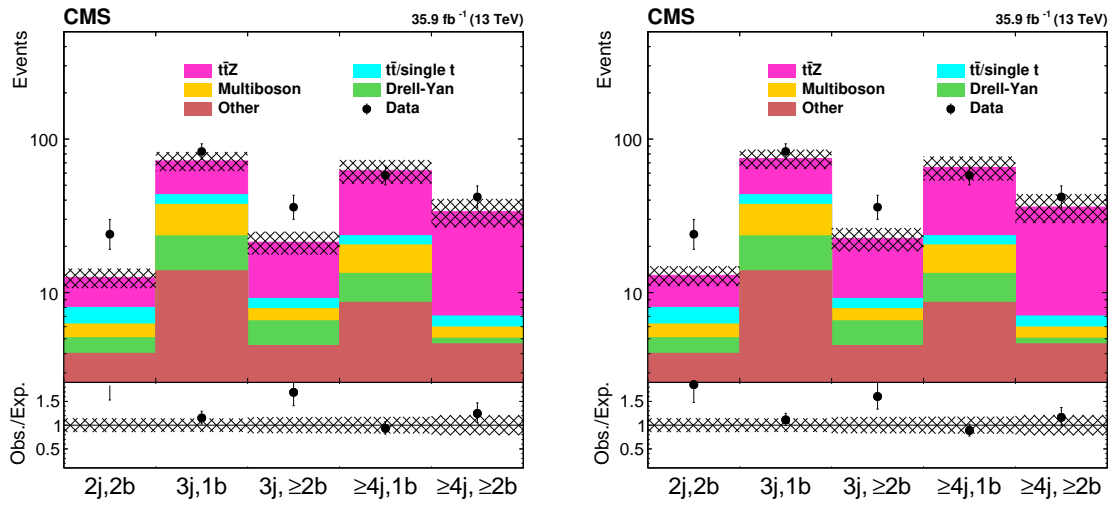


Figure 4.16: Expected and observed yields in the five $t\bar{t}Z$ control regions, which are defined by different requirements on the number of reconstructed jets and b jets, before (left) and after the fit (right). The hatched band contains all systematic uncertainties [12].

Table 4.8: Photon selection criteria

	photons
p_T	$> 30 \text{ GeV}$
$ \eta $	< 2.5
identification	cut based tight ID

mass window of 10 GeV in order to construct the Z boson candidate. Simulated distributions in the 4 different combinations of the 3 lepton selection ($\mu\mu\mu$, eee , $\mu\mu e$, μee) are fitted to data in different control regions, requiring different jet and b-tagged jet multiplicities. This method yields a scale factor for $t\bar{t}Z$ events of $SF_{t\bar{t}Z} = 1.09 \pm 0.15$. Figure 4.16 shows the pre-fit and post-fit $t\bar{t}Z$ yields in the five control regions with jet and b-tag multiplicities of 2j/2b, 3j/1b, 3j/2b, 4j/1b and 4j/2b.

Shape control region using $t\bar{t}\gamma$ events

In order to verify the quality of the description of the p_T^{miss} and $M_{T2}(\ell\ell)$ tails in simulation for the $t\bar{t}Z$ background, $t\bar{t}\gamma$ events are selected in data. The photon p_T is then treated as additional missing transverse momentum such that it acts as a proxy for $t\bar{t}Z$. Photons are selected according to Tab. 4.8. Even though the kinematics of $t\bar{t}\gamma$ events differ from $t\bar{t}Z$ events due to the fact that the photon is massless, these kinematic differences can be mitigated by a reweighting of the boson p_T . Figure 4.17 shows that the p_T^{miss} , $M_{T2}(\ell\ell)$ and $M_{T2}(\ell b\ell b)$ variables at generator level between $t\bar{t}\gamma$ and $t\bar{t}Z$ are very similar after a bin-by-bin reweighting of the photon p_T to the Z boson p_T ,

In order to select a pure $t\bar{t}\gamma$ sample which is closely related to the control and signal regions of our main analysis, similar selections are used but with an additional photon with $p_T >$

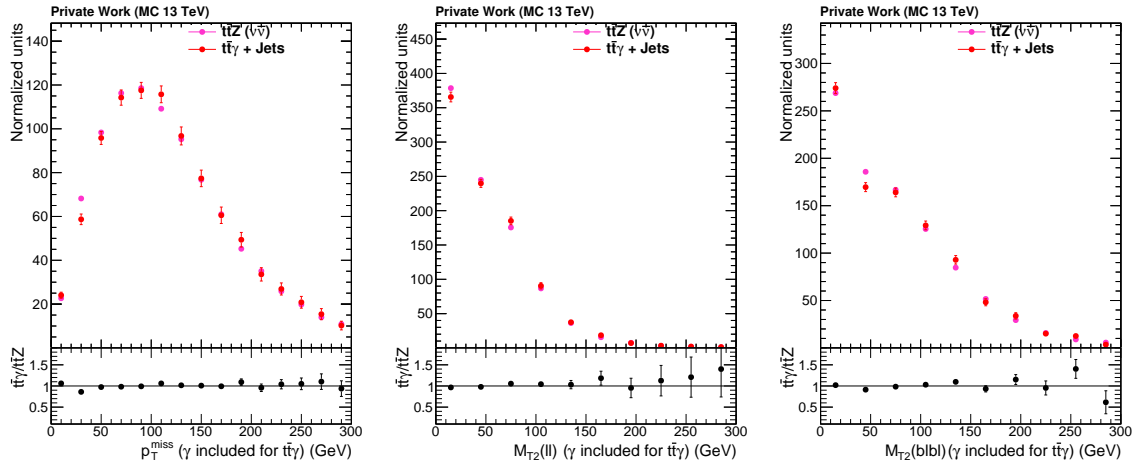


Figure 4.17: Generator-level comparison of $t\bar{t}\gamma$ (with the photon treated as additional p_T^{miss}) with $t\bar{t}Z$ for the p_T^{miss} , $M_{T2}(\ell\ell)$ and $M_{T2}(\ell\ell b)$ variables

30 GeV falling within $|\eta| < 2.5$. The p_T^{miss} requirements are now replaced by $p_T^{\text{miss}}(\gamma)$ and $p_T^{\text{miss}}(\gamma)/\sqrt{H_T}$ which are the photon estimated variants of p_T^{miss} and $p_T^{\text{miss}}/\sqrt{H_T}$. In order to reduce contributions of $Z\gamma$ events, the Z boson mass window cut is also applied on the invariant mass $m(\ell\ell\gamma)$ of the dilepton plus gamma system, as illustrated in Figure 4.18. Furthermore, photons are required to have $\Delta R(\gamma, \ell) > 0.3$ and $\Delta R(\gamma, j) > 0.3$, of which the latter is used to reject photons which are reconstructed as jets. Figure 4.19 shows the $p_T^{\text{miss}}(\gamma)$ before requiring the $p_T^{\text{miss}}(\gamma) > 80$ GeV requirement and $p_T^{\text{miss}}(\gamma)/\sqrt{H_T}$ before requiring $p_T^{\text{miss}}(\gamma)/\sqrt{H_T} > 5$. The distributions of the photon estimated $M_{T2}(\ell\ell)$ and $M_{T2}(\ell\ell b)$ variables before applying the $p_T^{\text{miss}}(\gamma)$ and $p_T^{\text{miss}}(\gamma)/\sqrt{H_T}$ requirements are shown in Figure 4.20. Figure 4.21 shows these variables after $p_T^{\text{miss}}(\gamma)$, $p_T^{\text{miss}}(\gamma)/\sqrt{H_T}$ and $\Delta\phi(p_T^{\text{miss}}, j)$ cuts. Based on the level of agreement of the $M_{T2}(\ell\ell)$ shape of $t\bar{t}Z$, a 20% uncertainty is assigned.

4.4.3 Estimation of Drell-Yan and multiboson backgrounds

The background from DY events is strongly reduced by the event selection which applies several cuts on p_T^{miss} -related variables. In this section, these cuts and the properties of the DY background are discussed in more detail using control regions defined by a 0 b-tagged jet and on-Z requirement defined by $|m_{\ell\ell} - m_Z| < 15$ GeV. These control regions are dominated by DY as well as di- and multiboson (commonly called multiboson in what follows) events if one requires $M_{T2}(\ell\ell) > 100$ GeV to suppress $t\bar{t}$ events. Figure 4.22 shows the purity of DY and multiboson events in such a control region. It is also shown that $M_{T2}(\ell\ell b)$ and p_T^{miss} nicely separate DY and multiboson contributions.

A fit of the simulated background to data is performed in 13 control regions orthogonal to the signal regions by inverting the b jet and off-Z requirement in each signal region. These fits

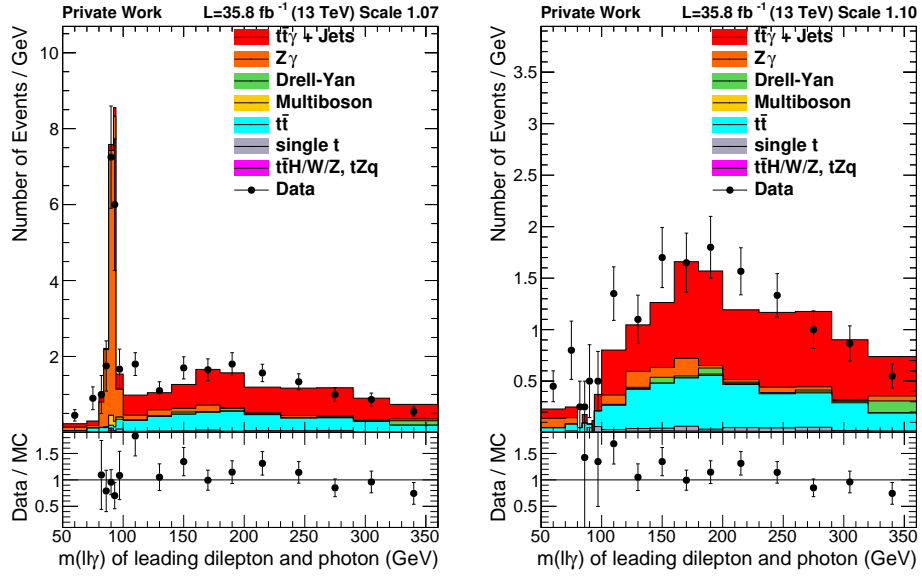


Figure 4.18: Distributions of $m(\ell\ell\gamma)$ for all lepton flavor channels combined, before (left) and after requiring $|m(\ell\ell\gamma)m_Z| > 10$ GeV for events with two same flavor leptons. The requirement removes the majority of the $Z\gamma$ background. Given the sharp Z peak in combination with a low-statistics tail, a dynamic binning is used in these figures, where each bin shows the average number of events per GeV for its $m(\ell\ell\gamma)$ range.

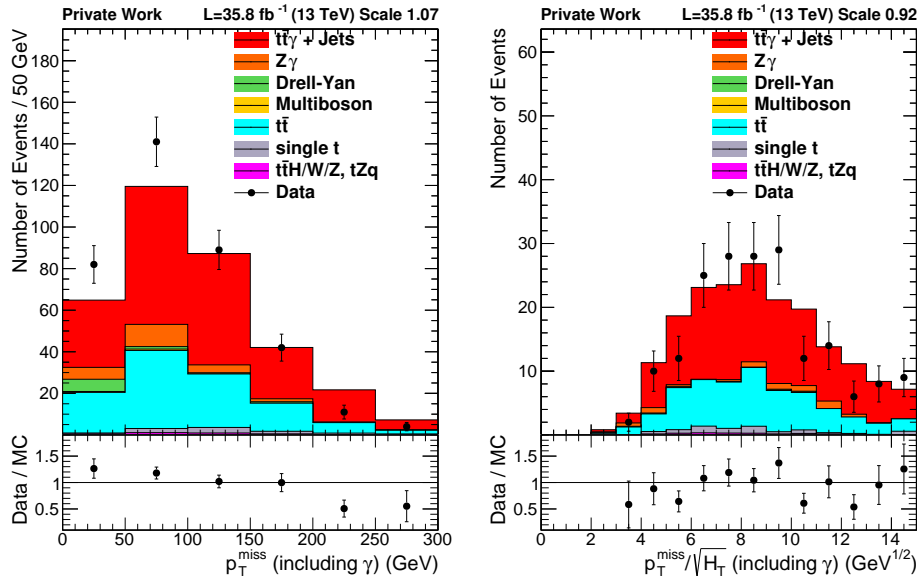


Figure 4.19: Distribution of $p_T^{\text{miss}}(\gamma)$ and $p_T^{\text{miss}}(\gamma)/\sqrt{H_T}$ with photon p_T included in the p_T^{miss} calculation, before cutting on them.

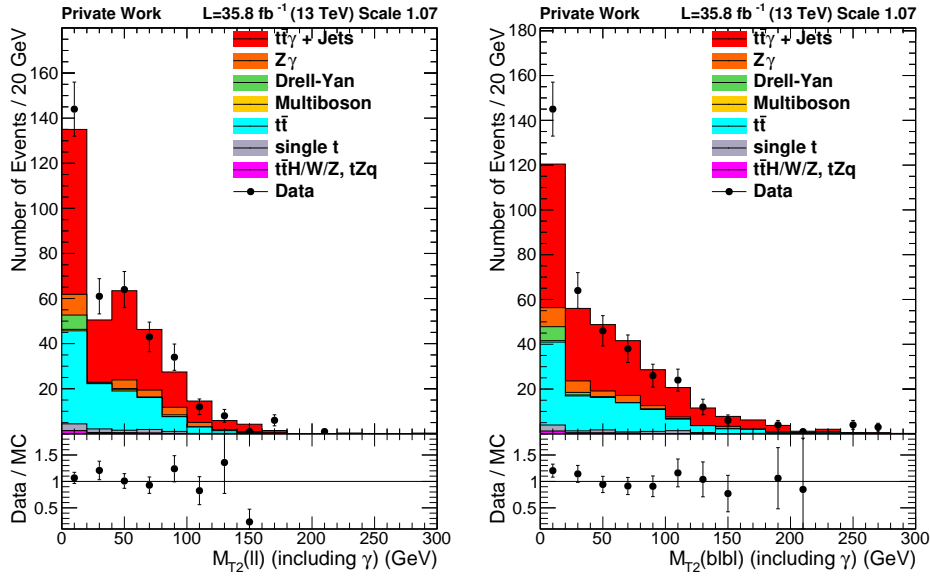


Figure 4.20: Distribution of $M_{T2}(\ell\ell)$ and $M_{T2}(\ell b\ell b)$ using the photon-estimated $p_T^{\text{miss}}(\gamma)$.

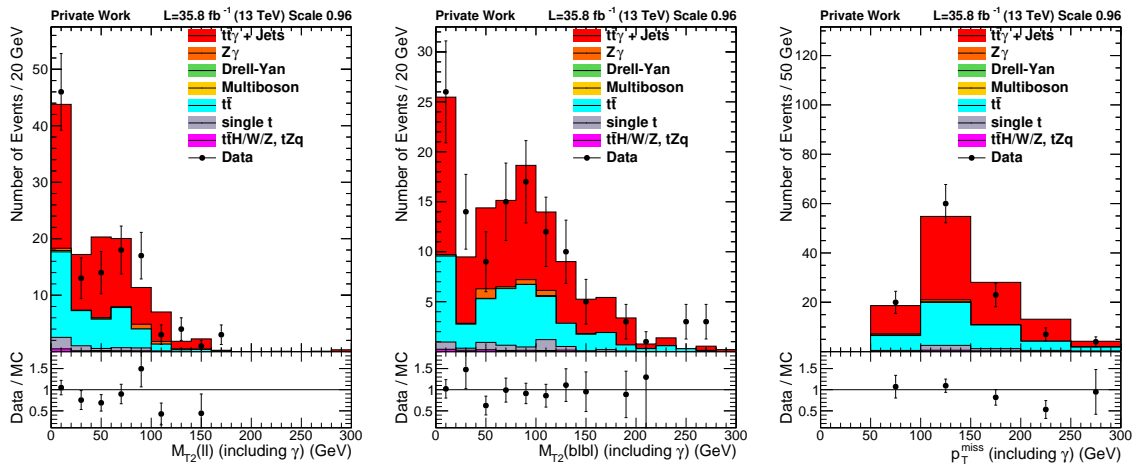


Figure 4.21: Distributions of $M_{T2}(\ell\ell)$, $M_{T2}(\ell b\ell b)$ and $p_T^{\text{miss}}(\gamma)$ using the photon-estimated $p_T^{\text{miss}}(\gamma)$, after applying selections on $p_T^{\text{miss}}(\gamma)$.

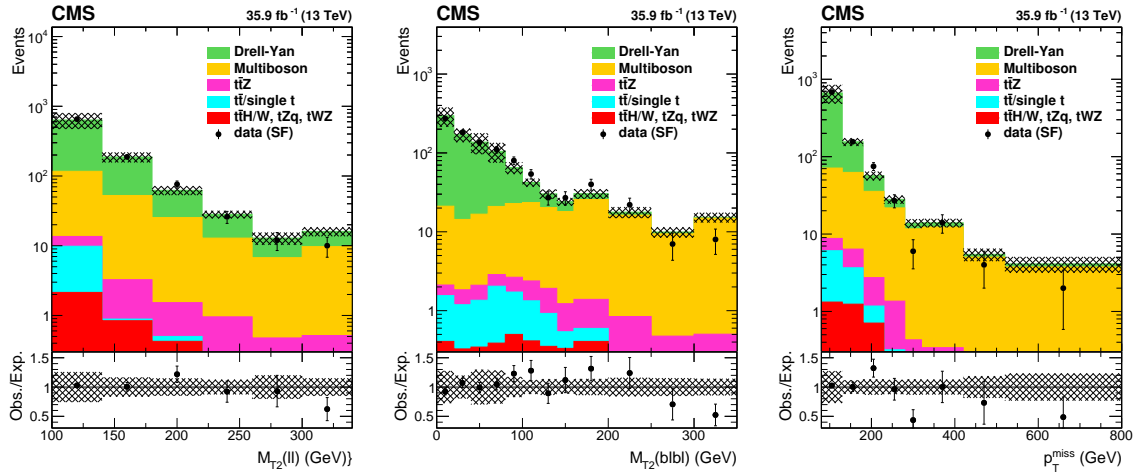


Figure 4.22: Distributions of $M_{T2}(\ell\ell)$ (left), $M_{T2}(\ell b\ell b)$ (center) and p_T^{miss} (right) for SF events falling within the Z boson mass window ($|m_{\ell\ell} - m_Z| < 15$ GeV), with at least two jets and $N_b = 0$, $p_T^{\text{miss}} > 80$ GeV, and $M_{T2}(\ell\ell) > 100$ GeV. The hatched band shows the uncertainties from experimental effects [12].

yield the normalization of the processes as observed in data, and effectively provide two scale factors for DY and multiboson events. Statistical uncertainties from the limited size of the simulated samples are treated as nuisances in each bin. By employing a maximum likelihood fit similar to the signal extraction all correlations of systematic uncertainties are optimally accounted for. Figure 4.23 shows the expected and observed yields in the control regions after the fit. The final scale factors yield

$$\begin{aligned} \text{SF}_{\text{MB}} &= 1.19 \pm 0.17 \\ \text{SF}_{\text{DY}} &= 1.31 \pm 0.19 \quad . \end{aligned} \quad (4.5)$$

Pulls of the fit are shown in Fig. 4.24. They are as expected; the parameters labeled *DY* and *multiboson* associated with the respective simulated yields get constrained and pulled, reflecting the rescaling of the respective process. The other nuisances stay mostly in place and only very few nuisances related to statistical uncertainties in the simulation get pulled by maximally 1 sigma.

In order to justify that the scale factor is applied inclusively to the sample it is checked that the N_b shape is consistent with a flat scaling, shown in Fig. 4.25 (left). In Fig. 4.25 (right) the N_b multiplicity is shown after removing $M_{T2}(\ell\ell)$, p_T^{miss} and $p_T^{\text{miss}}/\sqrt{H_T}$ requirements. This demonstrates the quality of N_b modeling in simulated DY events. The robustness of the scale factor is quantified by considering Fig. 4.26 which shows a large fraction of DY events without generated bottom quarks entering the $N_b \geq 1$ region. The uncertainties on events with only mistagged jets are covered by the experimental uncertainties in the measured tagging and mistagging efficiencies. In order to assess the uncertainties on the generated bottom quark

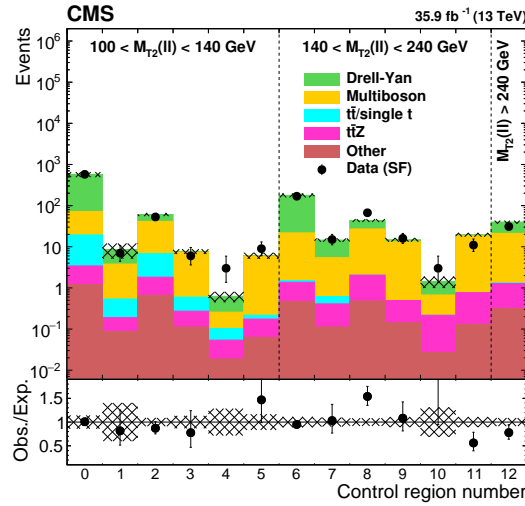


Figure 4.23: Event yields in the 13 DY and multiboson control regions for events with SF leptons falling within the Z boson mass window ($|m_{\ell\ell} - m_Z| < 15 \text{ GeV}$), with at least two jets and $N_b = 0$, $p_T^{\text{miss}} > 80 \text{ GeV}$, and $M_{T2}(\ell\ell) > 100 \text{ GeV}$, after renormalizing with the scale factors obtained from the fit. The hatched band shows the uncertainties from the fit including the uncertainties from experimental effects [12].

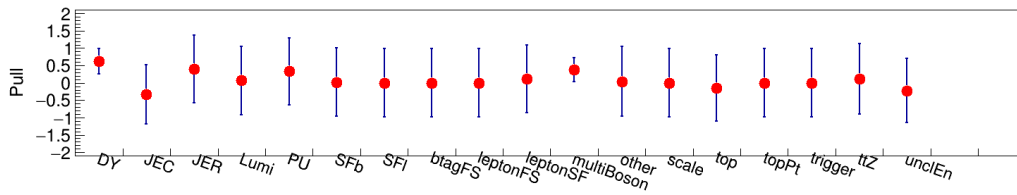


Figure 4.24: Pulls for the systematic uncertainties in the fit.

multiplicity the variations of the ratios as a function of the NNPDF replicas are calculated, resulting in a 2% uncertainty. In a measurement using 7 TeV data [135] it was found that the rate of gluon splitting is underestimated by simulation by up to 50%. In order to account for this potential mismodeling, the events with generated b quarks are scaled up and down by 50%, translating to an uncertainty of 25% on SF_{DY} .

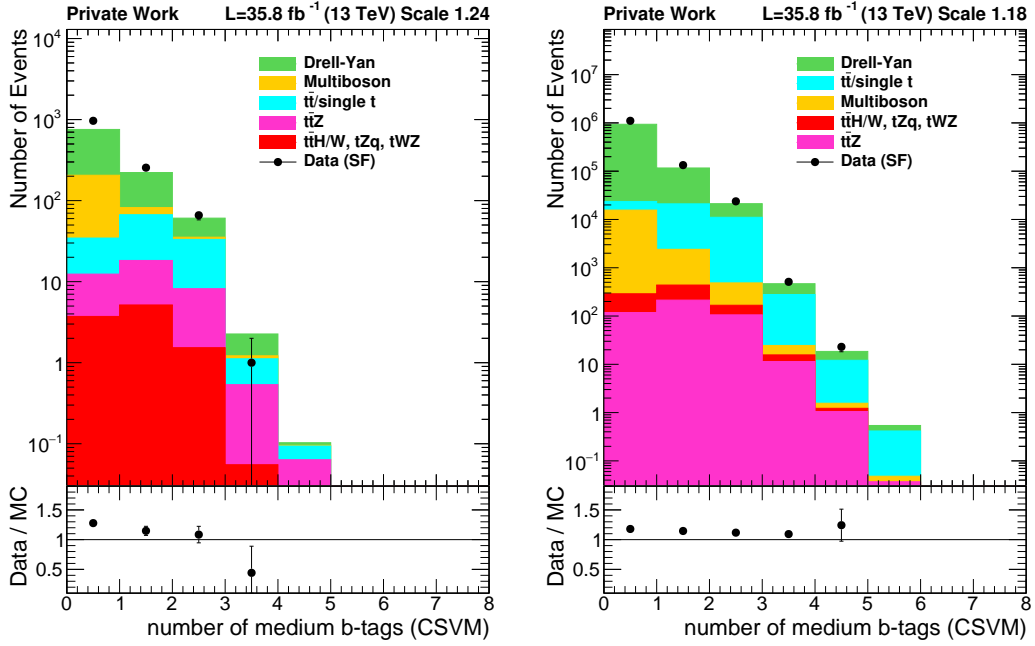


Figure 4.25: Distributions of N_b in a pure DY sample, requiring $M_{T2}(\ell\ell) > 100$ GeV (left), and inclusively with removed $M_{T2}(\ell\ell)$, p_T^{miss} and $p_T^{\text{miss}}/\sqrt{H_T}$ requirements (right).

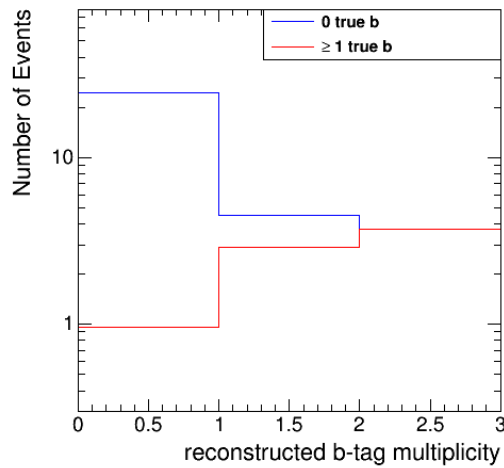


Figure 4.26: Distributions of N_b in simulated DY events in events with and without generated b-quarks.

4.4.4 Rare backgrounds

Backgrounds from rare processes only marginally contribute in the signal regions. These processes involve single top quark and $t\bar{t}$ production in association with at least one W or Higgs boson, as well as four top quark production. The contribution in the signal regions is estimated using simulated samples which are normalized to cross sections calculated with highest available order in perturbative QCD. An uncertainty in the normalization of 50% is assigned.

4.5 Systematic uncertainties

Systematic uncertainties related to the background estimation techniques were already discussed in Sec. 4.4. Additionally, experimental and theoretical uncertainties are assigned for signal and background processes which are discussed in the following.

The efficiencies of the di- and semilepton triggers are measured in a sample of events selected with p_T^{miss} based triggers, and range from 95% to 99%. The uncertainty on the measured efficiency is estimated to be about 1%, and is extracted from a comparison to an efficiency measurement in a event sample that is defined by jet p_T and H_T based triggers. Efficiencies for the reconstruction and identification of leptons are measured in bins of lepton p_T and η in $Z \rightarrow \ell\ell$ samples of simulated events and data and are usually between 70% and 80%. Scale factors are used to correct for the difference between the efficiencies obtained in data and simulation, and uncertainties on these scale factors are less than 3% per lepton in the majority of the search and control regions.

The jet energy scale (JES) is varied up and down within its uncertainties [90, 136] as a function of jet p_T and η , and the changes are propagated to all observables, including p_T^{miss} . The p_T^{miss} observable is moreover subject to uncertainties arising from soft particles that are not clustered into jets, commonly called unclustered energy. The variation of the unclustered energy results in an uncertainty around 3.5%, only reaching values of 25% in regions with a low $M_{T2}(\ell\ell)$ requirement. The simulated efficiencies for the identification of bottom quark jets and for the misidentification of charm quarks, as well as light quark and gluon jets need to be corrected for with scale factors and their respective uncertainties [134] result in an uncertainty of 1–6% in the predicted yields.

Events in simulated samples are reweighted according to the expected number of interactions at each bunch crossing in data, using an inelastic pp cross section of 69.2 mb [137]. Uncertainties are estimated by varying the inelastic cross section up and down by 5%, resulting in uncertainties of 1–6% in the expected yields. The uncertainty in the integrated luminosity is 2.5% [138]. Each experimental uncertainty is considered as correlated between the signal and control regions as well as the simulated processes.

Table 4.9: Relative systematic uncertainties in the background yields in the signal regions. Where given, ranges represent the minimal and maximal changes in yield across all signal regions.

Source of systematic uncertainty	Change in signal region yields (%)
Trigger efficiency	1
Lepton scale factors	1–5
Jet energy scale	1–12
Modeling of unclustered energy	1–25
b tagging	1–6
Top quark background normalization	3–20
$t\bar{t}Z$ background normalization	1–14
Multiboson background normalization	1–8
Drell-Yan background normalization	1–7
Integrated luminosity	2.5
Pileup modeling	1–6
Factorization/renormalization scales	1–19
PDFs	1–6
Top quark p_T modeling	1–2
$t\bar{t}X$ (excl. $t\bar{t}Z$) background normalization	1–6
Simulated sample event count	2–27

For $t\bar{t}$ and $t\bar{t}Z$ backgrounds the renormalization and factorization scales are varied while keeping the overall normalization constant. Uncorrelated uncertainties between the two processes are assigned, based on the envelope of the variations. The assumption of a certain parton distribution function (PDF) has an effect on the simulated $M_{T2}(\ell\ell)$ shape. The impact on the acceptance is estimated using the replicas of the NNPDF3.0 PDF set [139], and the envelope of the variations is assigned as systematic uncertainty, ranging from 1% to 6%.

The transverse momentum of the top quark in $t\bar{t}$ events is found to be softer in data compared to the theory prediction [140–142]. The description of the observation is improved when higher order corrections in perturbative QCD are used, e.g. NNLO+NNLL [143] and approximate NNLO [144]. A reweighting function is derived as a function of top quark p_T in order to improve the agreement of the presently used NLO simulation and data. The function is defined as $w(p_T) = e^{0.0615 - 0.0005 \times p_T(t)}$, and an event weight proportional to $\sqrt{w(t) \cdot w(\bar{t})}$ is applied to the $t\bar{t}$ simulation, preserving the normalization of the sample. The difference relative to the results obtained with the unweighted sample is assigned as a systematic uncertainty, yielding values below 2%. An overview of the ranges of all systematic uncertainties is given in Tab. 4.9. The effect of missing higher-order corrections in the signal simulation is estimated by varying the renormalization and factorization scales up and down by a factor of two [145, 146], and uncertainties in the range between 1–19% are obtained.

The modeling of initial-state radiation (ISR) is relevant for SUSY signals when the mass difference between the top squark and the LSP is small. Therefore, weights are derived to improve the description of ISR multiplicity (N_j^{ISR}) in simulated samples. The weights are measured in control samples with an opposite flavor lepton pair and exactly two b-tagged jets, where the untagged jets are treated as ISR jets. The extracted weights are applied to SUSY signal samples such that the normalization of the sample is preserved, and vary from 0.92 and 0.51 for N_j^{ISR} between 1 and 6. One half of the deviation from unity is taken as systematic uncertainty in the reweighting factors.

The modeling of p_T^{miss} differs between the fast and full detector simulation. To cover this difference the reconstructed and generated p_T^{miss} are compared, leading to a systematic uncertainty of up to 20% for the SUSY signals. Additional uncertainties are assigned on the lepton identification and b-tagging scale factors that are applied to simulation, covering residual differences of the two detector simulations.

The signal acceptance depends on the assumption of the PDF set used for the sample generation. The uncertainty in the acceptance is evaluated by using variations of the PDF set. While this uncertainty is found to be redundant with the ISR uncertainty and therefore neglected for SUSY signal models it is applied to the DM signal models where no ISR uncertainty is used.

4.6 Results

The observed data is well described within uncertainties by the predicted SM background. Figure 4.27 shows the $M_{T2}(\ell\ell)$ distributions for the different lepton flavor compositions, and Fig. 4.28 shows the $M_{T2}(\ell\ell)$, $M_{T2}(\ell b\ell b)$ and p_T^{miss} distributions of all flavor channels combined. No significant deviation of data over the SM is observed in these distributions. The results in the signal regions defined in Tab. 4.4 are shown in Fig. 4.29 separately for the SF and OF channels, and these results are ultimately used in the signal extraction fit. The results in the combined signal regions are shown in Fig. 4.30 for illustration. The hashed bands show the systematic and statistical uncertainties in the background prediction. The predicted and observed yields in all signal regions, including systematic uncertainties, are given in Tab. 4.10.

4.7 Interpretation

The results shown in Fig. 4.29 are interpreted in terms of several different simplified models. A likelihood function is formulated containing the Poissonian probability functions for the signal regions, and the DY and $t\bar{t}Z$ control regions shown in Fig. 4.23 and 4.16, respectively. Each systematic uncertainty is described by a nuisance parameter θ , and the uncertainties

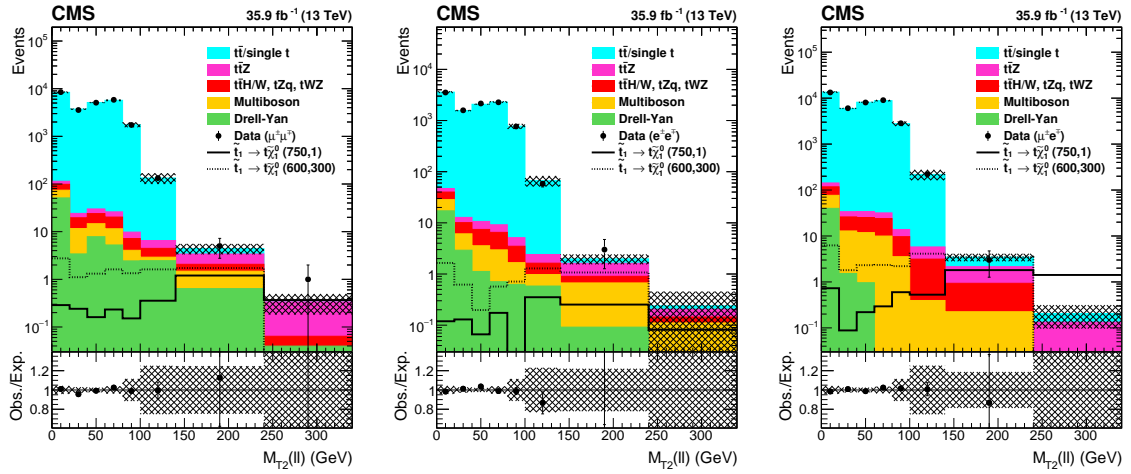


Figure 4.27: Distributions of $M_{T2}(\ell\ell)$ for observed events in the $\mu\mu$ (left), ee (center), and $e\mu$ (right) channels compared to the predicted SM backgrounds. The hatched band shows the uncertainty in the background prediction [12].

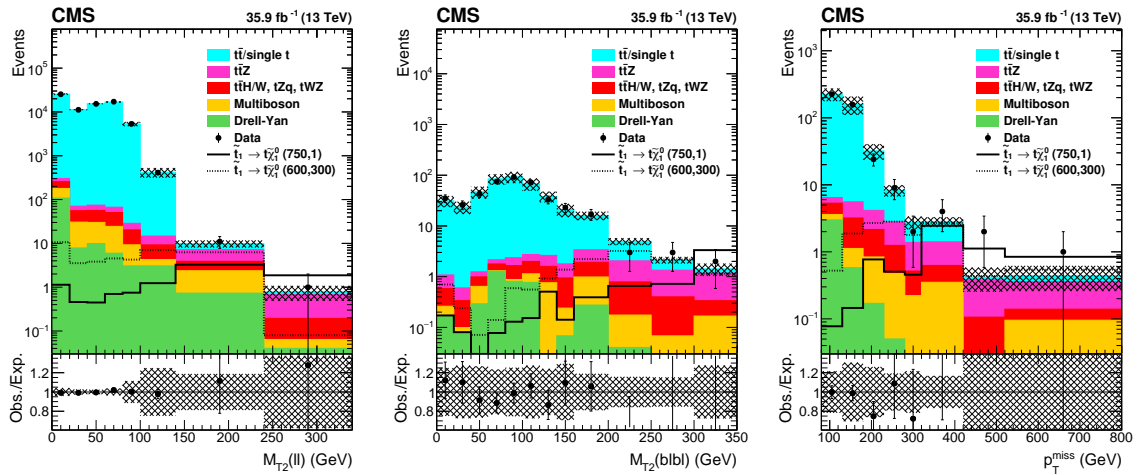


Figure 4.28: Distributions of $M_{T2}(\ell\ell)$ (left), $M_{T2}(\ell b\ell b)$ (center), and p_T^{miss} (right) for all lepton flavors. Additionally, $M_{T2}(\ell\ell) > 100$ GeV is required for the $M_{T2}(\ell b\ell b)$ and p_T^{miss} distributions. The hatched band shows the uncertainty in the background prediction [12].

are modeled by log-normal distributions $p(\tilde{\theta}|\theta)$. The likelihood function has the form of

$$\mathcal{L}(\text{data} | \mu, \theta) = \prod_j^{\text{regions}} \text{Pois}(n_j | \mu \cdot s_j(\theta) + b_j(\theta)) \cdot \prod_i^{\text{nuisances}} p(\tilde{\theta}_i | \theta_i) \quad , \quad (4.6)$$

where μ is the signal strength modifier, s and b the predicted number of signal and background events, and data corresponds either to the true observation, or the outcome of a toy experiment.

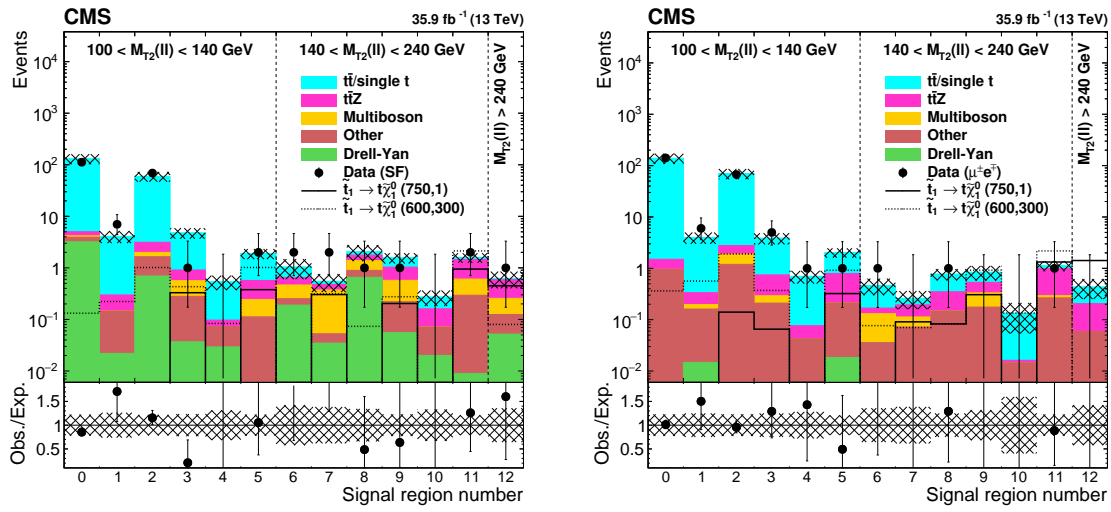


Figure 4.29: Predicted backgrounds and observed yields in the ee and $\mu\mu$ search regions (left) and the $e\mu$ search regions (right). The hatched band shows the uncertainty in the background prediction [12].

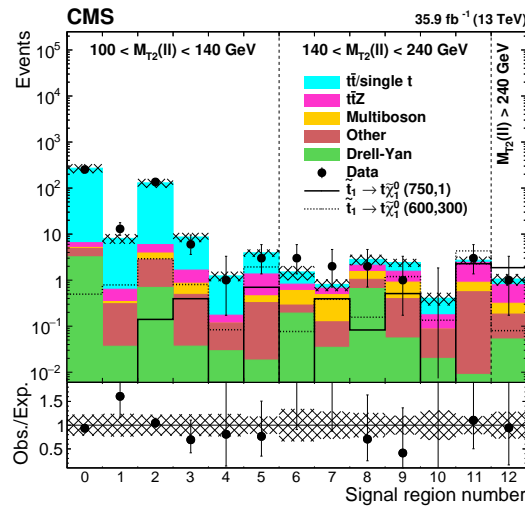


Figure 4.30: Predicted backgrounds and observed yields in the ee , $\mu\mu$, and $e\mu$ search regions combined. The hatched band shows the uncertainty in the background prediction [12].

A profile likelihood ratio in the asymptotic limit [147] is used as test statistic

$$\tilde{q}_\mu = -2 \ln \frac{\mathcal{L}(\text{data} | \mu, \hat{\theta}_\mu)}{\mathcal{L}(\text{data} | \hat{\mu}, \hat{\theta})}, \quad \text{with a constraint } 0 \leq \hat{\mu} \leq \mu, \quad (4.7)$$

where $\hat{\theta}_\mu$ is the conditional maximum likelihood estimator of θ given μ and data. $\hat{\mu}$ and $\hat{\theta}$ denote the signal strength and nuisance that provide the global maximum likelihood. The constraints on $\hat{\mu}$ are motivated by physics: The signal yield has to be larger than 0 hence $0 \leq \hat{\mu}$, and a potential upwards fluctuation of data such that $\hat{\mu} > \mu$ should not be used as

Table 4.10: Total expected background and event yields in data in each of the signal regions for same-flavor ($ee/\mu\mu$), different-flavor ($e\mu$), and all channels combined with all the systematic uncertainties included as described in Section 4.5.

Signal region	Same flavor		Different flavor		All	
	Expected	Observed	Expected	Observed	Expected	Observed
0	131 ± 30	112	139 ± 32	141	271 ± 61	253
1	4.1 ± 1.1	7	4.0 ± 1.1	6	8.1 ± 2.0	13
2	60 ± 13	69	70 ± 17	67	130 ± 29	136
3	4.8 ± 1.2	1	3.9 ± 1.0	5	8.7 ± 2.0	6
4	0.5 ± 0.2	0	0.7 ± 0.2	1	1.2 ± 0.4	1
5	1.9 ± 0.5	2	2.1 ± 0.5	1	4.0 ± 0.8	3
6	1.1 ± 0.6	2	0.5 ± 0.2	1	1.5 ± 0.7	3
7	0.6 ± 0.3	2	0.3 ± 0.2	0	0.8 ± 0.3	2
8	2.1 ± 0.7	1	0.8 ± 0.2	1	2.9 ± 0.7	2
9	1.6 ± 0.4	1	0.9 ± 0.3	0	2.5 ± 0.5	1
10	0.3 ± 0.1	0	0.1 ± 0.1	0	0.4 ± 0.2	0
11	1.7 ± 0.4	2	1.2 ± 0.3	1	2.9 ± 0.6	3
12	0.7 ± 0.3	1	0.5 ± 0.2	0	1.1 ± 0.4	1

evidence against the signal. The latter also ensures that the obtained confidence interval is one-sided. Upper limits on the production cross section times branching fraction are then calculated at a 95% confidence level (CL) using the asymptotic CL_S criterion [148–150].

4.7.1 Supersymmetry

Interpretations of the results in terms of SUSY simplified models are given in the $m_{\tilde{t}} - m_{\tilde{\chi}_1^0}$ mass plane, e.g. shown in Fig. 4.31, where the color map corresponds to the 95% CL upper limit on the cross section times branching fraction squared at each point on the plane. The area below the thick black curve represents the region excluded at 95% CL under the assumption of 100% branching fraction, while the dashed red line delimits the area of the expected limit at 95% CL. The accompanying thin red lines mark the region containing 68% of the distributions of limits expected under the background only hypothesis. The impact of the theoretical uncertainties on the signal cross section is reflected by the thin black lines. For the T2tt model with $\tilde{t} \rightarrow t\tilde{\chi}_1^0$ decays top squarks with masses up to $m_{\tilde{t}} < 800$ GeV are excluded for neutralinos with masses below $m_{\tilde{\chi}_1^0} < 360$ GeV. The T2bW model depends on three mass parameters owing to the intermediate chargino in the decay of the top squark, $\tilde{t} \rightarrow b\tilde{\chi}_1^\pm \rightarrow bW\tilde{\chi}_1^0$. The chargino mass is set to $(m_{\tilde{t}} - m_{\tilde{\chi}_1^0})/2$ in order to allow for interpretations in the $m_{\tilde{t}} - m_{\tilde{\chi}_1^0}$ plane. Top squarks with masses up to 750 GeV for $m_{\tilde{\chi}_1^0}$ below 320 GeV are excluded.

The limits presented in Fig. 4.31 are obtained under the assumption that the top squarks are unpolarized. This choice has an impact on the kinematics of the final state particles [151], and therefore the two other extreme polarization scenarios of purely left- and right-handed polarized top squarks are checked. The results are shown in Fig. 4.32. The exclusion limits are decreased by about 50 GeV in the top squark mass for the left-handed case, and increased

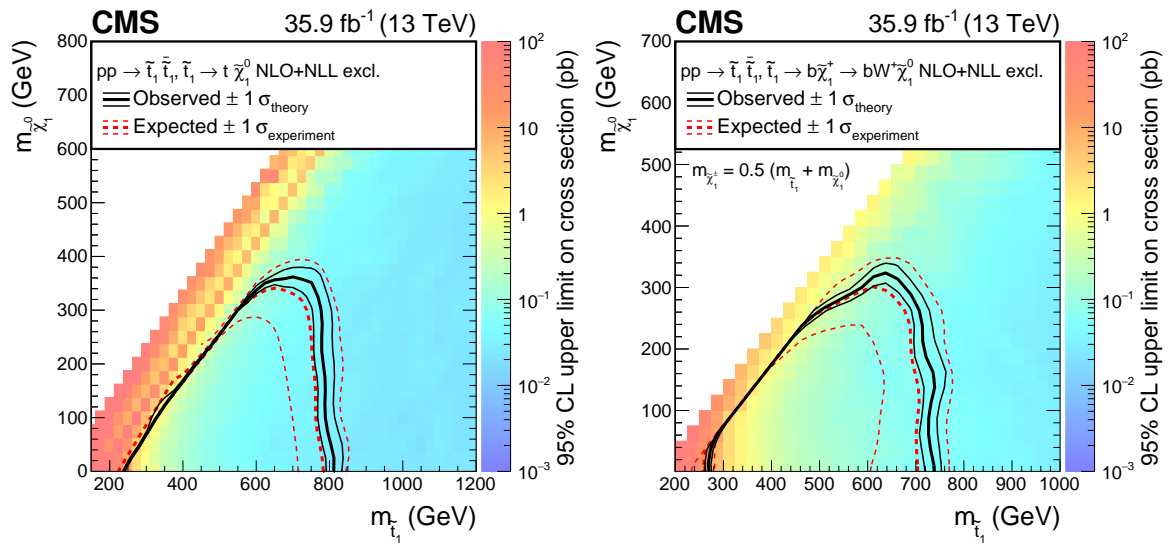


Figure 4.31: Expected and observed limits for the T2tt model with $\tilde{t} \rightarrow t \tilde{\chi}_1^0$ decays (left) and for the T2bW model with $\tilde{t} \rightarrow b \tilde{\chi}_1^\pm \rightarrow bW \tilde{\chi}_1^0$ decays (right) in the $m_{\tilde{t}} - m_{\tilde{\chi}_1^0}$ mass plane. For the latter, the chargino mass is chosen to be $(m_{\tilde{t}} - m_{\tilde{\chi}_1^0})/2$. The color indicates the 95% CL upper limit on the cross section times the square of the branching fraction at each point in the plane. The area below the thick black curve represents the observed exclusion region at 95% CL assuming 100% branching fraction, while the dashed red lines indicate the expected limits at 95% CL and the region containing 68% of the distribution of limits expected under the background-only hypothesis. The thin black lines show the effect of the theoretical uncertainties in the signal cross section [12].

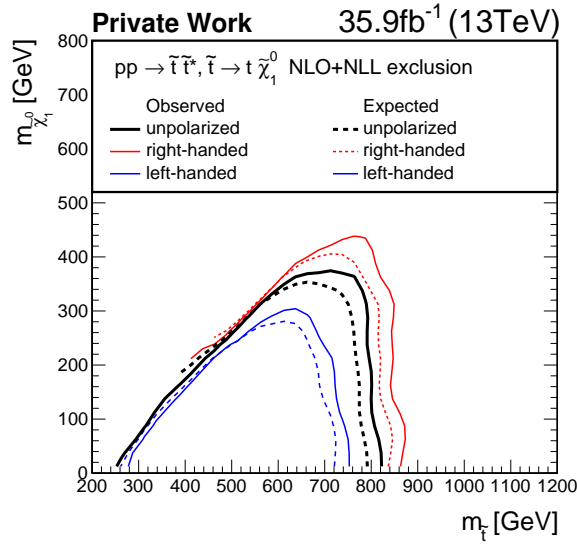


Figure 4.32: Expected and observed limits for the T2tt model with different assumptions for the top squark polarization. The black curves correspond to unpolarized top squarks, also shown in Fig. 4.31. The exclusion limits for left-handed polarization are about 50 GeV weaker in terms of $m_{\tilde{t}}$, indicated by the blue lines. For right-handed polarization, top squarks up to 860 GeV can be excluded. Solid and dashed lines correspond to observed and expected limits, respectively.

by a similar amount in the right-handed case.

The results for the T8bbll $\nu\nu$ model with the top squark decay chain $\tilde{t} \rightarrow b\tilde{\chi}_1^\pm \rightarrow b\nu\tilde{\ell} \rightarrow b\nu\ell\tilde{\chi}_1^0$ are shown in Fig. 4.33, which exhibit a strong dependence on the parameter x that defines the mass of the intermediate slepton via the relation $m_{\tilde{\ell}} = x \times (m_{\tilde{\chi}_1^\pm} - m_{\tilde{\chi}_1^0}) + m_{\tilde{\chi}_1^0}$. For $x = 0.05$, corresponding to a slepton mass close to the neutralino mass, the produced leptons are relatively soft and therefore often outside of the experimental acceptance. In this case, top squarks with masses up to $m_{\tilde{t}} < 1000$ GeV can be excluded for neutralino masses up to $m_{\tilde{\chi}_1^0} < 50$ GeV. If the mass of the slepton mass is exactly between the chargino and neutralino mass, i.e. $x = 0.5$, the excluded region in the $m_{\tilde{t}} - m_{\tilde{\chi}_1^0}$ plane is extended up to $m_{\tilde{t}} < 1200$ GeV for $m_{\tilde{\chi}_1^0} < 660$ GeV. For the case of $x = 0.95$ where the slepton mass is close to the chargino mass, top squarks up to $m_{\tilde{t}} < 1300$ GeV can be excluded for neutralinos with masses up to $m_{\tilde{\chi}_1^0} < 800$ GeV. These results exhibit the sensitivity of the analysis for models which have a large branching fraction into two leptons.

Searches for top squark pair production were also performed in all-jet final states [152] and final states with a single lepton [153]. Because the overlap of the signal and control regions is negligible it is logical to combine the results to set even tighter constraints on direct top squark pair production, shown in Fig. 4.34. The sensitivity for the T2tt model is driven by the all-hadronic final state search, and by the single-lepton result for the T2bW model. The combined result for the T2tt model excludes top squarks with masses below $m_{\tilde{t}} < 1050$ GeV for a massless LSP. For the T2bW model, top squarks are excluded if $m_{\tilde{t}} < 1000$ GeV for

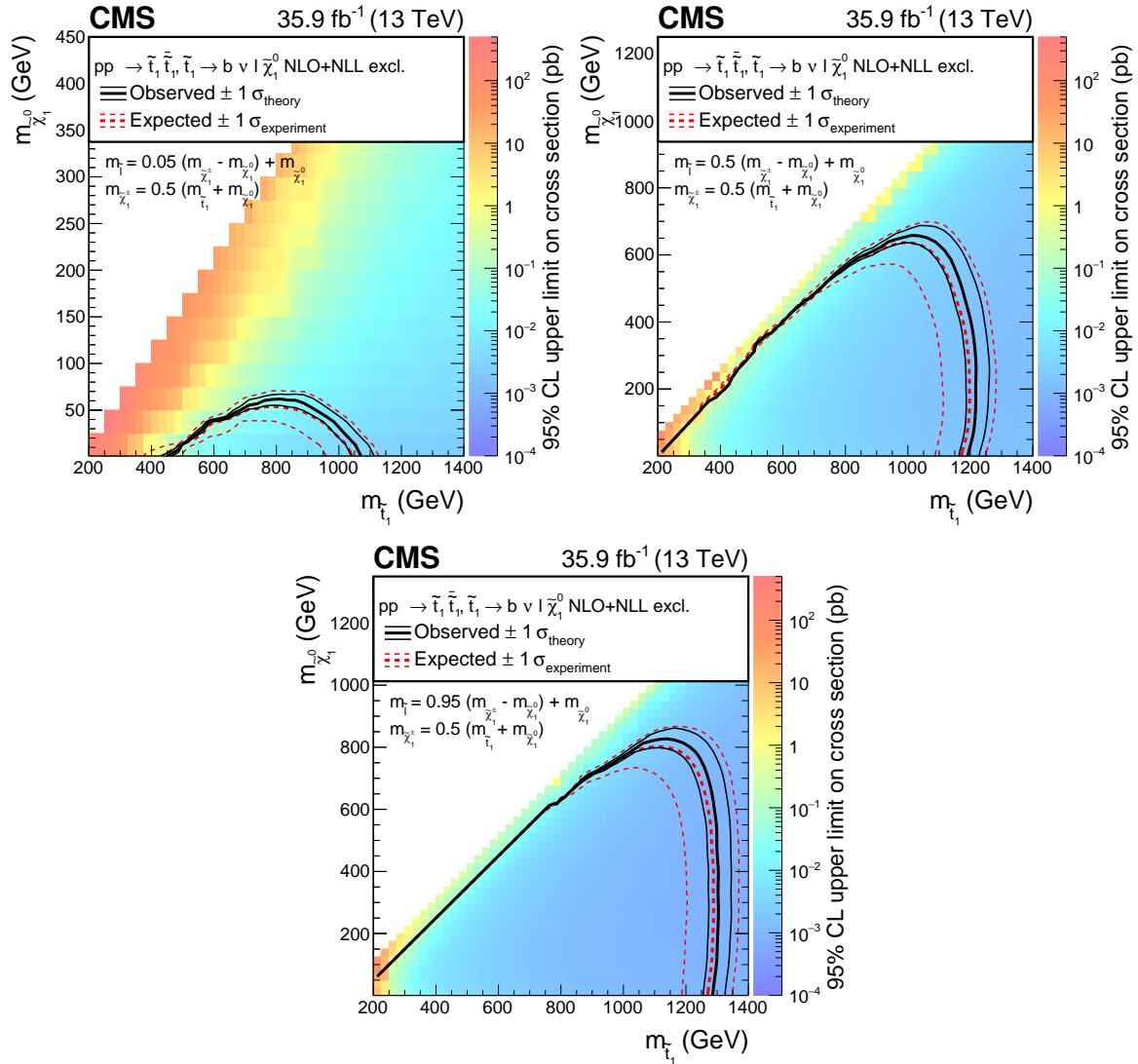


Figure 4.33: Expected and observed limits for the T8bbllνν model with $\tilde{t} \rightarrow b\tilde{\chi}_1^\pm \rightarrow b\nu\tilde{\ell} \rightarrow b\nu l\tilde{\chi}_1^0$ decays in the $m_{\tilde{t}} - m_{\tilde{\chi}_1^0}$ mass plane for three different mass configurations defined by $m_{\tilde{\ell}} = x + (m_{\tilde{\chi}_1^\pm} - m_{\tilde{\chi}_1^0}) + m_{\tilde{\chi}_1^0}$ with $x = 0.05$ (upper left), $x = 0.5$ (upper right), and $x = 0.95$ (lower) [12]. The description of curves is the same as in the caption of Fig. 4.31.

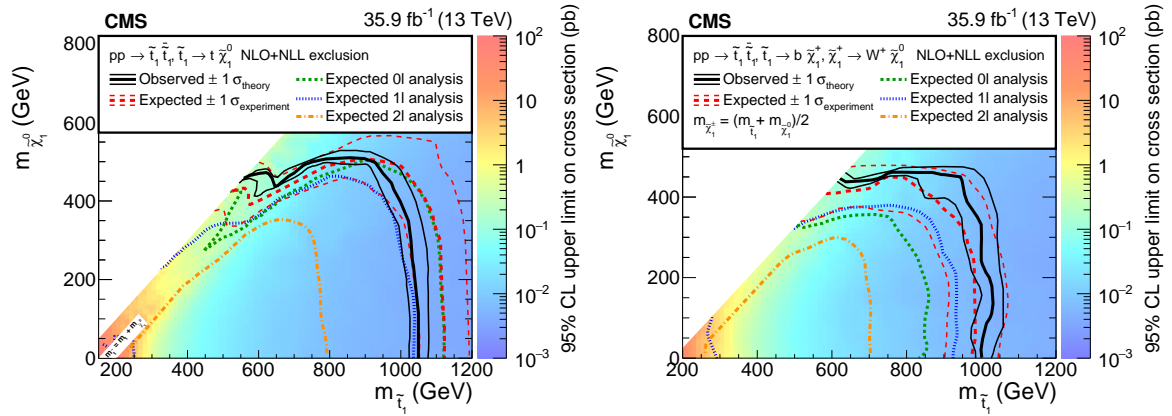


Figure 4.34: Expected and observed limits for the T2tt model with $\tilde{t} \rightarrow t\tilde{\chi}_1^0$ decays in the $m_{\tilde{t}} - m_{\tilde{\chi}_1^0}$ mass plane (left) and the T2bW model with $\tilde{t} \rightarrow b\tilde{\chi}_1^\pm \rightarrow bW\tilde{\chi}_1^0$ (right), combining the dilepton final state with the single-lepton and the all-hadronic final states as described in the text. The mass of the chargino is chosen to be $(m_{\tilde{t}} - m_{\tilde{\chi}_1^0})/2$. The color indicates the 95% CL upper limit on the cross section times the square of the branching fraction at each point in the plane. The area below the thick black curve represents the observed exclusion region at 95% CL assuming 100% branching fraction, while the dashed red lines indicate the expected limits at 95% CL and the region containing 68% of the distribution of limits expected under the background-only hypothesis. The thin black lines show the effect of the theoretical uncertainties in the signal cross section. The green short-dashed, blue dotted, and long-short-dashed orange curves show the expected individual limits for the all-hadronic, single-lepton, and dilepton analyses, respectively. The white-out area on the diagonal corresponds to configurations where the mass difference between \tilde{t} and $\tilde{\chi}_1^0$ is very close to the top quark mass. In this region the signal acceptance strongly depends on the $\tilde{\chi}_1^0$ mass and is therefore hard to model [12].

a massless LSP, and LSPs below $m_{\tilde{\chi}_1^0} < 450$ GeV for a top squark mass of 900 GeV. The combined result improves the constraints on top squark masses by about 50 GeV compared to the best individual results.

4.7.2 Dark Matter

The results shown in Fig. 4.29 and 4.30 are also interpreted in terms of a simplified DM model. A scalar or pseudoscalar mediator is produced in the $t\bar{t}$ t-channel which decays to the fermionic DM particles. The couplings g_q and g_{DM} are set to 1. Figure 4.35 shows the ratios of $\sigma/\sigma_{\text{theory}}$ of the 95% CL expected and observed upper limits on the cross section σ with respect to the predicted cross section by the simplified model σ_{theory} for DM particles with $m_\chi = 1$ GeV. Table 4.11 additionally shows expected and observed upper limits for DM particles with $m_\chi = 10$ GeV and $m_\chi = 50$ GeV, together with the corresponding predicted cross sections. It can be seen that the upper limit on a certain mediator mass $m_{\phi/a}$ is independent of m_χ as long as $m_{\phi/a} > 2m_\chi$. Scalar mediator particles are excluded up to masses of $m_\phi < 50$ GeV, and pseudoscalar particles up to $m_a < 100$ GeV.

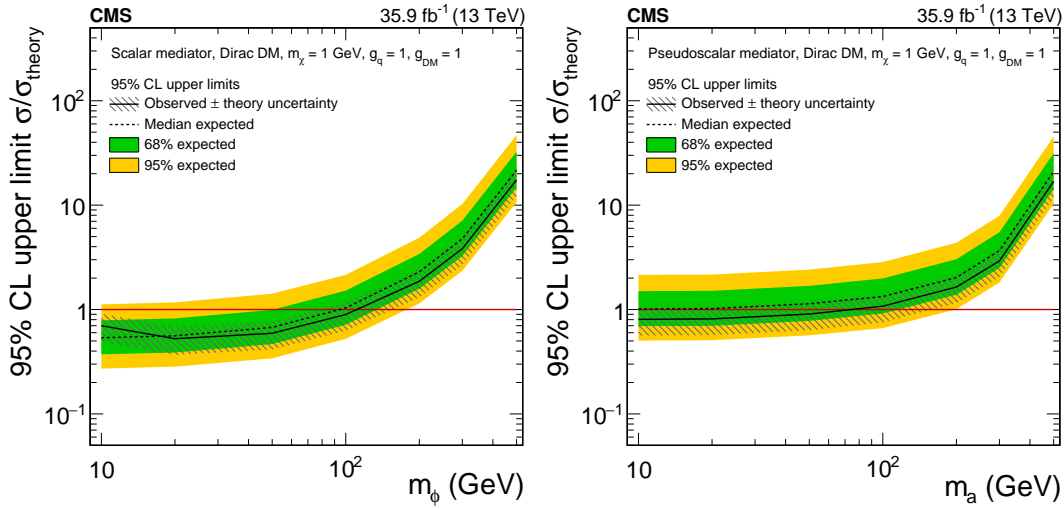


Figure 4.35: The 95% CL expected (dashed line) and observed limits (solid line) on $\mu = \sigma/\sigma_{\text{theory}}$ for a fermionic DM particle with $m_\chi = 1$ GeV assuming different scalar (left) and pseudoscalar (right) mediator masses. The green and yellow bands represent the regions containing 68 and 95%, respectively, of the distribution of limits expected under the background-only hypothesis. The horizontal red line indicates $\mu = 1$. The mediator couplings are set to $g_q = g_{\text{DM}} = 1$. The gray hashed band around the observed limit corresponds to a 30% theory uncertainty in the inclusive signal cross section [12].

4.7.3 Constraints on the invisible decay of the Higgs boson

The branching fraction of the Higgs boson into DM particles, or any other undetectable particles, is constrained to be below 20% [154, 155]. For these measurements Higgs production modes with a large cross section are selected, such as gluon fusion or vector boson fusion. The $t\bar{t}H$ process has a comparable small production cross section, and has only recently been observed by the CMS and ATLAS collaborations [156, 157]. The expected low rate of the $t\bar{t}H$ process can partially be compensated by the suppression of SM backgrounds due to the distinct topology. Additionally, if the Yukawa coupling of top quarks to the Higgs boson is enhanced by new physics the $t\bar{t}H$ process provides additional sensitivity. The top-Higgs coupling is also constrained by the loop process in gluon fusion Higgs production, however, the modification of the coupling could be compensated by additional colored particles contributing to the loop [158].

Invisible Higgs decays via $t\bar{t}H$ production result in a similar final state to top squark pair production, and therefore the results of the top squark searches in the all-jet, single and dilepton final states are reinterpreted to set constraints on $\mathcal{B}(H \rightarrow \text{inv.})$. The signal sample is generated assuming a Higgs boson mass of $m_H = 125$ GeV using the POWHEG v2 generator. The expected signal yield in the search regions of the dilepton analysis is shown in Fig. 4.36, together with the predicted SM background and the observed yields in data. No additional optimization of the signal regions defined in Tab. 4.4 targeting the $t\bar{t}H$ signal is performed.

Table 4.11: Ratios $\mu = \sigma/\sigma_{\text{theory}}$ of the 95% CL expected and observed limits to simplified model expectations for different DM particle masses and mediator masses and for scalar (ϕ) and pseudoscalar (a) mediators under the assumption $g_q = g_{\text{DM}} = 1$. The uncertainties reflect the 68% band of the expected limits.

m_χ (GeV)	$m_{\phi/a}$ (GeV)	$\sigma\mathcal{B}(2\ell)$ (fb)	Scalar		Pseudoscalar		
			Expected	Observed	$\sigma\mathcal{B}(2\ell)$ (fb)	Expected	Observed
1	10	2242	$0.54^{+0.25}_{-0.16}$	0.70	47.4	$1.01^{+0.49}_{-0.32}$	0.81
1	20	1150	$0.56^{+0.26}_{-0.17}$	0.53	43.2	$1.02^{+0.49}_{-0.32}$	0.81
1	50	324	$0.67^{+0.32}_{-0.21}$	0.59	32.3	$1.14^{+0.55}_{-0.36}$	0.91
1	100	75.6	$1.04^{+0.48}_{-0.32}$	0.90	20.3	$1.33^{+0.65}_{-0.42}$	1.08
1	200	10.7	$2.30^{+1.11}_{-0.72}$	1.87	9.22	$2.02^{+1.01}_{-0.64}$	1.64
1	300	3.20	$4.8^{+2.3}_{-1.5}$	3.8	4.15	$3.7^{+1.8}_{-1.2}$	2.9
1	500	0.52	$21.6^{+10.9}_{-6.9}$	17.4	0.54	$21.0^{+10.4}_{-6.7}$	16.9
10	10	10.6	$18.8^{+8.8}_{-5.8}$	16.6	1.60	$19.3^{+9.3}_{-6.1}$	15.3
10	15	13.4	$17.0^{+8.0}_{-5.2}$	13.8	2.05	$15.8^{+7.6}_{-5.0}$	12.7
10	50	325	$0.72^{+0.33}_{-0.22}$	0.69	32.5	$1.08^{+0.52}_{-0.34}$	0.86
10	100	77.9	$1.03^{+0.48}_{-0.32}$	0.84	20.7	$1.25^{+0.61}_{-0.39}$	0.98
50	10	0.22	125^{+61}_{-39}	102	0.25	72^{+36}_{-23}	58
50	50	0.27	104^{+50}_{-33}	84	0.31	62^{+30}_{-19}	49
50	95	0.76	52^{+25}_{-16}	43	1.13	$20.3^{+10.0}_{-6.4}$	16.2
50	200	10.5	$2.32^{+1.14}_{-0.73}$	1.86	8.90	$2.05^{+1.02}_{-0.64}$	1.64
50	300	3.20	$4.7^{+2.3}_{-1.5}$	3.8	4.04	$3.7^{+1.9}_{-1.2}$	3.0

The combined result of the three searches yields an observed (expected) upper limit on the decay of a Higgs boson with $m_H = 125$ GeV to invisible particles of $\mathcal{B}(H \rightarrow \text{inv.}) < 0.46$ (0.48). The combined and individual limits are shown in Fig. 4.37.

4.7.4 Reinterpretation

To facilitate reinterpretations of the analysis, the covariance and correlation matrices for a simplified likelihood [159] are provided, shown in Fig. 4.38. Additionally, a reduced set of signal regions is constructed, providing comparable sensitivity to the full set. The number of signal regions is reduced from 26 to 3 by combining the SF and OF lepton channels, merging the $M_{T2}(\ell b \ell b)$ regions and only selecting regions with p_T^{miss} larger than 200 GeV. The signal region with $M_{T2}(\ell \ell) > 240$ GeV is kept without any changes but the combination of the SF and OF channels. The definition of this set of aggregate regions is shown in Tab. 4.12 together with expected background and observed event yields. The covariance and correlation matrix for the aggregate regions is given in Tab. 4.13. The corresponding HEPData entry to the analysis is shown in [160].

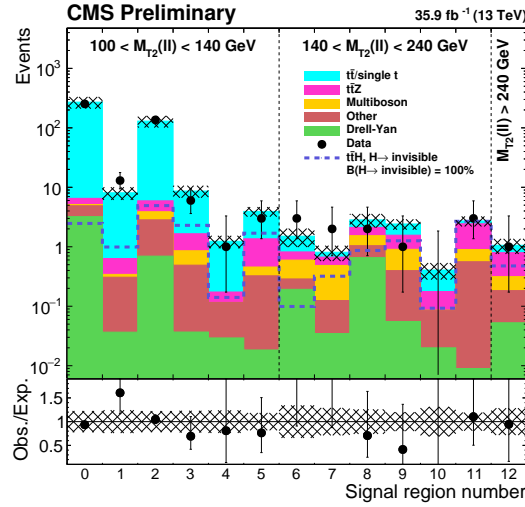


Figure 4.36: Predicted backgrounds and observed yields in the dilepton channel. The numbers on the x-axis indicate different signal regions. The hatched band shows the uncertainties discussed in the text. A 100% branching fraction is assumed for the $t\bar{t}H \rightarrow t\bar{t} + \text{inv.}$ signal [14].

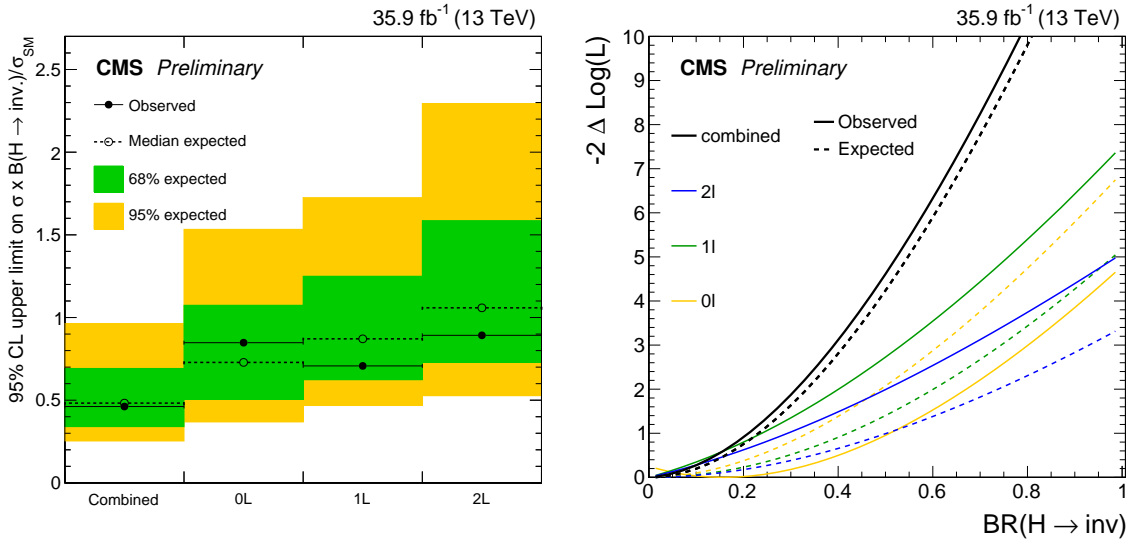


Figure 4.37: Observed and expected 95% CL upper limits on $\sigma\mathcal{B}(H \rightarrow \text{inv.})/\sigma_{\text{SM}}$ for the all-hadronic, semi-leptonic, and di-leptonic final states, as well as their combination, assuming an SM Higgs boson with a mass of 125 GeV (left). The solid curves represent the observations in data, while the dashed lines represent the expected result assuming the absence of any signal. Profile likelihood ratios as a function of $\mathcal{B}(H \rightarrow \text{inv.})$. The observed and expected likelihood scans are reported for the combination, as well as for the all-hadronic, semi-leptonic, and di-leptonic final states, respectively (right) [14].

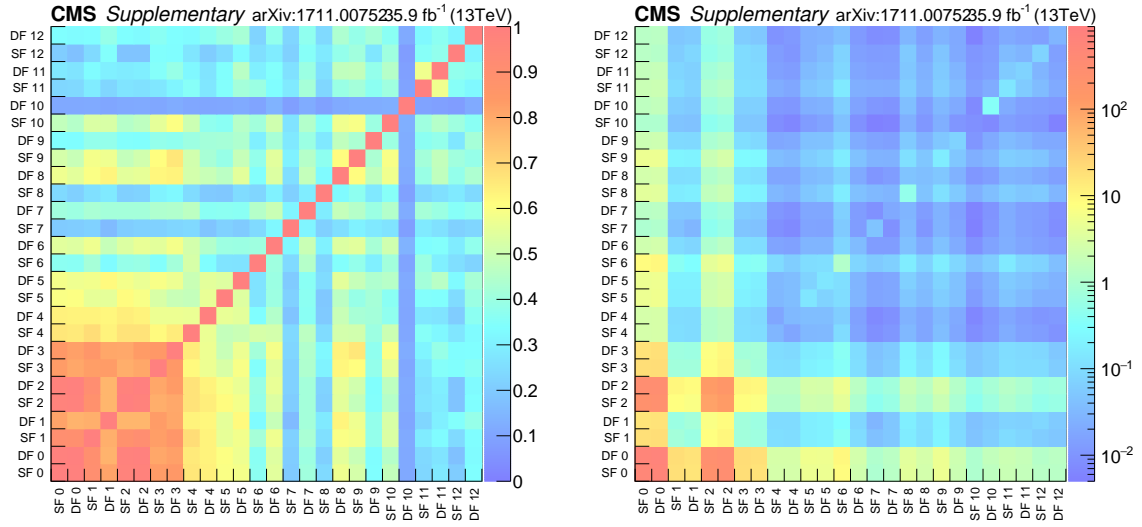


Figure 4.38: Correlation (left) and covariance (right) matrix of the 13 signal regions, split into same-flavor (SF) and different-flavor (DF) regions [12].

Table 4.12: Expected and observed event yields, summed over all lepton flavors, in the aggregate signal regions defined by the selection requirements in the table.

Signal region	p_T^{miss} (GeV)	$M_{T2}(\ell\ell)$ (GeV)	Expected	Observed
A0	> 200	100–140	20.8 ± 4.4	22
A1	> 200	140–240	6.2 ± 1.0	6
A2	> 80	> 240	1.1 ± 0.4	1

4.8 Improvements towards an analysis of the full Run 2 data set

The following paragraphs sketch potential improvements for a search using the full Run 2 data set corresponding to approximately 140 fb^{-1} . The instantaneous luminosity increased from 2016 to 2018, resulting in higher pileup conditions which have to be taken into account in the studies.

Table 4.13: Covariance (left) and correlation matrix (right) for the background prediction in the aggregate signal regions described in Table 4.12.

	A0	A1	A2		A0	A1	A2
A0	13.3	1.8	0.5	A0	1	0.51	0.38
A1		0.9	0.2	A1		1	0.49
A2			0.1	A2			1

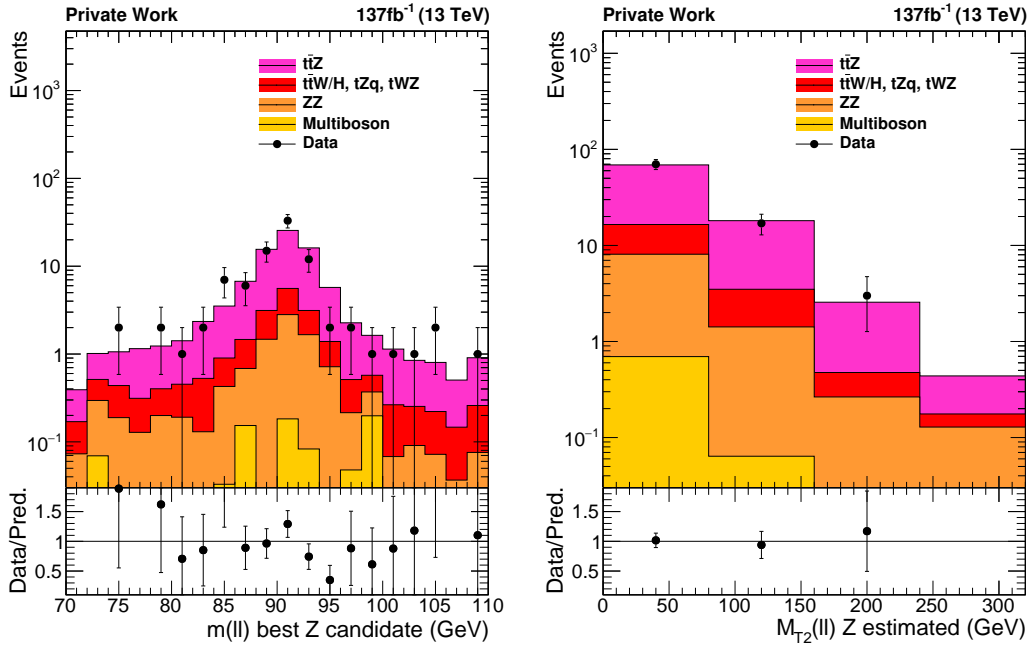


Figure 4.39: Distribution of the mass of best Z boson candidate reconstructed from OS SF leptons in the 4ℓ channel (left), and the $M_{T2}(\ell\ell)$ distribution where the p_T^{miss} is modified by adding the reconstructed Z boson p_T (right), using the full Run 2 data set corresponding to 137fb^{-1} . Good agreement of simulation and data is observed up to high values of $M_{T2}(\ell\ell)$, indicating good modeling of the $M_{T2}(\ell\ell)$ shape in the $t\bar{t}Z$ simulation.

4.8.1 $t\bar{t}Z$ background

A crucial ingredient to the search for direct top squark pair production is the precise knowledge of the cross section and kinematics of the $t\bar{t}Z$ background. The uncertainty in the $t\bar{t}Z$ process in the signal regions is 20% in the discussed analysis, and it is the single systematic uncertainty with the highest impact on the determination of a hypothetical signal strength. An improved inclusive cross section measurement together with a higher confidence in the $M_{T2}(\ell\ell)$ shape prediction of the simulation can therefore improve the sensitivity of the analysis. A measurement of the $t\bar{t}Z$ cross section in final states with three and four leptons is discussed in the following chapter. The precision of the inclusive cross section measurement is below 10%. The $M_{T2}(\ell\ell)$ shape of $t\bar{t}Z$ is validated using a $t\bar{t}\gamma$ control sample. An orthogonal approach is to select $t\bar{t}Z$ events in the four lepton final state, where the reconstructed Z boson p_T is added to p_T^{miss} to mimic $Z \rightarrow \nu\nu$, and $M_{T2}(\ell\ell)$ is recalculated using the modified p_T^{miss} . This approach is limited by the low branching fraction into this final state, and was therefore not followed up when analyzing the 2016 data set of 36fb^{-1} . With the almost four times larger data set of the entire Run 2 this check is feasible, and can be included in the analysis. Figure 4.39 shows distributions in the 4ℓ channel, and no excess of data over the $t\bar{t}Z$ simulation is observed in events with large $M_{T2}(\ell\ell)$.

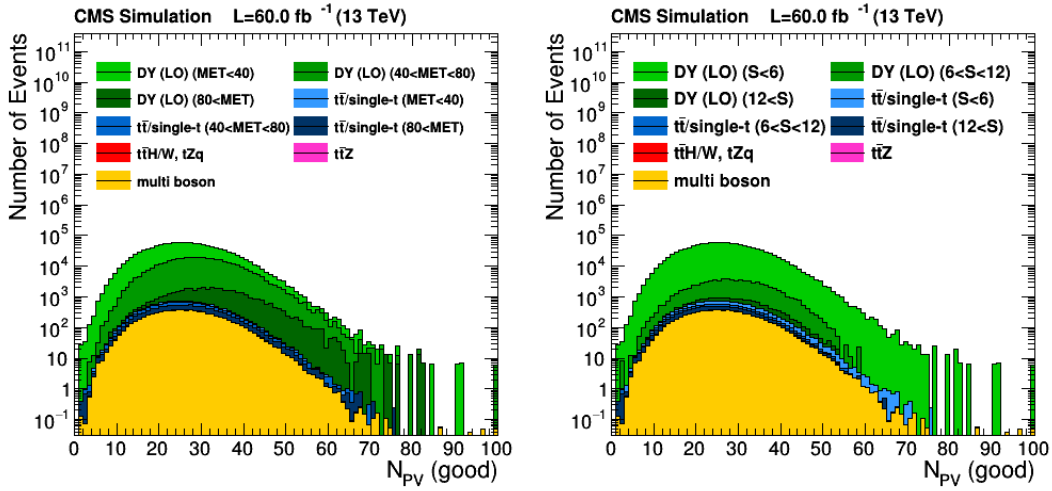


Figure 4.40: Multiplicity distributions of reconstructed primary vertices using simulated samples corresponding to data taken in 2018. The DY and $t\bar{t}$ samples are categorized in bins of p_T^{miss} (left) using thresholds of 40 and 80 GeV, and bins of \mathcal{S} (right) using thresholds of 6 and 12. DY events with $p_T^{\text{miss}} > 80$ GeV are strongly biased towards high values of N_{PV} , while a more uniform distribution is observed for $\mathcal{S} > 12$.

4.8.2 Missing transverse momentum significance

The missing transverse momentum is an important handle to suppress the large DY background, and the $p_T^{\text{miss}} > 80$ GeV and $p_T^{\text{miss}}/\sqrt{H_T} > 5$ requirements are highly efficient, shown in Tab. 4.3. Due to the high pileup conditions in the 2017 and 2018 data sets, DY events with large p_T^{miss} become more abundant, letting more DY events pass the $p_T^{\text{miss}} > 80$ GeV requirement. Therefore, events with a high number of pileup interactions are implicitly selected, shown in Fig. 4.40 (left).

This effect can be mitigated by using the so called missing transverse momentum significance \mathcal{S} [10, 161]. The \mathcal{S} algorithm incorporates the jet energy resolutions and low energy deposits, called unclustered energy, and is therefore more robust in discriminating events with genuine p_T^{miss} from those with p_T^{miss} arising from pileup and detector noise. In short, \mathcal{S} quantifies the compatibility of an event with the hypothesis of no genuine p_T^{miss} and is defined as

$$\mathcal{S} \equiv 2 \ln \left(\frac{\mathcal{L}(\vec{\varepsilon} = \sum \vec{\varepsilon}_i)}{\mathcal{L}(\vec{\varepsilon} = 0)} \right) , \quad (4.8)$$

where $\vec{\varepsilon}$ represents the true p_T^{miss} and $\sum \vec{\varepsilon}_i$ the reconstructed p_T^{miss} . The significance is calculated using the reconstructed p_T^{miss} and its 2×2 covariance matrix \mathbf{V} as

$$\mathcal{S} = \left(\sum \vec{\varepsilon}_i \right)^T \mathbf{V}^{-1} \left(\sum \vec{\varepsilon}_i \right) , \quad (4.9)$$

where \mathbf{V} is calculated per event using the resolutions of the hadronic components, namely jets

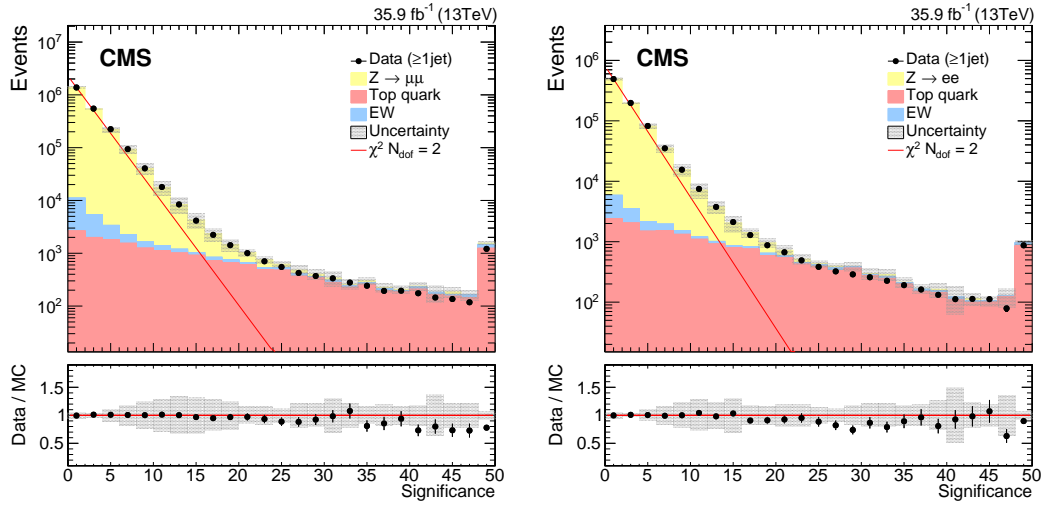


Figure 4.41: Distributions of \mathcal{S} in $Z \rightarrow \mu\mu$ (left) and $Z \rightarrow ee$ (right) samples of 2016 data, requiring at least one jet with $p_T > 30$ GeV. The hatched band shows the uncertainties obtained from variations of JES and JER as well as unclustered energy in simulation. The red line corresponds to a χ^2 distribution with two degrees of freedom [10].

and the unclustered energy. Jets contribute to \mathbf{V} as

$$\mathbf{U} = \begin{pmatrix} \sigma_{p_T}^2 & 0 \\ 0 & p_T^2 \sigma_\phi^2 \end{pmatrix}, \quad (4.10)$$

where σ_{p_T} and σ_ϕ are the measured jet resolutions that are rescaled using DY samples of data and simulation. The matrix \mathbf{U} is rotated into the x-y coordinate system. The unclustered energy that also includes jets with $p_T < 15$ GeV is combined into a single pseudo-jet object with a resolution that is parametrized by the scalar p_T sum of its constituents

$$\sigma_{\text{uc}}^2 = \sigma_0^2 + \sigma_s^2 \sum_{i=1}^n |\vec{p}_{T_i}|, \quad (4.11)$$

with the parameters σ_0 and σ_s which are determined in DY samples of data and simulation. For low values, the significance \mathcal{S} follows a χ^2 distribution with two degrees of freedom for events with no genuine p_T^{miss} , shown in Fig. 4.41 for $Z \rightarrow \mu\mu$ and $Z \rightarrow ee$ events. \mathcal{S} is almost independent of pileup for events with no genuine p_T^{miss} because the increase of p_T^{miss} is balanced by its larger variance. This robustness is shown in Fig. 4.42, and also in Fig. 4.40 (right). In events with genuine p_T^{miss} , e.g. $W \rightarrow e\nu$, the p_T^{miss} is not dominated by detector effects caused by hadronic activity and is therefore almost independent of pileup. The variance of p_T^{miss} on the other hand still increases with an increasing number of interactions, resulting in a decrease of \mathcal{S} with higher vertex multiplicity.

For the top quark search this implies that replacing the $p_T^{\text{miss}} > 80$ GeV requirement by $\mathcal{S} > 12$

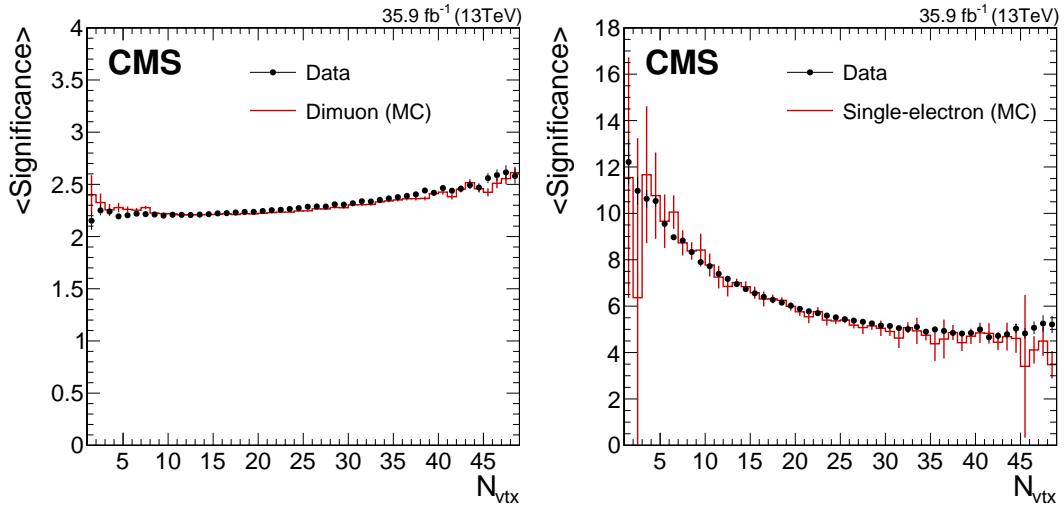


Figure 4.42: Distributions of the average \mathcal{S} with respect to pileup, for dimuon (left) and single-electron (right) events. For events with no genuine $p_{\text{T}}^{\text{miss}}$ the average \mathcal{S} is only weakly dependent on N_{vtx} [10].

should result in a better rejection of DY events. More importantly, and contrary to the $p_{\text{T}}^{\text{miss}}$ selection, events surpassing the selection requirement are not biased towards high pileup. This feature will prove to be essential when repeating the analysis with the high pileup data of 2017 and 2018.

4.9 Summary

The presented search for the pair production of top squarks, the SUSY partners of the top quark, searches for an excess of data over the SM prediction in events with large $p_{\text{T}}^{\text{miss}}$, $M_{\text{T}2}(\ell\ell)$ and $M_{\text{T}2}(\ell b\bar{b})$. Signatures similar to those of the decays of the top squarks emerge in many other BSM predictions, like DM production via scalar or pseudoscalar mediators, or the invisible decay of a Higgs boson produced in the $t\bar{t}H$ channel. The main SM backgrounds are coming from $t\bar{t}$ and DY processes, which are largely reduced by tight requirements on $M_{\text{T}2}(\ell\ell)$ as well as $p_{\text{T}}^{\text{miss}}$ and $p_{\text{T}}^{\text{miss}}/\sqrt{H_T}$, respectively. The largest irreducible background in the high $M_{\text{T}2}(\ell\ell)$ signal regions comes from the $t\bar{t}Z$ process with $Z \rightarrow \nu\nu$. The contribution of this process is estimated using simulated samples. The normalization is measured in a 3ℓ control region, and the modeling of the $M_{\text{T}2}(\ell\ell)$ shape of $t\bar{t}Z$ is validated using $t\bar{t}\gamma$ events. No significant deviation of data over the predicted SM backgrounds is observed in the signal regions. Exclusion limits at 95% CL are set on top squark masses for different simplified SUSY models. Top squark masses up to $m_{\tilde{t}} < 800$ GeV are excluded for the $\tilde{t} \rightarrow t\tilde{\chi}_1^0$ decay model. These limits are extended up to $m_{\tilde{t}} < 1050$ GeV when using a combined result with the all-hadronic and single-leptonic searches. If the top squark decays via an intermediate

chargino $\tilde{t} \rightarrow b\tilde{\chi}_1^\pm \rightarrow bW\tilde{\chi}_1^0$ exclusion limits reach up to $m_{\tilde{t}} < 750$ GeV. Again, the limits are extended up to $m_{\tilde{t}} < 1000$ GeV by the usage of a combined result. The T8bbll $\nu\nu$ model results in a dilepton final state with a branching fraction of 100%. The decay of the top squark involves two intermediate particles, $\tilde{t} \rightarrow b\tilde{\chi}_1^\pm \rightarrow b\nu\tilde{\ell} \rightarrow b\nu\ell\tilde{\chi}_1^0$, and the sensitivity of the analysis is highly dependent on the mass of the slepton. If $m_{\tilde{t}}$ is close to the chargino mass exclusion limits reach up to $m_{\tilde{t}} < 1300$ GeV.

Scalar and pseudoscalar mediators which decay to DM particles with a mass up to 100 GeV and 50 GeV are excluded for $m_{\text{DM}} = 1$ GeV. The constraints on scalar mediators were the tightest ones available at the time of publication. The reinterpretation of the results in terms of the invisible decay of a Higgs boson yields observed limits on the branching fraction to invisible particles of $\mathcal{B}(\text{H} \rightarrow \text{inv.}) < 0.46$.

Improvements for a future analysis of the full Run 2 data set were discussed, including the study of the missing transverse momentum significance \mathcal{S} and the precise measurement of the inclusive and differential $t\bar{t}Z$ cross section, discussed in detail in the following chapter.

Search for anomalous top-Z couplings

SEARCHES FOR PHYSICS BEYOND THE STANDARD MODEL often focus on spectacular signatures from high energetic events, predicted e.g. by supersymmetry or extra dimensions. These searches for deviations from the SM predictions in high energy tails potentially neglect BSM effects that can reveal themselves more subtly. The top quark plays a key role in many BSM models [162–168]. Its interactions, especially those to electroweak gauge bosons, are therefore sensitive probes of the SM. The large set of proton-proton collision data taken in 2016 and 2017 allows for detailed studies of these interactions. The coupling of the top quark to the Z boson is a prime example which best can be studied in processes of top quark-antiquark pair production in association with a Z boson, the $t\bar{t}Z$ process. An example Feynman diagram of this process is shown in Fig. 5.1. In the SM, the top-Z vertex is described by the Lagrangian term

$$\mathcal{L} = e\bar{u}_t \left[\gamma^\mu (C_{1,V} + \gamma_5 C_{1,A}) + \frac{i\sigma^{\mu\nu} p_\nu}{M_Z} (C_{2,V} + i\gamma_5 C_{2,A}) \right] Z_\mu v_{\bar{t}} \quad , \quad (5.1)$$

with the Z boson momentum p_ν . The parameters $C_{1,V}$ and $C_{1,A}$ are the neutral vector and axial-vector couplings that are exactly predicted by electroweak symmetry breaking within the SM as

$$\begin{aligned}
 C_{1,V}^{\text{SM}} &= \frac{I_{3,q}^f - 2Q_f \sin^2 \theta_W}{2 \sin \theta_W \cos \theta_W} = 0.2448(52) \\
 C_{1,A}^{\text{SM}} &= \frac{-I_{3,q}^f}{2 \sin \theta_W \cos \theta_W} = -0.6012(14) \quad ,
 \end{aligned} \quad (5.2)$$

inserting $I_{3,q}^f = 1/2$ and $Q_f = 2/3$ for the top quark. Any deviation of the measured values from these predictions is a direct hint for BSM physics. In the SM, the magnetic and electric dipole moments parametrized by $C_{2,V}$ and $C_{2,A}$ are zero at tree level, and non-zero values only emerge radiatively with numerical values below 10^{-3} [162, 169, 170]. Hence, measurements of the dipole moments are very sensitive to physics beyond the SM. Deviations of the vector and axial-vector current couplings as well as electroweak dipole couplings from the predicted SM

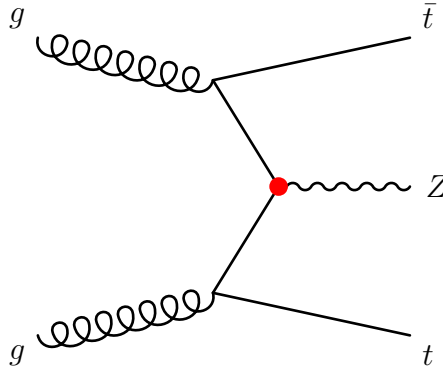


Figure 5.1: Z boson production in association with a top quark/antiquark pair. The red dot indicates the potentially modified vertex of the top quark to the Z boson.

values modify the overall cross section of the $t\bar{t}Z$ process, which is proportional to

$$\sigma(t\bar{t}Z)^{\text{BSM}} \propto (C_{1,V}^{\text{SM}} + \Delta C_{1,V})^2 + (C_{1,A}^{\text{SM}} + \Delta C_{1,A})^2 + C_{2,V}^2 + C_{2,A}^2 \quad . \quad (5.3)$$

However, not only the inclusive cross section is altered, but also the kinematic spectra of the $t\bar{t}Z$ decay products. Therefore, differential cross section data from this process can be used to separate BSM from the SM.

Past results on inclusive cross sections of the $t\bar{t}Z$ process at 8 and 13 TeV from the ATLAS and CMS collaborations were statistically limited because of the high production thresholds and either did not consider BSM hypotheses at all [171, 172], or only used inclusive cross section measurements, resulting in feeble limits [173, 174]. Differential cross section measurements of the $t\bar{t}Z$ process have not been attempted so far.

Final states of the $t\bar{t}Z$ process contain up to four charged leptons. Backgrounds from QCD multijet production, single vector boson production, usually referred to as W +jets and DY processes, as well as top quark pair production ($t\bar{t}$) dominate over $t\bar{t}Z$ in final states with up to two charged leptons. Requiring one pair of light same flavor opposite charge leptons with an invariant mass close to the Z boson mass, up to two additional charged leptons and at least one jet originating from b quarks results in a very pure sample of $t\bar{t}Z$ events. In leptonic final states, the Z boson can be reconstructed with high resolution, hence, its properties are the main probe for BSM effects. Modifications of the top quark momentum and angular distributions are small and easily washed out by experimental resolutions and reconstruction ambiguities. The transverse momentum spectrum of the Z boson, $p_T(Z)$, is highly dependent on the coupling values and can be used to set constraints on BSM effects. Additionally, the polarization of Z boson is sensitive to new physics and carries additional information about the nature of the top-Z couplings. The polarization can be parametrized by $\cos\theta^*$, which is

defined as the polar angle of the negatively charged lepton in the rest frame of the lepton pair that forms the Z boson candidate, w.r.t the Z boson candidate direction in the lab frame.

5.1 Data sets and simulation

The analysis is carried out on proton-proton collision data sets at a center-of-mass energy of $\sqrt{s} = 13$ TeV, recorded by the CMS experiment in 2016 and 2017, corresponding to an integrated luminosity of $L = 77.5 \text{ fb}^{-1}$. A combination of the single electron and muon, double electron and muon and electron/muon PDs is used for the analysis.

Simulated events for SM backgrounds and BSM signals are generated using Monte Carlo event generators. The $t\bar{t}Z$ process is simulated at next-to-leading-order (NLO) accuracy in QCD with the MADGRAPH5_aMC@NLO generator [94], and normalized to a cross section of $0.839 \pm 0.101 \text{ pb}$ [139], calculated at the same perturbative order using the PDF4LHC15 recommendation. The generators used for the different background processes are given in Tab. 5.1. The PYTHIA 8.2 program is used for parton showering and hadronization, using the CUETP8M1 [100] and CP5 [101] tunes for simulated samples of 2016 and 2017 data, respectively. Details on the jet matching between the ME calculation and the PS code are described in Sec. 4.1.

Table 5.1: Event generators used to simulate events for the various processes. The version of the used NNPDF set for the hard process is shown for samples corresponding to 2016 (2017) data sets.

Process	Cross-section calculation	Event generator	Perturbative order	NNPDF version
$t\bar{t}Z, tZq, WZ$ $t\bar{t}\gamma^{(*)}, W\gamma^{(*)}, Z\gamma^{(*)}$ Drell-Yan, triboson	NLO	MADGRAPH5_aMC@NLO	NLO	3.0 NLO (3.1 NNLO)
$gg \rightarrow ZZ$	NLO [175]	MCFM v7.0.1 [176], JHUGEN [177]	LO	3.0 LO (3.1 LO)
$q\bar{q} \rightarrow ZZ$	NNLO [178]	POWHEG v2 [179,180]	NLO	3.0 NLO (3.1 NNLO)
WH, ZH	NLO	POWHEG v2 MINLO HVJ [181], JHUGEN	NLO	3.0 NLO (3.1 NNLO)
WW, VBF H	NLO	POWHEG v2	NLO	3.0 NLO (3.1 NNLO)
$t\bar{t}H$	NLO	POWHEG v2 [124]	NLO	3.0 NLO (3.1 NNLO)
$t\bar{t}$	NNLO+NNLL [126]	POWHEG v2	NLO	3.0 NLO (3.1 NNLO)
$t\bar{t}VV, tHW, tHq, tWZ$	LO	MADGRAPH5_aMC@NLO	LO	3.0 LO (3.1 NNLO)

5.2 Event triggers

A combination of triggers requiring one, two and three leptons are used to achieve optimal selection efficiency. Triggers requiring one electron or muon have a transverse momentum threshold of 24 (27) GeV for muons and 27 (32) GeV for electrons in the 2016 (2017) data sets.

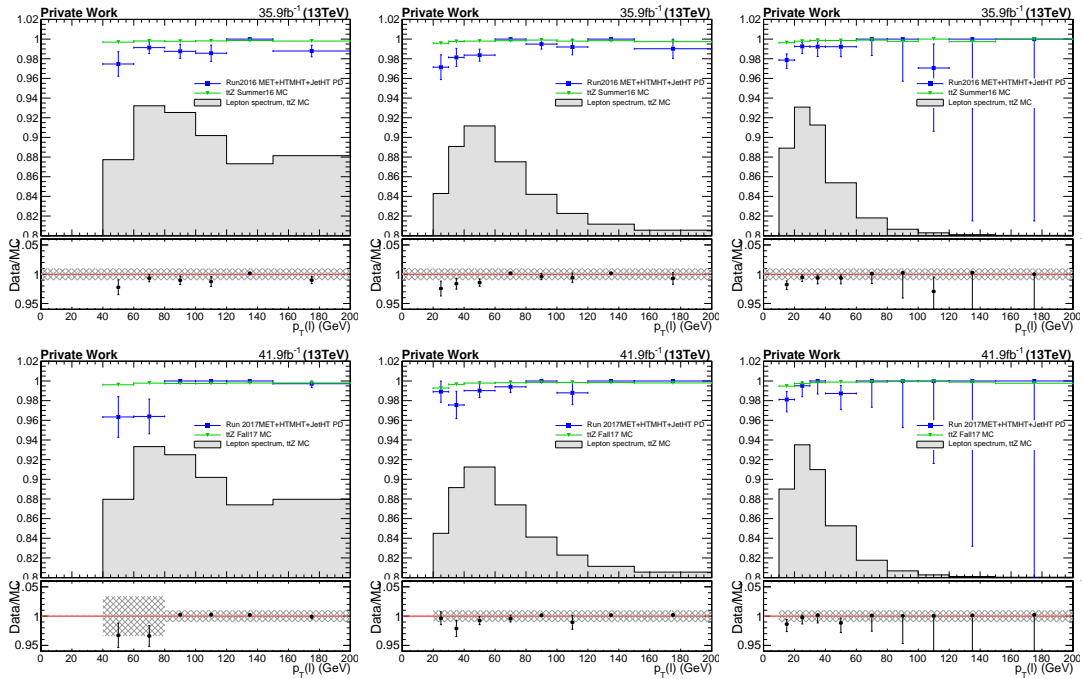


Figure 5.2: Efficiencies of the logic OR of triggers requiring one, two or three leptons in events with three leptons passing the analysis requirements, w.r.t. the transverse momentum of the leading (left), sub-leading (center) and trailing lepton (right), for the 2016 (upper) and 2017 (lower) data set. The expected lepton spectrum for $t\bar{t}Z$ events from simulated samples is shown as filled histograms. Good agreement between efficiencies measured in data and simulated samples is observed, as shown in the lower panel. The hashed band reflects the assigned systematic uncertainty.

For dilepton triggers, the thresholds for the leading lepton are reduced down to 17 GeV for muons and 23 GeV for electrons, varying slightly for the different combinations of electrons and muons and the two data taking periods. The threshold for the sub-leading lepton is around 8 GeV for muons, and between 8 to 12 GeV for electrons. Tripleton triggers further reduce the momentum requirement on the leading lepton, reaching down to 10 GeV for muons and 16 GeV for electrons. Selection efficiencies of the logical OR of the triggers are measured in events selected with independent triggers requiring jets with high momentum, large hadronic activity, or large missing transverse momentum, thus guaranteeing an unbiased measurement. In simulated events, the selection efficiency is measured in a $t\bar{t}Z$ sample. Efficiencies above 98% are measured for a large fraction of the phase space, reducing to 96% for events with a leading lepton p_T below 80 GeV in the 2017 data set. Good agreement of the selection efficiencies measured in data and simulated events is observed, with small deviations for events with relatively low transverse momentum of the leading lepton, shown in Fig. 5.2. In this case, a scale factor is applied to simulated events as a function of the leading lepton p_T , and the difference from unity is assigned as a systematic uncertainty. A flat uncertainty of 2% is applied to all other events.

5.3 Object and event selection

The main objects in this analysis are jets, electrons and muons. Particles are reconstructed and identified using the particle-flow (PF) algorithm [82]. The anti- k_t algorithm [85, 86] is used to cluster jets from PF candidates, using a distance parameter of $R=0.4$. A technique to subtract charged hadrons from vertices other than the PV, called charged hadron subtraction, is used [182]. Jets are calibrated to the average particle level response, and to account for residual differences of the jet energy in data and simulation. Jets with $p_T > 30$ GeV and $|\eta| < 2.4$ are selected in this analysis. The DeepCSV algorithm [134] is used to identify jets originating from b quarks which achieves an efficiency of about 70% over a wide p_T range. The rate of tagged jets that originate from charm quarks is 12%, while about 1% stem from jets from light quarks (up, down or strange) and gluon jets.

Only events with at least three light leptons, electrons or muons, are selected in the following analysis. Gradient boosted decision trees (BDTs) are used to discriminate between prompt leptons from weak boson decays and those either coming from heavy flavor hadron decays, unidentified electron conversions, long-lived light meson decays or misidentified jets, called nonprompt leptons. This “leptonMVA” discriminator is based on inputs of kinematic properties of the leptons (p_T , η), the impact parameter in the transverse plane of the lepton tracks with respect to the PV, the shower shape in the ECAL for electrons, the quality of the matching of the track from the tracking system with signals in the muon system, and lepton isolation variables. The ratio of the p_T of the lepton to the closest jet to the lepton within $\Delta R < 0.4$, p_T^{ratio} , as well as the DeepCSV score of the closest jet are also used as inputs to the BDTs. The training and evaluation of the classifier is done with the TMVA toolkit [183]. The performance is cross-checked with an alternative multivariate analysis using fully connected feed-forward neural networks trained with KERAS [184] using a TENSORFLOW [185] back end, and similar performance is found. The baseline selection on top of which the “leptonMVA” identification is applied is shown in the first column of Tab. 5.2 and 5.3 for electrons and muons, respectively. Loose isolation using a cone with p_T dependent size around the lepton (I_{mini}) is required, where pileup effects are mitigated using an effective area approach. Minimum quality requirements are placed on the distance from the PV (d_{xy} and d_z). The significance of the 3D impact parameter to the event vertex (SIP_{3D}) is required to be below 8.

For electrons a multivariate discriminant based on shower-shape, track cluster matching and track quality variables is used for a baseline selection. The shape of the discriminator is additionally used as input to the “leptonMVA” BDTs.

For muons two standard identification types are used as baseline [87]. Loose muons are defined as muons that are selected by the PF algorithm that are also either a tracker or global muon. The medium muon ID is tuned towards an overall efficiency of 99.5% for muons from simulated W or Z boson decays. Several additional requirements on top of the loose muon ID, mainly on

Table 5.2: Electron selection criteria for different working points for data taken in 2016 (2017). The fakeable object (FO) definition is used in the estimation of the nonprompt lepton background.

	loose	FO	4l tight	3l tight
p_T	≥ 7 GeV	≥ 10 GeV		
$ \eta $	< 2.5			
I_{mini}	< 0.4			
$ d_{xy} $	< 0.05			
$ d_z $	< 0.1			
SIP _{3D}	< 8			
missing hits	≤ 1			
p_T^{ratio}	-	> 0.4	-	-
electron MVA ($ \eta < 1.479$)	-	$\geq -0.1(-0.3)$	-	-
electron MVA ($ \eta \geq 1.479$)	-	$\geq 0.8(0.6)$	-	-
closest jet DeepCSV	-	$\leq 0.4(0.5)$	$\leq 0.8958(0.8001)$	$\leq 0.8958(0.8001)$
leptonMVA	-	< 0.4	≥ -0.4	≥ 0.4

Table 5.3: Muon selection criteria. Numbers that differ in 2017 from 2016 are given in parenthesis.

	loose	FO	4l tight	3l tight
p_T	≥ 5 GeV	≥ 10 GeV		
$ \eta $	< 2.4			
I_{mini}	< 0.4			
$ d_{xy} $	< 0.05			
$ d_z $	< 0.1			
SIP _{3D}	< 8			
is loose Muon	✓			
is medium Muon	-	✓		
p_T^{ratio}	-	> 0.4	-	-
closest jet DeepCSV	-	$\leq 0.4(0.5)$	$\leq 0.8958(0.8001)$	$\leq 0.8958(0.8001)$
leptonMVA	-	< 0.4	≥ -0.4	≥ 0.4

the muon segment compatibility and the track quality, are applied to target prompt muons and those from heavy flavor decays.

The rate of events containing nonprompt leptons is larger in final states with three leptons compared to those with four leptons. Therefore, different working points for lepton identification are used, denoted as “4l tight” and “3l tight” in Tab. 5.2 and 5.3. The additional fakeable object (FO) working point is used for the estimation of the nonprompt background component described in Section 5.4. The selection efficiencies are measured in data and simulation using a “tag-and-probe” method [88, 133] in bins of lepton p_T and η . Efficiencies are larger than 95% for both the “3l tight” and “4l tight” working points for leptons with $p_T > 25$ GeV, and above 60% and 80% for the “3l tight” and “4l tight” working points, respectively, for $p_T < 25$ GeV. In order to be well above the transverse momentum thresholds of the triggers the leading lepton

is required have a p_T above 40 GeV. In the case of presence of three (four) leptons fulfilling the respective ID criteria the sub-leading lepton is required to be above $p_T > 20$ (10) GeV, and all remaining leptons are required to surpass $p_T > 10$ GeV. A sample enriched in $t\bar{t}Z$ events is selected by requiring exactly three or four leptons passing the respective ID criteria. Exactly one pair of opposite charge same flavor leptons is required with a mass close to the Z boson mass, $|m_{\ell\ell} - m_Z| < 10$ (20) GeV for the three (four) lepton case. A second lepton pair fulfilling the criteria is vetoed to reject backgrounds with more than one Z boson. At least one jet passing loose ID criteria with $p_T > 30$ GeV and $|\eta| < 2.4$ has to be present in selected events. This requirement is tightened further to at least three jets for events with three leptons. At least one of the selected jets has to be tagged as b quark jet. Finally, dedicated filters are used to remove events containing excessive detector noise, spurious particles reconstructed with low accuracy, and deposits from beam halo particles [10].

5.4 Backgrounds

Several processes form backgrounds to the $t\bar{t}Z$ signal. Events from processes with dilepton final states and high rates, like $t\bar{t}$ and DY, that additionally contain nonprompt leptons, are reducible with tight lepton identification requirements. In order to also have a reasonable efficiency for prompt leptons, the nonprompt lepton contribution cannot be arbitrarily suppressed. Other backgrounds involve production of pairs of vector bosons, giving rise to three or four leptons in the final state. Single top quark or top quark pair production in association with one or more vector bosons form the leading background in several signal enriched regions due to the similar final states.

Nonprompt lepton background

In previous analyses [173, 174], events containing nonprompt leptons from heavy flavor hadron decays, long-lived light mesons or unidentified photon conversions represented the leading background in the three lepton final state. The background mainly consists of processes with large production cross section, e.g. DY and $t\bar{t}$ production, and one additional nonprompt lepton. The improved lepton identification algorithm with a higher suppression of nonprompt leptons reduces this category to a subdominant background contribution. Nonetheless, the rate of such events is estimated from data control samples using the “tight-to-loose” ratio method, introduced in [186, 187] and improved in [188]. The probability of nonprompt leptons passing loose selection criteria to also pass the tight selection, f_{TL} , is measured in data in a multijet control sample as a function of the lepton transverse momentum. This ratio is then used in a data sample called application region (AR) containing N_{AR} events. At least three loose leptons, with not more than two of them also passing the tight identification criteria, are

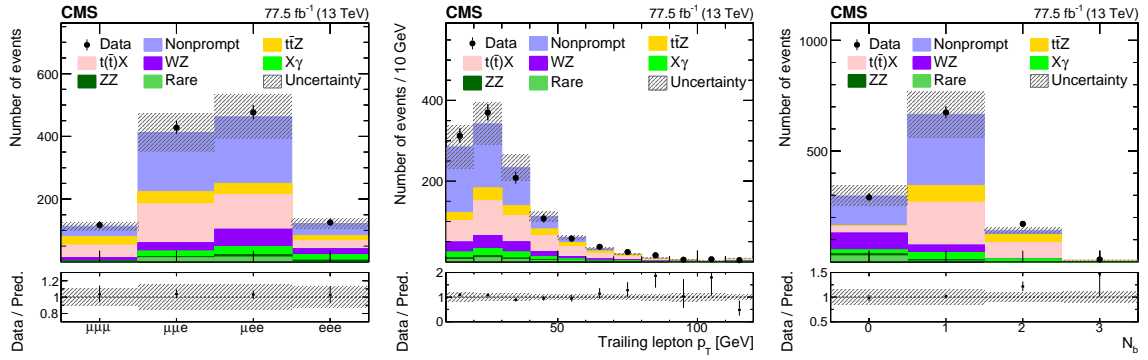


Figure 5.3: Distributions of the predicted and observed yields in regions enriched with nonprompt lepton backgrounds in $t\bar{t}$ -like final states as a function of the lepton flavors (left), the transverse momentum of the lowest- p_T lepton (center), and b-tagged jet multiplicity (right) [9]. The shaded band represents the total uncertainty in the prediction.

required for selection, with otherwise similar selection criteria as the signal enriched regions. Tight leptons are combined with loose but not tight (LnT) leptons to form combinations of three. Each event of the AR contributes to the total estimate of nonprompt leptons in the signal enriched regions as

$$w_{\text{NP}} = \sum_{\text{combinations}} \left(\prod_{N_{\text{LnT}}} \frac{f_{\text{TL}}}{1 - f_{\text{TL}}} (-1)^{N_{\text{LnT}}+1} \right), \quad (5.4)$$

where the sign term is needed in order to avoid double counting. The estimated number of events containing nonprompt leptons in the signal regions N_{NP} is calculated as

$$N_{\text{NP}} = \sum_{N_{\text{AR}}} w_{\text{NP}}. \quad (5.5)$$

The prediction is validated in control samples enriched in DY and $t\bar{t}$ events, a $t\bar{t}$ enriched region is shown in Fig. 5.3. A 30% systematic uncertainty is assigned to the prediction to account for residual differences between the estimate and observation in the most relevant kinematic distributions. Additionally, statistical uncertainties in the prediction from the application region amount to up to 50%, depending on the signal region.

WZ and ZZ production

The WZ and ZZ process form a significant part of the background in the three and four lepton final state. The normalization of these processes is measured in control regions with lower jet multiplicity and no b quark jets. In order to get a very pure sample of ZZ events, a second same flavor opposite charge lepton pair is required in the four lepton final state. The detailed selection criteria for the control regions are shown in Tab. 5.4. These regions are included

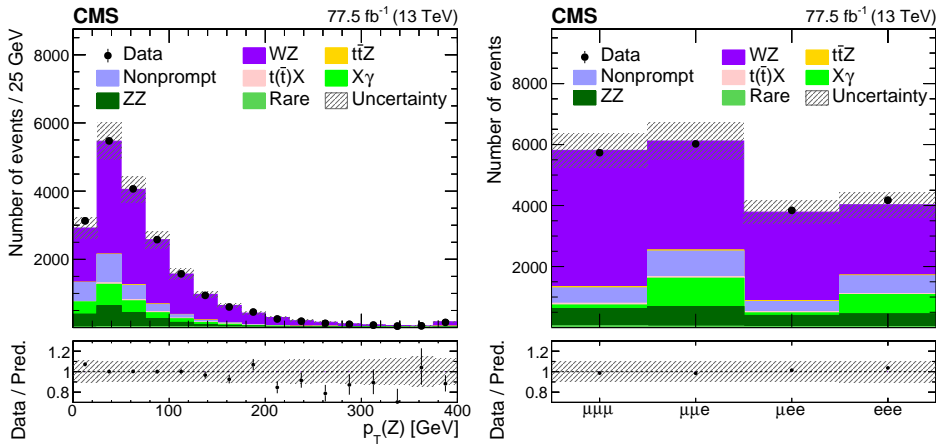


Figure 5.4: Distributions of the predicted and observed yields versus lepton flavor (left) and the reconstructed transverse momentum of the dilepton system (right) in a WZ enriched control region [9]. The shaded band represents the total uncertainty in the prediction.

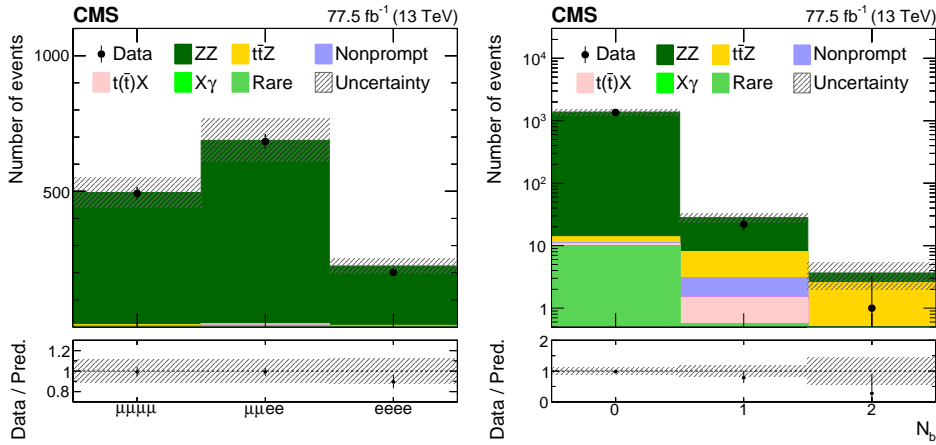


Figure 5.5: Distributions of the predicted and observed yields versus lepton flavor (left) and b-tagged jet multiplicity (right) in a ZZ enriched control region [9]. The shaded band represents the total uncertainty in the prediction.

in the signal extraction fit, providing a precise measurement of the normalization where all correlations of nuisances are automatically taken into account. Relevant distributions in the WZ and ZZ control regions are shown in Fig. 5.4 and Fig. 5.5, respectively.

WZ + heavy flavor

WZ diboson production in association with heavy flavor jets is the largest irreducible single background process to $t\bar{t}Z$ production in the three lepton final state. Generator truth information is used to measure the composition of those events. Figure 5.6 shows that mistagging of light flavor and gluon jets is the origin of the majority of WZ events with at least one b-tagged jet. The rate of these events is dependent on the precise knowledge of the b-tagging efficiency

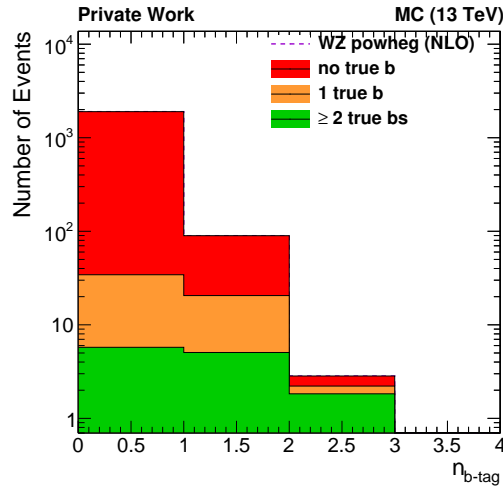


Figure 5.6: Composition of WZ events, binned in number of b-tagged jets. The majority of events with at least one b-tagged jets arises from events without true b jets due to jet mistagging (red). A smaller fraction of events also contains true b jets (orange and green).

and mistag rate, and deviations are covered by the assigned systematic uncertainties.

At tree level, WZ events with true b jets can only emerge from radiated gluons that produce a bottom quark-antiquark pair, commonly called gluon splitting. Previous measurements of the gluon splitting rate in Drell-Yan events at 7 TeV showed a 50% underestimation in simulated events with respect to data [135]. The modelling of gluon splitting can be checked in events with two same flavor opposite charge leptons with an invariant mass within 5 GeV of the Z boson mass, and two b-tagged jets. This selection results in a relatively pure sample of Drell-Yan events with additional heavy flavor jets. Contributions from top quark pair production and di- and multiboson production are suppressed by either the tight invariant mass requirement or the b-tag requirement. Figure 5.7 shows the dominant diagrams leading to final states with a Z boson and b quarks.

Generator information is used in order to distinguish processes involving b-tagged jets from gluon splitting from others. In events where b quarks originate from gluon splitting, the Z boson comes from a vertex with light quarks, illustrated in the top left diagram in Fig. 5.7. If the Z boson originates from b quarks, no gluon splitting is expected, corresponding to bottom left diagram in Fig. 5.7. For the remaining diagrams of Fig. 5.7, the pruned generator history stored in the CMS event data model doesn't allow for a clear distinction. Figure 5.8 shows distributions of ΔR and $\Delta\phi$ between the two selected b-tagged jets. Events with b quarks from gluon splitting populate regions with small separation between the b-tagged jets. Potential mismodelling of the gluon splitting rate in simulation would therefore be visible as discrepancies of observed data and simulation in low ΔR and $\Delta\phi$ regions of Fig. 5.8. Good agreement between prediction and data is observed, indicating good description of gluon splitting processes in simulation.

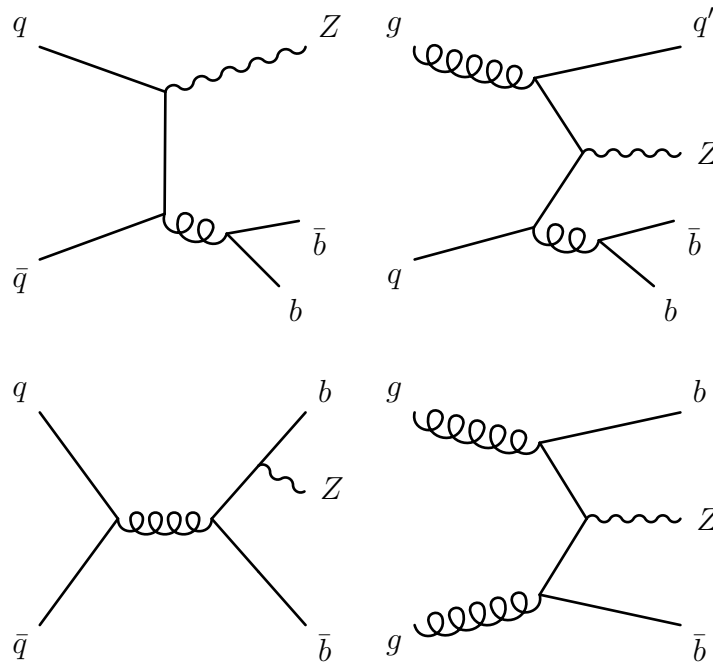


Figure 5.7: Diagrams of Z boson production in association with two b quarks. Diagrams in the top row show processes containing gluon splitting.

Top quark backgrounds: $t\bar{t}X$, $tX/\bar{t}X$ and $t\bar{t}\bar{t}$

Processes with at least one top quark and additional vector bosons, e.g. tZq , $t\bar{t}W$ and tWZ , or four top quark production $t\bar{t}\bar{t}$, are important backgrounds in the signal regions. They are estimated using simulated samples generated with highest available precision in QCD [94, 189, 190]. Theoretical or experimental uncertainties on the cross sections are between 11-15%, and are assigned along the common experimental uncertainties. The uncertainty in the normalization of the tZq process is 15% according to the precision of the recently measured inclusive cross section [191].

Photon conversions and rare backgrounds

Processes with a vector boson or top quarks and a photon, like $Z\gamma$, $t\gamma$ and $t\bar{t}\gamma$, are collectively denoted by $X\gamma$ and are estimated using simulated samples, with an uncertainty in the normalization of 20% [192, 193]. Similarly, rare processes like the production of three vector bosons are directly estimated using simulated samples, and 50% uncertainty is assigned to the normalization [194]. In both cases scale factors are applied to the prediction to correct for small differences between simulation and data. Experimental uncertainties assigned to these scale factors as well as the statistical uncertainties of the simulated samples are taken into

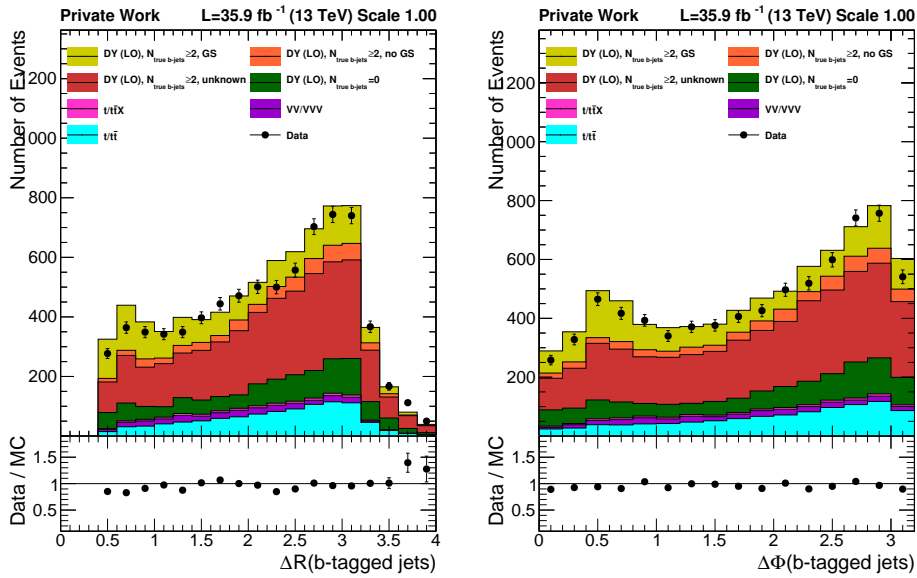


Figure 5.8: Distributions of ΔR (left) and $\Delta\phi$ (right) for events with two same flavor (electron or muon) opposite charge leptons with invariant mass within 5 GeV of the Z boson mass, and two b-tagged jets. Events with and without b quarks from gluon splitting are shown in yellow and orange, respectively. Events where no categorization is possible due to the pruned generator history are shown in red, while events without true b jets are shown in green. Top quark pair production and di- and multiboson production are shown in light blue and purple.

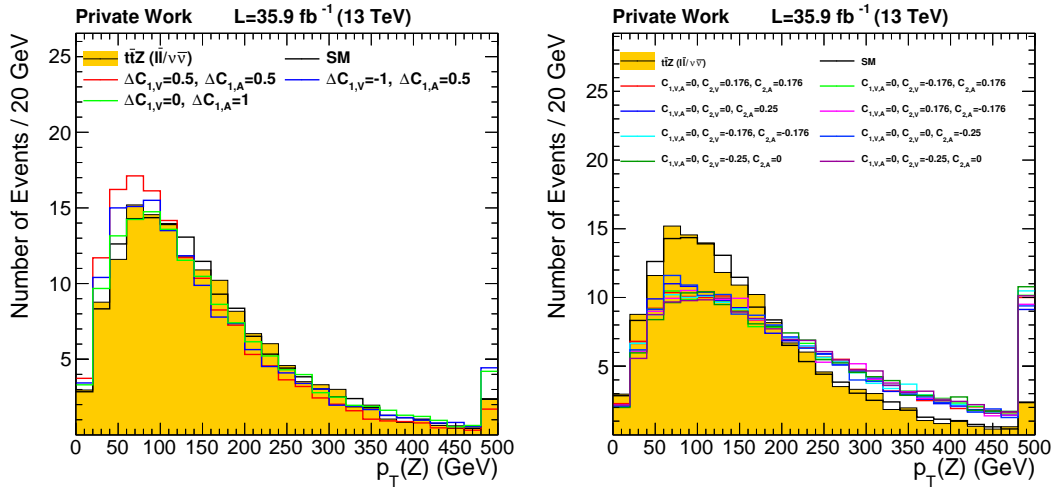


Figure 5.9: Distributions of Z boson transverse momenta. The filled histogram shows the spectrum of the $t\bar{t}Z$ process as predicted by the SM sample, simulated at NLO in perturbative QCD. As comparison, the LO simulation of SM $t\bar{t}Z$ is shown as solid black line and shows agreement over the full $p_T(Z)$ range. Colored lines represent different BSM predictions. Mild modifications of the $p_T(Z)$ spectrum are observed for modifications of the vector and axial-vector couplings, $C_{1,V}$ and $C_{1,A}$ (left). Dipole interactions have a larger impact on $p_T(Z)$ (right). All predictions are normalized to the SM $t\bar{t}Z$ cross section in order to only show the shape differences.

account.

5.5 Observables and signal regions

Guided by literature reviews [195, 196], the highly discriminating nature of $p_T(Z)$ between the SM $t\bar{t}Z$ process and potential BSM modifications is confirmed in Fig. 5.9. Equation 5.1 shows a direct energy dependence in the dipole term, hence a larger modification of the $p_T(Z)$ spectrum is expected for non-zero values of $C_{2,V}$ and $C_{2,A}$ compared to modifications of $C_{1,V}$ and $C_{1,A}$. The azimuthal opening angle of the leptons from the Z boson decay $\Delta\phi(\ell\ell)$ is also sensitive to the BSM effects, however, it is found to be correlated with $p_T(Z)$. This modification can be seen as a change of the Z boson polarization, which can be decorrelated from $p_T(Z)$ on an event-by-event basis by boosting into the Z boson rest frame

$$\gamma = \sqrt{1 + \left(\frac{p_{T,\ell\ell}}{m_{\ell\ell}}\right)^2 \cosh^2 \eta_{\ell\ell}} \quad , \quad (5.6)$$

with $p_{T,\ell\ell}$, $m_{\ell\ell}$ and $\eta_{\ell\ell}$ all in the lab frame. One can then define $\theta_{\ell-Z}$ as the polar angle between the negative charged lepton and the Z boson in the lab frame. For the Z boson rest

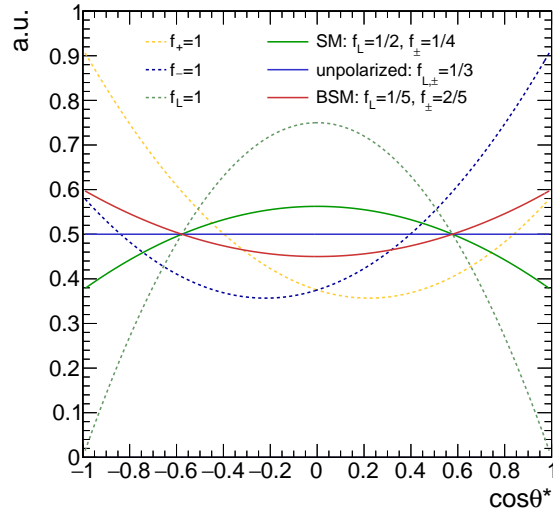


Figure 5.10: Helicity fractions of Z bosons decaying to a pair of leptons in the $t\bar{t}Z$ process. The $\cos\theta^*$ distribution is flat for an unpolarized Z boson (solid blue line). In the SM $t\bar{t}Z$ process, $f_L = 1/2$ and $f_{\pm} = 1/4$ (solid green line), while fractions are modified for BSM interactions, e.g. $f_L = 1/5$ and $f_{\pm} = 2/5$ for $C_{2,A} = 0.25$ (solid red line). $\cos\theta^*$ distributions for totally longitudinal, plus and minus polarized Z bosons are shown as green, blue and yellow dotted lines.

frame one gets

$$\cos\theta^* = \frac{-\beta + \cos\theta_{\ell-Z}}{1 - \beta \cos\theta_{\ell-Z}}, \quad (5.7)$$

with $\beta = \sqrt{1 - 1/\gamma^2}$. $\cos\theta^*$ is independent of the boost of the Z boson by construction. The normalized differential cross section of Z bosons decaying to two leptons can be expressed in terms of helicity fractions

$$\frac{1}{\Gamma} \frac{d\Gamma}{d\cos\theta^*} = f_L \frac{3}{4} (1 - \cos^2\theta^*) + \sum_{\pm} f_{\pm} \frac{3}{8} [1 + \cos^2\theta^* \pm \sin\theta_W \cos\theta^*], \quad (5.8)$$

with the condition that $f_L + f_+ + f_- = 1$. In the SM the Z bosons in the $t\bar{t}Z$ process are slightly longitudinally polarized, shown as green solid line in Fig. 5.10. Modified top-Z couplings change the Z boson polarization and e.g. reduce the longitudinal fraction, which is the case for a non-zero electric dipole moment ($C_{2,A} = 0.25$) exhibited in Fig. 5.10. The parametrization of the Z boson polarization in terms of the experimentally accessible observable $\cos\theta^*$ provides a powerful handle to discriminate between the SM $t\bar{t}Z$ process and potential modifications. Distributions of $\cos\theta^*$ for several BSM points are shown in Fig. 5.11. In these examples, Z bosons have a larger fraction of f_{\pm} polarization.

In the three lepton final state the leptonic W boson can be reconstructed from the missing transverse momentum and the lepton that is not associated with the Z boson decay. From this starting point, other observables that include and combine the lepton from the W boson decay,

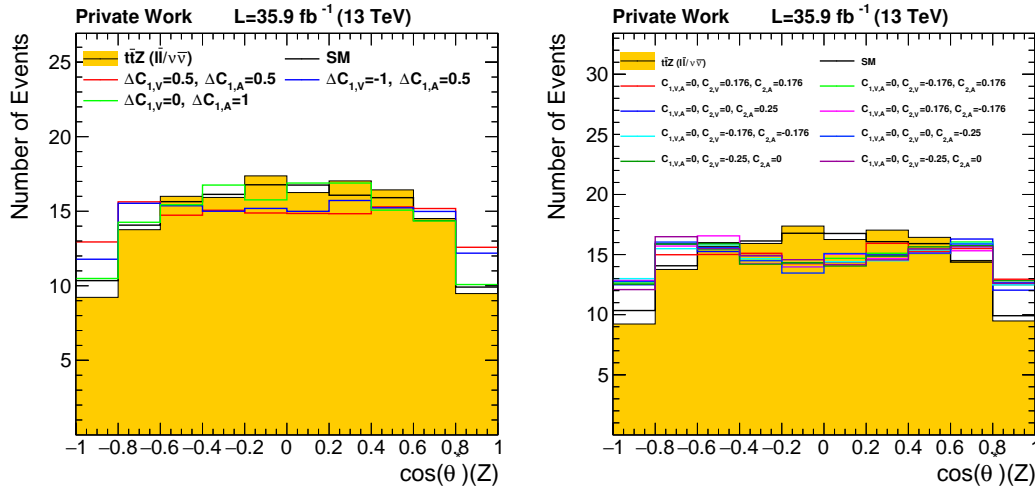


Figure 5.11: Distributions of $\cos\theta^*$ for modified vector and axial-vector couplings (left) and dipole couplings (right). Similar to Fig. 5.9 the SM $t\bar{t}Z$ distribution simulated at NLO is given as filled histogram and compared to the LO prediction, shown as solid black line. Colored lines represent different BSM configurations.

b-tagged jets and missing transverse momentum, were systematically constructed and studied. In order to remove the correlation of these constructed observables with $p_T(Z)$, BSM events are reweighted such that the $p_T(Z)$ spectrum resembles the SM spectrum. Good agreement between the BSM and the reweighted SM spectra is observed, indicating that no additional information can be extracted from the constructed observables. Therefore, $p_T(Z)$ and $\cos\theta^*$ are chosen as the main discriminating observables in this analysis.

For highly polarized Z bosons, the trailing lepton of the Z boson decay is likely to be out of the experimental acceptance because of its low transverse momentum. This effect is visible as a dip at high $|\cos\theta^*|$ values, shown in Fig. 5.11. It is checked that this acceptance effect is well understood and properly modelled in simulation in a WZ enriched sample. In order to obtain a WZ enriched sample, events are required to contain at least one jet, while events with b-tagged jets are vetoed. Good agreement between data and simulated samples is observed, shown in Fig. 5.12. As this acceptance effect is amplified for boosted Z bosons the check is repeated for events with $p_T(Z) \geq 200$ GeV. Again, no significant deviation between data and simulation is observed as shown in Fig. 5.13.

Signal regions are defined in terms of $p_T(Z)$ and $\cos\theta^*$ in order to achieve best sensitivity to BSM signals, shown in Tab. 5.4. In final states with four leptons the $\cos\theta^*$ bins are merged due to the lower branching fraction leading to a lower number of expected events. Control regions with the same bin borders in terms of $p_T(Z)$ and $\cos\theta^*$ are defined to constrain the WZ and ZZ background contributions. In order to obtain a pure WZ sample, the requirement for b-tagged jets is inverted and the jet multiplicity requirement relaxed, while for a ZZ sample a second Z boson candidate is required.

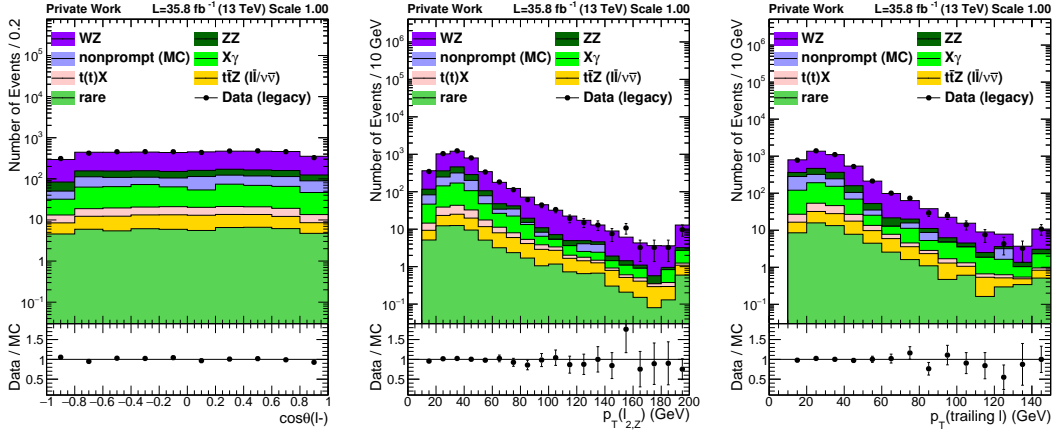


Figure 5.12: Distributions of $\cos\theta^*$ (left) and transverse momenta of the trailing lepton of the same flavor opposite charge lepton pair (center) and overall trailing lepton (right) in a WZ enriched control region. Good agreement between data and simulated samples is observed.

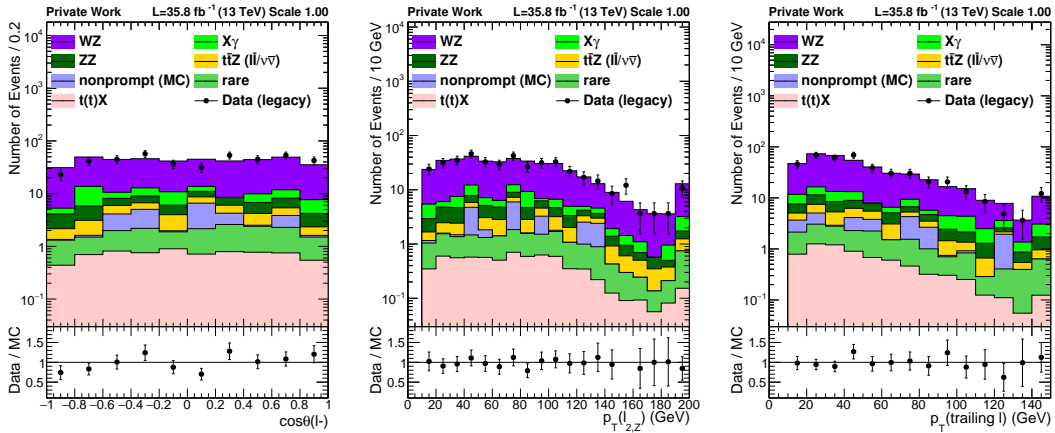


Figure 5.13: Distributions of $\cos\theta^*$ (left) and transverse momenta of the trailing lepton of the same flavor opposite charge lepton pair (center) and overall trailing lepton (right) in a WZ enriched control region with $p_T(Z) \geq 200$ GeV. Good agreement between data and simulated samples is observed.

Table 5.4: Definition of the signal and control regions.

N_ℓ	N_j	N_b	N_Z	$p_T(Z)$ (GeV)	$-1 \leq \cos \theta^* < -0.6$	$-0.6 \leq \cos \theta^* < 0.6$	$0.6 \leq \cos \theta^*$
3	≥ 3	≥ 1	1	0–100	SR1	SR2	SR3
				100–200	SR4	SR5	SR6
				200–400	SR7	SR8	SR9
				≥ 400	SR10	SR11	SR12
4	≥ 1	≥ 1	1	0–100	SR13		
				100–200	SR14		
				≥ 200	SR15		
3	≥ 1	0	1	0–100	CR1	CR2	CR3
				100–200	CR4	CR5	CR6
				200–400	CR7	CR8	CR9
				≥ 400	CR10	CR11	CR12
4	≥ 1	≥ 0	2	0–100	CR13		
				100–200	CR14		
				≥ 200	CR15		

Constraints on vector and dipole couplings will be extracted in separate two-dimensional likelihood scans. Additionally, individual likelihood scans are performed where all but one coupling value are kept at their respective SM value. The leading contributions to modifications of the $t\bar{t}Z$ cross section stem from single operator insertions in the Feynman diagrams. The cross section can then be written as

$$\sigma = \sigma_0 + \sum_i (C_i^{\text{SM}} + \Delta C_i) \sigma_i + \sum_{i < j} (C_i^{\text{SM}} + \Delta C_i) (C_j^{\text{SM}} + \Delta C_j) \sigma_{ij} \quad . \quad (5.9)$$

For inclusive cross section measurements this means that if the second term in 5.9 is small and $C^{\text{SM}} \simeq 0$, one-sided circular or elliptical constraints around the origin are expected. This behaviour can be seen in Fig. 5.14 (top left). For the current couplings C^{SM} is comparably large, and therefore annulus regions in configuration space are predicted, leading to donut shaped constraints, which is shown in Fig. 5.15 (top left). Using differential cross section information, some of the ambiguities that are left from inclusive measurements can be resolved. Figures 5.14 and 5.15 show the evolution of constraints from using only inclusive cross section information (top left), to only shape information of $p_T(Z)$ and $\cos \theta^*$ corresponding to the signal regions defined in Tab. 5.4 (top right), to a combination of shape and inclusive cross section information (bottom). For current couplings, the modification of the Z boson polarization and momentum helps to resolve ambiguities left by the inclusive measurement, and the donut-shaped 68% and 95% CL regions are cut into two segments. At first sight, the improvements from using shape information for the dipole couplings are less visible. No disambiguation between $C_{2,A}$ and $C_{2,V}$ is provided by the Z boson polarization and momentum. However, due to the large

modification of the Z boson momentum spectrum by non-zero dipole couplings the shape information provides even tighter constraints than the inclusive cross section information. Therefore, significant improvements of dipole coupling constraints are expected from the differential cross section measurement.

5.6 Signal scans

Samples of the $t\bar{t}Z$ process with anomalous couplings are simulated at LO using the MADGRAPH5_aMC@NLO event generator. A model based on Eq. 5.1 is implemented in FEYNRULES [197] and interfaced to MADGRAPH5_aMC@NLO using the UFO interface [198]. Productions of signal scans with fine granularity of BSM coupling values using the full detector simulation and reconstruction are computationally very expensive. Therefore, an alternative approach is employed to significantly reduce the needed CPU time. Studies about observables that are sensitive to BSM effects in the $t\bar{t}Z$ vertex showed vanishing correlations of $\cos\theta^*$ and $p_T(Z)$ with other observables. Hence, reweighting SM events to BSM configurations according to their simulated truth values of $\cos\theta^*$ and $p_T(Z)$ is expected to provide good predictions of BSM distributions. In order to obtain these weights, simulated events are generated up to the hadronization step, using similar generator configurations as the fully reconstructed SM $t\bar{t}Z$ sample. Two-dimensional weight matrices are extracted for each BSM model point, which are subsequently applied to the SM sample. The weights are calculated before applying any event selection other than requiring a leptonically decaying Z boson. No kinematic requirements are applied in order to omit biases by the dependence of the acceptance on the polarization and $p_T(Z)$. Two examples for reweighting matrices are given in Fig. 5.16, showing the harder $p_T(Z)$ spectrum and higher polarization of the Z boson at the BSM point compared to the reference SM point. The reweighted SM sample is then normalized according to the obtained leading order BSM cross section.

The closure of this method is checked for different BSM benchmark points where a full detector simulation and reconstruction was performed. Good closure is observed in several kinematic distributions, shown in Fig. 5.17, as well as the signal regions. Residual mild discrepancies correlated between the different BSM points are understood as a statistical upwards fluctuation of the reference SM $t\bar{t}Z$ sample.

5.7 Systematic uncertainties

Several experimental and theoretical uncertainties affect the signal and background efficiency. A complete list of systematic uncertainties is given in Tab. 5.5, which shows the range of variations and the correlations between the 2016 and 2017 data sets.

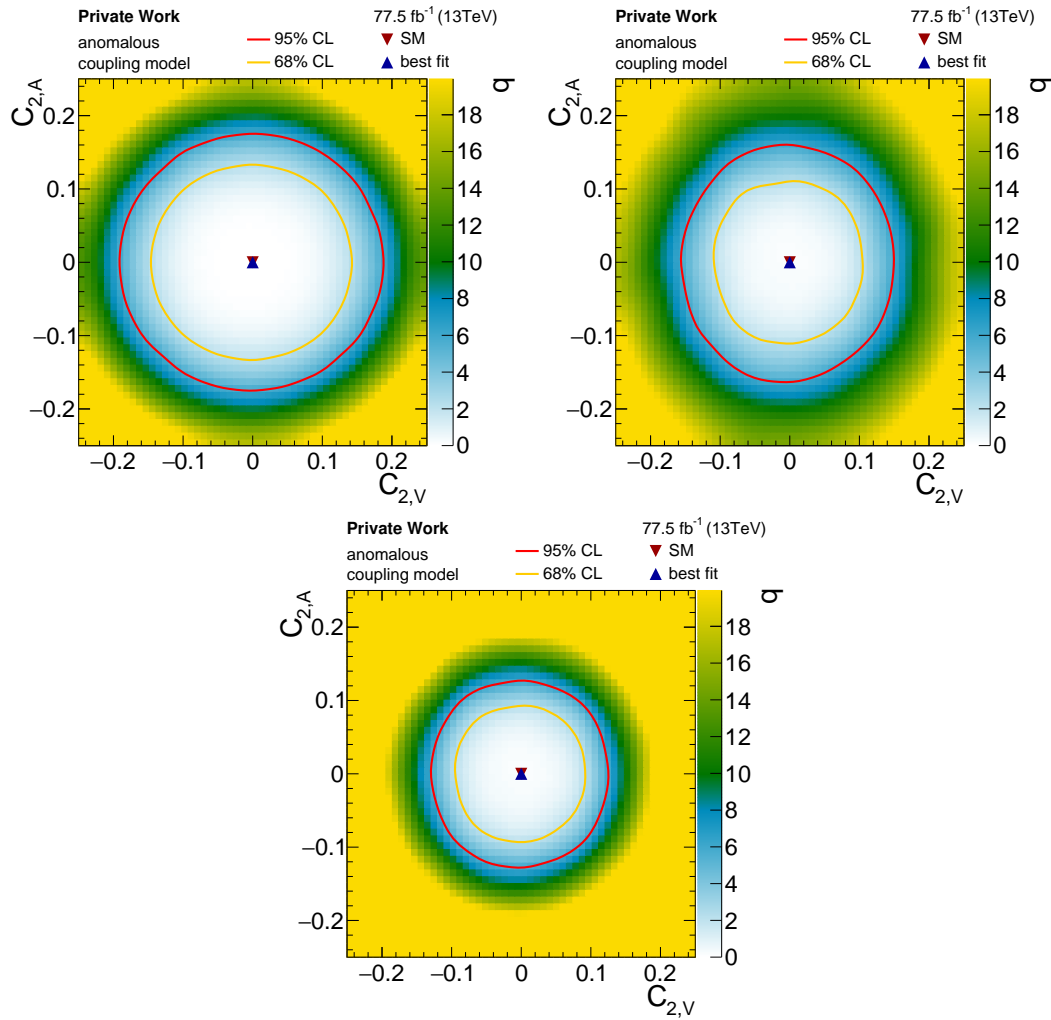


Figure 5.14: Two dimensional log-likelihood scans of top-Z dipole couplings. The color map shows the expected log-likelihood ratio (see Sec. 5.8 for details), with the orange and red line limiting the 68% and 95% CL area. The SM point (red downward triangle) and best fit point (blue upward triangle) coincide for the expected results. Expected constraints using only inclusive cross section information (top left), only shape information (top right) and both combined (bottom). Constraints from shape information are stronger than those extracted from inclusive cross section due to the strong modification of the $p_T(Z)$ spectrum.

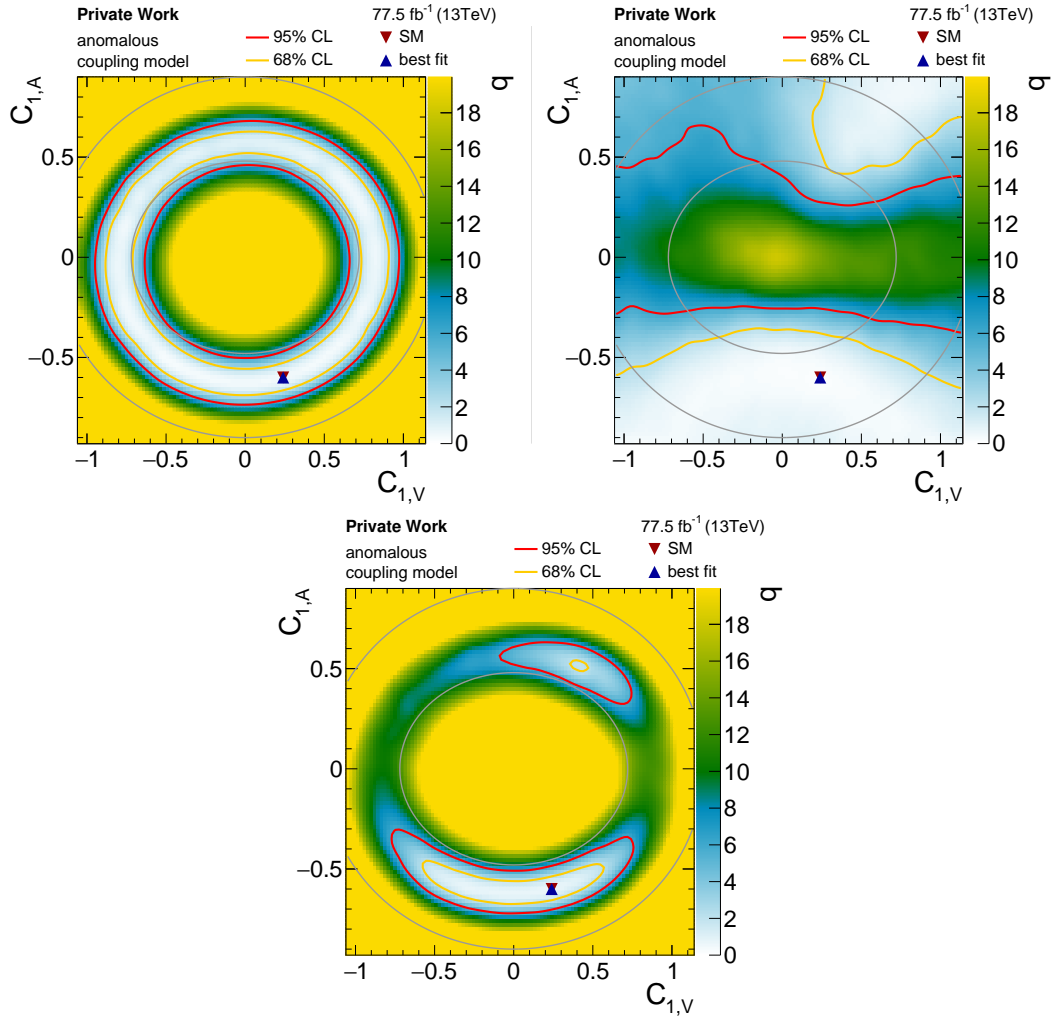


Figure 5.15: Two dimensional log-likelihood scans of top-Z current couplings. The color map shows the expected log-likelihood ratio, with the orange and red line limiting the 68% and 95% CL area. The SM point (red downward triangle) and best fit point (blue upward triangle) coincide for the expected results. Expected constraints using only inclusive cross section information (top left), only shape information (top right) and both combined (bottom). The donut shaped 68% and 95% CL areas are cut into two segments owing to the complementary shape information. The gray lines indicate the 68% CL area obtained in a previous CMS measurement [173].

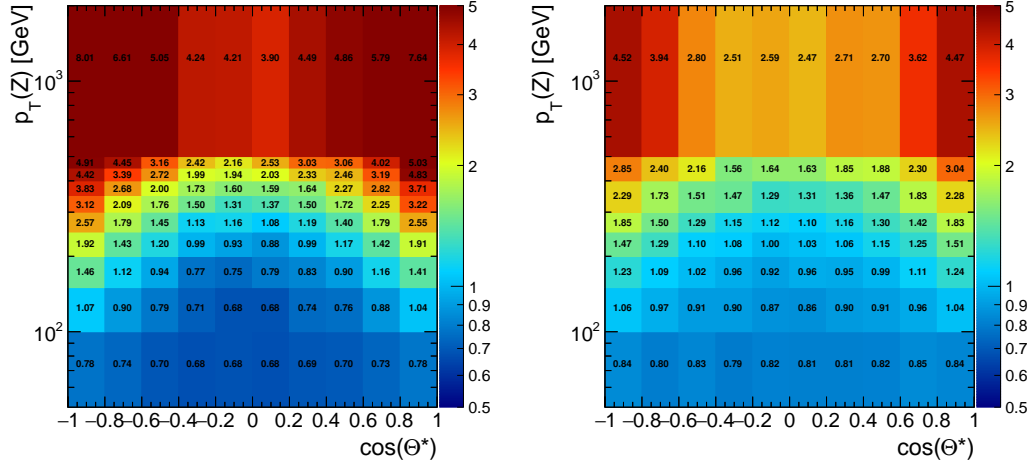


Figure 5.16: Reweighting matrices for two BSM points. Left: Complete cancellation of vector and axial-vector current couplings to zero ($C_{1,A}=0.0$, $C_{1,V}=0.0$), and non-zero magnetic dipole moment ($C_{2,V}=0.25$). Right: SM current couplings ($C_{1,A}=-0.60$, $C_{1,V}=0.24$), and non-zero electromagnetic dipole moments ($C_{2,A}=0.2$, $C_{2,V}=0.2$).

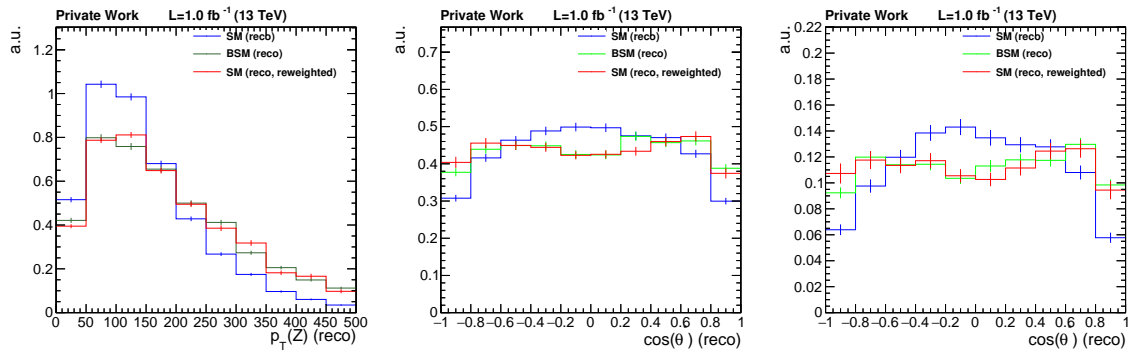


Figure 5.17: Closure tests of the reweighting method for $p_T(Z)$ (left), $\cos\theta^*$ (center) and $\cos\theta^*$ requiring $p_T(Z) > 200$ GeV (right). Blue lines represent distributions predicted by the SM, while green lines show distribution with a certain BSM configuration, both using full detector simulation and reconstruction. Distributions using the reweighted SM sample are shown in red. Good agreement between the BSM sample (green) and the reweighted SM sample (red) is observed.

The integrated luminosity is measured to a precision of 2.5% in 2016 [138] and 2.3% in 2017 [199], and corresponding uncorrelated systematic uncertainties are assigned to the signal as well as background processes that are estimated using simulated samples. Simulated events are reweighted to match the distribution of the expected number of simultaneous interactions at each bunch crossing in data, corresponding to an inelastic pp cross section of 69.2 mb. The cross section is varied up and down by 5% in order to assess the systematic uncertainty of this pileup estimate [137].

The efficiency of the event triggers is found to be in good agreement between data and simulation. An uncertainty of 2% is assigned to cover for residual differences, which is increased to 3.5% for events where the leading lepton has low transverse momentum. Lepton selection efficiencies are measured separately in data and simulation using a “tag-and-probe” method [88, 133]. The measurement is done in bins of p_T and η of the leptons and shows differences between data and simulation of 1–10%, where larger differences are seen for leptons with $p_T < 20$ GeV. Scale factors are used to correct the simulated event yields to match the efficiencies in data, and systematic uncertainties of 4.5–6% are assigned based on detailed studies.

Corrections to the jet energy scale are measured in bins of p_T and η [90]. The uncertainty arising from the jet energy scale is evaluated by varying the scale up and down within its uncertainties. Propagating the resulting shift of the jet energy through the analysis one obtains an uncertainty of 2–5%. Similarly, the uncertainty from the jet energy resolution is evaluated, resulting in values below 1%. The efficiency of the b-tagging algorithm is corrected in simulation to match the measured efficiency in data using scale factors [134, 200]. These scale factors are varied up and down within their uncertainties, separately for correctly tagged and misidentified jets, resulting in an uncertainty of 1–4%.

The chosen values of the renormalization and factorization scales μ_R and μ_F at ME level are varied up and down independently by factors of two with respect to their nominal values. The anticorrelated variation where one scale is varied up and the other one down can be ignored, as was shown in [145, 146]. The envelope of the variations is chosen to assign systematic uncertainties, resulting in values below 4%. In the PS simulation, the uncertainty in the scale choice of initial- and final-state radiation is evaluated by varying the scale up and down by factors of 2 and $\sqrt{2}$, respectively, as recommended in [201]. The resulting uncertainty, again taking the maximum deviation from the nominal prediction, is 1–4%.

The effect of the uncertainty from the choice of the PDF in the ME is evaluated by reweighting the simulated samples to variations of the Hessian PDF4LHC15 combined set with 100 eigenvectors, following the PDF4LHC prescription [139]. The assigned uncertainty is 2–5%. The color reconnection model used in the default PYTHIA 8.2 tunes is a multi-parton-interaction-based (MPI) model with early resonance decays switched off [100, 101, 125]. The impact of different models is checked by using simulated samples with tunes using a MPI model with

early resonance decays switched on, a gluon-move model [202], and a QCD-inspired model [203]. The maximum deviation from the nominal result is used to assign a systematic uncertainty that amounts to 1.5%. No significant impact is found when using up and down variations of the PYTHIA 8.2 tune, corresponding to varied parameters related to MPI and color reconnection.

Table 5.5: Summary of the sources, magnitudes, treatments, and effects of the systematic uncertainties in the final $t\bar{t}Z$ cross section measurement. The first column indicates the source of the uncertainty, the second column shows the corresponding input uncertainty range for each background source and the signal. The third column indicates how correlations are treated between the uncertainties in the 2016 and the 2017 data.

Source	Uncertainty range (%)	Correlated 2016/2017
Integrated luminosity	2.5	×
PU modeling	1–2	✓
Trigger	2	×
Lepton ID efficiency	4.5–6	✓
Jet energy scale	1–9	✓
Jet energy resolution	0–1	✓
B tagging light flavor	0–4	×
B tagging heavy flavor	1–4	×
Choice in μ_R and μ_F	1–4	✓
PDF choice	2–5	✓
Color reconnection	1.5	✓
Parton shower	1–4	✓
WZ cross section	10–20	✓
WZ + heavy flavor	8	✓
ZZ cross section	10	✓
$t\bar{t}X$ bkg	10–15	✓
$X\gamma$ background	20	✓
Nonprompt background	30	✓
Rare SM background	50	✓
Stat. unc. in nonprompt bkg	5–50	×
Stat. unc. in rare SM bkg	5–100	×

Several other potential sources of uncertainties are checked. To this end, $p_T(Z)$ and $\cos\theta^*$ distributions of $t\bar{t}Z$ samples generated at LO and NLO in perturbative QCD are compared. No significant difference between the distributions is observed, and therefore no additional systematic uncertainty is assigned.

The observed p_T spectra of top quarks were found to be significantly softer than predicted by various MC event generators at NLO in QCD [140–142]. The description of the observed

data is improved by predictions using higher order corrections, e.g. NNLO+NNLL [143] and approximate NNLO [144]. Corrections can be applied to simulated samples of $t\bar{t}$ events in terms of reweighting functions in order to achieve better description of the observation. It is of interest to check whether an imperfect description of the p_T spectrum of the top quark would have a significant impact on the measurement of the Z boson p_T spectrum. Therefore, the impact of reweighting the top quark p_T spectrum on $p_T(Z)$ is assessed but found to be negligible.

Data in WZ control regions is very well described by simulation. It is found that the prediction obtained with the POWHEG v2 generator gives the best results, in agreement with the measurements done at 13 TeV by the CMS collaboration [204, 205]. Samples generated with the MADGRAPH5_aMC@NLO generator predict a slightly harder Z boson p_T spectrum which is not observed in data. However, up to two additional partons are included in the ME calculation when using the MADGRAPH5_aMC@NLO generator, resulting in a better description of the jet multiplicity distribution when compared to POWHEG v2. Therefore, samples generated with the MADGRAPH5_aMC@NLO program are used in the analysis. The difference between the two predicted Z boson p_T spectra is applied as systematic uncertainty to the WZ background, where values are below 5% in all signal and control regions.

Systematic uncertainties on the rate of WZ events with additional heavy quarks are assigned based on the study presented in Sec. 5.4. Motivated by the residual disagreement of prediction and observation in gluon splitting enriched regions, the fraction of WZ events with true b-jets is varied up and down by 20%, respectively. This variation translates to a 6–8% uncertainty that is assigned on the transfer factor between the $N_b = 0$ WZ control regions and the signal regions, applied to WZ events.

5.8 Results

The inclusive $t\bar{t}Z$ production cross section is measured in bins of jet and b-tagged jet multiplicity and found to be [9]

$$\sigma(pp \rightarrow t\bar{t}Z) = 0.95 \pm 0.05(\text{stat}) \pm 0.06(\text{syst}) \text{ pb} \quad . \quad (5.10)$$

This measured value is compatible with the theory prediction of $\sigma_{t\bar{t}Z}^{\text{SM}} = 0.839 \pm 0.101 \text{ pb}$ at a 95% CL. For the first time, the precision of the measured cross section value is competing with the theoretical value. Improvements in the trigger strategy as well the lepton identification result in a significant reduction of the systematic uncertainty, leading to the total uncertainty of 8% on the measured $t\bar{t}Z$ cross section. Figure 5.18 shows the predicted and observed yields in the control and signal regions which are defined in Tab. 5.4. Very good agreement between prediction and data is observed in the control regions for the WZ and ZZ processes, yielding

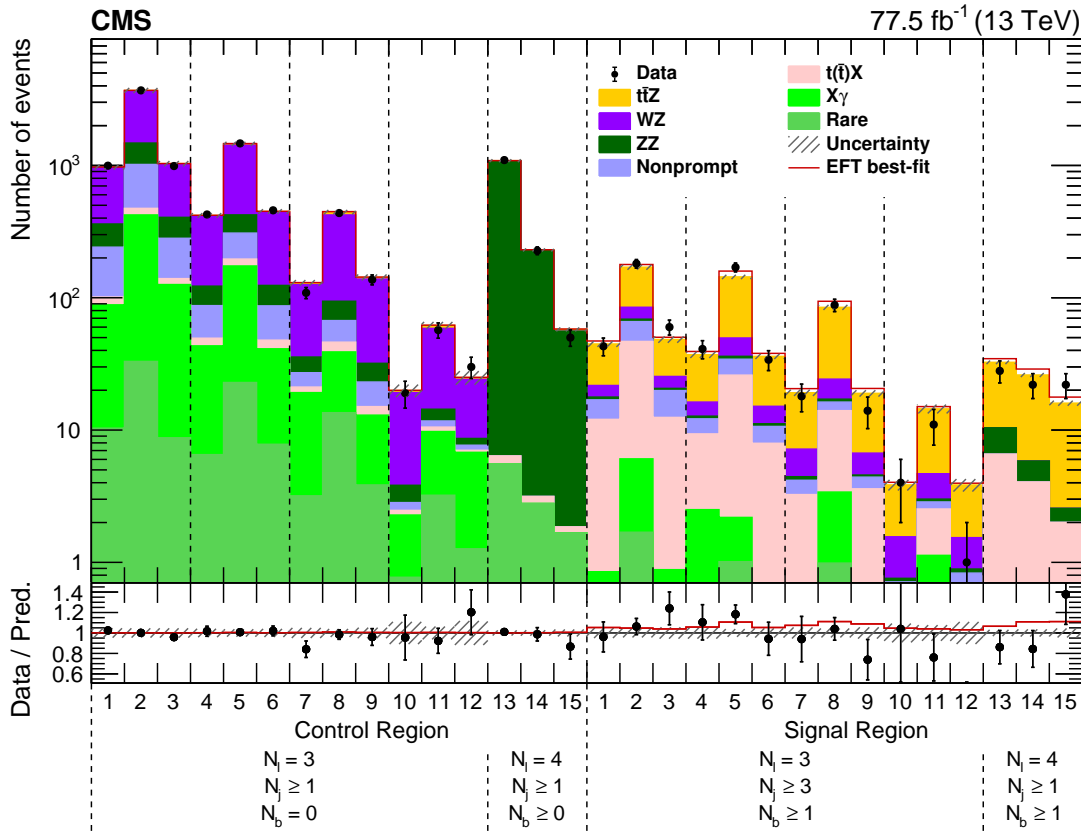


Figure 5.18: Predicted and observed yields in the control and signal regions. Control region 1-12 employ a 3 lepton requirement and are enriched in WZ, while the presence of 4 leptons is required for control regions 13-15 in order to obtain a pure ZZ sample. Good agreement between data and the SM prediction is observed in the control regions. The solid red line corresponds to the prediction of the best fit EFT point ($c_{\varphi Q}^- = -4.0$, $c_{\varphi t} = -2.0$) shown in the right plot of Fig. 5.22.

normalization scale factors compatible with unity. In the signal regions the data seems to favor a larger cross section of $t\bar{t}Z$, compatible with the inclusive cross section measurement. No significant trend in the $p_T(Z)$ spectrum or stronger polarization of the Z boson is observed. Data in the signal regions is best described by a BSM signal point shown as solid red line in Fig. 5.18 and corresponds to a configuration where vector and axial-vector couplings are slightly modified. In this case, no strong modification of the Z boson momentum is expected as discussed in Sec. 5.5.

Anomalous couplings

The results shown in Fig. 5.18 are used to set constraints on anomalous couplings of the top quark. The yields and uncertainties of every control and signal region of Fig. 5.18 are used to construct a binned likelihood function $L(\theta)$ as a product of Poisson probabilities, where θ

represents the set of nuisance parameters. A profiled likelihood fit is performed at each BSM parameter point in order to identify the BSM point with the maximum likelihood $L(\hat{\theta}_{\max})$. Then, a log-likelihood ratio is constructed as

$$q = -2 \log \frac{L(\hat{\theta}, \vec{C})}{L(\hat{\theta}_{\max})} , \quad (5.11)$$

where $\hat{\theta}$ denotes the set of nuisance parameters maximizing the likelihood at a given BSM parameter point defined by the anomalous coupling coefficients \vec{C} . Scans of q for individual anomalous couplings, with all other couplings set to their respective SM values, are shown in Fig. 5.19. 68% and 95% CL intervals are given as colored areas.

Log-likelihood scans of the dipole couplings $C_{2,V}$ and $C_{2,A}$, and the current couplings $C_{1,V}$ and $C_{1,A}$ are shown in Fig. 5.20. The limits on $C_{2,V}$ and $C_{2,A}$ represent the first direct measurement of the top quark electroweak dipole moments. The large improvement of the constraints on anomalous axial-vector and vector current couplings with respect to the previous CMS result [173] can be seen by comparing the 68% CL contours, indicated by the solid and dot-dashed lines in Fig. 5.20 (right).

Effective Field Theories

The observed results are additionally interpreted in terms of SMEFT, focussing on dimension-six operators that give rise to top quark interactions [65]. Degrees of freedom in SMEFT are combinations of Warsaw-basis operators [60, 206, 207]. The $t\bar{t}Z$ process is found to be especially sensitive to a subset of these degrees of freedom. For example, modifications of the Wtb vertex do have an impact on the $t\bar{t}Z$ final state, but are better constrained in single-top measurements [208]. Similarly, anomalous couplings of the top quark to the gluon are tightly constrained in the $t\bar{t}$ final state [142]. The Wilson coefficients that are most relevant for the analysis modify the $t\bar{t}Z$ vertex and are defined as

$$\begin{aligned} c_{tZ} &\equiv \text{Re}[-\sin\theta_W C_{uB} + \cos\theta_W C_{uW}] \\ c_{tZ}^{[I]} &\equiv \text{Im}[-\sin\theta_W C_{uB} + \cos\theta_W C_{uW}] \\ c_{\varphi t} &\equiv C_{\varphi u}^{(33)} \\ c_{\varphi Q}^- &\equiv C_{\varphi q}^{1(33)} - C_{\varphi q}^{3(33)} . \end{aligned} \quad (5.12)$$

The Wilson coefficients c_{tZ} and $c_{tZ}^{[I]}$ introduce electroweak dipole moments, while $c_{\varphi t}$ and $c_{\varphi Q}^-$ induce anomalous vector and axial-vector current couplings. The correspondence between the

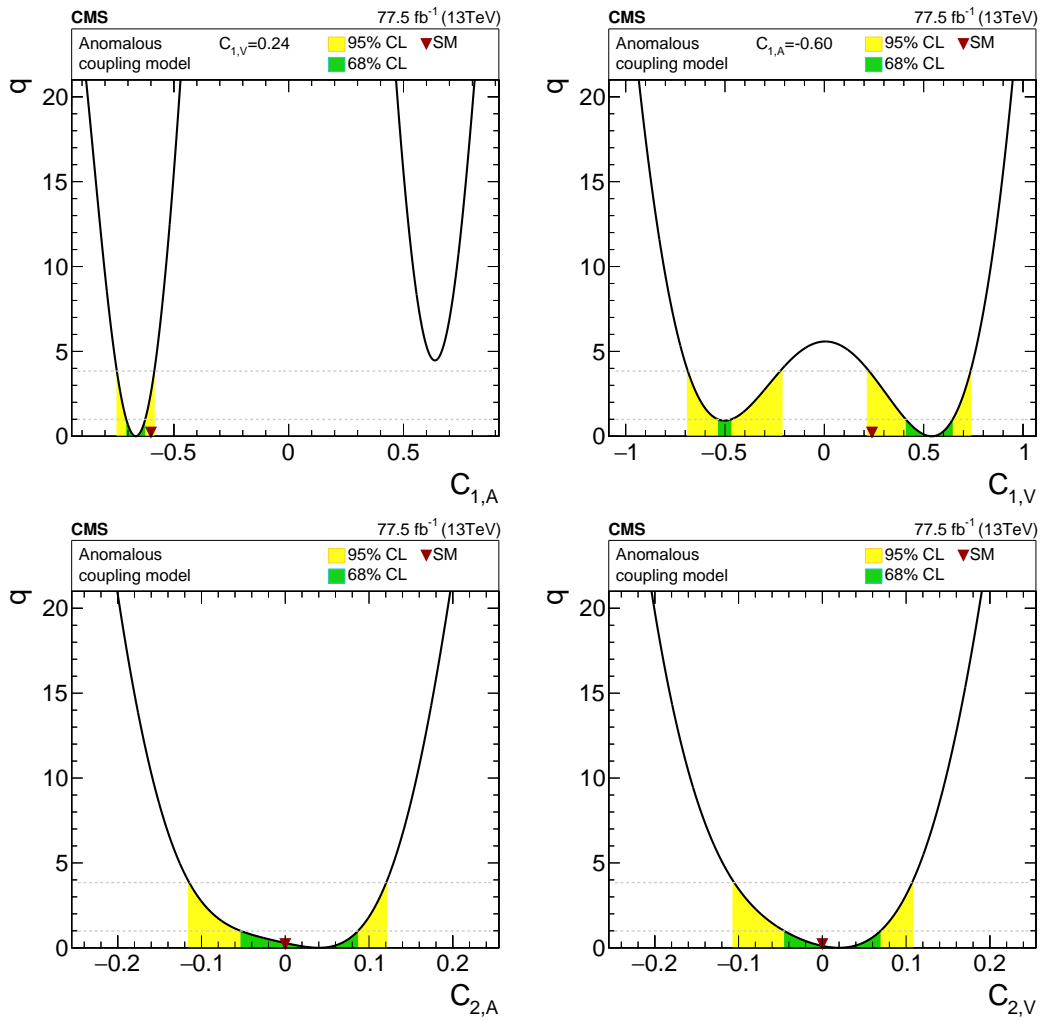


Figure 5.19: Log-likelihood ratios for 1D scans of anomalous couplings. $C_{1,V} = 0.24$ (SM value) for the scan of $C_{1,A}$ (top left) and $C_{1,A} = -0.60$ (SM value) for the scan of $C_{1,V}$ (top right). $C_{2,A}$ (bottom left) and $C_{2,V}$ (bottom right) correspond to electroweak dipole moments of the top quark. The colored areas correspond to the 68% and 95% CL intervals around the best-fit value, respectively. The SM coupling values are indicated by a triangle.

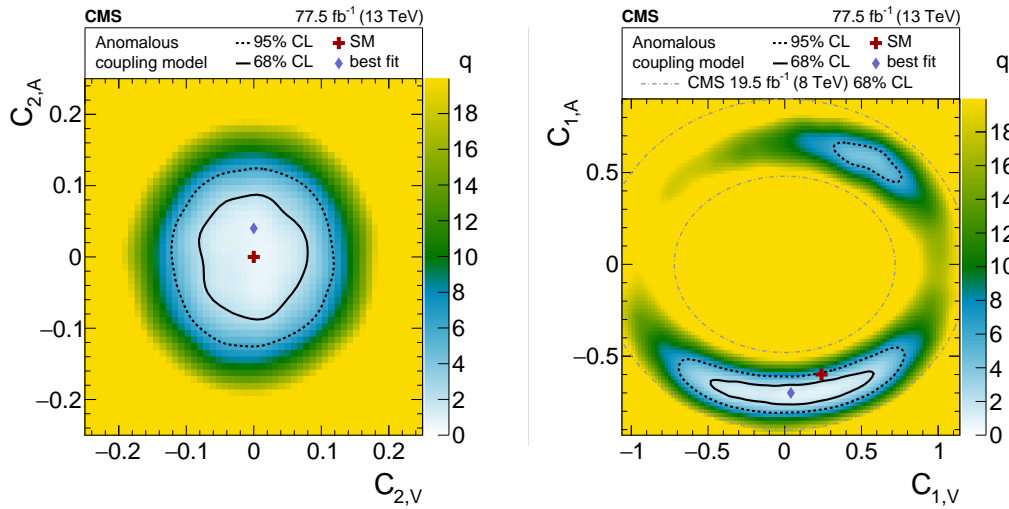


Figure 5.20: Observed log-likelihood ratios for two anomalous coupling scans: $C_{2,V}/C_{2,A}$ corresponding to dipole moments (left) and $C_{1,V}/C_{1,A}$ corresponding to axial-vector and vector current couplings (right). The best-fit point (blue diamond) deviates from the SM expectation (red cross) by about two standard deviations in the current coupling plane. The dot-dashed lines in the right figure show the 68% CL contours of the previous CMS result [173].

EFT approach and the anomalous couplings is given by [206]

$$\begin{aligned}
 C_{2,V} &= \frac{1}{\sqrt{2} \cos\theta_W \sin\theta_W} \left(\frac{v}{\Lambda^2}\right)^2 c_{tZ} \\
 C_{2,A} &= \frac{1}{\sqrt{2} \cos\theta_W \sin\theta_W} \left(\frac{v}{\Lambda^2}\right)^2 c_{tZ}^{[I]} \\
 \Delta C_{1,V} &= \frac{-1}{\cos\theta_W \sin\theta_W} \left(\frac{v}{2\Lambda^2}\right)^2 (c_{\varphi Q}^- + c_{\varphi t}) \\
 \Delta C_{1,A} &= \frac{1}{\cos\theta_W \sin\theta_W} \left(\frac{v}{2\Lambda^2}\right)^2 (c_{\varphi Q}^- - c_{\varphi t}) \quad .
 \end{aligned} \tag{5.13}$$

Within SMEFT, $C_{\varphi q}^{3(33)}$ is defined as separate degree of freedom, $c_{\varphi Q}^3$ as shown in Eq. 2.42, that modifies the Wtb vertex. Because Wilson coefficients of degrees of freedom that are not considered in the analysis are set to zero, $c_{\varphi Q}^-$ is effectively equivalent to $C_{\varphi q}^{1(33)}$ in what follows. Log-likelihood scans for individual Wilson coefficients, with all other Wilson coefficients set to zero, are shown in Fig. 5.21. The 68% and 95% CL intervals are given as colored areas. For both c_{tZ} and $c_{tZ}^{[I]}$ the SM value of zero is within the 68% CL, while the SM point is slightly outside the 95% CL for $c_{\varphi t}$ and $c_{\varphi Q}^-$. This difference can be understood from the nature of the excess of data over the predicted yields. Non-zero electroweak dipole moments, corresponding to c_{tZ} and $c_{tZ}^{[I]}$, produce a harder $p_T(Z)$ spectrum which is not observed in data. Hence, the best fit point is not far off the SM point.

In Fig. 5.23, the obtained 95% CL results are compared to previous constraints from the CMS and ATLAS collaboration [174, 210], direct limits from experimental results by the TOPFITTER

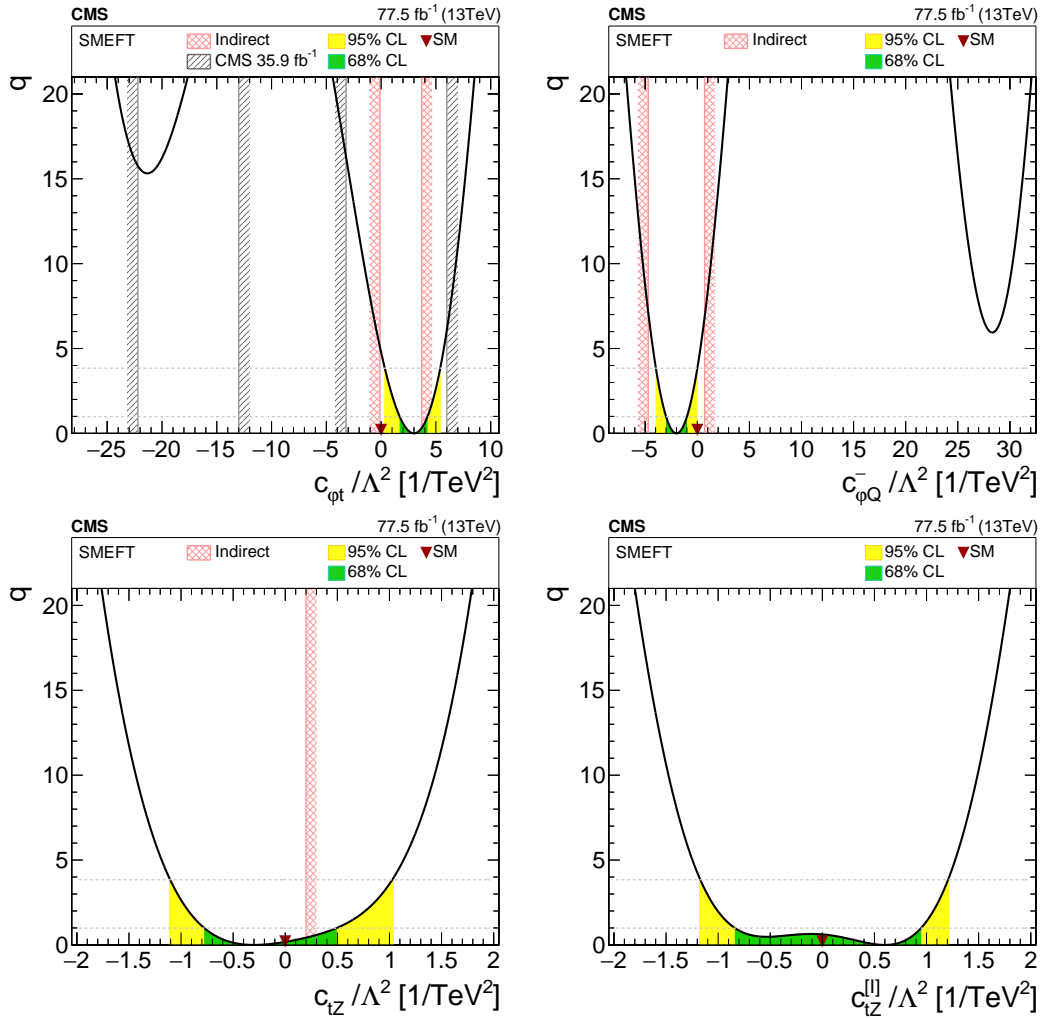


Figure 5.21: Log-likelihood ratios of individual Wilson coefficient scans. Non-zero values of $c_{\phi t}$ (top left) and $c_{\phi Q}^-$ (top right) correspond to modified vector and axial-vector couplings. c_{tZ} (bottom left) and c_{tZ}^{II} (bottom right) correspond to electroweak dipole moments of the top quark. 95% CL intervals from previous CMS results [174], when available, are indicated by the gray hatched delimiters, while 68% CL intervals from electroweak precision measurements [209] are shown with red cross-hatched ones. The colored areas correspond to the 68% and 95% CL intervals around the best-fit value, respectively. The SM value of the Wilson coefficients is indicated with the red triangle.

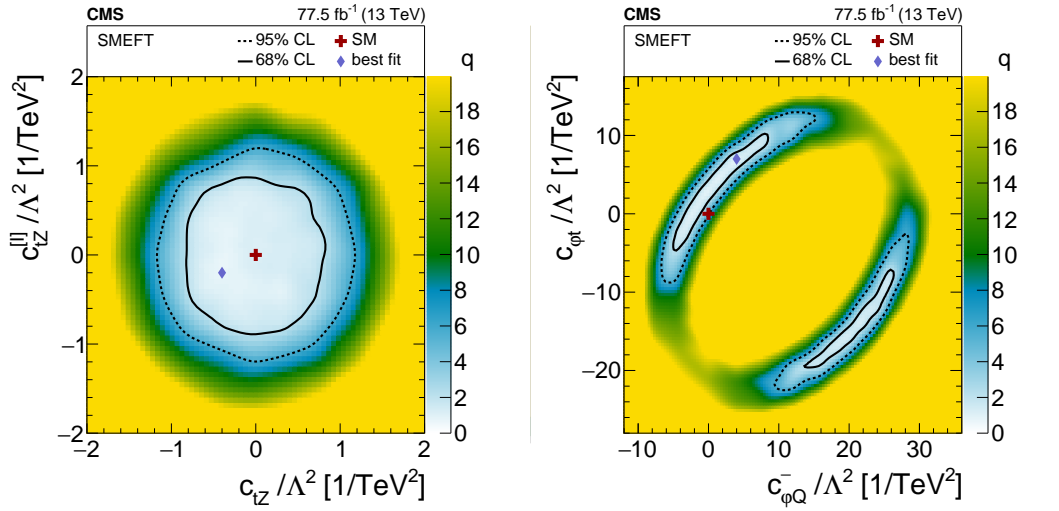


Figure 5.22: Observed log-likelihood ratios for two EFT scans: $c_{tZ}/c_{tZ}^{[I]}$ corresponding to dipole moments (left) and $c_{\phi Q}^-/c_{\phi t}$ corresponding to axial-vector and vector current couplings (right). The best-fit point (blue diamond) deviates from the SM expectation (red cross) by about two standard deviations in the current coupling plane.

collaboration [211] and from the SMEFT framework [212], as well as indirect limits from electroweak precision measurements [209]. Table 5.6 shows the 68% and 95% observed and expected CL intervals together with a comparison to the previous CMS result [174]. Significant improvements with respect to previous top quark analyses are achieved especially for $c_{\phi t}$ and $c_{\phi Q}^-$ owing to the exploitation of the $\cos\theta^*$ shapes. For c_{tZ} the constraints are improved by about a factor of two. Here, the analysis heavily profits from the discriminating feature of the Z boson momentum. The constraints on $c_{tZ}^{[I]}$ are the first to be set by a top quark analysis, and are similar to the constraints on c_{tZ} .

Table 5.6: Expected and observed 68% and 95% CL intervals from this measurement for the listed Wilson coefficients. Constraints from a previous CMS measurement [174] and indirect constraints from precision electroweak data [209] are shown for comparison.

Coefficient	Expected		Observed		Previous CMS constraints		Indirect constraints 68% CL
	68% CL	95% CL	68% CL	95% CL	Exp, 95% CL	Obs, 95% CL	
c_{tZ}/Λ^2	[-0.7, 0.7]	[-1.1, 1.1]	[-0.8, 0.5]	[-1.1, 1.1]	[-2.0, 2.0]	[-2.6, 2.6]	[-4.7, 0.2]
$c_{tZ}^{[I]}/\Lambda^2$	[-0.7, 0.7]	[-1.1, 1.1]	[-0.8, 1.0]	[-1.2, 1.2]	-	-	-
$c_{\phi t}/\Lambda^2$	[-1.6, 1.4]	[-3.4, 2.8]	[1.7, 4.2]	[0.3, 5.4]	[-20.2, 4.0]	[-22.2, -13.0] [-3.2, 6.0]	[-0.1, 3.7]
$c_{\phi Q}^-/\Lambda^2$	[-1.1, 1.1]	[-2.1, 2.2]	[-3.0, -1.0]	[-4.0, 0.0]	-	-	[-4.7, 0.7]

In the context of studies for the high-luminosity LHC (HL-LHC) prospects, the sensitivity of a similar analysis strategy with the full HL-LHC data set using projected systematic uncertainties was examined [15]. A comparison of the expected 95% CL intervals obtained with 77.5 fb^{-1} and 3000 fb^{-1} is shown in Tab. 5.7. An improvement of a factor of two for the

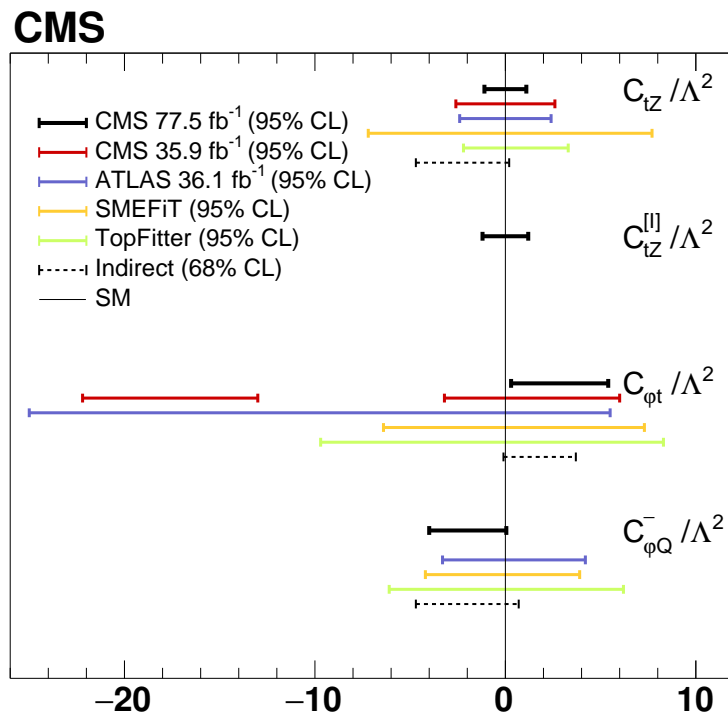


Figure 5.23: Comparison of the observed 95% confidence level intervals (solid black) with the previous CMS results based on the inclusive $t\bar{t}Z$ cross section measurement [174] (red), the most recent ATLAS result [210] (blue), direct limits from the SMEFiT framework [212] (orange) and the TOPFITTER collaboration [211] (green), as well as indirect constraints from electroweak precision measurements [209] (dashed black) on the Wilson coefficients.

Wilson coefficients of the electroweak dipole operators is expected, reaching up to a threefold improvement of the constraints on $c_{\varphi t}$ and $c_{\varphi Q}^-$.

Table 5.7: Expected 95% CL intervals for this measurement and the HL-LHC projection.

Coefficient	Expected 95% CL	
	77.5 fb ⁻¹	3000 fb ⁻¹
c_{tZ}/Λ^2	[-1.1, 1.1]	[-0.5, 0.5]
$c_{tZ}^{[I]}/\Lambda^2$	[-1.1, 1.1]	[-0.5, 0.5]
$c_{\phi t}/\Lambda^2$	[-3.4, 2.8]	[-0.9, 0.9]
$c_{\phi Q}^-/\Lambda^2$	[-2.1, 2.2]	[-0.8, 0.7]

5.9 Summary

The $t\bar{t}Z$ process is a very important probe for anomalous top quark couplings. By utilizing a large data set corresponding to an integrated luminosity of 77.5 fb⁻¹, a differential cross section measurement of the $t\bar{t}Z$ process is possible. This measurement allows to set stringent constraints on anomalous top quark couplings as well as EFT Wilson coefficients. The presented limits surpass constraints from previous direct measurements of the ATLAS and CMS collaborations. 95% CL limits on Wilson coefficients are now at or close to the order of one. In the picture of anomalous couplings, stringent first direct constraints on the electroweak dipole moments have been placed. In the near future, differential measurements of the tZq will provide additional constraints on related Wilson coefficients. Projections have been made for the prospects of a similar analysis strategy at the HL-LHC. Improvements of the constraints by a factor of two to three are expected with the full data set of 3000 fb⁻¹ and projected systematic uncertainties.

Conclusions

THE SEARCH FOR EVIDENCE for physics beyond the SM is one of the main goals of the LHC program. The successful observation of a Higgs boson in 2012, and the now following measurements of its properties were a huge step for completing and establishing the SM. With this observation the particle content of the SM has been completed, and experimental results at particle colliders so far could all be explained by the SM within theoretical and experimental uncertainties. Direct evidence for its invalidity through the discovery of additional new particles, or the breakdown of the SM predictions of couplings at higher energy scales, are highly anticipated, but still missing.

The presented thesis adds new chapters to these searches by using different approaches to probe the validity of the SM. The search for direct top squark production, using data recorded by the CMS experiment during 2016, yields stringent limits on the masses of top squarks. These limits are further enhanced by combining results with similar searches in all-jet or single-leptonic events. In certain simplified SUSY models, top squarks can be excluded up to masses of 1.3 TeV at 95% CL. At the same time, the results can be used to constrain the branching fraction of the Higgs boson to invisible particles, as well as the production of DM particles via scalar or pseudoscalar mediators. The sensitivity of the top squark searches will be enhanced by 100–200 GeV in terms of the top squark mass by using the entire data set recorded by the CMS experiment from 2016 to 2018, amounting to about 140 fb^{-1} . Additional improvements by optimized experimental methods and better understanding of SM backgrounds will lead to an additional gain of a few percent.

Top quark pair production in association with a Z boson ($t\bar{t}Z$) with $Z \rightarrow \nu\nu$ is the most important irreducible SM background to the search for top squarks. At the same time it is a powerful probe of BSM effects itself, motivating precise measurements of the inclusive and differential cross sections of the $t\bar{t}Z$ process. For the first time, measurements of the transverse momentum spectrum of the Z boson and the angular distributions of the leptons from its decay, are used to constrain anomalous couplings of the top quark to the Z boson. The measurement is based on data recorded in 2016 and 2017 by the CMS experiment, using events with a Z

boson decaying to pairs of electrons or muons, and at least one leptonic decay of a W boson from a top quark. The results are interpreted in terms of the SMEFT and provide the most stringent limits on several Wilson coefficients that are obtained in searches at the LHC. The 95% CL limits on the Wilson coefficients under study are of $\mathcal{O}(1)$, and will be improved by a factor of 2–3 with the data set from the HL-LHC, using a similar measurement strategy with the projected detector performance.

Appendix

A.1 Trigger efficiencies

Trigger efficiency maps for the $\mu\mu$, μe and ee channel, and for low and high pseudorapidity, corresponding to Sec. 4.2. In all channels, the efficiency is increased when using a logical OR of double and single lepton triggers, most visibly in the $\mu\mu$ channel in Fig. A.1.

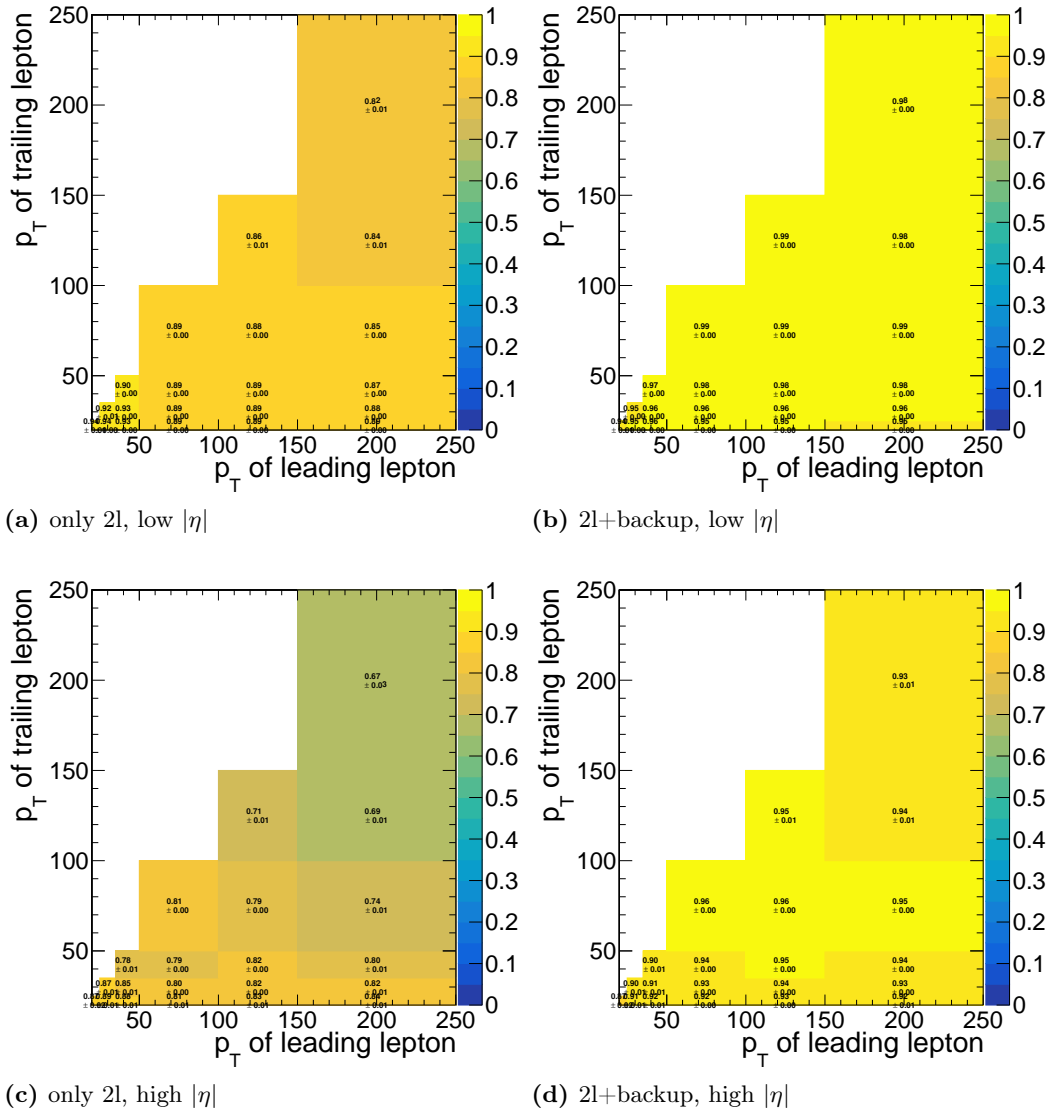


Figure A.1: Trigger efficiency maps for the $\mu\mu$ channel for $\eta < 1.5$ (top) and $\eta > 1.5$ (bottom) of the leading lepton. The plots on the left show the efficiency of the double lepton triggers without the single lepton backup.

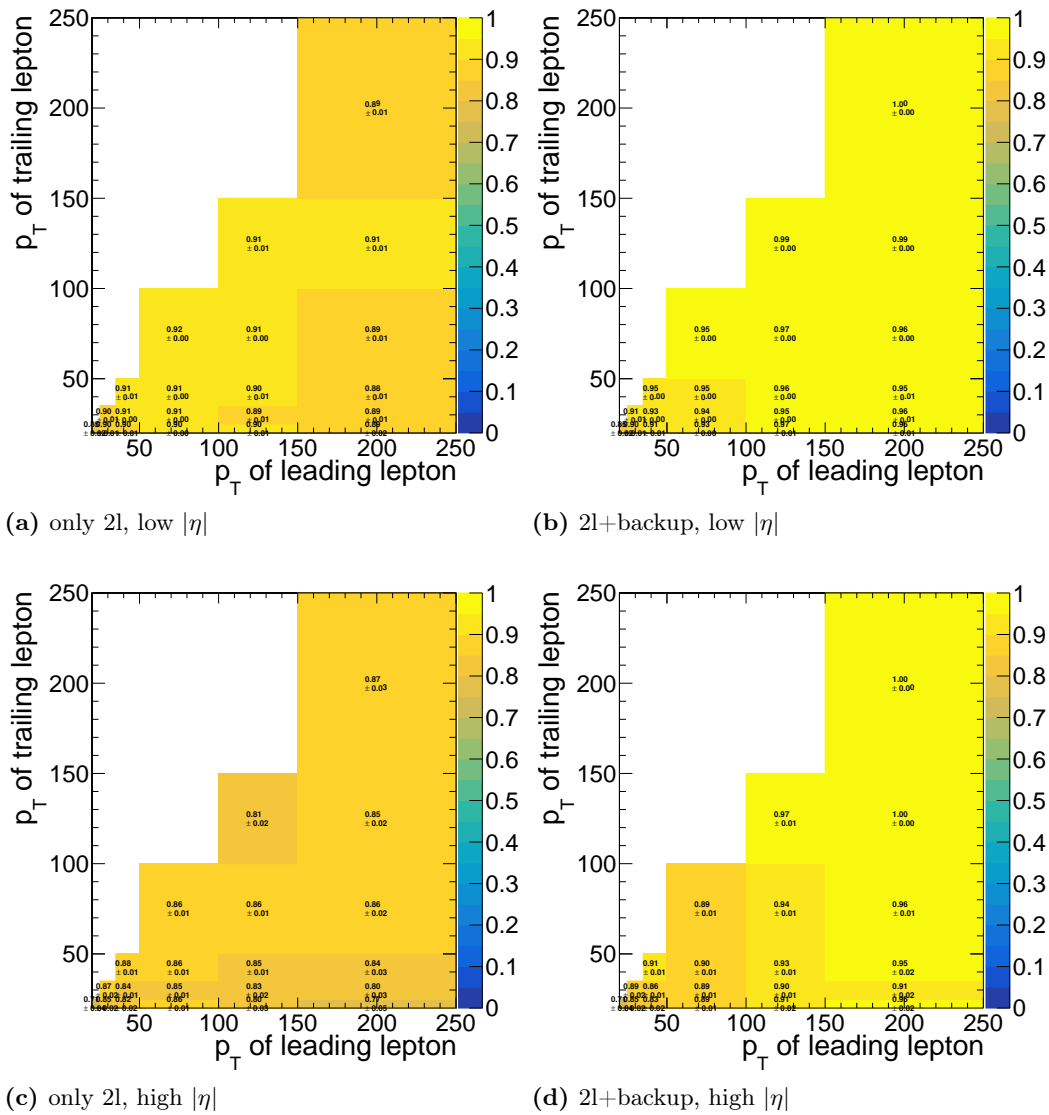


Figure A.2: Trigger efficiency maps for the $e\mu$ channel for $|\eta| < 1.5$ (top) and $|\eta| > 1.5$ (bottom) of the muon. The plots on the left show the efficiency of the double lepton triggers without the single lepton backup.

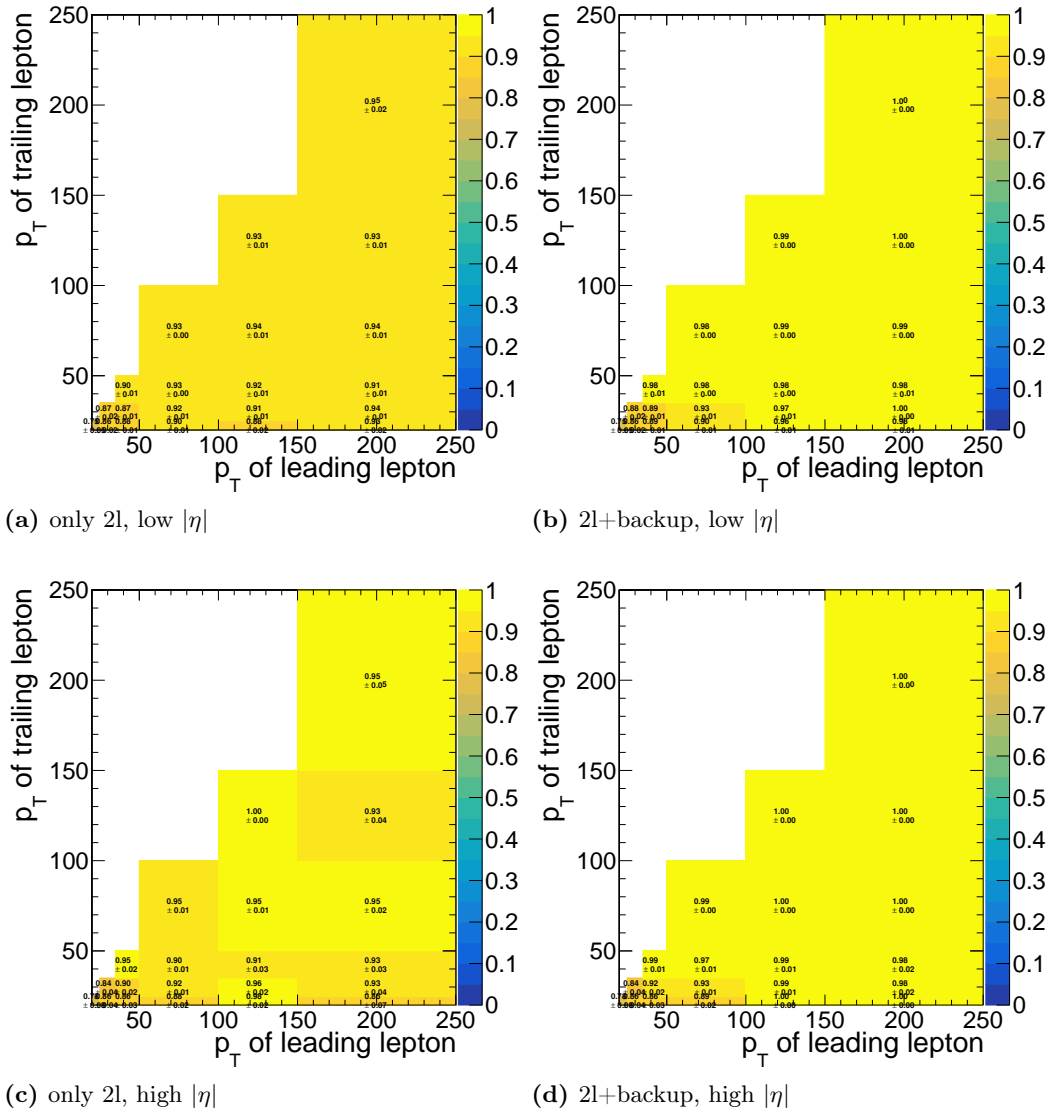
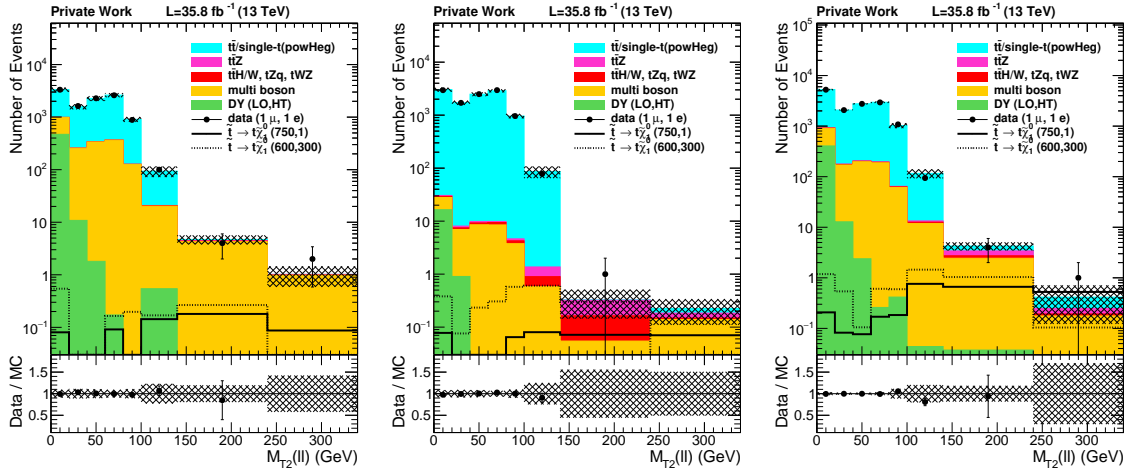


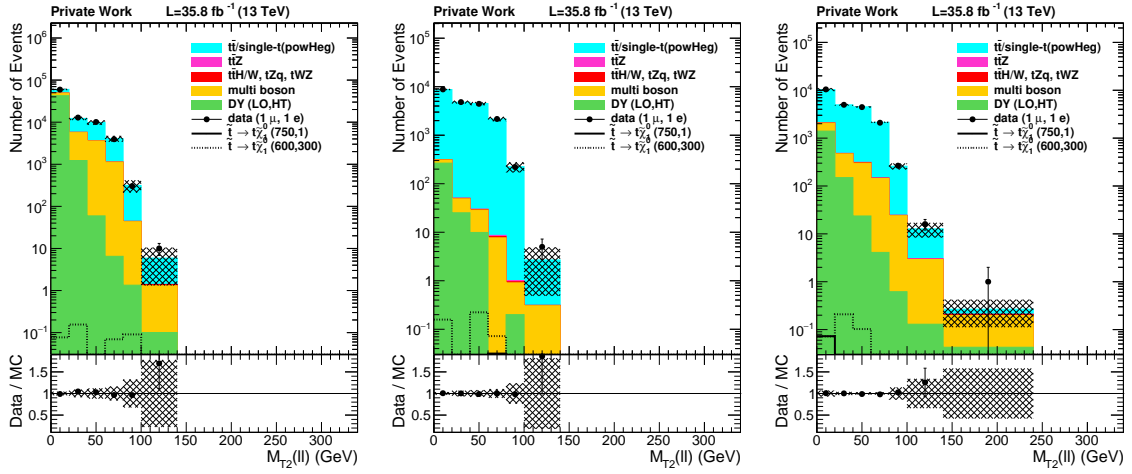
Figure A.3: Trigger efficiency maps for the ee channel for $\eta < 1.5$ (top) and $\eta > 1.5$ (bottom) of the leading lepton. The plots on the left show the efficiency of the double lepton triggers without the single lepton backup.

A.2 Control region plots

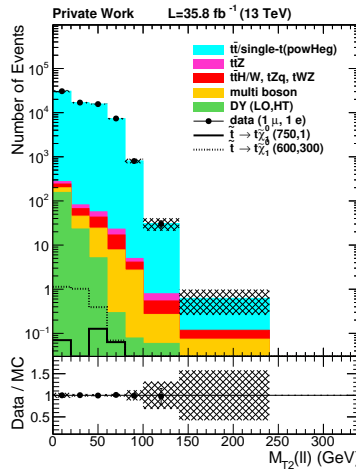
The shape of the $M_{T2}(\ell\ell)$ distributions in $t\bar{t}$ events due to p_T^{miss} mismeasurements and any other potential sources is checked in control regions with inverted N_j , N_b or p_T^{miss} requirements. In order to suppress contributions from DY events, different flavor lepton pairs are required. Figure A.4 shows the $M_{T2}(\ell\ell)$ distribution compared to simulation for various selections. Comparisons are performed in low and high p_T^{miss} regions, where high p_T^{miss} is defined by $p_T^{\text{miss}} > 80 \text{ GeV}$ and $p_T^{\text{miss}}/\sqrt{H_T} > 5$, and low p_T^{miss} by $p_T^{\text{miss}} < 80 \text{ GeV}$. In both low and high p_T^{miss} regions, events are further categorized in terms of jet and b-tag multiplicities. The signal region is omitted by skipping the case of high p_T^{miss} , $N_j \geq 2$ and $N_b \geq 1$. Good agreement between $M_{T2}(\ell\ell)$ shape from data and simulation is observed over a change of yields per bin of several orders of magnitude. The uncertainty due to experimental effects is shown with a hatched band.



(a) $N_j \leq 1, N_b = 0$, high p_T^{miss} (b) $N_j \leq 1, N_b \geq 1$, high p_T^{miss} (c) $N_j \geq 2, N_b = 0$, high p_T^{miss}



(d) $N_j \leq 1, N_b = 0$, low p_T^{miss} (e) $N_j \leq 1, N_b \geq 1$, low p_T^{miss} (f) $N_j \geq 2, N_b = 0$, low p_T^{miss}



(g) $N_j \geq 2, N_b \geq 1$, low p_T^{miss}

Figure A.4: $M_{T2}(\ell\ell)$ distributions in opposite flavor control regions enriched by $t\bar{t}$ events. MC yields are normalized to data using the yields at $M_{T2}(\ell\ell) < 100$ GeV.

A.3 Correlation studies

If the systematic uncertainty on the top quark background component ($t\bar{t}$ and single top quark processes) are treated as 100% correlated between all signal regions, the maximum likelihood fit is able to constrain the nuisance in signal regions with high event counts. These are regions with $M_{T2}(\ell\ell) < 140$ GeV where the top quark background is dominating. This induces a reduction of this uncertainty down to 27% of its initial value (50% or 100% depending on the signal region), which is exhibited in the pull distribution in Fig. A.5 (top). Expected limits using this initial correlation pattern of uncertainties on the top background are shown in Tab. A.1.

To test whether this introduces artificial sensitivity of this analysis, the dependency of the expected limits on the correlation pattern of the top background is studied. First, the top background uncertainty of signal regions with $M_{T2}(\ell\ell)$ 100–140 GeV is decorrelated from signal regions with $M_{T2}(\ell\ell) > 140$ GeV. The pulls of the systematic uncertainties in this case are shown in Fig. A.5 (center). The initially constrained uncertainty, called “top” in the figure, does not get constrained by the fit. However, the additional uncertainty on the top backgrounds of the low $M_{T2}(\ell\ell)$ signal regions, “top_highStat1”, gets constrained as expected because there still is an unrealistically large input value. Nevertheless, no significant change of the expected limits in Tab. A.2 is observed compared to Tab. A.1.

Next, it is tested whether individually decorrelating all low $M_{T2}(\ell\ell)$ regions changes the pull on the uncertainties or the expected limits. The resulting pull distribution is shown in Fig. A.5 (bottom) where the additional entries called “top_highStati”, with i from 1 to 6, represent uncorrelated uncertainties of the signal regions SR0 to SR5. Again, only a small difference in the expected limits shown in Tab. A.3 with respect to Tab. A.1 and Tab. A.2 is observed. The same independence of the expected limits from correlation patterns of the top background component is observed when removing the high statistic signal regions all together. It is therefore concluded that the sensitivity of the analysis is driven by signal acceptance rather than constrained systematic uncertainties. Nevertheless, a realistic correlation pattern is introduced in Sec. 4.4.1 and used in the main analysis.

Table A.1: Expected limits for scalar mediator with the initial correlation pattern of top quark backgrounds.

m_χ (GeV)	m_Φ (GeV)									
	10	15	20	50	95	100	200	300	500	10000
1	0.5		0.6	0.7		1.0	2.3	4.7	21.6	
10	18.7	16.8		0.7		1.0				
50	123.5			104.5	52.3		2.3	4.6		

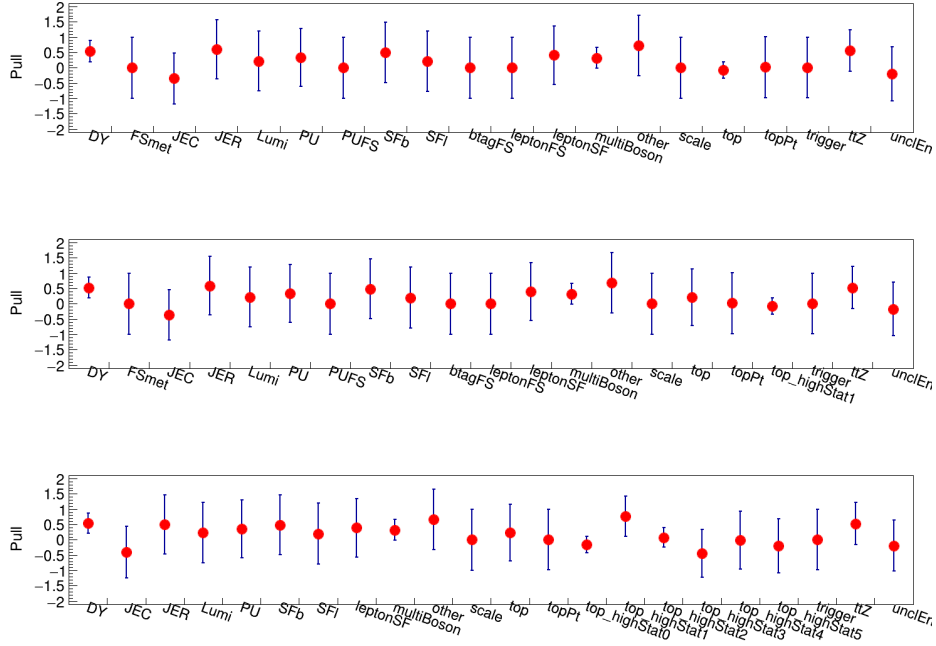


Figure A.5: Pulls on the systematic uncertainties with different correlation patterns for the systematic uncertainty on the top backgrounds.

Table A.2: Expected limits for scalar mediator with systematic uncertainties of top backgrounds in $M_{T_2}(\ell\ell)$ 100–140 GeV signal regions decorrelated from regions with $M_{T_2}(\ell\ell) > 140$ GeV.

m_χ (GeV)	m_Φ (GeV)									
	10	15	20	50	95	100	200	300	500	10000
1	0.5		0.6	0.7		1.0	2.3	4.8	21.8	
10	18.8	17.1		0.7		1.0				
50	125.3			106.3	52.8		2.3	4.7		

Table A.3: Expected limits for scalar mediator with uncorrelated top background uncertainties of all individual low $M_{T_2}(\ell\ell)$ regions.

m_χ (GeV)	m_Φ (GeV)									
	10	15	20	50	95	100	200	300	500	10000
1	0.6		0.6	0.7		1.1	2.4	4.9	22.2	
10	20.1	18.1		0.8		1.1				
50	128.8			109.3	54.6		2.4	4.8		

A.4 Curriculum vitae

Address	Deinhardsteingasse 29/34 1160 Wien, Austria
Date of birth	July 1st, 1990
Citizenship	Austrian

Professional Career

	HEPHY - Institute of High Energy Physics, Vienna, Austria <i>Ph.D. Researcher</i>
Period	June 2016 – June 2019
	HEPHY - Institute of High Energy Physics, Vienna, Austria <i>Master's Student</i>
Period	April 2015 – April 2016
	EPC Handelsges.m.b.H, Wiener Neudorf, Austria <i>Research and Development engineer</i>
Period	May 2011 – April 2015
	CERN, Meyrin, Switzerland <i>Technical student, Bachelor's thesis</i>
Period	September – November 2013
	Technical University Wien, Austria <i>Tutor in fundamentals of physics course</i>
Period	October 2012 – June 2013
	Samariterbund Traiskirchen / Trumau, Austria <i>Mandatory social service / paramedic</i>
Period	September 2009 – May 2010

Education

	Technical University Wien <i>Doctoral programme in Engineering Sciences Technical Physics</i>
Period	September 2016 – today
Scholarship	Associate member of the Doctoral Program Particles & Interactions (DKPI)
	Technical University Wien <i>Master programme Technical Physics</i>
Period	September 2014 – Juni 2016
Graduation	with distinction
	Technical University Wien <i>Bachelor programme Technical Physics</i>
Period	September 2010 – September 2014
Graduation	with distinction
	HTBLuVA Mödling <i>Mechatronics and precision engineering</i>
Period	September 2004 – June 2009
Graduation	with distinction

Skills and Interests

	Languages
German	Mother tongue
English	Fluent
Spanish	Basics
	IT
Software	Mathematica, LabView, Solid Works, Solid Edge ROOT, OpenFOAM, SixTrack
Languages	Python, C/C++, Fortran, L ^A T _E X
	Personal
Interests	Literature, Alternative music, Travelling, Mountainbiking, Skiing, Surfing, Football
Misc.	Voluntary paramedic and ambulance driver, Samariterbund Traiskirchen, 2010–2015

Publications

peer reviewed

	Measurement of top quark pair production in association with a Z boson in proton-proton collisions at $\sqrt{s} = 13$ TeV
Journal	CMS-PAS-TOP-18-009, submitted to JHEP
Authors	The CMS Collaboration
Year	2019
	Performance of missing transverse momentum in proton-proton collisions at $\sqrt{s} = 13$ TeV using the CMS detector
Journal	JINST 14 (2019), P07004
Authors	The CMS Collaboration
Year	2019
	Search for top squarks and dark matter particles in opposite-charge dilepton final states at CMS
Journal	PoS (ALPS2018) 055
Authors	Daniel Spitzbart on behalf of the CMS Collaboration
Year	2018
	Search for top squarks and dark matter particles in opposite-charge dilepton final states at $\sqrt{s} = 13$ TeV
Journal	Phys. Rev. D97 (2018), 032009
Authors	The CMS Collaboration
Year	2018
	Search for supersymmetry in events with one lepton and multiple jets exploiting the angular correlation between the lepton and the missing transverse momentum in proton-proton collisions at $\sqrt{s} = 13$ TeV
Journal	Phys. Lett. B780 (2018), 384-409
Authors	The CMS Collaboration
Year	2018

non-peer reviewed

	Standard Model Physics at the HL-LHC and HE-LHC
Journal	CERN-LPCC-2018-03
Authors	HL-LHC and HE-LHC Working Group
Year	2019
	First constraints on invisible Higgs boson decays using ttH production at $\sqrt{s} = 13$ TeV
Journal	CMS-PAS-HIG-18-008
Authors	The CMS Collaboration
Year	2018
	Performance of missing transverse momentum in pp collisions at $\sqrt{s}=13$ TeV using the CMS detector
Journal	CMS-PAS-JME-17-001
Authors	The CMS Collaboration
Year	2018
	Search for supersymmetry in events with one lepton and multiple jets in proton-proton collisions at $\sqrt{s}=13$ TeV in 2016
Journal	CMS-PAS-SUS-16-019
Authors	The CMS Collaboration
Year	2016
	High-Power Proton-Synchrotron Collimation Studies
Journal	Proceedings, 5th International Particle Accelerator Conference (IPAC 2014)
Authors	A. Alekou, Y. Papaphilippou, D. Spitzbart
Year	2014

Schools

	2018 European School of High Energy Physics
	Maratea, Italy
Date	June 20 – July 3, 2018
	DKPI Summer School 2017
	Söchau, Austria
Date	September 17 – 21, 2017

Talks and Posters

CERN Collider Cross Talk, CERN, Switzerland

Date March 14th, 2019
Talk The top-Z coupling: theory and recent results (with Eleni Vryonidou)

DISCRETE 2018, Vienna, Austria

Date November 26 – 30, 2018
Talk CMS SUSY searches: hot topics, new results and future prospects

2018 European School of HEP, Maratea, Italy

Date June 20 – July 3, 2018
Poster Search for top squarks and dark matter particles in opposite-charge dilepton final states with the CMS experiment

Third Alpine LHC Physics Summit, Obergurgl, Austria

Date April 15 – 20, 2018
Talk Search for top squarks and dark matter particles in opposite-charge dilepton final states at CMS

SUSY 2017, Mumbai, India

Date December 11 – 15, 2017
Talk Search for supersymmetry in the single-lepton final state at CMS

2017 Vienna Central European Seminar, Austria

Date November 30 – December 1, 2017
Poster Search for new elementary scalars in opposite-charge dilepton final states with the CMS experiment

JetMET Workshop 2017, Helsinki, Finland

Date May 10 – 12, 2017
Talk The MET Significance algorithm

2016 Vienna Central European Seminar, Austria

Date December 1 – 2, 2016
Poster Search for supersymmetry in pp collisions at 13 TeV in the single lepton final state with the CMS experiment

APS Annual Meeting 2016, Vienna, Austria

Date September 27 – 29, 2016
Talk Search for supersymmetry in pp collisions at 13 TeV in the single lepton final state with the CMS experiment

Bibliography

- [1] ATLAS Collaboration, “Observation of a new particle in the search for the Standard Model Higgs boson with the ATLAS detector at the LHC”, *Phys. Lett.* **B716** (2012) 1–29, [doi:10.1016/j.physletb.2012.08.020](https://doi.org/10.1016/j.physletb.2012.08.020), [arXiv:1207.7214](https://arxiv.org/abs/1207.7214).
- [2] CMS Collaboration, “Observation of a new boson at a mass of 125 GeV with the CMS experiment at the LHC”, *Phys. Lett.* **B716** (2012) 30–61, [doi:10.1016/j.physletb.2012.08.021](https://doi.org/10.1016/j.physletb.2012.08.021), [arXiv:1207.7235](https://arxiv.org/abs/1207.7235).
- [3] P. W. Higgs, “Broken Symmetries and the Masses of Gauge Bosons”, *Phys. Rev. Lett.* **13** (1964) 508–509, [doi:10.1103/PhysRevLett.13.508](https://doi.org/10.1103/PhysRevLett.13.508).
- [4] F. Englert and R. Brout, “Broken Symmetry and the Mass of Gauge Vector Mesons”, *Phys. Rev. Lett.* **13** (1964) 321–323, [doi:10.1103/PhysRevLett.13.321](https://doi.org/10.1103/PhysRevLett.13.321).
- [5] M. L. Perl et al., “Evidence for Anomalous Lepton Production in e^+e^- Annihilation”, *Phys. Rev. Lett.* **35** (1975) 1489–1492, [doi:10.1103/PhysRevLett.35.1489](https://doi.org/10.1103/PhysRevLett.35.1489).
- [6] CDF Collaboration, “Observation of top quark production in $\bar{p}p$ collisions”, *Phys. Rev. Lett.* **74** (1995) 2626–2631, [doi:10.1103/PhysRevLett.74.2626](https://doi.org/10.1103/PhysRevLett.74.2626), [arXiv:hep-ex/9503002](https://arxiv.org/abs/hep-ex/9503002).
- [7] D0 Collaboration, “Observation of the top quark”, *Phys. Rev. Lett.* **74** (1995) 2632–2637, [doi:10.1103/PhysRevLett.74.2632](https://doi.org/10.1103/PhysRevLett.74.2632), [arXiv:hep-ex/9503003](https://arxiv.org/abs/hep-ex/9503003).
- [8] D. Schaile, “Precision tests of the electroweak interaction”, *Conf. Proc.* **C940720** (1994) 27–52.
- [9] CMS Collaboration, “Measurement of top quark pair production in association with a Z boson in proton-proton collisions at $\sqrt{s} = 13$ TeV”, [Technical Report CMS-PAS-TOP-18-009](#), CERN, Geneva, 2019.
- [10] CMS Collaboration, “Performance of missing transverse momentum reconstruction in proton-proton collisions at $\sqrt{s} = 13$ TeV using the CMS detector”, [arXiv:1903.06078](https://arxiv.org/abs/1903.06078).

- [11] CMS Collaboration, “Search for top squarks and dark matter particles in opposite-charge dilepton final states at CMS”, *PoS ALPS2018* (2018) 055, [doi:10.22323/1.330.0055](https://doi.org/10.22323/1.330.0055).
- [12] CMS Collaboration, “Search for top squarks and dark matter particles in opposite-charge dilepton final states at $\sqrt{s} = 13$ TeV”, *Phys. Rev.* **D97** (2018), no. 3, 032009, [doi:10.1103/PhysRevD.97.032009](https://doi.org/10.1103/PhysRevD.97.032009), [arXiv:1711.00752](https://arxiv.org/abs/1711.00752).
- [13] CMS Collaboration, “Search for supersymmetry in events with one lepton and multiple jets exploiting the angular correlation between the lepton and the missing transverse momentum in proton-proton collisions at $\sqrt{s} = 13$ TeV”, *Phys. Lett.* **B780** (2018) 384–409, [doi:10.1016/j.physletb.2018.03.028](https://doi.org/10.1016/j.physletb.2018.03.028), [arXiv:1709.09814](https://arxiv.org/abs/1709.09814).
- [14] CMS Collaboration Collaboration, “First constraints on invisible Higgs boson decays using $t\bar{t}H$ production at $\sqrt{s} = 13$ TeV”, *Technical Report CMS-PAS-HIG-18-008*, CERN, Geneva, 2019.
- [15] HL-LHC, HE-LHC Working Group Collaboration, “Standard Model Physics at the HL-LHC and HE-LHC”, [arXiv:1902.04070](https://arxiv.org/abs/1902.04070).
- [16] D. J. Gross and F. Wilczek, “Ultraviolet Behavior of Nonabelian Gauge Theories”, *Phys. Rev. Lett.* **30** (1973) 1343–1346, [doi:10.1103/PhysRevLett.30.1343](https://doi.org/10.1103/PhysRevLett.30.1343).
- [17] H. D. Politzer, “Reliable Perturbative Results for Strong Interactions?”, *Phys. Rev. Lett.* **30** (1973) 1346–1349, [doi:10.1103/PhysRevLett.30.1346](https://doi.org/10.1103/PhysRevLett.30.1346).
- [18] D0 Collaboration, “Evidence for a $B_s^0\pi^\pm$ state”, *Phys. Rev. Lett.* **117** (2016), no. 2, 022003, [doi:10.1103/PhysRevLett.117.022003](https://doi.org/10.1103/PhysRevLett.117.022003), [arXiv:1602.07588](https://arxiv.org/abs/1602.07588).
- [19] LHCb Collaboration, “Observation of $J/\psi p$ Resonances Consistent with Pentaquark States in $\Lambda_b^0 \rightarrow J/\psi K^- p$ Decays”, *Phys. Rev. Lett.* **115** (2015) 072001, [doi:10.1103/PhysRevLett.115.072001](https://doi.org/10.1103/PhysRevLett.115.072001), [arXiv:1507.03414](https://arxiv.org/abs/1507.03414).
- [20] S. L. Glashow, “Partial Symmetries of Weak Interactions”, *Nucl. Phys.* **22** (1961) 579–588, [doi:10.1016/0029-5582\(61\)90469-2](https://doi.org/10.1016/0029-5582(61)90469-2).
- [21] S. Weinberg, “A Model of Leptons”, *Phys. Rev. Lett.* **19** (1967) 1264–1266, [doi:10.1103/PhysRevLett.19.1264](https://doi.org/10.1103/PhysRevLett.19.1264).
- [22] UA1 Collaboration, “Experimental Observation of Isolated Large Transverse Energy Electrons with Associated Missing Energy at $s^{*(1/2)} = 540$ -GeV”, *Phys. Lett.* **B122** (1983) 103–116, [doi:10.1016/0370-2693\(83\)91177-2](https://doi.org/10.1016/0370-2693(83)91177-2).

- [23] UA1 Collaboration, “Experimental Observation of Lepton Pairs of Invariant Mass Around 95-GeV/ c^{**2} at the CERN SPS Collider”, *Phys. Lett.* **B126** (1983) 398–410, [doi:10.1016/0370-2693\(83\)90188-0](https://doi.org/10.1016/0370-2693(83)90188-0).
- [24] M. Kobayashi and T. Maskawa, “CP Violation in the Renormalizable Theory of Weak Interaction”, *Prog. Theor. Phys.* **49** (1973) 652–657, [doi:10.1143/PTP.49.652](https://doi.org/10.1143/PTP.49.652).
- [25] Super-Kamiokande Collaboration, “Evidence for oscillation of atmospheric neutrinos”, *Phys. Rev. Lett.* **81** (1998) 1562–1567, [doi:10.1103/PhysRevLett.81.1562](https://doi.org/10.1103/PhysRevLett.81.1562), [arXiv:hep-ex/9807003](https://arxiv.org/abs/hep-ex/9807003).
- [26] SNO Collaboration, “Measurement of the rate of $\nu_e + d \rightarrow p + p + e^-$ interactions produced by 8B solar neutrinos at the Sudbury Neutrino Observatory”, *Phys. Rev. Lett.* **87** (2001) 071301, [doi:10.1103/PhysRevLett.87.071301](https://doi.org/10.1103/PhysRevLett.87.071301), [arXiv:nuc1-ex/0106015](https://arxiv.org/abs/nuc1-ex/0106015).
- [27] B. Pontecorvo, “Inverse beta processes and nonconservation of lepton charge”, *Sov. Phys. JETP* **7** (1958) 172–173. [Zh. Eksp. Teor. Fiz.34,247(1957)].
- [28] Z. Maki, M. Nakagawa, and S. Sakata, “Remarks on the unified model of elementary particles”, *Prog. Theor. Phys.* **28** (1962) 870–880, [doi:10.1143/PTP.28.870](https://doi.org/10.1143/PTP.28.870).
- [29] M. Gell-Mann, P. Ramond, and R. Slansky, “Complex Spinors and Unified Theories”, *Conf. Proc.* **C790927** (1979) 315–321, [arXiv:1306.4669](https://arxiv.org/abs/1306.4669).
- [30] F. Zwicky, “Die Rotverschiebung von extragalaktischen Nebeln”, *Helv. Phys. Acta* **6** (1933) 110–127, [doi:10.1007/s10714-008-0707-4](https://doi.org/10.1007/s10714-008-0707-4). [Gen. Rel. Grav.41,207(2009)].
- [31] V. C. Rubin, N. Thonnard, and W. K. Ford, Jr., “Rotational properties of 21 SC galaxies with a large range of luminosities and radii, from NGC 4605 / $R = 4\text{kpc}$ / to UGC 2885 / $R = 122\text{ kpc}$ /”, *Astrophys. J.* **238** (1980) 471, [doi:10.1086/158003](https://doi.org/10.1086/158003).
- [32] D. Maoz and H.-W. Rix, “Early type galaxies, dark halos, and gravitational lensing statistics”, *Astrophys. J.* **416** (1993) 425, [doi:10.1086/173248](https://doi.org/10.1086/173248).
- [33] Planck Collaboration, “Planck 2018 results. VI. Cosmological parameters”, [arXiv:1807.06209](https://arxiv.org/abs/1807.06209).
- [34] D. Clowe et al., “A direct empirical proof of the existence of dark matter”, *Astrophys. J.* **648** (2006) L109–L113, [doi:10.1086/508162](https://doi.org/10.1086/508162), [arXiv:astro-ph/0608407](https://arxiv.org/abs/astro-ph/0608407).
- [35] Muon $g-2$ Collaboration, “Final Report of the Muon E821 Anomalous Magnetic Moment Measurement at BNL”, *Phys. Rev.* **D73** (2006) 072003, [doi:10.1103/PhysRevD.73.072003](https://doi.org/10.1103/PhysRevD.73.072003), [arXiv:hep-ex/0602035](https://arxiv.org/abs/hep-ex/0602035).

- [36] P. Ramond, “Dual Theory for Free Fermions”, *Phys. Rev.* **D3** (1971) 2415–2418, doi:[10.1103/PhysRevD.3.2415](https://doi.org/10.1103/PhysRevD.3.2415).
- [37] Yu. A. Golfand and E. P. Likhtman, “Extension of the Algebra of Poincare Group Generators and Violation of p Invariance”, *JETP Lett.* **13** (1971) 323–326. [Pisma Zh. Eksp. Teor. Fiz.13,452(1971)].
- [38] D. V. Volkov and V. P. Akulov, “Possible universal neutrino interaction”, *JETP Lett.* **16** (1972) 438–440. [Pisma Zh. Eksp. Teor. Fiz.16,621(1972)].
- [39] J. Wess and B. Zumino, “A Lagrangian Model Invariant Under Supergauge Transformations”, *Phys. Lett.* **49B** (1974) 52, doi:[10.1016/0370-2693\(74\)90578-4](https://doi.org/10.1016/0370-2693(74)90578-4).
- [40] A. Neveu and J. H. Schwarz, “Factorizable dual model of pions”, *Nucl. Phys.* **B31** (1971) 86–112, doi:[10.1016/0550-3213\(71\)90448-2](https://doi.org/10.1016/0550-3213(71)90448-2).
- [41] J. Wess and B. Zumino, “Supergauge Transformations in Four-Dimensions”, *Nucl. Phys.* **B70** (1974) 39–50, doi:[10.1016/0550-3213\(74\)90355-1](https://doi.org/10.1016/0550-3213(74)90355-1).
- [42] A. Salam and J. A. Strathdee, “Supergauge Transformations”, *Nucl. Phys.* **B76** (1974) 477–482, doi:[10.1016/0550-3213\(74\)90537-9](https://doi.org/10.1016/0550-3213(74)90537-9).
- [43] S. R. Coleman and J. Mandula, “All Possible Symmetries of the S Matrix”, *Phys. Rev.* **159** (1967) 1251–1256, doi:[10.1103/PhysRev.159.1251](https://doi.org/10.1103/PhysRev.159.1251).
- [44] R. Haag, J. T. Lopuszanski, and M. Sohnius, “All Possible Generators of Supersymmetries of the s Matrix”, *Nucl. Phys.* **B88** (1975) 257, doi:[10.1016/0550-3213\(75\)90279-5](https://doi.org/10.1016/0550-3213(75)90279-5).
- [45] S. P. Martin, “A Supersymmetry primer”, doi:[10.1142/9789812839657_0001](https://doi.org/10.1142/9789812839657_0001), [10.1142/9789814307505_0001](https://doi.org/10.1142/9789814307505_0001), arXiv:[hep-ph/9709356](https://arxiv.org/abs/hep-ph/9709356). [Adv. Ser. Direct. High Energy Phys.18,1(1998)].
- [46] MSSM Working Group Collaboration, A. Djouadi et al., “The Minimal supersymmetric standard model: Group summary report”, in *GDR (Groupement De Recherche) - Supersymetrie Montpellier, France, April 15-17, 1998*. 1998. arXiv:[hep-ph/9901246](https://arxiv.org/abs/hep-ph/9901246).
- [47] P. Fayet, “Supergauge Invariant Extension of the Higgs Mechanism and a Model for the electron and Its Neutrino”, *Nucl. Phys.* **B90** (1975) 104–124, doi:[10.1016/0550-3213\(75\)90636-7](https://doi.org/10.1016/0550-3213(75)90636-7).
- [48] G. R. Farrar and P. Fayet, “Phenomenology of the Production, Decay, and Detection of New Hadronic States Associated with Supersymmetry”, *Phys. Lett.* **76B** (1978) 575–579, doi:[10.1016/0370-2693\(78\)90858-4](https://doi.org/10.1016/0370-2693(78)90858-4).

- [49] P. Fayet and J. Iliopoulos, “Spontaneously Broken Supergauge Symmetries and Goldstone Spinors”, *Phys. Lett.* **51B** (1974) 461–464, [doi:10.1016/0370-2693\(74\)90310-4](https://doi.org/10.1016/0370-2693(74)90310-4).
- [50] A. H. Chamseddine, R. L. Arnowitt, and P. Nath, “Locally Supersymmetric Grand Unification”, *Phys. Rev. Lett.* **49** (1982) 970, [doi:10.1103/PhysRevLett.49.970](https://doi.org/10.1103/PhysRevLett.49.970).
- [51] S. Dimopoulos and H. Georgi, “Softly Broken Supersymmetry and SU(5)”, *Nucl. Phys.* **B193** (1981) 150–162, [doi:10.1016/0550-3213\(81\)90522-8](https://doi.org/10.1016/0550-3213(81)90522-8).
- [52] L. Girardello and M. T. Grisaru, “Soft Breaking of Supersymmetry”, *Nucl. Phys.* **B194** (1982) 65, [doi:10.1016/0550-3213\(82\)90512-0](https://doi.org/10.1016/0550-3213(82)90512-0).
- [53] M. Beck et al., “Searching for dark matter with the enriched detectors of the Heidelberg - Moscow Double Beta Decay Experiment”, *Phys. Lett.* **B336** (1994) 141–146, [doi:10.1016/0370-2693\(94\)01000-5](https://doi.org/10.1016/0370-2693(94)01000-5).
- [54] S. R. Coleman, J. Wess, and B. Zumino, “Structure of phenomenological Lagrangians. 1.”, *Phys. Rev.* **177** (1969) 2239–2247, [doi:10.1103/PhysRev.177.2239](https://doi.org/10.1103/PhysRev.177.2239).
- [55] C. G. Callan, Jr., S. R. Coleman, J. Wess, and B. Zumino, “Structure of phenomenological Lagrangians. 2.”, *Phys. Rev.* **177** (1969) 2247–2250, [doi:10.1103/PhysRev.177.2247](https://doi.org/10.1103/PhysRev.177.2247).
- [56] S. Weinberg, “Effective Gauge Theories”, *Phys. Lett.* **91B** (1980) 51–55, [doi:10.1016/0370-2693\(80\)90660-7](https://doi.org/10.1016/0370-2693(80)90660-7).
- [57] C. N. Leung, S. T. Love, and S. Rao, “Low-Energy Manifestations of a New Interaction Scale: Operator Analysis”, *Z. Phys.* **C31** (1986) 433, [doi:10.1007/BF01588041](https://doi.org/10.1007/BF01588041).
- [58] W. Buchmuller and D. Wyler, “Effective Lagrangian Analysis of New Interactions and Flavor Conservation”, *Nucl. Phys.* **B268** (1986) 621–653, [doi:10.1016/0550-3213\(86\)90262-2](https://doi.org/10.1016/0550-3213(86)90262-2).
- [59] E. Fermi, “An attempt of a theory of beta radiation. 1.”, *Z. Phys.* **88** (1934) 161–177, [doi:10.1007/BF01351864](https://doi.org/10.1007/BF01351864).
- [60] B. Grzadkowski, M. Iskrzynski, M. Misiak, and J. Rosiek, “Dimension-Six Terms in the Standard Model Lagrangian”, *JHEP* **10** (2010) 085, [doi:10.1007/JHEP10\(2010\)085](https://doi.org/10.1007/JHEP10(2010)085), [arXiv:1008.4884](https://arxiv.org/abs/1008.4884).
- [61] C. Degrande et al., “Effective Field Theory: A Modern Approach to Anomalous Couplings”, *Annals Phys.* **335** (2013) 21–32, [doi:10.1016/j.aop.2013.04.016](https://doi.org/10.1016/j.aop.2013.04.016), [arXiv:1205.4231](https://arxiv.org/abs/1205.4231).

- [62] A. Kobach, “Baryon Number, Lepton Number, and Operator Dimension in the Standard Model”, *Phys. Lett.* **B758** (2016) 455–457, [doi:10.1016/j.physletb.2016.05.050](https://doi.org/10.1016/j.physletb.2016.05.050), [arXiv:1604.05726](https://arxiv.org/abs/1604.05726).
- [63] A. Falkowski et al., “Rosetta: an operator basis translator for Standard Model effective field theory”, *Eur. Phys. J.* **C75** (2015), no. 12, 583, [doi:10.1140/epjc/s10052-015-3806-x](https://doi.org/10.1140/epjc/s10052-015-3806-x), [arXiv:1508.05895](https://arxiv.org/abs/1508.05895).
- [64] R. Alonso, E. E. Jenkins, A. V. Manohar, and M. Trott, “Renormalization Group Evolution of the Standard Model Dimension Six Operators III: Gauge Coupling Dependence and Phenomenology”, *JHEP* **04** (2014) 159, [doi:10.1007/JHEP04\(2014\)159](https://doi.org/10.1007/JHEP04(2014)159), [arXiv:1312.2014](https://arxiv.org/abs/1312.2014).
- [65] D. Barducci et al., “Interpreting top-quark LHC measurements in the standard-model effective field theory”, [arXiv:1802.07237](https://arxiv.org/abs/1802.07237).
- [66] LHC New Physics Working Group Collaboration, “Simplified Models for LHC New Physics Searches”, *J. Phys.* **G39** (2012) 105005, [doi:10.1088/0954-3899/39/10/105005](https://doi.org/10.1088/0954-3899/39/10/105005), [arXiv:1105.2838](https://arxiv.org/abs/1105.2838).
- [67] CMS Collaboration, “Interpretation of Searches for Supersymmetry with Simplified Models”, *Phys. Rev.* **D88** (2013), no. 5, 052017, [doi:10.1103/PhysRevD.88.052017](https://doi.org/10.1103/PhysRevD.88.052017), [arXiv:1301.2175](https://arxiv.org/abs/1301.2175).
- [68] T. Lin, E. W. Kolb, and L.-T. Wang, “Probing dark matter couplings to top and bottom quarks at the LHC”, *Phys. Rev.* **D88** (2013), no. 6, 063510, [doi:10.1103/PhysRevD.88.063510](https://doi.org/10.1103/PhysRevD.88.063510), [arXiv:1303.6638](https://arxiv.org/abs/1303.6638).
- [69] M. R. Buckley, D. Feld, and D. Goncalves, “Scalar Simplified Models for Dark Matter”, *Phys. Rev.* **D91** (2015) 015017, [doi:10.1103/PhysRevD.91.015017](https://doi.org/10.1103/PhysRevD.91.015017), [arXiv:1410.6497](https://arxiv.org/abs/1410.6497).
- [70] P. Harris, V. V. Khoze, M. Spannowsky, and C. Williams, “Constraining Dark Sectors at Colliders: Beyond the Effective Theory Approach”, *Phys. Rev.* **D91** (2015) 055009, [doi:10.1103/PhysRevD.91.055009](https://doi.org/10.1103/PhysRevD.91.055009), [arXiv:1411.0535](https://arxiv.org/abs/1411.0535).
- [71] U. Haisch and E. Re, “Simplified dark matter top-quark interactions at the LHC”, *JHEP* **06** (2015) 078, [doi:10.1007/JHEP06\(2015\)078](https://doi.org/10.1007/JHEP06(2015)078), [arXiv:1503.00691](https://arxiv.org/abs/1503.00691).
- [72] J. Abdallah et al., “Simplified Models for Dark Matter Searches at the LHC”, *Phys. Dark Univ.* **9-10** (2015) 8–23, [doi:10.1016/j.dark.2015.08.001](https://doi.org/10.1016/j.dark.2015.08.001), [arXiv:1506.03116](https://arxiv.org/abs/1506.03116).

- [73] D. Abercrombie et al., “Dark Matter Benchmark Models for Early LHC Run-2 Searches: Report of the ATLAS/CMS Dark Matter Forum”, [arXiv:1507.00966](https://arxiv.org/abs/1507.00966).
- [74] CMS Collaboration, “The CMS experiment at the CERN LHC”, *JINST* **3** (2008) S08004, [doi:10.1088/1748-0221/3/08/S08004](https://doi.org/10.1088/1748-0221/3/08/S08004).
- [75] L. Evans and P. Bryant, “LHC Machine”, *JINST* **3** (2008) S08001, [doi:10.1088/1748-0221/3/08/S08001](https://doi.org/10.1088/1748-0221/3/08/S08001).
- [76] ALICE Collaboration, “The ALICE experiment at the CERN LHC”, *JINST* **3** (2008) S08002, [doi:10.1088/1748-0221/3/08/S08002](https://doi.org/10.1088/1748-0221/3/08/S08002).
- [77] ATLAS Collaboration, “The ATLAS Experiment at the CERN Large Hadron Collider”, *JINST* **3** (2008) S08003, [doi:10.1088/1748-0221/3/08/S08003](https://doi.org/10.1088/1748-0221/3/08/S08003).
- [78] LHCb Collaboration, “The LHCb Detector at the LHC”, *JINST* **3** (2008) S08005, [doi:10.1088/1748-0221/3/08/S08005](https://doi.org/10.1088/1748-0221/3/08/S08005).
- [79] W. Weteringset al., “Status of the 160 MeV H- Injection into the CERN PSB”, *Conf. Proc.* **C1205201** (Aug, 2012) TUPPR091. 4 p.
- [80] T. Sakuma and T. McCauley, “Detector and Event Visualization with SketchUp at the CMS Experiment”, *J. Phys. Conf. Ser.* **513** (2014) 022032, [doi:10.1088/1742-6596/513/2/022032](https://doi.org/10.1088/1742-6596/513/2/022032), [arXiv:1311.4942](https://arxiv.org/abs/1311.4942).
- [81] A. Dominguez et al., “CMS Technical Design Report for the Pixel Detector Upgrade”, [Technical Report CERN-LHCC-2012-016. CMS-TDR-11](https://arxiv.org/abs/1209.4344), CERN, Sep, 2012. Additional contacts: Jeffrey Spalding, Fermilab, Jeffrey.Spalding@cern.ch Didier Contardo, Universite Claude Bernard-Lyon I, didier.claude.contardo@cern.ch.
- [82] CMS Collaboration, “Particle-flow reconstruction and global event description with the CMS detector”, *JINST* **12** (2017), no. 10, P10003, [doi:10.1088/1748-0221/12/10/P10003](https://doi.org/10.1088/1748-0221/12/10/P10003), [arXiv:1706.04965](https://arxiv.org/abs/1706.04965).
- [83] R. Fruhwirth, “Application of Kalman filtering to track and vertex fitting”, *Nucl. Instrum. Meth.* **A262** (1987) 444–450, [doi:10.1016/0168-9002\(87\)90887-4](https://doi.org/10.1016/0168-9002(87)90887-4).
- [84] W. Adam, R. Frühwirth, A. Strandlie, and T. Todorov, “Reconstruction of electrons with the Gaussian-sum filter in the CMS tracker at the LHC”, *Journal of Physics G: Nuclear and Particle Physics* **31** (July, 2005) N9–N20.
- [85] M. Cacciari, G. P. Salam, and G. Soyez, “The anti- k_t jet clustering algorithm”, *JHEP* **04** (2008) 063, [doi:10.1088/1126-6708/2008/04/063](https://doi.org/10.1088/1126-6708/2008/04/063), [arXiv:0802.1189](https://arxiv.org/abs/0802.1189).

- [86] M. Cacciari, G. P. Salam, and G. Soyez, “FastJet user manual”, *Eur. Phys. J. C* **72** (2012) 1896, [doi:10.1140/epjc/s10052-012-1896-2](https://doi.org/10.1140/epjc/s10052-012-1896-2), [arXiv:1111.6097](https://arxiv.org/abs/1111.6097).
- [87] CMS Collaboration, “Performance of the CMS muon detector and muon reconstruction with proton-proton collisions at $\sqrt{s} = 13$ TeV”, *JINST* **13** (2018), no. 06, P06015, [doi:10.1088/1748-0221/13/06/P06015](https://doi.org/10.1088/1748-0221/13/06/P06015), [arXiv:1804.04528](https://arxiv.org/abs/1804.04528).
- [88] CMS Collaboration, “Performance of Electron Reconstruction and Selection with the CMS Detector in Proton-Proton Collisions at 8 TeV”, *JINST* **10** (2015), no. 06, P06005, [doi:10.1088/1748-0221/10/06/P06005](https://doi.org/10.1088/1748-0221/10/06/P06005), [arXiv:1502.02701](https://arxiv.org/abs/1502.02701).
- [89] CMS Collaboration, “Performance of Photon Reconstruction and Identification with the CMS Detector in Proton-Proton Collisions at $\sqrt{s} = 8$ TeV”, *JINST* **10** (2015), no. 08, P08010, [doi:10.1088/1748-0221/10/08/P08010](https://doi.org/10.1088/1748-0221/10/08/P08010), [arXiv:1502.02702](https://arxiv.org/abs/1502.02702).
- [90] CMS Collaboration, “Jet energy scale and resolution in the CMS experiment in pp collisions at 8 TeV”, *JINST* **12** (2017), no. 02, P02014, [doi:10.1088/1748-0221/12/02/P02014](https://doi.org/10.1088/1748-0221/12/02/P02014), [arXiv:1607.03663](https://arxiv.org/abs/1607.03663).
- [91] K. Rehermann and B. Tweedie, “Efficient Identification of Boosted Semileptonic Top Quarks at the LHC”, *JHEP* **03** (2011) 059, [doi:10.1007/JHEP03\(2011\)059](https://doi.org/10.1007/JHEP03(2011)059), [arXiv:1007.2221](https://arxiv.org/abs/1007.2221).
- [92] R. K. Ellis, W. J. Stirling, and B. R. Webber, “QCD and collider physics”, *Camb. Monogr. Part. Phys. Nucl. Phys. Cosmol.* **8** (1996) 1–435.
- [93] A. Buckley et al., “General-purpose event generators for LHC physics”, *Phys. Rept.* **504** (2011) 145–233, [doi:10.1016/j.physrep.2011.03.005](https://doi.org/10.1016/j.physrep.2011.03.005), [arXiv:1101.2599](https://arxiv.org/abs/1101.2599).
- [94] J. Alwall et al., “The automated computation of tree-level and next-to-leading order differential cross sections, and their matching to parton shower simulations”, *JHEP* **07** (2014) 079, [doi:10.1007/JHEP07\(2014\)079](https://doi.org/10.1007/JHEP07(2014)079), [arXiv:1405.0301](https://arxiv.org/abs/1405.0301).
- [95] S. Alioli, P. Nason, C. Oleari, and E. Re, “A general framework for implementing NLO calculations in shower Monte Carlo programs: the POWHEG BOX”, *JHEP* **06** (2010) 043, [doi:10.1007/JHEP06\(2010\)043](https://doi.org/10.1007/JHEP06(2010)043), [arXiv:1002.2581](https://arxiv.org/abs/1002.2581).
- [96] R. D. Ball et al., “Parton distributions with LHC data”, *Nucl. Phys.* **B867** (2013) 244–289, [doi:10.1016/j.nuclphysb.2012.10.003](https://doi.org/10.1016/j.nuclphysb.2012.10.003), [arXiv:1207.1303](https://arxiv.org/abs/1207.1303).
- [97] NNPDF Collaboration, “Parton distributions for the LHC Run II”, *JHEP* **04** (2015) 040, [doi:10.1007/JHEP04\(2015\)040](https://doi.org/10.1007/JHEP04(2015)040), [arXiv:1410.8849](https://arxiv.org/abs/1410.8849).

- [98] NNPDF Collaboration, “Parton distributions from high-precision collider data”, *Eur. Phys. J.* **C77** (2017), no. 10, 663, [doi:10.1140/epjc/s10052-017-5199-5](https://doi.org/10.1140/epjc/s10052-017-5199-5), [arXiv:1706.00428](https://arxiv.org/abs/1706.00428).
- [99] T. Sjöstrand et al., “An Introduction to PYTHIA 8.2”, *Comput. Phys. Commun.* **191** (2015) 159–177, [doi:10.1016/j.cpc.2015.01.024](https://doi.org/10.1016/j.cpc.2015.01.024), [arXiv:1410.3012](https://arxiv.org/abs/1410.3012).
- [100] CMS Collaboration, “Event generator tunes obtained from underlying event and multiparton scattering measurements”, *Eur. Phys. J.* **C76** (2016), no. 3, 155, [doi:10.1140/epjc/s10052-016-3988-x](https://doi.org/10.1140/epjc/s10052-016-3988-x), [arXiv:1512.00815](https://arxiv.org/abs/1512.00815).
- [101] CMS Collaboration, “Extraction and validation of a new set of CMS PYTHIA8 tunes from underlying-event measurements”, [arXiv:1903.12179](https://arxiv.org/abs/1903.12179).
- [102] GEANT4 Collaboration, “GEANT4: A Simulation toolkit”, *Nucl. Instrum. Meth.* **A506** (2003) 250–303, [doi:10.1016/S0168-9002\(03\)01368-8](https://doi.org/10.1016/S0168-9002(03)01368-8).
- [103] A. Giammanco, “The Fast Simulation of the CMS Experiment”, *J. Phys. Conf. Ser.* **513** (2014) 022012, [doi:10.1088/1742-6596/513/2/022012](https://doi.org/10.1088/1742-6596/513/2/022012).
- [104] J. Alwall, P. Schuster, and N. Toro, “Simplified Models for a First Characterization of New Physics at the LHC”, *Phys. Rev.* **D79** (2009) 075020, [doi:10.1103/PhysRevD.79.075020](https://doi.org/10.1103/PhysRevD.79.075020), [arXiv:0810.3921](https://arxiv.org/abs/0810.3921).
- [105] J. Alwall, M.-P. Le, M. Lisanti, and J. G. Wacker, “Model-Independent Jets plus Missing Energy Searches”, *Phys. Rev.* **D79** (2009) 015005, [doi:10.1103/PhysRevD.79.015005](https://doi.org/10.1103/PhysRevD.79.015005), [arXiv:0809.3264](https://arxiv.org/abs/0809.3264).
- [106] CMS Collaboration, “Search for top-squark pair production in the single-lepton final state in pp collisions at $\sqrt{s} = 8$ TeV”, *Eur. Phys. J.* **C73** (2013), no. 12, 2677, [doi:10.1140/epjc/s10052-013-2677-2](https://doi.org/10.1140/epjc/s10052-013-2677-2), [arXiv:1308.1586](https://arxiv.org/abs/1308.1586).
- [107] ATLAS Collaboration, “Search for top squark pair production in final states with one isolated lepton, jets, and missing transverse momentum in $\sqrt{s} = 8$ TeV pp collisions with the ATLAS detector”, *JHEP* **11** (2014) 118, [doi:10.1007/JHEP11\(2014\)118](https://doi.org/10.1007/JHEP11(2014)118), [arXiv:1407.0583](https://arxiv.org/abs/1407.0583).
- [108] ATLAS Collaboration, “Search for direct top-squark pair production in final states with two leptons in pp collisions at $\sqrt{s} = 8$ TeV with the ATLAS detector”, *JHEP* **06** (2014) 124, [doi:10.1007/JHEP06\(2014\)124](https://doi.org/10.1007/JHEP06(2014)124), [arXiv:1403.4853](https://arxiv.org/abs/1403.4853).
- [109] ATLAS Collaboration, “ATLAS Run 1 searches for direct pair production of third-generation squarks at the Large Hadron Collider”, *Eur. Phys. J.* **C75** (2015),

- no. 10, 510,
[doi:10.1140/epjc/s10052-015-3726-9](https://doi.org/10.1140/epjc/s10052-015-3726-9), [10.1140/epjc/s10052-016-3935-x](https://doi.org/10.1140/epjc/s10052-016-3935-x),
[arXiv:1506.08616](https://arxiv.org/abs/1506.08616). [Erratum: *Eur. Phys. J.* C76,no.3,153(2016)].
- [110] CMS Collaboration, “Search for direct pair production of scalar top quarks in the single- and dilepton channels in proton-proton collisions at $\sqrt{s} = 8$ TeV”, *JHEP* **07** (2016) 027, [doi:10.1007/JHEP07\(2016\)027](https://doi.org/10.1007/JHEP07(2016)027), [10.1007/JHEP09\(2016\)056](https://doi.org/10.1007/JHEP09(2016)056), [arXiv:1602.03169](https://arxiv.org/abs/1602.03169). [Erratum: *JHEP*09,056(2016)].
- [111] CMS Collaboration, “Searches for pair production of third-generation squarks in $\sqrt{s} = 13$ TeV pp collisions”, *Eur. Phys. J.* **C77** (2017), no. 5, 327, [doi:10.1140/epjc/s10052-017-4853-2](https://doi.org/10.1140/epjc/s10052-017-4853-2), [arXiv:1612.03877](https://arxiv.org/abs/1612.03877).
- [112] ATLAS Collaboration, “Search for direct top squark pair production in final states with two leptons in $\sqrt{s} = 13$ TeV pp collisions with the ATLAS detector”, *Eur. Phys. J.* **C77** (2017), no. 12, 898, [doi:10.1140/epjc/s10052-017-5445-x](https://doi.org/10.1140/epjc/s10052-017-5445-x), [arXiv:1708.03247](https://arxiv.org/abs/1708.03247).
- [113] ATLAS Collaboration, “Search for top squarks in final states with one isolated lepton, jets, and missing transverse momentum in $\sqrt{s} = 13$ TeV pp collisions with the ATLAS detector”, *Phys. Rev.* **D94** (2016), no. 5, 052009, [doi:10.1103/PhysRevD.94.052009](https://doi.org/10.1103/PhysRevD.94.052009), [arXiv:1606.03903](https://arxiv.org/abs/1606.03903).
- [114] ATLAS Collaboration, “Search for dark matter in events with heavy quarks and missing transverse momentum in pp collisions with the ATLAS detector”, *Eur. Phys. J.* **C75** (2015), no. 2, 92, [doi:10.1140/epjc/s10052-015-3306-z](https://doi.org/10.1140/epjc/s10052-015-3306-z), [arXiv:1410.4031](https://arxiv.org/abs/1410.4031).
- [115] CMS Collaboration, “Search for the production of dark matter in association with top-quark pairs in the single-lepton final state in proton-proton collisions at $\sqrt{s} = 8$ TeV”, *JHEP* **06** (2015) 121, [doi:10.1007/JHEP06\(2015\)121](https://doi.org/10.1007/JHEP06(2015)121), [arXiv:1504.03198](https://arxiv.org/abs/1504.03198).
- [116] CMS Collaboration, “Search for dark matter produced in association with heavy-flavor quark pairs in proton-proton collisions at $\sqrt{s} = 13$ TeV”, *Eur. Phys. J.* **C77** (2017), no. 12, 845, [doi:10.1140/epjc/s10052-017-5317-4](https://doi.org/10.1140/epjc/s10052-017-5317-4), [arXiv:1706.02581](https://arxiv.org/abs/1706.02581).
- [117] CMS Collaboration, “Search for dark matter produced with an energetic jet or a hadronically decaying W or Z boson at $\sqrt{s} = 13$ TeV”, *JHEP* **07** (2017) 014, [doi:10.1007/JHEP07\(2017\)014](https://doi.org/10.1007/JHEP07(2017)014), [arXiv:1703.01651](https://arxiv.org/abs/1703.01651).
- [118] ATLAS Collaboration, “Search for dark matter produced in association with bottom or top quarks in $\sqrt{s} = 13$ TeV pp collisions with the ATLAS detector”, *Eur. Phys. J.* **C78** (2018), no. 1, 18, [doi:10.1140/epjc/s10052-017-5486-1](https://doi.org/10.1140/epjc/s10052-017-5486-1), [arXiv:1710.11412](https://arxiv.org/abs/1710.11412).

- [119] J. Smith, W. L. van Neerven, and J. A. M. Vermaseren, “The Transverse Mass and Width of the W Boson”, *Phys. Rev. Lett.* **50** (1983) 1738, [doi:10.1103/PhysRevLett.50.1738](https://doi.org/10.1103/PhysRevLett.50.1738).
- [120] C. G. Lester and D. J. Summers, “Measuring masses of semiinvisibly decaying particles pair produced at hadron colliders”, *Phys. Lett.* **B463** (1999) 99–103, [doi:10.1016/S0370-2693\(99\)00945-4](https://doi.org/10.1016/S0370-2693(99)00945-4), [arXiv:hep-ph/9906349](https://arxiv.org/abs/hep-ph/9906349).
- [121] S. Frixione, P. Nason, and G. Ridolfi, “A Positive-weight next-to-leading-order Monte Carlo for heavy flavour hadroproduction”, *JHEP* **09** (2007) 126, [doi:10.1088/1126-6708/2007/09/126](https://doi.org/10.1088/1126-6708/2007/09/126), [arXiv:0707.3088](https://arxiv.org/abs/0707.3088).
- [122] P. Nason, “A New method for combining NLO QCD with shower Monte Carlo algorithms”, *JHEP* **11** (2004) 040, [doi:10.1088/1126-6708/2004/11/040](https://doi.org/10.1088/1126-6708/2004/11/040), [arXiv:hep-ph/0409146](https://arxiv.org/abs/hep-ph/0409146).
- [123] S. Frixione, P. Nason, and C. Oleari, “Matching NLO QCD computations with Parton Shower simulations: the POWHEG method”, *JHEP* **11** (2007) 070, [doi:10.1088/1126-6708/2007/11/070](https://doi.org/10.1088/1126-6708/2007/11/070), [arXiv:0709.2092](https://arxiv.org/abs/0709.2092).
- [124] H. B. Hartanto, B. Jager, L. Reina, and D. Wackerroth, “Higgs boson production in association with top quarks in the POWHEG BOX”, *Phys. Rev. D* **91** (2015) 094003, [doi:10.1103/PhysRevD.91.094003](https://doi.org/10.1103/PhysRevD.91.094003), [arXiv:1501.04498](https://arxiv.org/abs/1501.04498).
- [125] CMS Collaboration Collaboration, “Investigations of the impact of the parton shower tuning in Pythia 8 in the modelling of $t\bar{t}$ at $\sqrt{s} = 8$ and 13 TeV”, [Technical Report CMS-PAS-TOP-16-021](https://arxiv.org/abs/1602.021), CERN, Geneva, 2016.
- [126] M. Czakon and A. Mitov, “Top++: A program for the calculation of the top-pair cross section at hadron colliders”, *Comput. Phys. Commun.* **185** (2014) 2930, [doi:10.1016/j.cpc.2014.06.021](https://doi.org/10.1016/j.cpc.2014.06.021), [arXiv:1112.5675](https://arxiv.org/abs/1112.5675).
- [127] S. Alioli, P. Nason, C. Oleari, and E. Re, “NLO single-top production matched with shower in POWHEG: s- and t-channel contributions”, *JHEP* **09** (2009) 111, [doi:10.1007/JHEP02\(2010\)011](https://doi.org/10.1007/JHEP02(2010)011), [10.1088/1126-6708/2009/09/111](https://doi.org/10.1088/1126-6708/2009/09/111), [arXiv:0907.4076](https://arxiv.org/abs/0907.4076). [Erratum: *JHEP02,011(2010)*].
- [128] E. Re, “Single-top Wt -channel production matched with parton showers using the POWHEG method”, *Eur. Phys. J.* **C71** (2011) 1547, [doi:10.1140/epjc/s10052-011-1547-z](https://doi.org/10.1140/epjc/s10052-011-1547-z), [arXiv:1009.2450](https://arxiv.org/abs/1009.2450).
- [129] R. Gavin, Y. Li, F. Petriello, and S. Quackenbush, “FEWZ 2.0: A code for hadronic Z production at next-to-next-to-leading order”, *Comput. Phys. Commun.* **182** (2011) 2388–2403, [doi:10.1016/j.cpc.2011.06.008](https://doi.org/10.1016/j.cpc.2011.06.008), [arXiv:1011.3540](https://arxiv.org/abs/1011.3540).

- [130] J. Alwall et al., “Comparative study of various algorithms for the merging of parton showers and matrix elements in hadronic collisions”, *Eur. Phys. J.* **C53** (2008) 473–500, [doi:10.1140/epjc/s10052-007-0490-5](https://doi.org/10.1140/epjc/s10052-007-0490-5), [arXiv:0706.2569](https://arxiv.org/abs/0706.2569).
- [131] R. Frederix and S. Frixione, “Merging meets matching in MC@NLO”, *JHEP* **12** (2012) 061, [doi:10.1007/JHEP12\(2012\)061](https://doi.org/10.1007/JHEP12(2012)061), [arXiv:1209.6215](https://arxiv.org/abs/1209.6215).
- [132] C. Borschensky et al., “Squark and gluino production cross sections in pp collisions at $\sqrt{s} = 13, 14, 33$ and 100 TeV”, *Eur. Phys. J.* **C74** (2014), no. 12, 3174, [doi:10.1140/epjc/s10052-014-3174-y](https://doi.org/10.1140/epjc/s10052-014-3174-y), [arXiv:1407.5066](https://arxiv.org/abs/1407.5066).
- [133] CMS Collaboration, “Performance of CMS muon reconstruction in *pp* collision events at $\sqrt{s} = 7$ TeV”, *JINST* **7** (2012) P10002, [doi:10.1088/1748-0221/7/10/P10002](https://doi.org/10.1088/1748-0221/7/10/P10002), [arXiv:1206.4071](https://arxiv.org/abs/1206.4071).
- [134] CMS Collaboration, “Identification of heavy-flavour jets with the CMS detector in pp collisions at 13 TeV”, *JINST* **13** (2018), no. 05, P05011, [doi:10.1088/1748-0221/13/05/P05011](https://doi.org/10.1088/1748-0221/13/05/P05011), [arXiv:1712.07158](https://arxiv.org/abs/1712.07158).
- [135] CMS Collaboration, “Measurement of the cross section and angular correlations for associated production of a Z boson with b hadrons in pp collisions at $\sqrt{s} = 7$ TeV”, *JHEP* **12** (2013) 039, [doi:10.1007/JHEP12\(2013\)039](https://doi.org/10.1007/JHEP12(2013)039), [arXiv:1310.1349](https://arxiv.org/abs/1310.1349).
- [136] CMS Collaboration, “Determination of Jet Energy Calibration and Transverse Momentum Resolution in CMS”, *JINST* **6** (2011) P11002, [doi:10.1088/1748-0221/6/11/P11002](https://doi.org/10.1088/1748-0221/6/11/P11002), [arXiv:1107.4277](https://arxiv.org/abs/1107.4277).
- [137] CMS Collaboration, “Measurement of the inelastic proton-proton cross section at $\sqrt{s} = 13$ TeV”, *JHEP* **07** (2018) 161, [doi:10.1007/JHEP07\(2018\)161](https://doi.org/10.1007/JHEP07(2018)161), [arXiv:1802.02613](https://arxiv.org/abs/1802.02613).
- [138] CMS Collaboration Collaboration, “CMS Luminosity Measurements for the 2016 Data Taking Period”, [Technical Report CMS-PAS-LUM-17-001](https://arxiv.org/abs/1708.05848), CERN, Geneva, 2017.
- [139] J. Butterworth et al., “PDF4LHC recommendations for LHC Run II”, *J. Phys.* **G43** (2016) 023001, [doi:10.1088/0954-3899/43/2/023001](https://doi.org/10.1088/0954-3899/43/2/023001), [arXiv:1510.03865](https://arxiv.org/abs/1510.03865).
- [140] CMS Collaboration, “Measurement of the differential cross section for top quark pair production in pp collisions at $\sqrt{s} = 8$ TeV”, *Eur. Phys. J.* **C75** (2015), no. 11, 542, [doi:10.1140/epjc/s10052-015-3709-x](https://doi.org/10.1140/epjc/s10052-015-3709-x), [arXiv:1505.04480](https://arxiv.org/abs/1505.04480).
- [141] CMS Collaboration, “Measurement of differential cross sections for top quark pair production using the lepton+jets final state in proton-proton collisions at 13 TeV”,

- Phys. Rev.* **D95** (2017), no. 9, 092001, [doi:10.1103/PhysRevD.95.092001](https://doi.org/10.1103/PhysRevD.95.092001), [arXiv:1610.04191](https://arxiv.org/abs/1610.04191).
- [142] CMS Collaboration, “Measurements of $t\bar{t}$ differential cross sections in proton-proton collisions at $\sqrt{s} = 13$ TeV using events containing two leptons”, *JHEP* **02** (2019) 149, [doi:10.1007/JHEP02\(2019\)149](https://doi.org/10.1007/JHEP02(2019)149), [arXiv:1811.06625](https://arxiv.org/abs/1811.06625).
- [143] M. Czakon, D. Heymes, and A. Mitov, “High-precision differential predictions for top-quark pairs at the LHC”, *Phys. Rev. Lett.* **116** (2016), no. 8, 082003, [doi:10.1103/PhysRevLett.116.082003](https://doi.org/10.1103/PhysRevLett.116.082003), [arXiv:1511.00549](https://arxiv.org/abs/1511.00549).
- [144] N. Kidonakis, “NNLL threshold resummation for top-pair and single-top production”, *Phys. Part. Nucl.* **45** (2014), no. 4, 714–722, [doi:10.1134/S1063779614040091](https://doi.org/10.1134/S1063779614040091), [arXiv:1210.7813](https://arxiv.org/abs/1210.7813).
- [145] M. Cacciari et al., “The t anti- t cross-section at 1.8-TeV and 1.96-TeV: A Study of the systematics due to parton densities and scale dependence”, *JHEP* **04** (2004) 068, [doi:10.1088/1126-6708/2004/04/068](https://doi.org/10.1088/1126-6708/2004/04/068), [arXiv:hep-ph/0303085](https://arxiv.org/abs/hep-ph/0303085).
- [146] S. Catani, D. de Florian, M. Grazzini, and P. Nason, “Soft gluon resummation for Higgs boson production at hadron colliders”, *JHEP* **07** (2003) 028, [doi:10.1088/1126-6708/2003/07/028](https://doi.org/10.1088/1126-6708/2003/07/028), [arXiv:hep-ph/0306211](https://arxiv.org/abs/hep-ph/0306211).
- [147] G. Cowan, K. Cranmer, E. Gross, and O. Vitells, “Asymptotic formulae for likelihood-based tests of new physics”, *Eur. Phys. J.* **C71** (2011) 1554, [doi:10.1140/epjc/s10052-011-1554-0](https://doi.org/10.1140/epjc/s10052-011-1554-0), [10.1140/epjc/s10052-013-2501-z](https://doi.org/10.1140/epjc/s10052-013-2501-z), [arXiv:1007.1727](https://arxiv.org/abs/1007.1727). [Erratum: *Eur. Phys. J.*C73,2501(2013)].
- [148] T. Junk, “Confidence level computation for combining searches with small statistics”, *Nucl. Instrum. Meth.* **A434** (1999) 435–443, [doi:10.1016/S0168-9002\(99\)00498-2](https://doi.org/10.1016/S0168-9002(99)00498-2), [arXiv:hep-ex/9902006](https://arxiv.org/abs/hep-ex/9902006).
- [149] A. L. Read, “Presentation of search results: The CL(s) technique”, *J. Phys.* **G28** (2002) 2693–2704, [doi:10.1088/0954-3899/28/10/313](https://doi.org/10.1088/0954-3899/28/10/313).
- [150] The ATLAS Collaboration, The CMS Collaboration, The LHC Higgs Combination Group Collaboration, “Procedure for the LHC Higgs boson search combination in Summer 2011”, [Technical Report CMS-NOTE-2011-005. ATL-PHYS-PUB-2011-11](https://arxiv.org/abs/1107.3541), CERN, Geneva, Aug, 2011.
- [151] G. Belanger, R. M. Godbole, L. Hartgring, and I. Niessen, “Top Polarization in Stop Production at the LHC”, *JHEP* **05** (2013) 167, [doi:10.1007/JHEP05\(2013\)167](https://doi.org/10.1007/JHEP05(2013)167), [arXiv:1212.3526](https://arxiv.org/abs/1212.3526).

- [152] CMS Collaboration, “Search for direct production of supersymmetric partners of the top quark in the all-jets final state in proton-proton collisions at $\sqrt{s} = 13$ TeV”, *JHEP* **10** (2017) 005, [doi:10.1007/JHEP10\(2017\)005](https://doi.org/10.1007/JHEP10(2017)005), [arXiv:1707.03316](https://arxiv.org/abs/1707.03316).
- [153] CMS Collaboration, “Search for top squark pair production in pp collisions at $\sqrt{s} = 13$ TeV using single lepton events”, *JHEP* **10** (2017) 019, [doi:10.1007/JHEP10\(2017\)019](https://doi.org/10.1007/JHEP10(2017)019), [arXiv:1706.04402](https://arxiv.org/abs/1706.04402).
- [154] CMS Collaboration, “Searches for invisible decays of the Higgs boson in pp collisions at $\sqrt{s} = 7, 8,$ and 13 TeV”, *JHEP* **02** (2017) 135, [doi:10.1007/JHEP02\(2017\)135](https://doi.org/10.1007/JHEP02(2017)135), [arXiv:1610.09218](https://arxiv.org/abs/1610.09218).
- [155] CMS Collaboration, “Search for invisible decays of a Higgs boson produced through vector boson fusion in proton-proton collisions at $\sqrt{s} = 13$ TeV”, [doi:10.1016/j.physletb.2019.04.025](https://doi.org/10.1016/j.physletb.2019.04.025), [arXiv:1809.05937](https://arxiv.org/abs/1809.05937).
- [156] CMS Collaboration, “Observation of $t\bar{t}H$ production”, *Phys. Rev. Lett.* **120** (2018), no. 23, 231801, [doi:10.1103/PhysRevLett.120.231801](https://doi.org/10.1103/PhysRevLett.120.231801), [arXiv:1804.02610](https://arxiv.org/abs/1804.02610).
- [157] ATLAS Collaboration, “Observation of Higgs boson production in association with a top quark pair at the LHC with the ATLAS detector”, *Phys. Lett.* **B784** (2018) 173–191, [doi:10.1016/j.physletb.2018.07.035](https://doi.org/10.1016/j.physletb.2018.07.035), [arXiv:1806.00425](https://arxiv.org/abs/1806.00425).
- [158] B. A. Dobrescu, G. D. Kribs, and A. Martin, “Higgs Underproduction at the LHC”, *Phys. Rev.* **D85** (2012) 074031, [doi:10.1103/PhysRevD.85.074031](https://doi.org/10.1103/PhysRevD.85.074031), [arXiv:1112.2208](https://arxiv.org/abs/1112.2208).
- [159] CMS Collaboration Collaboration, “Simplified likelihood for the re-interpretation of public CMS results”, [Technical Report CMS-NOTE-2017-001](https://arxiv.org/abs/1707.001), [CERN-CMS-NOTE-2017-001](https://arxiv.org/abs/1707.001), CERN, Geneva, Jan, 2017.
- [160] CMS Collaboration, “Search for top squarks and dark matter particles in opposite-charge dilepton final states at $\sqrt{s} = 13$ TeV”, 2018, [doi:10.17182/hepdata.79809](https://doi.org/10.17182/hepdata.79809).
- [161] CMS Collaboration, “Performance of the CMS missing transverse momentum reconstruction in pp data at $\sqrt{s} = 8$ TeV”, *JINST* **10** (2015), no. 02, P02006, [doi:10.1088/1748-0221/10/02/P02006](https://doi.org/10.1088/1748-0221/10/02/P02006), [arXiv:1411.0511](https://arxiv.org/abs/1411.0511).
- [162] W. Hollik et al., “Top dipole form-factors and loop induced CP violation in supersymmetry”, *Nucl. Phys.* **B551** (1999) 3–40, [doi:10.1016/S0550-3213\(99\)00396-X](https://doi.org/10.1016/S0550-3213(99)00396-X), [10.1016/S0550-3213\(99\)00201-1](https://doi.org/10.1016/S0550-3213(99)00201-1), [arXiv:hep-ph/9812298](https://arxiv.org/abs/hep-ph/9812298). [Erratum: *Nucl. Phys.*B557,407(1999)].

- [163] K. Agashe, G. Perez, and A. Soni, “Collider Signals of Top Quark Flavor Violation from a Warped Extra Dimension”, *Phys. Rev.* **D75** (2007) 015002, [doi:10.1103/PhysRevD.75.015002](https://doi.org/10.1103/PhysRevD.75.015002), [arXiv:hep-ph/0606293](https://arxiv.org/abs/hep-ph/0606293).
- [164] A. L. Kagan, G. Perez, T. Volansky, and J. Zupan, “General Minimal Flavor Violation”, *Phys. Rev.* **D80** (2009) 076002, [doi:10.1103/PhysRevD.80.076002](https://doi.org/10.1103/PhysRevD.80.076002), [arXiv:0903.1794](https://arxiv.org/abs/0903.1794).
- [165] T. Ibrahim and P. Nath, “The Top quark electric dipole moment in an MSSM extension with vector like multiplets”, *Phys. Rev.* **D82** (2010) 055001, [doi:10.1103/PhysRevD.82.055001](https://doi.org/10.1103/PhysRevD.82.055001), [arXiv:1007.0432](https://arxiv.org/abs/1007.0432).
- [166] T. Ibrahim and P. Nath, “The Chromoelectric Dipole Moment of the Top Quark in Models with Vector Like Multiplets”, *Phys. Rev.* **D84** (2011) 015003, [doi:10.1103/PhysRevD.84.015003](https://doi.org/10.1103/PhysRevD.84.015003), [arXiv:1104.3851](https://arxiv.org/abs/1104.3851).
- [167] C. Grojean, O. Matsedonskyi, and G. Panico, “Light top partners and precision physics”, *JHEP* **10** (2013) 160, [doi:10.1007/JHEP10\(2013\)160](https://doi.org/10.1007/JHEP10(2013)160), [arXiv:1306.4655](https://arxiv.org/abs/1306.4655).
- [168] F. Richard, “Can LHC observe an anomaly in $t\bar{t}Z$ production?”, [arXiv:1304.3594](https://arxiv.org/abs/1304.3594).
- [169] J. Bernabeu, D. Comelli, L. Lavoura, and J. P. Silva, “Weak magnetic dipole moments in two Higgs doublet models”, *Phys. Rev.* **D53** (1996) 5222–5232, [doi:10.1103/PhysRevD.53.5222](https://doi.org/10.1103/PhysRevD.53.5222), [arXiv:hep-ph/9509416](https://arxiv.org/abs/hep-ph/9509416).
- [170] A. Czarnecki and B. Krause, “On the dipole moments of fermions at two loops”, *Acta Phys. Polon.* **B28** (1997) 829–834, [arXiv:hep-ph/9611299](https://arxiv.org/abs/hep-ph/9611299).
- [171] ATLAS Collaboration, “Measurement of the $t\bar{t}W$ and $t\bar{t}Z$ production cross sections in pp collisions at $\sqrt{s} = 8$ TeV with the ATLAS detector”, *JHEP* **11** (2015) 172, [doi:10.1007/JHEP11\(2015\)172](https://doi.org/10.1007/JHEP11(2015)172), [arXiv:1509.05276](https://arxiv.org/abs/1509.05276).
- [172] ATLAS Collaboration, “Measurement of the $t\bar{t}Z$ and $t\bar{t}W$ production cross sections in multilepton final states using 3.2 fb^{-1} of pp collisions at $\sqrt{s} = 13$ TeV with the ATLAS detector”, *Eur. Phys. J.* **C77** (2017), no. 1, 40, [doi:10.1140/epjc/s10052-016-4574-y](https://doi.org/10.1140/epjc/s10052-016-4574-y), [arXiv:1609.01599](https://arxiv.org/abs/1609.01599).
- [173] CMS Collaboration, “Observation of top quark pairs produced in association with a vector boson in pp collisions at $\sqrt{s} = 8$ TeV”, *JHEP* **01** (2016) 096, [doi:10.1007/JHEP01\(2016\)096](https://doi.org/10.1007/JHEP01(2016)096), [arXiv:1510.01131](https://arxiv.org/abs/1510.01131).
- [174] CMS Collaboration, “Measurement of the cross section for top quark pair production in association with a W or Z boson in proton-proton collisions at $\sqrt{s} = 13$ TeV”, *JHEP* **08** (2018) 011, [doi:10.1007/JHEP08\(2018\)011](https://doi.org/10.1007/JHEP08(2018)011), [arXiv:1711.02547](https://arxiv.org/abs/1711.02547).

- [175] F. Caola, K. Melnikov, R. Röntsch, and L. Tancredi, “QCD corrections to ZZ production in gluon fusion at the LHC”, *Phys. Rev. D* **92** (2015) 094028, [doi:10.1103/PhysRevD.92.094028](https://doi.org/10.1103/PhysRevD.92.094028), [arXiv:1509.06734](https://arxiv.org/abs/1509.06734).
- [176] J. M. Campbell and R. K. Ellis, “MCFM for the Tevatron and the LHC”, *Nucl. Phys. Proc. Suppl.* **205-206** (2010) 10, [doi:10.1016/j.nuclphysbps.2010.08.011](https://doi.org/10.1016/j.nuclphysbps.2010.08.011), [arXiv:1007.3492](https://arxiv.org/abs/1007.3492).
- [177] S. Bolognesi et al., “On the spin and parity of a single-produced resonance at the LHC”, *Phys. Rev. D* **86** (2012) 095031, [doi:10.1103/PhysRevD.86.095031](https://doi.org/10.1103/PhysRevD.86.095031), [arXiv:1208.4018](https://arxiv.org/abs/1208.4018).
- [178] F. Cascioli et al., “ZZ production at hadron colliders in NNLO QCD”, *Phys. Lett. B* **735** (2014) 311, [doi:10.1016/j.physletb.2014.06.056](https://doi.org/10.1016/j.physletb.2014.06.056), [arXiv:1405.2219](https://arxiv.org/abs/1405.2219).
- [179] T. Melia, P. Nason, R. Rontsch, and G. Zanderighi, “W⁺W⁻, WZ and ZZ production in the POWHEG BOX”, *JHEP* **11** (2011) 078, [doi:10.1007/JHEP11\(2011\)078](https://doi.org/10.1007/JHEP11(2011)078), [arXiv:1107.5051](https://arxiv.org/abs/1107.5051).
- [180] P. Nason and G. Zanderighi, “W⁺W⁻, WZ and ZZ production in the POWHEG-BOX-V2”, *Eur. Phys. J. C* **74** (2014) 2702, [doi:10.1140/epjc/s10052-013-2702-5](https://doi.org/10.1140/epjc/s10052-013-2702-5), [arXiv:1311.1365](https://arxiv.org/abs/1311.1365).
- [181] G. Luisoni, P. Nason, C. Oleari, and F. Tramontano, “HW[±]/HZ + 0 and 1 jet at NLO with the POWHEG BOX interfaced to GoSam and their merging within MiNLO”, *JHEP* **10** (2013) 083, [doi:10.1007/JHEP10\(2013\)083](https://doi.org/10.1007/JHEP10(2013)083), [arXiv:1306.2542](https://arxiv.org/abs/1306.2542).
- [182] CMS Collaboration Collaboration, “Pileup Removal Algorithms”, [Technical Report CMS-PAS-JME-14-001](https://arxiv.org/abs/1404.001), CERN, Geneva, 2014.
- [183] A. Hocker et al., “TMVA - Toolkit for Multivariate Data Analysis”, [arXiv:physics/0703039](https://arxiv.org/abs/physics/0703039).
- [184] F. Chollet et al., “Keras”. <https://keras.io>, 2015.
- [185] M. Abadi et al., “TensorFlow: Large-Scale Machine Learning on Heterogeneous Systems”, 2015. Software available from [tensorflow.org](https://www.tensorflow.org).
- [186] CMS Collaboration, “First Measurement of the Cross Section for Top-Quark Pair Production in Proton-Proton Collisions at $\sqrt{s} = 7$ TeV”, *Phys. Lett.* **B695** (2011) 424–443, [doi:10.1016/j.physletb.2010.11.058](https://doi.org/10.1016/j.physletb.2010.11.058), [arXiv:1010.5994](https://arxiv.org/abs/1010.5994).
- [187] CMS Collaboration Collaboration, “Performance of Methods for Data-Driven Background Estimation in SUSY Searches”, [Technical Report CMS-PAS-SUS-10-001](https://arxiv.org/abs/1004.001), CERN, Geneva, 2010.

- [188] CMS Collaboration, “Search for new physics in same-sign dilepton events in proton–proton collisions at $\sqrt{s} = 13$ TeV”, *Eur. Phys. J.* **C76** (2016), no. 8, 439, [doi:10.1140/epjc/s10052-016-4261-z](https://doi.org/10.1140/epjc/s10052-016-4261-z), [arXiv:1605.03171](https://arxiv.org/abs/1605.03171).
- [189] J. Campbell, R. K. Ellis, and R. Röntsch, “Single top production in association with a Z boson at the LHC”, *Phys. Rev.* **D87** (2013) 114006, [doi:10.1103/PhysRevD.87.114006](https://doi.org/10.1103/PhysRevD.87.114006), [arXiv:1302.3856](https://arxiv.org/abs/1302.3856).
- [190] S. Frixione et al., “Electroweak and QCD corrections to top-pair hadroproduction in association with heavy bosons”, *JHEP* **06** (2015) 184, [doi:10.1007/JHEP06\(2015\)184](https://doi.org/10.1007/JHEP06(2015)184), [arXiv:1504.03446](https://arxiv.org/abs/1504.03446).
- [191] CMS Collaboration, “Observation of single top quark production in association with a Z boson in proton-proton collisions at $\sqrt{s} = 13$ TeV”, *Phys. Rev. Lett.* **122** (2019) 132003, [doi:10.1103/PhysRevLett.122.132003](https://doi.org/10.1103/PhysRevLett.122.132003), [arXiv:1812.05900](https://arxiv.org/abs/1812.05900).
- [192] CMS Collaboration, “Measurement of the $Z\gamma$ Production Cross Section in pp Collisions at 8 TeV and Search for Anomalous Triple Gauge Boson Couplings”, *JHEP* **04** (2015) 164, [doi:10.1007/JHEP04\(2015\)164](https://doi.org/10.1007/JHEP04(2015)164), [arXiv:1502.05664](https://arxiv.org/abs/1502.05664).
- [193] CMS Collaboration, “Measurement of the cross section for electroweak production of $Z\gamma$ in association with two jets and constraints on anomalous quartic gauge couplings in proton–proton collisions at $\sqrt{s} = 8$ TeV”, *Phys. Lett.* **B770** (2017) 380–402, [doi:10.1016/j.physletb.2017.04.071](https://doi.org/10.1016/j.physletb.2017.04.071), [arXiv:1702.03025](https://arxiv.org/abs/1702.03025).
- [194] LHC Higgs Cross Section Working Group Collaboration, “Handbook of LHC Higgs Cross Sections: 4. Deciphering the Nature of the Higgs Sector”, [doi:10.23731/CYRM-2017-002](https://doi.org/10.23731/CYRM-2017-002), [arXiv:1610.07922](https://arxiv.org/abs/1610.07922).
- [195] R. Röntsch and M. Schulze, “Constraining couplings of top quarks to the Z boson in $t\bar{t} + Z$ production at the LHC”, *JHEP* **07** (2014) 091, [doi:10.1007/JHEP09\(2015\)132](https://doi.org/10.1007/JHEP09(2015)132), [10.1007/JHEP07\(2014\)091](https://doi.org/10.1007/JHEP07(2014)091), [arXiv:1404.1005](https://arxiv.org/abs/1404.1005).
[Erratum: *JHEP*09,132(2015)].
- [196] R. Röntsch and M. Schulze, “Probing top-Z dipole moments at the LHC and ILC”, *JHEP* **08** (2015) 044, [doi:10.1007/JHEP08\(2015\)044](https://doi.org/10.1007/JHEP08(2015)044), [arXiv:1501.05939](https://arxiv.org/abs/1501.05939).
- [197] N. D. Christensen and C. Duhr, “FeynRules - Feynman rules made easy”, *Comput. Phys. Commun.* **180** (2009) 1614–1641, [doi:10.1016/j.cpc.2009.02.018](https://doi.org/10.1016/j.cpc.2009.02.018), [arXiv:0806.4194](https://arxiv.org/abs/0806.4194).
- [198] C. Degrande et al., “UFO - The Universal FeynRules Output”, *Comput. Phys. Commun.* **183** (2012) 1201–1214, [doi:10.1016/j.cpc.2012.01.022](https://doi.org/10.1016/j.cpc.2012.01.022), [arXiv:1108.2040](https://arxiv.org/abs/1108.2040).

- [199] CMS Collaboration Collaboration, “CMS luminosity measurement for the 2017 data-taking period at $\sqrt{s} = 13$ TeV”, [Technical Report CMS-PAS-LUM-17-004](#), CERN, Geneva, 2018.
- [200] CMS Collaboration, “Identification of b-quark jets with the CMS experiment”, *JINST* **8** (2013) P04013, [doi:10.1088/1748-0221/8/04/P04013](#), [arXiv:1211.4462](#).
- [201] P. Skands, S. Carrazza, and J. Rojo, “Tuning PYTHIA 8.1: the Monash 2013 Tune”, *Eur. Phys. J.* **C74** (2014), no. 8, 3024, [doi:10.1140/epjc/s10052-014-3024-y](#), [arXiv:1404.5630](#).
- [202] S. Argyropoulos and T. Sjöstrand, “Effects of color reconnection on $t\bar{t}$ final states at the LHC”, *JHEP* **11** (2014) 043, [doi:10.1007/JHEP11\(2014\)043](#), [arXiv:1407.6653](#).
- [203] J. R. Christiansen and P. Z. Skands, “String Formation Beyond Leading Colour”, *JHEP* **08** (2015) 003, [doi:10.1007/JHEP08\(2015\)003](#), [arXiv:1505.01681](#).
- [204] CMS Collaboration, “Measurement of the WZ production cross section in pp collisions at $\sqrt{s} = 13$ TeV”, *Phys. Lett.* **B766** (2017) 268–290, [doi:10.1016/j.physletb.2017.01.011](#), [arXiv:1607.06943](#).
- [205] CMS Collaboration, “Measurements of the $pp \rightarrow WZ$ inclusive and differential production cross section and constraints on charged anomalous triple gauge couplings at $\sqrt{s} = 13$ TeV”, [arXiv:1901.03428](#).
- [206] J. A. Aguilar-Saavedra, “A Minimal set of top anomalous couplings”, *Nucl. Phys.* **B812** (2009) 181–204, [doi:10.1016/j.nuclphysb.2008.12.012](#), [arXiv:0811.3842](#).
- [207] C. Zhang and S. Willenbrock, “Effective-Field-Theory Approach to Top-Quark Production and Decay”, *Phys. Rev.* **D83** (2011) 034006, [doi:10.1103/PhysRevD.83.034006](#), [arXiv:1008.3869](#).
- [208] J. A. Aguilar-Saavedra and J. Bernabeu, “W polarisation beyond helicity fractions in top quark decays”, *Nucl. Phys.* **B840** (2010) 349–378, [doi:10.1016/j.nuclphysb.2010.07.012](#), [arXiv:1005.5382](#).
- [209] C. Zhang, N. Greiner, and S. Willenbrock, “Constraints on Non-standard Top Quark Couplings”, *Phys. Rev.* **D86** (2012) 014024, [doi:10.1103/PhysRevD.86.014024](#), [arXiv:1201.6670](#).
- [210] ATLAS Collaboration, “Measurement of the $t\bar{t}Z$ and $t\bar{t}W$ cross sections in proton-proton collisions at $\sqrt{s} = 13$ TeV with the ATLAS detector”, [arXiv:1901.03584](#).

- [211] A. Buckley et al., “Constraining top quark effective theory in the LHC Run II era”, *JHEP* **04** (2016) 015, [doi:10.1007/JHEP04\(2016\)015](https://doi.org/10.1007/JHEP04(2016)015), [arXiv:1512.03360](https://arxiv.org/abs/1512.03360).
- [212] N. P. Hartland et al., “A Monte Carlo global analysis of the Standard Model Effective Field Theory: the top quark sector”, [arXiv:1901.05965](https://arxiv.org/abs/1901.05965).

Acknowledgements

A PhD thesis is never the product of just one individual alone. Several people helped, motivated and encouraged me during the work on this thesis, and their impact cannot be overestimated. I spent almost five years at HEPHY, and what started out as a small project during my master's studies culminated in the highlights presented in this thesis. Therefore, I'm especially thankful to Robert Schöffbeck, who introduced me to experimental particle physics, and who made this thesis possible by providing the funding through a binational research project. His eye for interesting topics, as well as his encouraging and direct way of supervision motivated me to always give my very best. I am very grateful to Jochen Schieck, who accepted me as his PhD student, and to all colleagues at HEPHY who provided invaluable input and support. Wolfgang, Ivan, Manfred and Claudia for their feedback and discussions, be it at short term stays at CERN or in Vienna. Illia, Didar and Tom for their hospitality during my stay in Ghent, and for the nice collaboration during most of the projects that are included in this thesis. I spent years of my life with great fellow students at different locations of HEPHY, especially Ece, Mateusz and Navid with whom I shared the notorious office at $\Omega\Delta\Gamma$ (kudos to David for the name!). Thanks to all other fellow PhD and master students, the various Lukas and Markus, to Federico, Thomas, Sebastian, Janik, Priya, Jui-Lin ... and everybody else that I worked with (or for). Not to forget Alberto, Suchita, Josef, Martin, Wolfgang, Vasile, Dietrich, Xiaoyong and Ilse for nice lunch time discussions with more or less physics content, computing support, and everything else. Sorry to all the ones I did forget to mention in the end. I didn't mean to. Thanks to the doctoral program particles and interactions (DKPI) for accepting me as associated student, for providing additional funding, and for organizing interesting seminars, schools and retreats. Getting together with students and faculty members from different parts of particle physics cannot be valued enough.

I also want to show gratitude to my friends outside of HEP with whom I enjoyed my rare spare time during the last years. You know who you are, and I don't want to embarrass myself by forgetting someone important. I am grateful to my parents and grandparents, to my sisters Tini and Sonja, to Holger and Paulina for their unconditional support during all the years of my studies, for providing backing during tough periods and support in various ways, and bringing joy to my life. This thesis marks the end of an almost nine year long academic

Acknowledgements

journey, eight of which I shared with my beautiful girlfriend Madeleine. I cannot thank her enough for the wonderful time together, and her encouraging attitude during the better or worse times.

Thank you!